Title
Femtosecond Dynamics in Liquid Microjets Studied by Extreme Ultraviolet Photoelectron Spectroscopy

Author
Heim, Zachary N

Publication Date
2023

Peer reviewed|Thesis/dissertation

Femtosecond Dynamics in Liquid Microjets Studied by Extreme Ultraviolet Photoelectron Spectroscopy

by

Zachary N. Heim

A dissertation submitted in partial satisfaction of the

requirements for the degree of

Doctor of Philosophy

in

Chemistry

in the

Graduate Division

of the

University of California, Berkeley

Committee in charge:

Professor Daniel M. Neumark, Chair
Professor Stephen R. Leone
Professor Eva Nogales

Summer 2023

Abstract

Femtosecond Dynamics in Liquid Microjets Studied by Extreme Ultraviolet Photoelectron Spectroscopy

by

Zachary Nicholas Heim

Doctor of Philosophy in Chemistry

University of California, Berkeley

Professor Daniel M. Neumark, Chair

The combination of the liquid microjet technique and femtosecond time-resolved photoelectron spectroscopy offers a valuable means to study the electronic photoinduced dynamics of liquids and solvated species. Here, a liquid microjet formed by forcing fluid through a few micron-diameter capillary is crossed with pump and probe pulses to first excite the sample some known time before the sample is photoionized. By collecting and energy analyzing the resultant photoelectrons, the transient electronic states populated by the pump pulse can be observed and excited state population tracked as it relaxes on femtosecond to picosecond timescales.

A major limitation for the study of solvated species using femtosecond photoelectron spectroscopy has been the ability to reach probe energies greater than 10 eV in a tabletop experiment. A readily accessible solution to this limitation exists in the high harmonic generation (HHG) technique, by which femtosecond pulses well in excess of 10 eV can be generated in a tabletop setup. This dissertation details the implementation of an HHG-based beamline used to generate probe pulses of 21.7 eV integrated into the liquid jet time-resolved photoelectron spectroscopy (LJ-TRPES) experiment.

Previously, this project had employed UV pump/UV probe LJ-TRPES to study the excited state dynamics of solvated electrons and nucleic acid constituents (NACs). A summary of this work is given and the respective mechanisms for relaxation discussed. Additionally, the advances in tabletop light sources extending into the extreme ultraviolet (XUV) and soft x-ray regimes are discussed in the context of observation of full valence level dynamics and the potential for tracking dynamics with element specificity.

Finally, the characterization and application of these new XUV probe capabilities is discussed. The XUV probe has been used to take static, pump-probe, and LAPE

spectra of a variety of gas and solution phase systems, thereby demonstrating the capabilities of the technique. In particular, the observation of the ultrafast relaxation pathways in a variety of NACs is presented. The first time-resolved photoelectron spectroscopy studies using a liquid flat jet source and observation of adenine excited state relaxation using an XUV probe are notable results. These studies reveal dynamics that the experiment was previously blind to due to the probe energy limitations.

To Amy and Beans

Thanks for the useful discussions

Contents

Contents ii

List of Figures v

List of Tables ix

List of Acronyms x

1 Introduction 1

1.1 Overview ... 1
1.2 Light Induced Dynamics in Solution ... 2
1.2.1 Photochemistry in DNA ... 4
1.3 Photoelectron spectroscopy ... 7
1.3.1 General Principles and Selection Rules ... 8
1.3.2 Time-Resolved Photoelectron Spectroscopy ... 11
1.4 Non-Adiabatic Dynamics ... 14
1.4.1 Conical Intersections ... 15
1.5 Generation and Use of XUV Light ... 17
1.5.1 High Harmonic Generation ... 17
1.5.2 Laser Assisted Photoelectric Effect ... 21
1.6 Summary of Following Chapters ... 22
1.7 References ... 23

2 Experimental Methods and Materials 33

2.1 Overview ... 33
2.2 Generating Ultrafast Laser Pulses ... 34
2.2.1 The Ultrafast Amplifier ... 35
2.2.2 Optical Parametric Amplification ... 36
2.2.3 Second Harmonic and Sum Frequency Generation ... 39
2.2.4 High Harmonic Generation ... 41
2.2.5 Measuring and Steering XUV Harmonics ... 44
2.3 Liquid Microjets and Flatjets for Photoelectron Spectroscopy ... 55
2.3.1 The Liquid Microjet Technique ... 56
2.3.2 Liquid Flatjets for Photoelectron Spectroscopy ... 58
2.3.3 Liquid Jet Mount and Catcher ... 61

2.3.4 Electron Scattering and Probe Depth Considerations 67
2.3.5 Streaming Potentials in Liquid Microjets 71
2.3.6 Applying a Bias Voltage to Liquid Jets 72
2.3.7 Space-Charge Effect 75
2.4 Photoelectron Spectrometer 76
2.4.1 Interaction Region 76
2.4.2 Magnetic Bottle Time-of-Flight Spectrometer 79
2.4.3 Calibrating the Spectrometer 82
2.4.4 Photoelectron Decelerator 84
2.4.5 Detector Assembly 86
2.5 Data Collection and Processing 88
2.5.1 LabVIEW Data Collection Software 89
2.5.2 Post-Processing of Spectra 91
2.5.3 Data Analysis Methods 92
2.6 References 93

3 Nonadiabatic Dynamics Studied by Liquid-Jet Time-Resolved Photoelectron Spectroscopy 100
3.1 Conspectus 100
3.2 Introduction 102
3.3 Experimental Apparatus 104
3.4 Results and Discussion 106
3.4.1 Ultrafast Dynamics of Solvated Electrons 106
3.4.2 Ultrafast Excited State Dynamics in NACs 108
3.4.2.1 Relaxation from the $S_1(^1\pi\pi^*)$ Excited State 110
3.4.2.2 Differences in Nucleotide Relaxation Lifetimes 112
3.5 Future Prospects of Using Femtosecond XUV Probes 113
3.6 Concluding Remarks 115
3.7 References 116

4 Implementation and Initial TRPES Results Using an XUV Probe 126
4.1 Overview 126
4.2 Characterizing XUV Probe 127
4.2.1 Photoelectron Spectra Collected to Characterize Harmonics ... 127
4.2.2 Spatial Characterization 129
4.3 Photoelectron Spectra of Gaseous Species 131
4.3.1 Water Vapor 131
4.3.2 LAPE in $Ar_{(g)}$ and $H_2O_{(g)}$ 132
4.3.3 Methyl Iodide TRPES as a Test System 136
4.4 Photoelectron Spectra of Solvated Species Studied 137
4.4.1 Static PES of $H_2O_{(l)}$ and I^- 138

4.4.2 LAPE Spectra from Solutions 139
4.4.3 LJ-TRPES of Several NACs 140
4.5 Conclusion and Outlook 145
4.6 References 146

A LabVIEW Code Updates 150
A.1 Overview 150
A.2 Changes to Static Collection Code 150
A.3 Changes to Time-Resolved Data Collection Code 153
A.4 References 156

B Machine Drawings 157
B.1 Overview 157

C Laser Alignment Tips and Tricks 186
C.1 Alignment Instructions and Tips 186
C.2 Aligning Ultrafast Laser Pulses 187
C.2.1 General Alignment Safety Concerns 188
C.2.2 Internal Alignment 189
C.2.3 TOPAS-Prime and NirUVis Alignment 198
C.2.4 External optic alignment 207
C.2.5 XUV Beamline Alignment Notes 209

D Publications from Graduate Work 213

List of Figures

Chapter 1 Figures

1.1 Absorption spectra and structure of the canonical nucleobases 4
1.2 Absorption spectra of the thymine-derived and adenine-derived NACs 5
1.3 Schematic of oligonucleotide relaxation processes 7
1.4 Three step model of HHG 18

Chapter 2 Figures

2.1 Detailed optical table layout 34
2.2 Quadrupler layout 39
2.3 Semi-infinite gas cell assembly and schematic representation of HHG occurring at the exit of the gas cell 43
2.4 XUV beamline with relevant components labeled 45
2.5 Nanograting-based spectrometer assembly 47
2.6 Beam analyzer harmonic image 48
2.7 Schematic diagram of the multilayer mirror 50
2.8 Transmission of filters and reflectivity of the multilayer mirror and their effect on photoelectron spectra 51
2.9 XUV beamline layout from toroidal mirror to annular mirror 52
2.10 XUV photodiode responsivity and oscilloscope trace 54
2.11 Images of the liquid microjet 57
2.12 Liquid flat jet images 60
2.13 Liquid jet motion and catcher apparatus 62
2.14 Schematic of catcher apparatus 65
2.15 Inelastic mean free path and electron attenuation length plotted 69
2.16 Images of the jet biasing setup 73
2.17 Effect of biasing potential on photoelectron spectra 74
2.18 Interaction region overview 78
2.19 Schematic of the magnetic bottle 80
2.20 Xenon calibration spectra 83
2.21 Various images of the decelerator assembly 85
2.22 MCP detector images and circuit diagram 87
2.23 Thresholding noise reduction algorithm schematic 91

Chapter 3 Figures

3.1 Schematic diagram of the interaction region 105
3.2 CTTS energy level diagram and LJ-TRPES spectra 108
3.3 Schematic of relevant electronic states in thymine, thymidine, and thymidine monophosphate relaxation 109
3.4 TRPE spectra of thymine and thymidine monophosphate 111
3.5 Main conformers of thymidine and thymidine monophosphate 112
3.6 Optical layout used to generate pump and probe pulses in the XUV LJ-TRPES experiments 115

Chapter 4 Figures

4.1 Harmonic spectrum of 800 nm harmonics used to ionize argon 128
4.2 Harmonic spectrum of 400 nm harmonics ionizing xenon and argon 129
4.3 400 nm pump focus profile taken as an image on a CMOS sensor 130
4.4 Pump – probe overlap profile scans 131
4.5 Water vapor photoelectron spectra 132
4.6 Argon LAPE spectra 133
4.7 Temporal response taken from LAPE signal in argon 134
4.8 Water vapor LAPE spectra 135
4.9 Methyl iodide potential surfaces 136
4.10 Methyl iodide TRPES 137
4.11 Water vapor, liquid water, and aqueous iodide spectra 138
4.12 LAPE spectra of liquid water 140
4.13 Proposed relaxation mechanism for thymine-derived NACs 141
4.14 Thymine and Uridine TRPES 142
4.15 Comparison of Thymine TRPE spectra taken with a flat jet versus with a cylindrical jet 143
4.16 Adenine and Adenosine TRPES 144

Appendix A Figures

A.1 Effect of thresholding algorithms on single-shot spectra 151
A.2 Static averaging LabVIEW code 152
A.3 Modified portion of LabVIEW code showing thresholding 153
A.4 Front panel of time-resolved LabVIEW code 153
A.5 Implementation of the DC thresholding algorithm 154
A.6 Delay randomization and background subtraction code 155
A.7 Shutter functionality in time-resolved code 155

Appendix B Figures

B.1 Jet and catcher manipulation assembly overview 158
B.2 Jet and catcher motion assembly overview 159
B.3 Flange with feedthroughs for motion assembly 160
B.4 Modified 10" CF flange with holes for BNC feedthroughs 161
B.5 Base plate for mounting stages for catcher and jet assembly 162
B.6 Thread adapter for adapting stages to base plate 163
B.7 Mounting arms assembly 164
B.8 Horizontal adapter bracket for microjet 165
B.9 Back side microjet mount 166
B.10 Front side microjet mount 167
B.11 Vertical mounting arm for microjet 168
B.12 Thread adapter for catcher stage 169
B.13 Vertical catcher arm 170
B.14 Horizontal catcher arm 171
B.15 ½" NPT PEEK union 172
B.16 Copper catcher v1.0 173
B.17 Copper catcher v2.0 174
B.18 Thread adapter for catcher v2.0 175
B.19 Decelerator assembly shown inside the flight tube 176
B.20 Decelerator assembly 177
B.21 Decelerator front electrode assembly 178
B.22 Flight tube flange modified with BNC feedthroughs 179
B.23 Decelerator tube 180
B.24 Mounting collars welded to interior of existing flight tube 181
B.25 Ring welded to back of decelerator tube for attaching mesh 182
B.26 Ring welded to front of decelerator for mounting to flight tube and attaching front mesh assembly 183
B.27 Copper electrode plate for securing mesh 184
B.28 PEEK collar electrically isolating decelerator 185

Appendix C Figures

C.1 Amplifier cavity of the Astrella with important components labeled 192
C.2 Signal from unused diffraction orders repurposed for alignment centered on a target 193
C.3 Amplifier seed alignment onto Ti:Sapphire crystal mount 194
C.4 Typical spectrum of Oscillator output 195
C.5 Amplifier spectrum showing (a) modulation and (b) no modulation 198
C.6 Overall internal alignment of the TOPAS 200
C.7 WLG leg of the TOPAS alignment diagram 201
C.8 Alternative view of the optical components shown in Figure C.7 201
C.9 TOPAS preamplifier stage 202

C.10 Alternative view of the optical components shown in Figure C.9 203
C.11 TOPAS power amplification stage 204
C.12 NirUVis beam path for SHSFS (235-265 nm) 205
C.13 External beam path with relevant optics labeled 206

List of Tables

Chapter 1 Tables

1.1 Ionization potentials of common harmonic generation media..... 19

Chapter 2 Tables

2.1 Diffraction angle from a 100 nm periodicity nanograting for relevant harmonics..... 47

List of Acronyms

A	Adenine
AC	Alternating Current
ADC	Analog-to-Digital Converter
Ado	Adenosine
AM	Annular Mirror
AMP	Adenosine Monophosphate
AOI	Angle-of-Incidence
AR	Anti-reflective
ASE	Amplified Spontaneous Emission
AWG	American Wire Gauge
BA	Beam Analyzer
BBO	ß-Barium Borate
BD	Beam Dump
BNC	Bayonet Nut Coupling
BOA	Born-Oppenheimer Approximation
BS	Beam Splitter
C	Cytosine
CF	Conflat
CI	Conical Intersection
CM	Curved Mirror
CPA	Chirped Pulse Amplification
CTTS	Charge-Transfer-to-Solvent
CW	Continuous Wave
CXRO	Center for X-ray Optics
DAC	Digital to Analog Converter
DAS	Decay-Associated Spectrum
DC	Direct Current
DFG	Difference Frequency Generation
DM	Dichroic Mirror
DNA	Deoxyribonucleic Acid
DS	Delay Stage
EAL	Electron Attenuation Length
eBE	Electron Binding Energy
eKE	Electron Kinetic Energy
EM	End Mirror
FC	Franck-Condon

FEMM	Finite Element Method Magnetics
FGR	Fermi's Golden Rule
FHG	Fourth Harmonic Generation
FPS	Frames per Second
FROG	Frequency Resolved Optical Gating
FSR	Full Scale Range
FU	Fluorescence Upconversion
FWHM	Full Width at Half Maximum
G	Guanine
GDD	Group Delay Dispersion
GLA	Global Lifetime Analysis
GRENOUILLE	Grating-Eliminated No-Nonsense Observation of Ultrafast Incident Laser Light E-Fields
GUI	Graphical User Interface
GVD	Group Velocity Delay
HHG	High Harmonic Generation
HOMO	Highest Occupied Molecular Orbital
HPLC	High Performance Liquid Chromatography
HR	High-Reflector
I	Iris
I.D.	Inner Diameter
IC	Internal Conversion
IMFP	Inelastic Mean Free Path
IR	Infrared
IRF	Instrument Response Function
ISC	Intersystem Crossing
KF	Kleinflansch
L	Lens
LAPE	Laser Assisted Photoelectric Effect
LBL	Lawrence Berkeley Lab
LBNL	Lawrence Berkeley National Lab
LBO	Lithium Triborate
LJ-PES	Liquid Jet Photoelectron Spectroscopy
LJ-TRPES	Liquid Jet Time-Resolved Photoelectron Spectroscopy
LPI	Lines Per Inch
LUMO	Lowest Unoccupied Molecular Orbital
M	Mirror
MB	Magnetic Bottle
MB-ToF	Magnetic Bottle Time-of-Flight
MCP	Microchannel Plate
MFP	Mean Free Path
ML	Multilayer
MM	Multilayer Mirror
MP	Megapixel

MPI	Multi-Photon Ionization
MS	Manual Stage
NAC	Nucleic Acid Constituent
NC	Nonlinear Crystal
ND	Neutral Density
Nd:YAG	Neodymium Yttrium Aluminum Garnett
Nd:YLF	Neodymium Yttrium Lithium Fluoride
NIST	National Institute for Standards and Technology
NPT	National Pipe Thread
O.D.	Outer Diameter
OD	Optical Density
OPA	Optical Parametric Amplification
OPG	Optical Parametric Generation
OPS	Optically Pumped Semiconductor
PBS	Polarizing Beam Splitter
PC	Pockels Cell
PEEK	Polyether Ether Ketone
PES	Photoelectron Spectroscopy
PM	Pickoff Mirror
Pol	Polarizer
PVC	Polyvinyl Chloride
RNA	Ribonucleic Acid
RR	Retroreflector
S/N	Signal to Noise
SDG	Synchronization and Delay Generator
SFG	Sum Frequency Generation
SFI	Sum Frequency Idler
SHG	Second Harmonic Generation
SHI	Second Harmonic Idler
SHS	Second Harmonic Signal
SIGC	Semi-Infinite Gas Cell
subVI	sub-Virtual Instrument
T	Thymine
TA	Transient Absorption
Thd	Thymidine
THG	Third Harmonic Generation
TM	Toroidal Mirror
TMP	Thymidine Monophosphate
ToF	Time-of-Flight
TOPAS	Travelling-wave Optical Parametic Amplification System
TPI	Turns-per-Inch
TRPES	Time-Resolved Photoelectron Spectroscopy
TUV	Tunable Ultraviolet
U	Uracil

Urd	Uridine
USB	Universal Serial Bus
UV	Ultraviolet
VBE	Vertical Binding Energy
VF	Variable Neutral Density Filter
VIE	Vertical Ionization Energy
WLC	White Light Continuum
XUV	Extreme Ultraviolet

Acknowledgements

My time in grad school has given me the opportunity to both work with and become friends with some of the most spectacular people I've ever known. Given that my time in grad school has been somewhat longer than most, I've accumulated quite the motley crew of friends and colleagues that I need to recognize.

First, I should thank Dan for being an exceptional advisor and mentor to me these past 6 years. Thank you for all your excellent advice and suggestions and for giving me the latitude to choose how to approach the multitude of problems that have sprung up over the years. I am grateful you let me work in your group where your (and the rest of the group's) expansive knowledge and high standards have molded me into the scientist I am today.

I would be remiss if I didn't take the time to acknowledge all of the Neumark group alumni who I would argue have had the greatest impact on who I am as a person today. First, I need to recognize Blake for putting up with me for the majority of his Ph.D.. From teaching me the ropes in lab to dealing with my qual-ing phase to always being down to split a beer and talk about life, grad school wouldn't have been the same without you. Thank you to Holly, you were only around for a few months when I joined the group but had some of the best advice for grad school and I thoroughly enjoyed getting to hang out with Linus. Thank you, Alice, for always being open to trouble-shooting and passing along your tips and tricks for patching things back together. Thank you to Erin and Isaac, whose unexpected visits always kept me on my feet and kept things light. To Chin and Val, my cohort mates who joined the group with me, I'm thankful to have had such amazing lab mates supporting each other while we navigated joining groups and qual-ing. Thanks to Mark, who was a fantastic lab mate and an even better roommate. Thanks for always being down to share a beer and talk about lab. To the incredible postdocs that have been a part of the group while I've been here, Lou, Romain, Hugo, Marvin, Katherine, James, thanks for passing along so much of your wisdom. To the undergrads who I've had the pleasure of mentoring throughout my time here, Erica, Negar, Neil, thank you for helping make me a better mentor and scientist. To Masa and Do, I'm thankful for the many months we worked together and all we achieved together, and I'm incredibly excited to see all the two of you accomplish in the years to come. To all the other group members I'm leaving behind, thank you for your companionship on the d-level and best of luck finishing your own Ph.D.'s.

I was incredibly fortunate to start grad school with an extraordinary group of people. From working on quantum problem sets to closing out molo, I'm lucky to have found so many friends right away when I showed up to Berkeley. Thanks to Abdul, Bryan, Collin, David, Dipti, Eric, Isabel, Jenna, Jonathan, Josie, Katie, Kaydren, Maria, and Paul – you were all amazing people from day 1 and I'm extremely happy to have gotten to know you all.

To the beer bois – Mark, Blake, Chuck, Eugene, Katherine, and Michael – thanks for being my partners in crime and for helping make sure I actually socialized instead of being my usual shut-in self. To the friends in the Rittle and Arnold (x2) groups I've made in the last years of grad school, thank you for making my last years in grad school an unexpectedly fun experience.

To all of the staff, technicians, and administrators who've helped me along the way, I never could have succeeded without your help and expertise. In particular, our administrative assistant Michelle was always the one I turned to whenever I needed to do anything as she always knew exactly who to email. To our masterful machinist Doug, thank you for your extensive help making the lab run and for always being there to talk. The department will never be the same when you're gone. To Clint, Jody, and the rest of the shop personnel, you are really the ones who make research happen here and I thank you for all the help you've given me over the years.

To my parents, thank you for always being just a phone call away. I'm forever grateful for the oversized care packages filled with little bits of home that kept me going through all of this. Thank you for the recipes that let me spread a little taste of the Midwest to the bay area and introduce all of my friends to the delicacies that are caramel rolls and funeral hotdish. To the rest of my family, thank you for your constant love and support that has meant the world to me while I've been away from home.

Finally, to my wife Amy, I am eternally grateful to have had you and Beans by my side through thick and thin. I am so fortunate to have found someone as fiercely loving and compassionate as you. Your brilliance, courage, fearless curiosity, and dedication set the example of what I aspire to be. I love you forevermore and hope you know that, without you, none of this would have been possible.

Chapter 1 – Introduction

1.1 Overview

Water is ubiquitous throughout chemistry. Despite its prevalence, there are still open questions relating to the exact means by which it interacts with solutes on a molecular level and how exactly this interaction can affect ultrafast electronic dynamics [1-8]. The means to follow the full range of ultrafast dynamical processes for a given solute following absorption of light, especially high-energy light on the order of what's required to break chemical bonds [9], on the natural timescale of these processes is a requisite for being able to answer these questions. Progress towards this goal is presented using photoelectron spectroscopy employing a femtosecond extreme ultraviolet (XUV) probe in conjunction with a liquid microjet.

As a solvent, water is inextricably linked to the chemistry of biological systems. At the core of most biological systems is deoxyribonucleic acid (DNA), which can undergo a diverse array of photoinduced processes [9-14]. These processes primarily involve the photodeactivation of DNA following electronic excitation in the ultraviolet (UV), with fewer than 1% of excitations leading to formation of photolesions [15]. This remarkable photostability can be attributed to processes that occur on timescales as short as 10s of femtoseconds (1 fs = 10^{-15} seconds). Understanding these ultrafast processes by studying macromolecular DNA is nearly impossible due to the complexity of the system; as such, a bottom-up approach starting from isolated nucleobase and working through the nucleosides, nucleotides,

dinucleotides, etc., to understand the individual contributions of each subunit to the dynamics observed in the macromolecular DNA system [16].

Observing the full dynamical process of electronic relaxation to either the ground state or to long-lived excited states is crucial to understanding the complete process in which most energy from UV irradiation is converted into vibrational degrees of freedom [17]. To do this with photoelectron spectroscopy, wavelengths sufficient to ionize the solute of interest along the entire reaction coordinate must be used. To this end, a high-harmonic generation source upconverting the fundamental and second harmonic of the Ti:Sapphire femtosecond laser used into the XUV has been implemented as a means of reaching the probe wavelengths necessary to ionize any of the nucleic acid constituents (NACs) studied.

In this chapter, the influence of solvation on excited state dynamics is discussed generally and for NACs specifically. The theoretical underpinnings of photoelectron spectroscopy, both static and time-resolved, are discussed in the context of this experiment. An explanation of relevant non-adiabatic dynamics is included. The mathematical framework for high-harmonic generation is discussed briefly as it relates to the XUV light generated as well as the mathematical framework for describing the laser-assisted photoelectric effect, a significant diagnostic tool in this experiment. Finally, a brief summary of the content that can be found in the following chapters is given.

1.2 Light Induced Dynamics in Solution

Studying dynamics in the gas phase is advantageous as gas phase techniques offer high resolution and reduced complexity allowing an atomic-level understanding of the dynamics. However, the dynamics of isolated molecules or even clusters are ultimately only approximations of the dynamics of solutes in bulk solvent [1]. The effects of solvation can often be dramatic, altering the potential surface along a reaction coordinate so drastically that analogous photoinduced reactions can have distinct products depending on the presence of solvation effects [4, 7]. One of the most important solvents, water is capable of affecting dynamics through a myriad of interactions ranging from the semi-classical to the quantum: as a dielectric continuum, through hydrogen bonding, as a source of labile protons, as an electron donor, as a bath of vibrational modes to which solute motion can couple, and many more [3, 18-20].

Due to the complicated nature of water as a solvent, its interactions with solutes, particularly those interactions which affect electronic dynamics on ultrafast

timescales, are difficult to study and even more difficult to model theoretically [5, 7, 21, 22]. Liquid-jet time-resolved photoelectron spectroscopy (LJ-TRPES) is a state-specific means by which the effects of solvation on the dynamics following photoexcitation can be studied in a manner analogous to gas phase experiments, offering an invaluable point of comparison for theoretical calculations [23-25].

One of the most immediate consequences of solvation is the relative stabilization of electronic states due to effects such as polarization and hydrogen bonding. For example, in the NAC thymine the relevant photoinitiated dynamics involve an electron excited into the lowest unoccupied molecular orbital (LUMO) π^* orbital with the hole originating in the highest occupied molecular orbital (HOMO) π-type orbital with a chance for the molecule to undergo internal conversion such that the hole is in an n-type orbital localized on a carbonyl-oxygen. Due to the solvent interaction, the resultant $^1\pi\pi^*$ and $^1n\pi^*$ states are energetically reordered – the removal of electron density from the oxygen lone pair in the $^1n\pi^*$ state reduces overall stabilization from hydrogen bonding interactions with the lone pair relative to the effectively unchanged $^1\pi\pi^*$ state energy [26]. Additionally, charged states are stabilized substantially relative to neutral states – again using thymine as an example, the ground state neutral to ground state doublet cation spacing is reduced by over 1 eV relative to the same spacing between states in the gas phase [6]. This effect is explained by the Born equation for Gibbs free energy of solvation of ions, as given in Equation 1.1 [27].

$$\Delta G = -\frac{N_A z^2 e^2}{8\pi\varepsilon_0 r_0}\left(1 - \frac{1}{\varepsilon_r}\right) \tag{1.1}$$

Here, ΔG is the Gibbs free energy of solvation of an ion from gas phase to a dielectric medium, N_A is the Avogadro constant, z is the charge of the ion, e is the elementary charge (1.602×10^{-19} C), ε_0 is the permittivity of free space (8.854×10^{-12} F/m) , r_0 is the effective radius of the ion, and ε_r is the dielectric constant for the solvent (ε_r = 78.38 at 298 K for water [28]). Another important consequence of solvation is the introduction of a bath of vibrational modes that can couple to the solute motion. This leads to intermolecular energy transfer, by which a solute with internal energy corresponding to an effective temperature, T_{eff}, greater than the temperature of the surrounding bath, T_B, can dissipate the excess energy to the surrounding solvent [12, 29-33]. This is typically described as the coupling of vibrational motion in the solute to a combination of vibrational, rotational, and translational degrees of freedom in the solvent. The rate at which this happens is difficult to express simply, but it can be shown that the rate at which energy is transferred depends on the strength of coupling, solvent mass (relating to the amount of energy carried away due to collisions), and relative energy spacings of vibrations in the solvent and solute [1, 29, 34]. Water is an exceptionally good solvent for redistributing excess

vibrational energy from a solute for several reasons, including strong intermolecular interactions due to hydrogen bonding, light weight enabling efficient coupling of solute vibrations to rotational and translational solvent degrees of freedom, and broad energetic range of solvent vibrational modes to couple through. Typical shifting of photoelectron spectra due to vibrational energy redistribution in water occurs on the 1-2 picosecond timescale [35]. This is observed as a rapid narrowing and slight shift to higher binding energy in LJ-TRPES spectra.

1.2.1 Photochemistry in DNA

DNA is a polymeric material consisting of two chains of nucleotides held together through hydrogen-bonding interactions. The nucleotide monomers are made up of a phosphate group, a deoxyribose linker, and a nucleobase. The individual monomers are linked through phosphodiester bonds between the phosphate group of one nucleotide and the deoxyribose group of the adjoining nucleotide [36, 37]. The nucleobases encode information within DNA, with the purines (adenine and guanine) pairing with the pyrimidines (thymine and cytosine). In ribonucleic acid (RNA), thymine is substituted for uracil in addition to the addition of a hydroxyl group at the 2' position of the pentose ring in the monomers. In DNA or RNA assemblies, π-stacking leads [38] to interactions between neighboring bases in a single strand allowing for excitonic behavior of excited states in the polymer, further adding to the complexity of the system [9, 10, 39, 40].

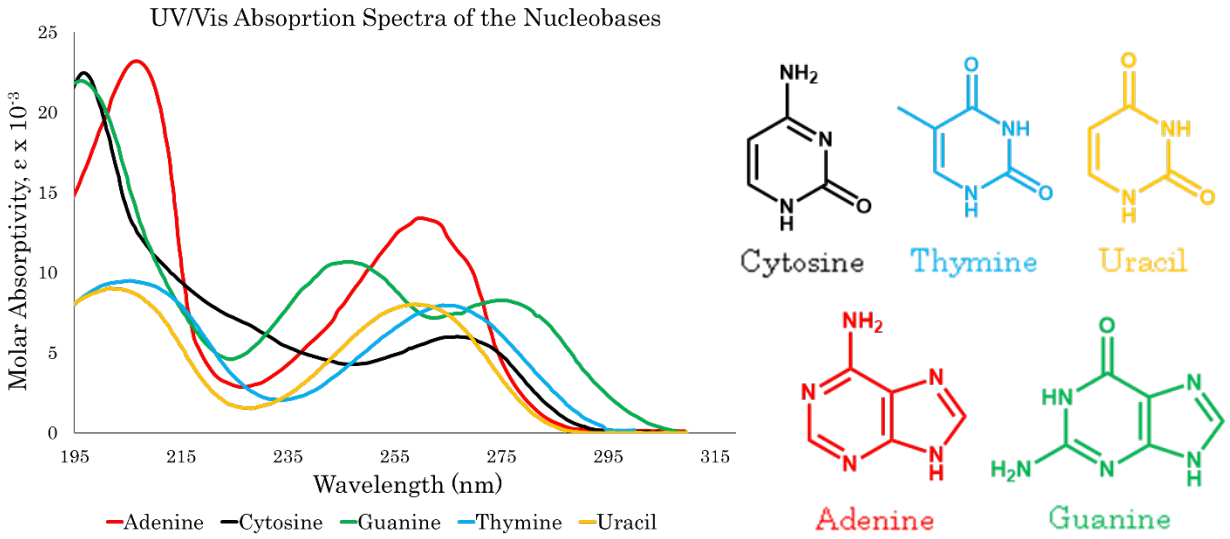

Figure 1.1 – Left: Absorption spectra of the canonical nucleobases. Adapted from [41]. Right: Structure of the nucleobases shown in the graph on the left.

To study dynamics in nucleic acids, reducing the complexity of the system to the base units through a bottom-up approach has been the basis for building a foundational knowledge of the dynamics subsequent to photoexcitation [10, 16]. The five canonical nucleobases, thymine (T), cytosine (C), adenine (A), guanine (G), and uracil (U), make up the core of nucleic acids and, as such, are a logical place to start studying ultrafast photophysics in nucleic acids. The nucleobases exhibit a UV absorption spectrum that closely resembles that of macromolecular nucleic acids [41], leading to the conclusion that the excitations induced by UV absorption are localized to the nucleobases. All nucleobases have absorption bands center around 260 nm and 200 nm; these absorption bands are nearly identical in the corresponding nucleosides and nucleotides [10, 41]. Absorption spectra for the nucleobases are shown in Figure 1.1. In Figure 1.2, a comparison of absorption spectra for the thymine and adenine families on NACs compared to E. Coli DNA demonstrating the essentially constant absorption features due to the nucleobases especially at ~260 nm.

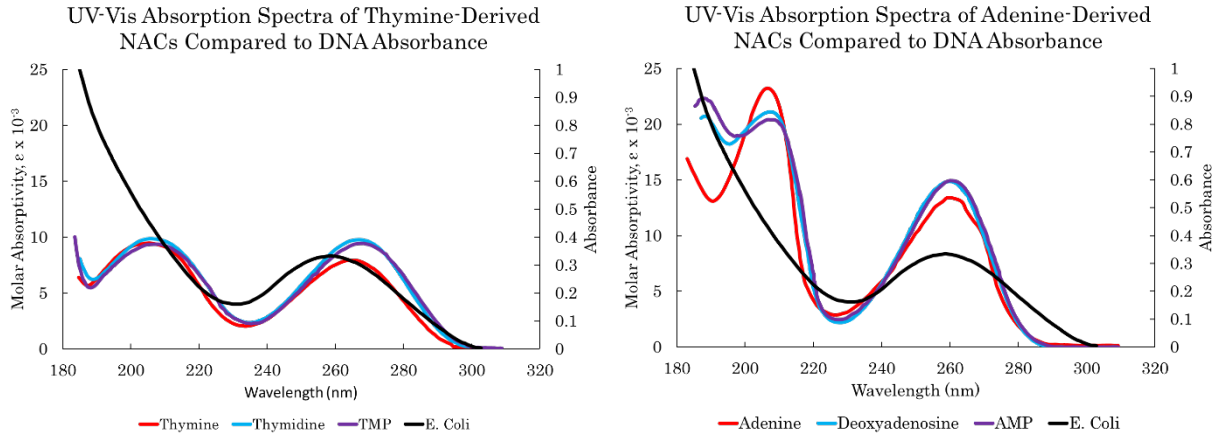

Figure 1.2 – Left: Absorption spectra of thymine (red), thymidine (blue), and thymidine monophosphate (TMP, purple) plotted alongside the absorbance of E. Coli DNA (black). The NACs are plotted with respect to molar absorptivity and the DNA is plotted in terms of absorbance. Adapted from [41]. Right: Absorption spectra of adenine (red), deoxyadenosine (blue), and adenosine monophosphate (AMP, purple) plotted alongside the absorbance of E. Coli DNA (black). The NACs are plotted with respect to molar absorptivity and the DNA is plotted in terms of absorbance. Adapted from [41].

The UV absorption bands, both at 200 nm and 260 nm, are attributed to excitations of $^1\pi\pi^*$ character [42-44]. The higher energy band consists of multiple states of comparable energy and character. The lower energy band consists of excitation of a single $^1\pi\pi^*$ transition. After excitation in the 260 nm band, a series of relaxation processes can occur, with internal conversion and intersystem crossing involving states of $^1n\pi^*$, $^3\pi\pi^*$, $^3n\pi^*$, and $^1\pi\sigma^*$ character all posited to play a role in the

relaxation process of the various nucleobases [14, 26, 43-53]. The dominant process in relaxation dynamics is understood to be the efficient repopulation of the ground electronic state through non-radiative transitions as implied by the miniscule fluorescence yield of ~10^{-4} [10]. A small portion of the excited state population can relax through an intermediate $^1n\pi^*$ state, potentially getting trapped in an excited electronic state for 10s of picoseconds [14, 54] and potentially leading to formation of genotoxic photolesions. Purine bases can also undergo bond dissociation through internal conversion to a $^1\pi\sigma^*$, generating a reactive adenyl radical as a result of photoexcitation [51, 52].

With the understanding of ultrafast dynamics in nucleic acid monomers rapidly reaching some semblance on consensus between contrasting experimental techniques, moving forward to the study of oligonucleotides is the logical progression of the bottom-up approach. Oligonucleotide relaxation dynamics are complicated by contributions from exciton dynamics, a schematic representation of the relevant processes is given in Figure 1.3. The initial excitation generates an exciton along the π-stacked nucleobases [55]. This exciton can interconvert to a localized excitation, undergoing internal conversion in a fashion mirroring what is seen in isolated monomers [56]. The initial exciton can also rapidly internally convert to the lowest energy exciton, with the excitation delocalized across the oligonucleotide . This fully delocalized exciton is thought to form a charge-transfer minimum in which an exciplex forms between two nucleobases [57-59], characterized by a conformationally distinct geometry with lifetime on the order of ~100 ps and rough approximation of the eBE ~0.8 eV greater than the excitonic minimum and ~1.6 eV greater eBE than the initially formed exciton [60]. The exact mechanism and relative contributions of these states is not well understood through absorption and fluorescence measurements alone, so progress towards characterizing the oligonucleotide systems through LJ-TRPES is presented in addition to studies of the NACs containing adenine and thymine.

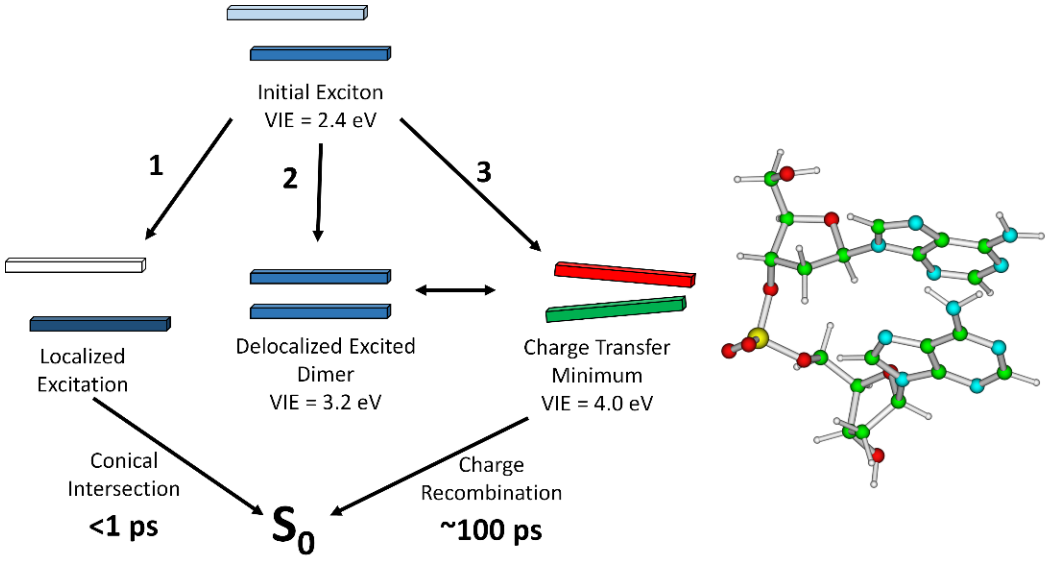

Figure 1.3 – Schematic of relaxation processes in oligonucleotides due to photoexcitation. Calculated ionization energies and approximate lifetimes given for each intermediate [60].

1.3 Photoelectron Spectroscopy

The experiments presented in this dissertation all rely on photoelectron spectroscopy (PES) to elucidate the light-induced dynamics at play. When a single photon interacts with a molecule,[1] an electron can be ejected from the molecule if the photon energy (hν) is greater than the binding energy of the ejected electron (eBE) [61]. The kinetic energy of the ejected photoelectron (eKE) can be determined through conservation of energy and can be represented by Equation 1.2.

$$eKE = h\upsilon - eBE \tag{1.2}$$

For any given molecule, depending on the photon energy, electrons from multiple orbitals can in principle be ionized. These electrons will have a characteristic kinetic energy that can then be used to distinguish the electronic state from which they originated. As will be discussed in the following sections, ejecting photoelectrons into a continuum of states in vacuum rather than exciting to a bound state substantially increases the electronic states observable in a given experiment compared to other techniques used to study the systems discussed in this dissertation [62]. Using photoelectrons as reporters of the dynamics in each experiment is also advantageous as many techniques for the manipulation and

[1] Multiphoton ionization is also possible for photons insufficient to ionize the molecule through a single photon process but will not be discussed here.

detection of charged particles exist. Together, these considerations make PES a powerful tool for studying the time-evolving electronic structure of a molecule.

1.3.1 General Principles and Selection Rules

To understand the theoretical foundation of PES, a few assumptions must first be made. First among these assumptions is that the nuclear and electronic degrees of freedom can be treated separately, also known as the Born-Oppenheimer Approximation (BOA) [63, 64]. This approximation holds so long as the nuclei making up the molecule of interest can be considered stationary relative to the motion of the electrons. If so, the electronic wavefunction will still be dependent on the position of the nuclei but can be treated separately when considering a Hamiltonian acting on the total molecular wavefunction.

Additional important approximations are made while simplifying the representation of the Hamiltonian for light-matter interactions. The full quantum Hamiltonian for an electron in an electromagnetic field is given by Equation 1.3 [63]:

$$\boldsymbol{\mathcal{H}} = -\frac{\hbar^2}{2m}\nabla^2 + V_s + \frac{i\hbar e}{2mc}(\boldsymbol{\nabla}\cdot\boldsymbol{A} + \boldsymbol{A}\cdot\boldsymbol{\nabla}) + \frac{e^2}{2mc^2}(\boldsymbol{A}\cdot\boldsymbol{A}) \tag{1.3}$$

where $\boldsymbol{\mathcal{H}}$ is the total Hamiltonian, $-\frac{\hbar^2}{2m}\nabla^2$ is the usual kinetic portion of the Hamiltonian, V_s is a static potential term to account for electron-nuclei interactions as well as any other static electric fields, $\boldsymbol{A}$ is the vector potential of the electromagnetic field acting on the charged particle to change its effective momentum, and $\frac{i\hbar e}{2mc}(\boldsymbol{\nabla}\cdot\boldsymbol{A} + \boldsymbol{A}\cdot\boldsymbol{\nabla}) + \frac{e^2}{2mc^2}(\boldsymbol{A}\cdot\boldsymbol{A})$ is the portion of the potential from the electromagnetic field interacting with a charged particle. For photoelectron spectroscopy, laser intensities are always kept low to avoid detrimental effects of space-charge interactions so it is a very good approximation to assume contributions from the $\frac{e^2}{2mc^2}(\boldsymbol{A}\cdot\boldsymbol{A})$ term are negligible. This is also known as the weak-field approximation. Choosing the appropriate gauge condition, $(\boldsymbol{\nabla}\cdot\boldsymbol{A} + \boldsymbol{A}\cdot\boldsymbol{\nabla})$ simplifies to $\boldsymbol{A}\cdot\boldsymbol{\nabla}$. After these approximations, the time-varying potential can be rewritten as Equation 1.4.

$$V = -\frac{e}{mc}A_0\cos(\boldsymbol{k}\cdot\boldsymbol{r} - \omega t)\,\boldsymbol{E}\cdot\boldsymbol{p} = -\frac{e}{2mc}A_0\left(e^{i(\boldsymbol{k}\cdot\boldsymbol{r}-\omega t)} + e^{-i(\boldsymbol{k}\cdot\boldsymbol{r}-\omega t)}\right)\boldsymbol{E}\cdot\boldsymbol{p} \tag{1.4}$$

Here, A_0 is the field amplitude, $\boldsymbol{E}$ is the unit vector pointing along $\boldsymbol{A}$, $\boldsymbol{p}$ is the momentum operator equivalent to $-i\hbar\boldsymbol{\nabla}$, $\boldsymbol{k}$ is the wavevector of the light field, $\boldsymbol{r}$ is the position, ω is the frequency of the light wave, and t is time. To calculate transition probabilities using this model for an oscillating field, we can invoke Fermi's Golden Rule (FGR). Important assumptions that need to be made to use this formalism for transition probability, including assuming the possible final states can be assumed to be a near continuum of states rather than a discrete set, assuming the perturbing field applied lasts much longer than the natural timescale of the transition such that only long-time behavior is retrieved,[2] and that first-order perturbation theory applies. We can now define the molecular wavefunction, $|\Psi(t)\rangle$, as a time-dependent function of electron and nuclear position, $\boldsymbol{r}$ and $\boldsymbol{R}$, respectively. The wavefunction can also be expressed as a set of eigenstates, $|n\rangle$, with energies E_n and time-dependent complex coefficients $c_n(t)$ as shown in Equation 1.5.

$$|\Psi(t)\rangle = |\Psi(\boldsymbol{r}, \boldsymbol{R};\ t)\rangle = \sum_n c_n(t) e^{-\frac{iE_n(t-t_0)}{\hbar}} |n\rangle \tag{1.5}$$

This molecular wavefunction is a solution for the time-dependent Schrödinger equation, $-i\hbar\frac{\partial|\Psi(t)\rangle}{\partial x} = \boldsymbol{\mathcal{H}}|\Psi(t)\rangle$. For the one-photon photoionization of some arbitrary molecule X with ground state energy $E_{gs} = E_i$ to a cationic state with energy $E_{cat} = E_f$ through emission of an electron with energy E_k as shown here:

$$X\left(E_{gs}\right) + \hbar\omega \rightarrow X^+(E_{cat}) + e^-(E_k) \tag{1.6}$$

where $E_{cat} + E_k$ are taken to be E_f, the total energy of the final cationic state combined with the emitted photoelectron with kinetic energy E_k. We then take $|\Phi_i\rangle = |\Psi(t=0)\rangle$ as the initial molecular wavefunction of the neutral X and $\left|\Phi_f\right\rangle$ the total wavefunction describing the final configuration of the cation X^+ combined with that of the emitted photoelectron with kinetic energy E_k. Under the conditions and assumptions stated above, the transition probability, $\mathrm{P}_{f\leftarrow i}$, and transition rate, $\Gamma_{f\leftarrow i} = \frac{d\mathrm{P}_{f\leftarrow i}}{dt}$, can be given generally as Equations 1.7 and 1.8 [63, 65]:

$$\mathrm{P}_{f\leftarrow i} = \left(\frac{-i}{\hbar}\right)^2 \left|\left\langle\Phi_f\middle|V\middle|\Phi_i\right\rangle\right|^2 \left|\frac{e^{i\left(E_f - E_i - \hbar\omega\right)t/\hbar}}{\frac{i\left(E_f - E_i - \hbar\omega\right)}{\hbar}}\right|^2 \tag{1.7}$$

[2] The uncertainty principle would indicate the natural timescale for electronic transitions to be on the order of 10s-100s of attoseconds (10^{-18}) depending on the energy spacing of initial and final states.

$$\Gamma_{f\leftarrow i} = \frac{2\pi}{\hbar}\left|\langle\Phi_f|V|\Phi_i\rangle\right|^2 \cdot \rho(E_f) \cdot \delta(E_f - E_i - \hbar\omega) \tag{1.8}$$

where V is the time-varying potential term linking the two states, $\rho(E_f)$ is the density of final states, and $\delta(E_f - E_i - \hbar\omega)$ is included to enforce conservation of energy upon absorption of a photon. Before arriving at a final transition probability, the form of 1.3 can be simplified by taking into consideration the magnitude of $e^{i\boldsymbol{k}\cdot\boldsymbol{r}}$. Given that even in the XUV $\boldsymbol{k}\cdot\boldsymbol{r} < 1$ we can assume that $e^{i\boldsymbol{k}\cdot\boldsymbol{r}} \sim 1$, which is the long-wave approximation. Further, $\boldsymbol{E}\cdot\boldsymbol{p}$ can be substituted as $\hbar\omega(\boldsymbol{E}\cdot\boldsymbol{r})$ where $\hbar\omega$ is the energy linking two arbitrary states. By making the dipole approximation, namely that $\mu_{fi} = e\langle f|\boldsymbol{r}|i\rangle$ where f and i are arbitrary final and initial states, the final approximate transition rate can be represented as Equation 1.9.

$$\Gamma_{f\leftarrow i} \propto \left|\langle\Phi_f|\boldsymbol{E}\cdot\boldsymbol{\mu}|\Phi_i\rangle\right|^2 \cdot \rho(E_f) \cdot \delta(E_f - E_i - \hbar\omega) \tag{1.9}$$

Under the BOA, both the wavefunction and the dipole operator can be separated into components applying to the electronic and nuclear degrees of freedom. The total molecular wavefunction can therefore be represented as a product of the rotational (r), vibrational (vib), electronic (elec), and spin (spin) components and the dipole operator represented as a sum of the nuclear (nuc) and electronic (elec) components. The energy spacing of rotational levels is not resolvable with the energy resolution of the ultrafast laser used here, so will not be considered. The resultant representation of the dipole operator linking an initial and final state is given in Equation 1.10.

$$\begin{aligned}\left|\langle\Phi_f|\boldsymbol{\mu}|\Phi_i\rangle\right|^2 &= \left|\langle\psi^f_{vib}\psi^f_{elec}\psi^f_{spin}|\boldsymbol{\mu}_{elec} + \boldsymbol{\mu}_{nuc}|\psi^i_{vib}\psi^i_{elec}\psi^i_{spin}\rangle\right|^2 \\ &= \left|\begin{matrix}\langle\psi^f_{elec}|\boldsymbol{\mu}_{elec}|\psi^i_{elec}\rangle\langle\psi^f_{spin}|\psi^i_{spin}\rangle\langle\psi^f_{vib}|\psi^i_{vib}\rangle \\ +\langle\psi^f_{elec}|\psi^i_{elec}\rangle\langle\psi^f_{spin}|\psi^i_{spin}\rangle\langle\psi^f_{vib}|\boldsymbol{\mu}_{nuc}|\psi^i_{vib}\rangle\end{matrix}\right|^2\end{aligned} \tag{1.10}$$

Because electronic states are defined to be orthogonal for fixed nuclear coordinates, $\langle\psi^f_{elec}|\psi^i_{elec}\rangle$ is definitionally 0 so Equation 1.6 can be simplified to Equation 1.11.

$$\left|\langle\Phi_f|\boldsymbol{\mu}|\Phi_i\rangle\right|^2 = \left|\langle\psi^f_{elec}|\boldsymbol{\mu}_{elec}|\psi^i_{elec}\rangle\right|^2 \left|\langle\psi^f_{spin}|\psi^i_{spin}\rangle\right|^2 \left|\langle\psi^f_{vib}|\psi^i_{vib}\rangle\right|^2 \tag{1.11}$$

From this equation the selection rules governing what states are observable in a PES experiment become apparent.

The simplest factor to consider is $\left|\langle\psi_{spin}^{f}|\psi_{spin}^{i}\rangle\right|^2$. From this, we see that the total spin of the system must be conserved. As the emitted photoelectron carries away spin ±½, the spin of the molecular system after photoemission must compensate for this change in spin and a change in spin multiplicity from neutral to cation of ±1 must be satisfied. In short, for the singlet neutral ground and excited states involved in NAC relaxation, the final state would be a doublet cationic state.

The next factor to consider is the $\left|\langle\psi_{vib}^{f}|\psi_{vib}^{i}\rangle\right|^2$ term, also known as the Franck-Condon (FC) factor [66-68]. This factor requires there be appreciable overlap between the initial and final nuclear wavefunction. If too large a nuclear rearrangement is required to connect two states, the transition probability will be 0 regardless of the magnitude of the spin and electronic portions of the transition probability. With sufficient resolution, it is possible to observe that changes in vibrational quantum number for allowed transitions follows the rule $\Delta v = 0, \pm 1, \ldots$ for totally symmetric vibrational modes and $\Delta v = 0, \pm 2, \ldots$ for all other vibrational modes.

The final portion of Equation 1.8, $\left|\langle\psi_{elec}^{f}|\boldsymbol{\mu}_{elec}|\psi_{elec}^{i}\rangle\right|^2$, is the electronic symmetry condition. Here, $|\psi_{elec}^{f}\rangle$ is the product of the final electronic wavefunction of the cation, $|\phi_{elec}^{cat}\rangle$, and the wavefunction of the emitted photoelectron, $|k\rangle$. Under the assumption the wavefunction of the photoelectron is orthogonal to the remaining molecular electronic wavefunction, the direct product of the irreducible representations of the cation, photoelectron, dipole moment, and neutral must contain the totally symmetric representation. The electronic symmetry condition will be non-zero as long as it is possible for the photoelectron to carry away the appropriate symmetry and angular momentum required to fulfill the symmetry requirements.

1.3.2 Time-Resolved Photoelectron Spectroscopy

Advancements in ultrafast laser systems have enabled the application of PES to not only the equilibrium states in a given molecular system, but also to excited electronic states generated by photoexcitation. The application of PES to study the time-resolved relaxation mechanisms of light-prepared states is a powerful means to maximally utilize the state-specificity of PES in a manner that fully elucidates the relaxation of the photoexcited molecule back to its equilibrium state [25].

In the time-resolved PES experiments described in this dissertation, a pump pulse in the ultraviolet regime first optically excites a molecule. This prepares the

molecule in an excited electronic state that is allowed to evolve in time. After a known amount of time, Δt, a probe pulse of sufficient wavelength to ionize the molecule interacts with it emitting the photoelectron [23-25, 69-72]. Assuming these processes take place through interaction of single photons with the molecule, the mathematical formalism to describe the full process would require the use of time-dependent perturbation theory out to the second order. While a limited overview of the mathematical background is presented here, the complete derivation is left as an exercise to the reader or can be looked up [63].

First, we start with a few assumptions. We assume that the system is comprised of at least 3 states, with the transition from the final and initial states impossible except through an intermediate state. Additionally, we assume the interaction between states is small such that variations in coefficients of the basis set functions representing a solution to the time-dependent Schrödinger equation are small. Finally, the same assumptions that were made in Section 1.4.1 to represent the interaction of light with the molecule as $\boldsymbol{E} \cdot \boldsymbol{\mu}$ are assumed to also hold here. With this, the time-evolving coefficients of the wavefunction that serves as a solution to the time-dependent Schrödinger equation can be represented as shown in Equation 1.12 [63].

$$c_f^{(2)}(t) = \delta_{fi} + \frac{-i}{\hbar}\int_0^t dt' \langle f|\boldsymbol{E}_{pump}\cdot\boldsymbol{\mu}|i\rangle e^{i\omega_{fi}t} + \left(-\frac{i}{\hbar}\right)^2 \int_0^t \int_0^{t'} dt'\, dt''\, \langle f|\boldsymbol{E}_{probe}(t')\cdot\boldsymbol{\mu}|n\rangle \langle n|\boldsymbol{E}_{pump}(t'')\cdot\boldsymbol{\mu}|i\rangle e^{\frac{i\omega_{fn}t'}{\hbar}} e^{\frac{i\omega_{ni}t''}{\hbar}} \tag{1.12}$$

The first and second terms here are definitionally 0, so the third term is the only relevant portion of Equation 1.10 we consider. Substituting the toy wavefunctions for those described for the substitution to arrive at Equation 1.8 under the BOA, we arrive at Equation 1.13.

$$c_f^{(2)}(t) \propto \int_0^t \int_0^{t'} dt'\, dt''\, \langle k|\langle \psi_{elec}^f|\boldsymbol{E}_{probe}(t')\cdot\boldsymbol{\mu}|\psi_{elec}^n\rangle \langle \psi_{vib}^n|\psi_{vib}^i\rangle \langle \psi_{elec}^n|\boldsymbol{E}_{pump}(t'')\cdot\boldsymbol{\mu}|\psi_{elec}^i\rangle \cdot \left\langle \psi_{vib}^f \middle| e^{\frac{i\boldsymbol{H}_n'(t'-t'')}{\hbar}} \middle| \psi_{vib}^n \right\rangle e^{\frac{i(\omega_f t' - \omega_i t'')}{\hbar}} \tag{1.13}$$

By taking the square modulus of Equation 1.11, the total probability $P_{f\leftarrow i}(t)$ for a transition from the initial to final state in time t can be obtained. This probability is given in Equation 1.14.

$$P_{fi} = \left|\left(\frac{-i}{\hbar}\right)^2 \iint_{t_0}^{t_f} dt'dt''\left(\boldsymbol{E}_{probe}(t')\boldsymbol{\mu}_{f,n}\right)\left(\boldsymbol{E}_{pump}(t'')\boldsymbol{\mu}_{n,i}\right) e^{\frac{iE_f t'}{\hbar}} e^{\frac{iE_i t''}{\hbar}} \left\langle \psi_{vib}^{f} \middle| e^{\frac{i\boldsymbol{H}_n'(t'-t'')}{\hbar}} \middle| \psi_{vib}^{n} \right\rangle\right|^2 \tag{1.14}$$

By expressing the time-dependent nuclear Hamiltonian, $(\boldsymbol{H}_{probe}')$, to be an integral over all possible intermediate state energies E_n of the form given by Equation 1.15, the two photon transition probability P_{fi} can be represented as Equation 1.16.

$$e^{\frac{i\boldsymbol{H}_n'(t'-t'')}{\hbar}} = \int e^{-\frac{iE_n(t'-t'')}{\hbar}} |\psi_{vib}^{n}\rangle\langle\psi_{vib}^{n}| dE_n \tag{1.15}$$

$$P_{fi} \propto \left| \int dE_f \langle\psi_{vib}^{f}|\psi_{vib}^{n}\rangle\langle\psi_{vib}^{n}|\psi_{vib}^{i}\rangle \times \int dt e^{i(E_n-E_i)t/\hbar} e^{i\omega_{pump}t} \boldsymbol{E}_{pump}(t) \times \int dt e^{i(E_f-E_n)t/\hbar} e^{i\omega_{probe}(t-\Delta t)} \boldsymbol{E}_{probe}(t-\Delta t)\right|^2 \tag{1.16}$$

To express this explicitly as the time-varying two-photon photoelectron spectrum, the integral over final states must be evaluated over dE_f. This is given as Equation 1.17.

$$\begin{aligned} P_{fi} \propto \iint_{t_0}^{t_f} dt\, dt' e^{-i\omega_{probe}(t-\Delta t)}\, e^{-i\omega_{probe}(t'-\Delta t)}\, \boldsymbol{E}_{probe}(t-\Delta t)\boldsymbol{E}_{probe}(t'-\Delta t) \\ \times \int_{t_0}^{t} dt'' \int_{t_0}^{t'} dt''' e^{-i\omega_{pump}t''} e^{-i\omega_{pump}t'''} e^{-\frac{iE_k(t-t')}{\hbar}} e^{-\frac{iE_i(t'''-t'')}{\hbar}} \boldsymbol{E}_{probe}(t'')\boldsymbol{E}_{probe}(t''') \\ \times \left\langle \psi_{vib}^{i} \middle| e^{\frac{i\boldsymbol{H}_n(t'''-t')}{\hbar}} e^{\frac{i\boldsymbol{H}_f(t'-t)}{\hbar}} e^{\frac{i\boldsymbol{H}_n(t-t'')}{\hbar}} \middle| \psi_{vib}^{i} \right\rangle \end{aligned} \tag{1.17}$$

This is the explicit representation of the two-photon time-dependent photoelectron spectrum observed in our experiment. By evaluating the integrals in the long-time limit, the total spectrum can be expressed as Equation 1.18.

$$P_{fi} \propto \iint_{t_0}^{\infty} dt\, dt'\, \boldsymbol{E}_{probe}(t-\Delta t)\boldsymbol{E}_{probe}(t'-\Delta t) \times \left\langle \tilde{\psi}^i_{vib} \middle| e^{\frac{i\boldsymbol{H}_n(t'')}{\hbar}}\, e^{\frac{i(\boldsymbol{H}_f+E_k)(t-t')}{\hbar}}\, e^{\frac{i\boldsymbol{H}_n t}{\hbar}} \middle| \tilde{\psi}^i_{vib} \right\rangle \tag{1.18}$$

with

$$\left|\tilde{\psi}^i_{vib}\right\rangle = \int_{t_0}^{t} dt' \boldsymbol{E}_{pump}(t')\, e^{\frac{i(E_i-\boldsymbol{H}_n)t'}{\hbar}} \left|\psi^i_{vib}\right\rangle \tag{1.19}$$

1.4 Non-Adiabatic Dynamics

The previous derivations are all simplified greatly by making the assumption that nuclear and electronic degrees of freedom are separable and electronic motion can be considered for fixed nuclear arrangements. In certain instances, the nuclear and electronic wavefunctions couple strongly, known as vibronic coupling. This typically occurs when the kinetic energy terms in the Hamiltonian, T_n and T_e, are comparable in magnitude leading to a breakdown of the BOA. These couplings lead to so called "non-adiabatic" dynamics; ultrafast relaxation processes involving non-adiabatic couplings were once thought to be rare coincidences but it is now known these couplings responsible for ultrafast internal conversion are ubiquitous throughout chemistry.

To understand these couplings, it is useful to inspect the form of the term in the Hamiltonian corresponding to non-adiabatic couplings. We define Λ_{ij} as the nonadiabatic coupling term, which has the form given in Equation 1.20 [73].

$$\Lambda_{ij} = \delta_{ij} T_n - \left\langle \psi_j(\boldsymbol{R}) \middle| T_n \middle| \psi_i(\boldsymbol{R}) \right\rangle \tag{1.20}$$

Here, T_n relates to the nuclear kinetic energy and $\psi_j(\boldsymbol{R})$ is the nuclear wavefunction with respect to nuclear coordinates $\boldsymbol{R}$. Taking the definition of T_n to be proportional to the usual scalar product of gradients in the nuclear coordinate system $\boldsymbol{R}$, the nonadiabatic coupling can be broken into components as shown in Equation 1.21.

$$\Lambda_{ij} = \frac{1}{2M}\left[2\boldsymbol{F}_{ij} \cdot \boldsymbol{\nabla} + G_{ij}\right] \tag{1.21}$$

where $\boldsymbol{F}_{ij}$, known as the derivative coupling, is given be Equation 1.22 and G_{ij}, known as the scalar coupling, is given by Equation 1.23.

$$\boldsymbol{F}_{ij}(\boldsymbol{R}) = \langle \psi_j(\boldsymbol{R}) | \boldsymbol{\nabla}\, \psi_i(\boldsymbol{R}) \rangle \tag{1.22}$$

$$G_{ij}(\boldsymbol{R}) = \langle \psi_j(\boldsymbol{R}) | \boldsymbol{\nabla^2}\, \psi_i(\boldsymbol{R}) \rangle \tag{1.23}$$

Comparing $\boldsymbol{F}_{ij}$ and G_{ij}, it becomes apparent that assuming the magnitude of G_{ij} is much less than $\boldsymbol{F}_{ij}$ is a good assumption to make, and therefore can largely be ignored. Finally, $\boldsymbol{F}_{ij}$ can be rewritten as Equation 1.24 [74].

$$\boldsymbol{F}_{ij}(\boldsymbol{R}) = \frac{\langle \psi_j(\boldsymbol{R}) | \boldsymbol{\nabla} \boldsymbol{H}_{elec} | \psi_i(\boldsymbol{R}) \rangle}{E_j - E_i} \tag{1.24}$$

Here, the $\boldsymbol{F}_{ij}(\boldsymbol{R})$ is the derivative coupling between the states i and j, which is inversely proportional to the energetic spacing between the states. When the electronic states approach energetically, this term becomes non-negligible and can lead to coupling between the states [75, 76]. If the states diverge linearly away from the point where they are energetically equivalent, the point is called a conical intersection.

1.4.1 Conical Intersections

An important consequence of Equation 1.16 occurs when the energy separation between two states approaches zero. Conical intersections (CIs) are defined as a point in a 3 dimensional representation of two potential energy surfaces where the surfaces intersect, often with the respective surfaces shaped conically above and below the point of degeneracy close to the point of intersection [77]. Due to the breakdown of the BOA and near-degeneracy of electronic states near the region of the potential energy surface where the CI exists, theoretical predictions of dynamics in this region are notoriously difficult and emphasize the importance of a solid experimental foundation identifying and measuring internal conversion through CIs.

While calculating dynamics along the potential surface near a CI using the wavefunctions that represent the solutions to the time-dependent Schrödinger equation, it is possible to better understand the dynamics by a change of basis [74]. By employing a change-of-basis from the adiabatic basis ψ_i to the orthonormal diabatic set φ_i, a Hamiltonian and basis set can be defined for a two-level system.

$$\mathcal{H}_{elec} = \begin{bmatrix} H_{11} & H_{12} \\ H_{21} & H_{22} \end{bmatrix} \tag{1.25}$$

$$\begin{bmatrix} \psi_1 \\ \psi_2 \end{bmatrix} = \begin{bmatrix} c_{11} & c_{12} \\ c_{21} & c_{22} \end{bmatrix} \begin{bmatrix} \varphi_1 \\ \phi_2 \end{bmatrix} \tag{1.26}$$

Here, the matrix elements of the two-level Hamiltonian connect the diabatic states of the model system and the coefficients given in Equation 1.26 correspond to the rotations needed for the orthonormal transformation of the basis set [78]. The eigenvalues of the upper and lower states for this two level system can then be given by Equation 1.27.

$$E_{\pm} = \frac{(H_{11}+H_{22})}{2} \pm \sqrt{(H_{11} - H_{22})^2 + H_{12}^2} \tag{1.27}$$

At a CI the states are degenerate; the only way this is possible is if the second term in Equation 1.27 goes to 0, which is only the case when $H_{11} - H_{22} = 0$ and $H_{12}^2 = 0$ [77]. For this to happen, several conditions must be met. First, there must be sufficiently many internal (vibrational) degrees of freedom (N^{int}) for the above requirements to be met. Given there are two conditions to be met, conical intersections are only possible within an $N^{int} - 2$ subspace of the system i.e. triatomic systems or larger. Finally, for "accidental intersections" of the kind frequent in polyatomic systems, the electronic states must be linked by a vibration of appropriate symmetry such that the tensor product of the irreducible symmetry point groups for the two electronic states (i, j) and vibrational mode (q) linking the states must contain the totally symmetric point group Γ_A as shown in Equation 1.28 [79].

$$\Gamma_i \otimes \Gamma_j \otimes \Gamma_q \supset \Gamma_A \tag{1.28}$$

Given non-linear polyatomics have $3n - 6$ internal degrees of freedom, it is readily apparent why what was once thought to be an isolated and infrequent coincidence of symmetry has now been recognized as a ubiquitous feature of excited state dynamics and a means by which efficient internal conversion between electronic states on timescales the same order as the nuclear motion linking the FC region of a photoexcited molecule to the CI. The complicated, multidimensional nature of nuclear motion means that once an excited state wavepacket reaches a CI, there is not a 100% chance the full excited state population transits the seam between potential surfaces. The probability of crossing through the CI can be approximated by the Landau-Zener transition probability for a two state system as given in Equation 1.29 [80].

$$P_{12} = e^{-\frac{4\pi^2}{h}\frac{E_{12}^2}{\frac{d}{dt}(E_1 - E_2)}} \quad (1.29)$$

From Equation 1.29, it is apparent that the transition probability depends simply on the energy spacing between the states in the same fashion the non-adiabatic coupling strength increases with decreasing interstate spacing and the relative gradients of the potential surfaces [81]. The denominator in Equation 1.21 can also be represented as $v(F_1 - F_2)$, where v is the rate at which the excited state wavepacket is traversing the potential energy surface and $F_1 - F_2$ is the difference in "forces" acting on each state which can be thought of as equivalent to the time-dependent change in energy difference [82]. Using this framework, both the origin of and probability of transition through a CI can be understood.

1.5 Generation and Use of XUV Light

As has been mentioned previously, full elucidation of the relaxation dynamics for a given solute often requires probe energies in excess of 10 eV [6]. Generation of light at these wavelengths is exceptionally difficult due to light absorption in a given upconversion medium or atmosphere and inaccessible phase matching angles in common nonlinear media. To overcome these limitations, techniques involving directing intense laser beams into diffuse gaseous media have been an active area of investigation. Methods such as 4-wave mixing to upconvert to the required probe energies in a noble gas medium exist, but these sources offer limited flux in exchange for the added experimental complexity required to implement the source [83]. A solution to this problem is the high harmonic generation (HHG) technique to generate light in the XUV to soft x-ray regimes.

1.5.1 High Harmonic Generation

When laser intensities beyond the perturbative regime are reached by focusing a femtosecond pulse into a noble gas[3] medium, typically on the order of 10^{14} W/cm^2, it is possible to distort the atomic coulomb potential to the extent that electrons tunnel ionize [84-88]. Important aspects of this interaction are fundamentally atomic-scale processes, while others can only be arrived at by considering the macroscopic effects.

[3] Recent advances in HHG methods have extended the media that can be used to generate harmonics to polyatomic gases, solids, and liquids.

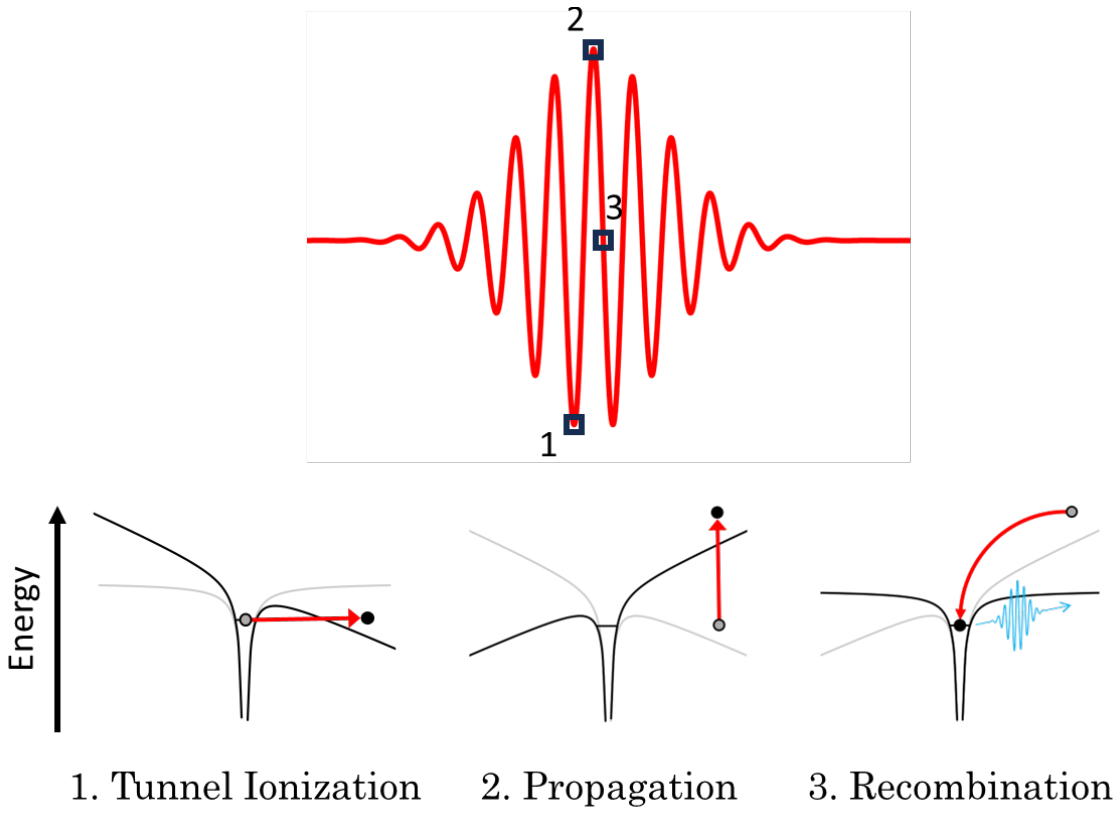

Figure 1.4 – Three step model of HHG. The driving field is depicted above, with the three points of interest shown for a single cycle. The relative shapes of the Coulomb potential are given for each step as described below. Adapted from [84, 87, 89].

On the atomic scale, the process of HHG can be described simply by a semi-classical 3-step model or by a quantum mechanical model, with the semi-classical model naturally being more simplistic to describe [84, 86, 87, 90]. As such, the 3-step model is presented here. The first step is achieved when the driving laser pulse reaches sufficiently high intensity to distort the Coulomb potential leading to tunnel ionization of a valence electron. In the second step, the electron propagates under the influence of the driving laser field, gaining energy as it does. The laser field, an inherently oscillatory field, switches sign according to the periodicity of the center wavelength and directs the propagating electron back towards the general vicinity of the parent ion. In the third step, the electron has some finite probability to recombine with the parent ion. Assuming the electron tunnel ionizes to a continuum state with zero initial kinetic energy and the atomic system ends in the electronic configuration in which it started, the electron will emit a photon upon recombination with energy between the driving laser energy and the upper bound for energy given by Equation 1.30.

$$h\upsilon_{cutoff} = I_p + 3.17U_p \tag{1.30}$$

$$U_p = \frac{q^2 E^2}{4 m_e \omega_0^2} \tag{1.31}$$

Here, U_p is the energy of a free electron in an electromagnetic field or ponderomotive energy, q is the charge of the electron, E is the amplitude of the linearly polarized electric field, m_e is the mass of the electron, and ω_0 is the driving laser frequency [84, 86, 87]. From Equation 1.31, we see the maximum attainable harmonic energy, which is achieved for electrons generated with 0 initial kinetic energy and with an ionization phase of 18° relative to the driving field, relies directly on ionization potential (I_p) of the gaseous medium used. Ionization potentials of common generation media are given in Table 1.1. Additionally, it is apparent the ponderomotive energy, U_p, relies directly on the intensity of the driving laser and inversely on the square of the driving field frequency. The pre-factor for the ponderomotive energy is derived from the ionization phase, $\omega_0 t_i$, that results in maximal electron energy [91]. Though this only comes from a relatively simple semi-classical model, these factors collectively outline a means by which harmonics of a given desired energy can be generated. For example, if higher energy harmonics (i.e. >30 eV) are not wanted, generating harmonics in a gas with a low I_p using a lower driving intensity and a shorter wavelength will lower the cutoff energy sufficiently. This is opposite the usual reasoning for optimizing harmonics, in which high intensity driving fields at long wavelength and a gaseous medium with large I_p are used to maximize the cutoff energy.

He	Ne	Ar	Kr	Xe
24.587	21.564	15.760	14.000	12.130

Table 1.1 – Ionization potentials of the common harmonic generation media He [92], Ne [93], Ar [94], Kr [95], and Xe [96].

For comparably long laser pulses relative to the optical period of the driving field (2.67 fs for 800 nm, 1.33 fs for 400 nm), the resulting XUV pulse can be determined by summing over the many half optical periods in which emission of XUV light through the process described above occurs in a medium with inversion symmetry. This summation is given by Equation 1.32.

$$E_{\omega_q} = A_{\omega_q} e^{-i(\omega_q t + \phi_q)} \sum e^{-i\left(\frac{\omega_q n T_0}{2} - n\pi\right)} \tag{1.32}$$

For many oscillations of the driving optical field, the summation can be represented as Equation 1.33.

$$\sum e^{-i\left(\frac{\omega_q n T_0}{2} - n\pi\right)} = \frac{1 - e^{-in\left(\frac{\omega_q T_0}{2} - \pi\right)}}{1 - e^{-i\left(\frac{\omega_q T_0}{2} - \pi\right)}} \tag{1.33}$$

For the XUV field to be non-zero, the denominator must be minimized which is only the case for odd harmonics of the fundamental driving frequency [91]. For short duration driving fields, this breaks down and a near-continuum can be obtained. For the purposes of photoelectron spectroscopy, this is precisely the opposite of what is wanted as an accurate binding energy can only be determined through the use of a discrete harmonic with small bandwidth. As such, driving fields in the 30-50 fs regime are required to generate discrete harmonics that are of appropriate energy.

To optimize the flux for any harmonic order being generated, phase-matching must be maintained over a region known as the coherence length. The coherence length should be as long as possible so the total number of photons produced is maximized [97]. This means phase-matching must be optimized for the longest possible length, a challenging balancing of various factors. The phase-mismatch between the driving laser and generated XUV harmonics can be given as Equation 1.34.

$$\Delta \boldsymbol{k}(q) = q\Delta \boldsymbol{k}_0 - \Delta \boldsymbol{k}_q \tag{1.34}$$

where $\Delta \boldsymbol{k}$ is the phase-mismatch for a given wavelength of light in the medium, q denotes the harmonic order, and $\Delta \boldsymbol{k}(q)$ denotes the phase mismatch between the driving pulse and generated harmonic. For HHG in a diffuse gaseous medium, each $\Delta \boldsymbol{k}$ term contains contributions from four contributions as shown in Equation 1.35 [98].

$$\Delta \boldsymbol{k} = \Delta \boldsymbol{k}_g + \Delta \boldsymbol{k}_d + \Delta \boldsymbol{k}_p + \Delta \boldsymbol{k}_n \tag{1.35}$$

where $\Delta \boldsymbol{k}_g$ is the mismatch due to the Gouy phase for a Gaussian focus, $\Delta \boldsymbol{k}_n$ is the phase mismatch from wavelength-dependent dispersion in the neutral gaseous medium, $\Delta \boldsymbol{k}_p$ is the mismatch from the wavelength-dependent dispersion in the plasma generated through ionization of the gaseous HHG medium by the driving laser as well as XUV harmonics generated earlier in the gas cell, and finally $\Delta \boldsymbol{k}_d$ is the mismatch due to what is known as the dipole phase which results from the relative contributions of short-path and long-path electron trajectories [97]. From this, it can be determined that the optimized HHG conditions depend on focusing conditions, gas density, and laser flux [99].

For example, to maximize HHG efficiency of 21.7 eV, a "soft" focusing geometry is employed by use of a f = 1.0 m transmissive lens, krypton gas pressure of ~ 6 Torr, and 1.0 W of 400 nm light. The "soft" focus refers to using a long focal length lens so the beam waist is substantially larger than what could optimally be obtained and placing the focal position either slightly inside or outside the region in which harmonics are to be generated.

Finally, the optimum flux from an HHG source can be further maximized by considering the wavelength scaling of the process. It has been shown that, for driving wavelengths in the infrared, the scaling efficiency for HHG is proportional to λ^{-5} in the cutoff region and λ^{-6} in the plateau region based on the single-atom response scaling [84, 85, 97]. For shorter wavelengths, it has been shown the scaling at low harmonic orders follow an efficiency proportional to $\lambda^{-3} - \lambda^{-4}$ which is more due to the macroscopic response of the apparatus rather than the single-atom response [100].

1.5.2 Laser Assisted Photoelectric Effect

The laser assisted photoelectric effect (LAPE) is the means by which the harmonics generated and the selected harmonic used in any given experiment are characterized in terms of the spatial and temporal profile of the convolution of a given pump wavelength and XUV probe pulse. LAPE, in short, is the absorption of an ionizing photon (typically in the XUV) in the presences of a dressing field such that the resultant photoelectrons are represented by a Volkov wavefunction for charged particles interacting with an electromagnetic field [101]. From this framework, the resultant exchange of energy between the dressing field and electrons can be understood and used as a means of characterization [102]. For LAPE to be possible, an electron packet typically produced in a continuum of states such as what is generated through photoemission must be overlapped a dressing field of sufficient intensity to induce stimulated absorption and emission from the electrons. Practically, this manifests as the appearance of satellite peaks of an XUV photoemission peak with kinetic energy of $\pm n\hbar\omega_0$ where n is a non-zero integer and ω_0 is the dressing field frequency [103].

The description of this process is possible by determining the modified differential cross-section of the XUV-ionized state for emission to a field-free state compared to the light-dressed state. The relationship between these differential cross-sections is given by Equation 1.36 [104].

$$\frac{d\sigma(n)}{d\Omega} = J_n^2(\alpha)\frac{d\sigma}{d\Omega} \tag{1.36}$$

Where $\frac{d\sigma(\ell)}{d\Omega}$ is the modified differential cross-section, J_n is an ordinary Bessel function of the first kind, and $\frac{d\sigma}{d\Omega}$ is the differential cross-section absent the dressing field. The argument of the Bessel function can be given by Equation 1.37 [105].

$$\alpha = \sqrt{\frac{16\pi\kappa I E_{kin}}{m_e \hbar \omega_0^4}} \tag{1.37}$$

Here, κ is the fine structure constant, I is the dressing field intensity, E_{kin} is the photoelectron kinetic energy, and ω_0 is the dressing field frequency. Combining 1.36 and 1.37, it is readily apparent that the amplitude of the first order satellite peak is directly proportional to the intensity of the dressing field, the second order proportional to the square of the intensity of the dressing field, etc. Additionally, peaks resulting from dressing fields of the same intensity but different wavelength will have relative intensity with wavelength scaling of λ^{-4} for first order LAPE. As such, it is only with great care and precision that observation of LAPE signal with a 267 nm dressing field is possible and it is with relative ease that 800 nm LAPE is observed.

This effect is observed for any phase of matter. Most useful to this experiment is from gas phase signals. Argon serves as an excellent system with reasonably small total linewidth with which LAPE can be readily observed. This system is ideal for measuring the spatial and temporal cross-correlations or simply finding spatiotemporal overlap after realignment of the laser system. As will be discussed later, when observing water signal it is substantially simpler to check and optimize overlap utilizing LAPE signal using water vapor ionization as the photoemission signal dressed by an additional laser field. This is due to the relatively narrow linewidth of photoemission from gas phase signals relative to the liquid. While the LAPE signal will always be present in liquid signals, the increased natural linewidth and convolution with space-charge effects make it substantially more difficult to observe without significant averaging.

1.6 Summary of Following Chapters

The instrumentation for carrying out the LJ-TRPES experiment has undergone substantial alterations over the course of the work detailed in this dissertation. Modifications to the light source, solution delivery, and detector have all been carried out with the ultimate goal being to collect time-resolve photoelectron spectra with a probe energy in excess of 20 eV and improved stability, data acquisition rate, and detection limit. These modifications, with commentary as to their efficacy, and

the existing instrument into which the modifications were integrated are described in great detail in Chapter 2.

In Chapter 3, an overview of UV pump/UV probe data for the thymine family of NACs is presented with additional insight provided by recent data taken with an XUV probe. In short, tunable 240 – 260 nm pump/200 nm probe experiments were carried out on liquid jets containing thymine, thymidine, and thymidine monophosphate. The involvement of an intermediate $^1n\pi^*$ populated from the initially excited $^1\pi\pi^*$ had long been posited by results from absorption and fluorescence experiments but had yet to be observed by photoelectron spectroscopy. The excited state lifetime for $^1\pi\pi^* \rightarrow S_0$ internal conversion was measured to be sub-picosecond for all three NACs. No statistically significant signal attributable to the $^1n\pi^*$ was observed. Additionally, the first measurements of relaxation lifetimes from the excitation band populated by 200 nm were taken. Recent work has called the null $^1n\pi^*$ result into question, so the system was revisited using an XUV probe. The work calling the result into question was confirmed, with the previous null result likely attributable to lack of sensitivity or probe energy considerations.

Chapter 4 presents initial results involving implementation of the XUV probe. One-color spectra of noble gases under a variety of harmonic generation conditions and with alternative beamline optical setups are presented. LAPE spectra demonstrating two color signal using 800 nm, 400 nm, and 267 nm dressing fields are presented for both gaseous and liquid samples. Initial solutes studied with the newly implemented XUV probe are then presented. Finally, the recently acquired time-resolved photoelectron spectra of a variety of NACs taken with an XUV probe are presented within the context of previous studies.

1.7 References

[1] Elles, C. G.; Crim, F. F. Connecting Chemical Dynamics in Gases and Liquids. *Annu. Rev. Phys. Chem.* **2006**, *57* (1), 273-302. DOI: 10.1146/annurev.physchem.57.032905.104538.

[2] Kumar, G.; Roy, A.; Mcmullen, R. S.; Kutagulla, S.; Bradforth, S. E. The influence of aqueous solvent on the electronic structure and non-adiabatic dynamics of indole explored by liquid-jet photoelectron spectroscopy. *Faraday Discuss.* **2018**, *212*, 359. DOI: 10.1039/C8FD00123E.

[3] Jimenez, R.; Fleming, G. R.; Kumar, P. V.; Maroncelli, M. Femtosecond solvation dynamics of water. *Nature* **1994**, *369* (6480), 471-473. DOI: 10.1038/369471a0.

[4] Orr-Ewing, A. J. Taking the plunge: chemical reaction dynamics in liquids. *Chem. Soc. Rev.* **2017**, *46* (24), 7597-7614. DOI: 10.1039/C7CS00331E.

[5] Rosspeintner, A.; Lang, B.; Vauthey, E. Ultrafast Photochemistry in Liquids. *Annu. Rev. Phys. Chem.* **2013**, *64* (1), 247-271. DOI: 10.1146/annurev-physchem-040412-110146.

[6] Seidel, R.; Winter, B.; Bradforth, S. E. Valence Electronic Structure of Aqueous Solutions: Insights from Photoelectron Spectroscopy. *Annu. Rev. Phys. Chem.* **2016**, *67* (1), 283-305. DOI: 10.1146/annurev-physchem-040513-103715.

[7] Venkatraman, R. K.; Orr-Ewing, A. J. Solvent Effects on Ultrafast Photochemical Pathways. *Accts. Chem. Res.* **2021**, *54* (23), 4383-4394. DOI: 10.1021/acs.accounts.1c00549.

[8] Riley, J. W.; Wang, B.; Woodhouse, J. L.; Assmann, M.; Worth, G. A.; Fielding, H. H. Unravelling the role of an aqueous environment on the electronic structure and ionization of phenol using photoelectron spectroscopy. *J. Phys. Chem. Lett.* **2018**, *9*, 678. DOI: 10.1021/acs.jpclett.7b03310.

[9] Schreier, W. J.; Gilch, P.; Zinth, W. Early Events of DNA Photodamage. *Annu. Rev. Phys. Chem.* **2015**, *66* (1), 497-519. DOI: 10.1146/annurev-physchem-040214-121821.

[10] Middleton, C. T.; Harpe, K. d. L.; Su, C.; Law, Y. K.; Crespo-Hernández, C. E.; Kohler, B. DNA Excited-State Dynamics: From Single Bases to the Double Helix. *Annu. Rev. Phys. Chem.* **2009**, *60* (1), 217-239. DOI: 10.1146/annurev.physchem.59.032607.093719.

[11] Prokhorenko, V. I.; Picchiotti, A.; Pola, M.; Dijkstra, A. G.; Miller, R. J. D. New Insights into the Photophysics of DNA Nucleobases. *J. Phys. Chem. Lett.* **2016**, *7* (22), 4445-4450. DOI: 10.1021/acs.jpclett.6b02085.

[12] Pecourt, J.-M. L.; Peon, J.; Kohler, B. DNA Excited-State Dynamics: Ultrafast Internal Conversion and Vibrational Cooling in a Series of Nucleosides. *J. Am. Chem. Soc.* **2001**, *123* (42), 10370-10378. DOI: 10.1021/ja0161453.

[13] Barbatti, M.; Aquino, A. J. A.; Szymczak, J. J.; Nachtigallová, D.; Hobza, P.; Lischka, H. Relaxation mechanisms of UV-photoexcited DNA and RNA nucleobases. *PNAS* **2010**, *107* (50), 21453-21458. DOI: 10.1073/pnas.1014982107.

[14] Hare, P. M.; Crespo-Hernández, C. E.; Kohler, B. Internal conversion to the electronic ground state occurs via two distinct pathways for pyrimidine bases in aqueous solution. *PNAS* **2007**, *104* (2), 435-440. DOI: 10.1073/pnas.0608055104.

[15] Pfeifer, G. P.; You, Y.-H.; Besaratinia, A. Mutations induced by ultraviolet light. *Mutat. Res.* **2005**, *571* (1-2), 19-31. DOI: 10.1016/j.mrfmmm.2004.06.057.

[16] Stavros, V. G.; Verlet, J. R. R. Gas-Phase Femtosecond Particle Spectroscopy: A Bottom-Up Approach to Nucleotide Dynamics. *Annu. Rev. Phys. Chem.* **2016**, *67* (1), 211-232. DOI: 10.1146/annurev-physchem-040215-112428.

[17] Heim, Z. N.; Neumark, D. M. Nonadiabatic Dynamics Studied by Liquid-Jet Time-Resolved Photoelectron Spectroscopy. *Accts. Chem. Res.* **2022**, *55* (24), 3652-3662. DOI: 10.1021/acs.accounts.2c00609.

[18] Fried, L. E.; Bernstein, N.; Mukamel, S. Simulation of the femtosecond optical response of a solute in water. *Phys. Rev. Lett.* **1992**, *68* (12), 1842-1845. DOI: 10.1103/PhysRevLett.68.1842.

[19] Glasbeek, M.; Zhang, H. Femtosecond Studies of Solvation and Intramolecular Configurational Dynamics of Fluorophores in Liquid Solution. *Chem. Rev.* **2004**, *104* (4), 1929-1954. DOI: 10.1021/cr0206723.

[20] Pal, S. K.; Peon, J.; Bagchi, B.; Zewail, A. H. Biological Water: Femtosecond Dynamics of Macromolecular Hydration. *J. Phys. Chem. B* **2002**, *106* (48), 12376-12395. DOI: 10.1021/jp0213506.

[21] Boereboom, J. M.; Fleurat-Lessard, P.; Bulo, R. E. Explicit Solvation Matters: Performance of QM/MM Solvation Models in Nucleophilic Addition. *J. Chem. Theory Comput.* **2018**, *14* (4), 1841-1852. DOI: 10.1021/acs.jctc.7b01206.

[22] Milanese, J. M.; Provorse, M. R.; Alameda, E., Jr.; Isborn, C. M. Convergence of Computed Aqueous Absorption Spectra with Explicit Quantum Mechanical Solvent. *J. Chem. Theory Comput.* **2017**, *13* (5), 2159-2171. DOI: 10.1021/acs.jctc.7b00159.

[23] Stolow, A.; Underwood, J. G. Time-resolved photoelectron spectroscopy. *Adv. Chem. Phys.* **2008**, *139*, 497. DOI: 10.1002/9780470259498.ch6.

[24] Stolow, A. Femtosecond Time-Resolved Photoelectron Spectroscopy of Polyatomic Molecules. *Annu. Rev. Phys. Chem.* **2003**, *54* (1), 89-119. DOI: 10.1146/annurev.physchem.54.011002.103809.

[25] Stolow, A.; Bragg, A. E.; Neumark, D. M. Femtosecond Time-Resolved Photoelectron Spectroscopy. *Chem. Rev.* **2004**, *104* (4), 1719-1758. DOI: 10.1021/cr020683w.

[26] Buchner, F.; Nakayama, A.; Yamazaki, S.; Ritze, H. H.; Lübcke, A. Excited-State Relaxation of Hydrated Thymine and Thymidine Measured by Liquid-Jet Photoelectron Spectroscopy: Experiment and Simulation. *J. Am. Chem. Soc.* **2015**, *137* (8), 2931-2938. DOI: 10.1021/ja511108u.

[27] Born, M. Volumen und Hydratationswärme der Ionen. *Z. Phys.* **1920**, *1* (1), 45-48. DOI: 10.1007/BF01881023.

[28] Archer, D. G.; Wang, P. The Dielectric Constant of Water and Debye-Hückel Limiting Law Slopes. *J. Phys. Chem. Ref. Data* **1990**, *19* (2), 371-411. DOI: 10.1063/1.55585.

[29] Owrutsky, J. C.; Raftery, D.; Hochstrasser, R. M. Vibrational Relaxation Dynamics in Solutions. *Annu. Rev. Phys. Chem.* **1994**, *45* (1), 519-555. DOI: 10.1146/annurev.pc.45.100194.002511.

[30] Grubb, M. P.; Coulter, P. M.; Marroux, H. J. B.; Orr-Ewing, A. J.; Ashfold, M. N. R. Unravelling the mechanisms of vibrational relaxation in solution. *Chem. Sci.* **2017**, *8* (4), 3062-3069. DOI: 10.1039/C6SC05234G.

[31] Middleton, C. T.; Cohen, B.; Kohler, B. Solvent and Solvent Isotope Effects on the Vibrational Cooling Dynamics of a DNA Base Derivative. *J. Phys. Chem. A* **2007**, *111* (42), 10460-10467. DOI: 10.1021/jp0740595.

[32] Pigliucci, A.; Duvanel, G.; Daku, L. M. L.; Vauthey, E. Investigation of the Influence of Solute−Solvent Interactions on the Vibrational Energy Relaxation Dynamics of Large Molecules in Liquids. *J. Phys. Chem. A* **2007**, *111* (28), 6135-6145. DOI: 10.1021/jp069010y.

[33] Zhang, Y.; Chen, J.; Kohler, B. Hydrogen Bond Donors Accelerate Vibrational Cooling of Hot Purine Derivatives in Heavy Water. *J. Phys. Chem. A* **2013**, *117* (31), 6771-6780. DOI: 10.1021/jp4040002.

[34] Nitzan, A. *Chemical dynamics in condensed phases: relaxation, transfer and reactions in condensed molecular systems*; Oxford university press, 2006.

[35] Williams, H. L. Ultrafast Dynamics of Adenine Derivatives Studied by Time-Resolved Photoelectron Spectroscopy in Water Microjets. Ph.D., University of California, Berkeley, United States -- California, 2017.

[36] Alberts, B. *Molecular biology of the cell*; Garland science, 2017.

[37] Watson, J. D.; Crick, F. H. C. Molecular Structure of Nucleic Acids: A Structure for Deoxyribose Nucleic Acid. *Nature* **1953**, *171* (4356), 737-738. DOI: 10.1038/171737a0.

[38] Martinez, C. R.; Iverson, B. L. Rethinking the term "pi-stacking". *Chem. Sci.* **2012**, *3* (7), 2191-2201. DOI: 10.1039/C2SC20045G.

[39] Rist, M.; Wagenknecht, H.-A.; Fiebig, T. Exciton and Excimer Formation in DNA at Room Temperature. *ChemPhysChem* **2002**, *3* (8), 704-707. DOI: 10.1002/1439-7641(20020816)3:8<704::AID-CPHC704>3.0.CO;2-F.

[40] Rössle, S.; Friedrichs, J.; Frank, I. The Formation of DNA Photodamage: The Role of Exciton Localization. *ChemPhysChem* **2010**, *11* (9), 2011-2015. DOI: 10.1002/cphc.201000081.

[41] Voet, D.; Gratzer, W. B.; Cox, R. A.; Doty, P. Absorption spectra of nucleotides, polynucleotides, and nucleic acids in the far ultraviolet. *Biopolymers* **1963**, *1* (3), 193-208. DOI: 10.1002/bip.360010302.

[42] Elkins, M. H.; Williams, H. L.; Shreve, A. T.; Neumark, D. M. Relaxation mechanism of the hydrated electron. *Science* **2013**, *342*, 1496. DOI: 10.1126/science.1246291.

[43] Williams, H. L.; Erickson, B. A.; Neumark, D. M. Time-resolved photoelectron spectroscopy of adenosine and adenosine monophosphate photodeactivation dynamics in water microjets. *J. Chem. Phys.* **2018**, *148* (19), 194303. DOI: 10.1063/1.5027258.

[44] Erickson, B. A.; Heim, Z. N.; Pieri, E.; Liu, E.; Martinez, T. J.; Neumark, D. M. Relaxation Dynamics of Hydrated Thymine, Thymidine, and Thymidine Monophosphate Probed by Liquid Jet Time-Resolved Photoelectron Spectroscopy. *J. Phys. Chem. A* **2019**, *123* (50), 10676-10684. DOI: 10.1021/acs.jpca.9b08258.

[45] Buchner, F.; Heggen, B.; Ritze, H.-H.; Thiel, W.; Lübcke, A. Excited-state dynamics of guanosine in aqueous solution revealed by time-resolved photoelectron spectroscopy: Experiment and theory. *Phys. Chem. Chem. Phys.* **2015**, *17* (47), 31978-31987. DOI: 10.1039/C5CP04394H.

[46] Buchner, F.; Ritze, H. H.; Lahl, J.; Lübcke, A. Time-resolved Photoelectron Spectroscopy of Adenine and Adenosine in Aqueous Solution. *Phys. Chem. Chem. Phys.* **2013**, *15* (27), 11402-11408. DOI: 10.1039/C3CP51057C.

[47] Cohen, B.; Hare, P. M.; Kohler, B. Ultrafast Excited-State Dynamics of Adenine and Monomethylated Adenines in Solution: Implications for the Nonradiative Decay Mechanism. *J. Am. Chem. Soc.* **2003**, *125* (44), 13594-13601. DOI: 10.1021/ja035628z.

[48] Gustavsson, T.; Bányász, Á.; Lazzarotto, E.; Markovitsi, D.; Scalmani, G.; Frisch, M. J.; Barone, V.; Improta, R. Singlet Excited-State Behavior of Uracil and Thymine in Aqueous Solution: A Combined Experimental and Computational Study of 11 Uracil Derivatives. *J. Am. Chem. Soc.* **2006**, *128* (2), 607-619. DOI: 10.1021/ja056181s.

[49] Gustavsson, T.; Sharonov, A.; Markovitsi, D. Thymine, thymidine and thymidine 5′-monophosphate studied by femtosecond fluorescence upconversion spectroscopy. *Chem. Phys. Lett.* **2002**, *351* (3), 195-200. DOI: 10.1016/S0009-2614(01)01375-6.

[50] Improta, R.; Santoro, F.; Blancafort, L. Quantum Mechanical Studies on the Photophysics and the Photochemistry of Nucleic Acids and Nucleobases. *Chem. Rev.* **2016**, *116* (6), 3540-3593. DOI: 10.1021/acs.chemrev.5b00444.

[51] Perun, S.; Sobolewski, A. L.; Domcke, W. Photostability of 9H-adenine: mechanisms of the radiationless deactivation of the lowest excited singlet states. *Chem. Phys.* **2005**, *313* (1), 107-112. DOI: 10.1016/j.chemphys.2005.01.005.

[52] Roberts, G. M.; Marroux, H. J. B.; Grubb, M. P.; Ashfold, M. N. R.; Orr-Ewing, A. J. On the Participation of Photoinduced N–H Bond Fission in Aqueous Adenine at 266 and 220 nm: A Combined Ultrafast Transient Electronic and Vibrational Absorption Spectroscopy Study. *J. Phys. Chem. A* **2014**, *118* (47), 11211-11225. DOI: 10.1021/jp508501w.

[53] Sharonov, A.; Gustavsson, T.; Carré, V.; Renault, E.; Markovitsi, D. Cytosine excited state dynamics studied by femtosecond fluorescence upconversion and transient absorption spectroscopy. *Chem. Phys. Lett.* **2003**, *380* (1-2), 173-180. DOI: 10.1016/j.cplett.2003.09.021.

[54] Miura, Y.; Yamamoto, Y.-i.; Karashima, S.; Orimo, N.; Hara, A.; Fukuoka, K.; Ishiyama, T.; Suzuki, T. Formation of Long-Lived Dark States during Electronic Relaxation of Pyrimidine Nucleobases Studied Using Extreme Ultraviolet Time-Resolved Photoelectron Spectroscopy. *J. Am. Chem. Soc.* **2023**, *145* (6), 3369-3381. DOI: 10.1021/jacs.2c09803.

[55] Markovitsi, D.; Gustavsson, T.; Talbot, F. Excited states and energy transfer among DNA bases in double helices. *Photochem. Photobiol. Sci.* **2007**, *6* (7), 717-724. DOI: 10.1039/b705674e.

[56] Borrego-Varillas, R.; Cerullo, G.; Markovitsi, D. Exciton Trapping Dynamics in DNA Multimers. *J. Phys. Chem. Lett.* **2019**, *10* (7), 1639-1643. DOI: 10.1021/acs.jpclett.9b00450.

[57] Improta, R.; Barone, V. Interplay between "Neutral" and "Charge-Transfer" Excimers Rules the Excited State Decay in Adenine-Rich Polynucleotides. *Angew. Chem. Int. Ed.* **2011**, *50* (50), 12016-12019. DOI: 10.1002/anie.201104382.

[58] Ibele, L. M.; Sánchez-Murcia, P. A.; Mai, S.; Nogueira, J. J.; González, L. Excimer Intermediates en Route to Long-Lived Charge-Transfer States in Single-Stranded Adenine DNA as Revealed by Nonadiabatic Dynamics. *J. Phys. Chem. Lett.* **2020**, *11* (18), 7483-7488. DOI: 10.1021/acs.jpclett.0c02193.

[59] Doorley, G. W.; Wojdyla, M.; Watson, G. W.; Towrie, M.; Parker, A. W.; Kelly, J. M.; Quinn, S. J. Tracking DNA Excited States by Picosecond-Time-Resolved Infrared Spectroscopy: Signature Band for a Charge-Transfer Excited State in Stacked Adenine–Thymine Systems. *J. Phys. Chem. Lett.* **2013**, *4* (16), 2739-2744. DOI: 10.1021/jz401258n.

[60] Improta, R. Vertical Ionization Energies computed for dApdA dinucleotide in solution in the ground and in the excited state. A preliminary Report. 2021.

[61] Reinert, F.; Hüfner, S. Photoemission spectroscopy—from early days to recent applications. *New J. Phys.* **2005**, *7* (1), 97. DOI: 10.1088/1367-2630/7/1/097.

[62] Stolow, A.; Underwood, J. G. Time-Resolved Photoelectron Spectroscopy of Nonadiabatic Dynamics in Polyatomic Molecules. In *Advances in Chemical Physics*, 2008; pp 497-584.

[63] Schatz, G. C.; Ratner, M. A. *Quantum mechanics in chemistry*; Courier Corporation, 2002.

[64] Born, M.; Oppenheimer, R. Zur Quantentheorie der Molekeln. *Ann. Phys.* **1927**, *389* (20), 457-484. DOI: 10.1002/andp.19273892002.

[65] Dirac, P. A. M.; Bohr, N. H. D. The quantum theory of the emission and absorption of radiation. *Proc. R. Soc. London, A Math. Phys.* **1927**, *114* (767), 243-265. DOI: 10.1098/rspa.1927.0039.

[66] Franck, J.; Dymond, E. G. Elementary processes of photochemical reactions. *Trans. Faraday Soc.* **1926**, *21* (February), 536-542, 10.1039/TF9262100536. DOI: 10.1039/TF9262100536.

[67] Condon, E. A Theory of Intensity Distribution in Band Systems. *Phys. Rev.* **1926**, *28* (6), 1182-1201. DOI: 10.1103/PhysRev.28.1182.

[68] Condon, E. U. Nuclear Motions Associated with Electron Transitions in Diatomic Molecules. *Phys. Rev.* **1928**, *32* (6), 858-872. DOI: 10.1103/PhysRev.32.858.

[69] Fielding, H. H.; Worth, G. A. Using time-resolved photoelectron spectroscopy to unravel the electronic relaxation dynamics of photoexcited molecules. *Chem. Soc. Rev.* **2018**, *47*, 309. DOI: 10.1039/C7CS00627F.

[70] Tang, Y.; Suzuki, Y.-i.; Shen, H.; Sekiguchi, K.; Kurahashi, N.; Nishizawa, K.; Zuo, P.; Suzuki, T. Time-resolved photoelectron spectroscopy of bulk liquids at ultra-low kinetic energy. *Chem. Phys. Lett.* **2010**, *494* (1), 111-116. DOI: 10.1016/j.cplett.2010.05.084.

[71] Suzuki, T. Time-resolved photoelectron spectroscopy of non-adiabatic electronic dynamics in gas and liquid phases. *Int. Rev. Phys. Chem.* **2012**, *31* (2), 265-318. DOI: 10.1080/0144235X.2012.699346.

[72] Buchner, F.; Lübcke, A.; Heine, N.; Schultz, T. Time-resolved photoelectron spectroscopy of liquids. *Rev. Sci. Instrum.* **2010**, *81*, 113107. DOI: 10.1063/1.3499240.

[73] Baer, M. Introduction to the theory of electronic non-adiabatic coupling terms in molecular systems. *Phys. Rep.* **2002**, *358* (2), 75-142. DOI: 10.1016/S0370-1573(01)00052-7.

[74] Schuurman, M. S.; Stolow, A. Dynamics at Conical Intersections. *Annu. Rev. Phys. Chem.* **2018**, *69* (1), 427-450. DOI: 10.1146/annurev-physchem-052516-050721.

[75] Englman, R.; Jortner, J. The energy gap law for radiationless transitions in large molecules. *Mol. Phys.* **1970**, *18* (2), 145-164. DOI: 10.1080/00268977000100171.

[76] Jang, S. J. A simple generalization of the energy gap law for nonradiative processes. *J. Chem. Phys.* **2021**, *155* (16). DOI: 10.1063/5.0068868.

[77] Worth, G. A.; Cederbaum, L. S. Beyond Born-Oppenheimer: Molecular Dynamics Through a Conical Intersection. *Annu. Rev. Phys. Chem.* **2004**, *55* (1), 127-158. DOI: 10.1146/annurev.physchem.55.091602.094335.

[78] Matsika, S.; Krause, P. Nonadiabatic Events and Conical Intersections. *Annu. Rev. Phys. Chem.* **2011**, *62* (1), 621-643. DOI: 10.1146/annurev-physchem-032210-103450.

[79] Paterson, M. J.; Bearpark, M. J.; Robb, M. A.; Blancafort, L.; Worth, G. A. Conical intersections: A perspective on the computation of spectroscopic Jahn–Teller parameters and the degenerate 'intersection space'. *Phys. Chem. Chem. Phys.* **2005**, *7* (10), 2100-2115. DOI: 10.1039/B416538A.

[80] Wittig, C. The Landau–Zener Formula. *J. Phys. Chem. B* **2005**, *109* (17), 8428-8430. DOI: 10.1021/jp040627u.

[81] Zener, C.; Fowler, R. H. Non-adiabatic crossing of energy levels. *Proc. R. Soc. London, A Math. Phys.* **1932**, *137* (833), 696-702. DOI: doi:10.1098/rspa.1932.0165.

[82] Volkov, M. V.; Ostrovsky, V. N. Exact results for survival probability in the multistate Landau–Zener model. *J. Phys. B* **2004**, *37* (20), 4069. DOI: 10.1088/0953-4075/37/20/003.

[83] Fuji, T.; Suzuki, T. Generation of sub-two-cycle mid-infrared pulses by four-wave mixing through filamentation in air. *Opt. Lett.* **2007**, *32* (22), 3330-3332. DOI: 10.1364/OL.32.003330.

[84] Corkum, P. B. Plasma perspective on strong field multiphoton ionization. *Phys. Rev. Lett.* **1993**, *71* (13), 1994-1997. DOI: 10.1103/PhysRevLett.71.1994.

[85] Lewenstein, M.; Balcou, P.; Ivanov, M. Y.; L'Huillier, A.; Corkum, P. B. Theory of high-harmonic generation by low-frequency laser fields. *Phys. Rev. A* **1994**, *49* (3), 2117-2132. DOI: 10.1103/PhysRevA.49.2117.

[86] Becker, W.; Lohr, A.; Kleber, M. Light at the end of the tunnel: two- and three-step models in intense-field laser-atom physics. *Quantum Semiclass. Opt.* **1995**, *7* (3), 423. DOI: 10.1088/1355-5111/7/3/017.

[87] Krause, J. L.; Schafer, K. J.; Kulander, K. C. High-order harmonic generation from atoms and ions in the high intensity regime. *Phys. Rev. Lett.* **1992**, *68* (24), 3535-3538. DOI: 10.1103/PhysRevLett.68.3535.

[88] Krausz, F.; Ivanov, M. Attosecond Physics. *Rev. Mod. Phys.* **2009**, *81*, 163.

[89] Corkum, P. B.; Krausz, F. Attosecond science. *Nat. Phys.* **2007**, *3* (6), 381-387. DOI: 10.1038/nphys620.

[90] Santra, R.; Gordon, A. Three-Step Model for High-Harmonic Generation in Many-Electron Systems. *Phys. Rev. Lett.* **2006**, *96* (7), 073906. DOI: 10.1103/PhysRevLett.96.073906.

[91] Constant, E.; Mével, E. Attosecond Pulses. In *Femtosecond Laser Pulses: Principles and Experiments*, Rullière, C. Ed.; Springer New York, 2005; pp 395-422.

[92] Kandula, D. Z.; Gohle, C.; Pinkert, T. J.; Ubachs, W.; Eikema, K. S. E. Extreme Ultraviolet Frequency Comb Metrology. *Phys. Rev. Lett.* **2010**, *105* (6), 063001. DOI: 10.1103/PhysRevLett.105.063001.

[93] Kaufman, V.; Minnhagen, L. Accurate Ground-Term Combinations in Ne i. *J. Opt. Soc. Am.* **1972**, *62* (1), 92-95. DOI: 10.1364/JOSA.62.000092.

[94] Velchev, I.; Hogervorst, W.; Ubachs, W. Precision VUV spectroscopy of Ar I at 105 nm. *J. Phys. B* **1999**, *32* (17), L511. DOI: 10.1088/0953-4075/32/17/105.

[95] Saloman, E. B. Energy Levels and Observed Spectral Lines of Krypton, Kr I through Kr XXXVI. *J. Phys. Chem. Ref. Data* **2007**, *36* (1), 215-386. DOI: 10.1063/1.2227036.

[96] Knight, R. D.; Wang, L.-g. One-photon laser spectroscopy of the np and nf Rydberg series in xenon. *J. Opt. Soc. Am. B* **1985**, *2* (7), 1084-1087. DOI: 10.1364/JOSAB.2.001084.

[97] Gaarde, M. B.; Tate, J. L.; Schafer, K. J. Macroscopic aspects of attosecond pulse generation. *J. Phys. B* **2008**, *41* (13), 132001. DOI: 10.1088/0953-4075/41/13/132001.

[98] Heyl, C. M.; Arnold, C. L.; Couairon, A.; L'Huillier, A. Introduction to macroscopic power scaling principles for high-order harmonic generation. *J. Phys. B* **2017**, *50* (1), 013001. DOI: 10.1088/1361-6455/50/1/013001.

[99] Weissenbilder, R.; Carlström, S.; Rego, L.; Guo, C.; Heyl, C.; Smorenburg, P.; Constant, E.; Arnold, C.; L'Huillier, A. Efficient generation of high-order harmonics in gases. *arXiv preprint arXiv:2202.08202* **2022**.

[100] Marceau, C.; Hammond, T. J.; Naumov, A. Y.; Corkum, P. B.; Villeneuve, D. M. Wavelength scaling of high harmonic generation for 267 nm, 400 nm and 800 nm driving laser pulses. *J. Phys. Commun* **2017**, *1* (1), 015009. DOI: 10.1088/2399-6528/aa74f6.

[101] Yakaboylu, E. Volkov wave function: its orthonormality and completeness. *arXiv preprint arXiv:1505.02801* **2015**.

[102] Glover, T. E.; Schoenlein, R. W.; Chin, A. H.; Shank, C. V. Observation of Laser Assisted Photoelectric Effect and Femtosecond High Order Harmonic Radiation. *Phys. Rev. Lett.* **1996**, *76* (14), 2468-2471. DOI: 10.1103/PhysRevLett.76.2468.

[103] Madsen, L. B. Strong-field approximation in laser-assisted dynamics. *Am. J. Phys.* **2005**, *73* (1), 57-62. DOI: 10.1119/1.1796791.

[104] Kroll, N. M.; Watson, K. M. Charged-Particle Scattering in the Presence of a Strong Electromagnetic Wave. *Phys. Rev. A* **1973**, *8* (2), 804-809. DOI: 10.1103/PhysRevA.8.804.

[105] Arrell, C. A.; Ojeda, J.; Mewes, L.; Grilj, J.; Frassetto, F.; Poletto, L.; van Mourik, F.; Chergui, M. Laser-Assisted Photoelectric Effect from Liquids. *Phys. Rev. Lett.* **2016**, *117* (14), 143001. DOI: 10.1103/PhysRevLett.117.143001.

Chapter 2 – Experimental Methods and Materials

2.1 Overview

This chapter will detail the various experimental components in the extreme ultraviolet (XUV) liquid microjet – time resolved photoelectron spectroscopy (LJ–TRPES) experiment and their underlying principles. The experiment currently consists of a commercial ultrafast oscillator/amplifier, a home built XUV tabletop light source, a liquid microjet sample delivery system, and a time-of-flight (ToF) photoelectron spectrometer. The experimental apparatus is controlled by a home-built LabVIEW code and the data collected is processed in MATLAB code developed in-house. Description of both the new components implemented in my time on the project as well as existing components implemented by previous graduate students are included due to the constantly evolving nature of the experiment. Additional details can also be found in the following chapters in relation to the data collection improvements resulting from the implementation of the new components and drawings found in Appendix B.

2.2 Generating Ultrafast Laser Pulses

As with any time-resolved experiment, the generation of pulsed light of sufficiently short duration and of appropriate wavelength to initiate and eventually probe the dynamics of interest is of the utmost importance. The laser system used in this experiment, also described in the theses of H. L. Williams [1] and B. A. Erickson [2], consists of a Ti:Sapphire femtosecond oscillator/amplifier combination, an optical parametric amplifier (OPA), a home-built, ß-barium borate (BBO) based second harmonic generation (SHG)/sum frequency generation (SFG) optical setup, and a home-built XUV source and beamline. The beamline at the time of writing this dissertation is shown in Figure 2.1.

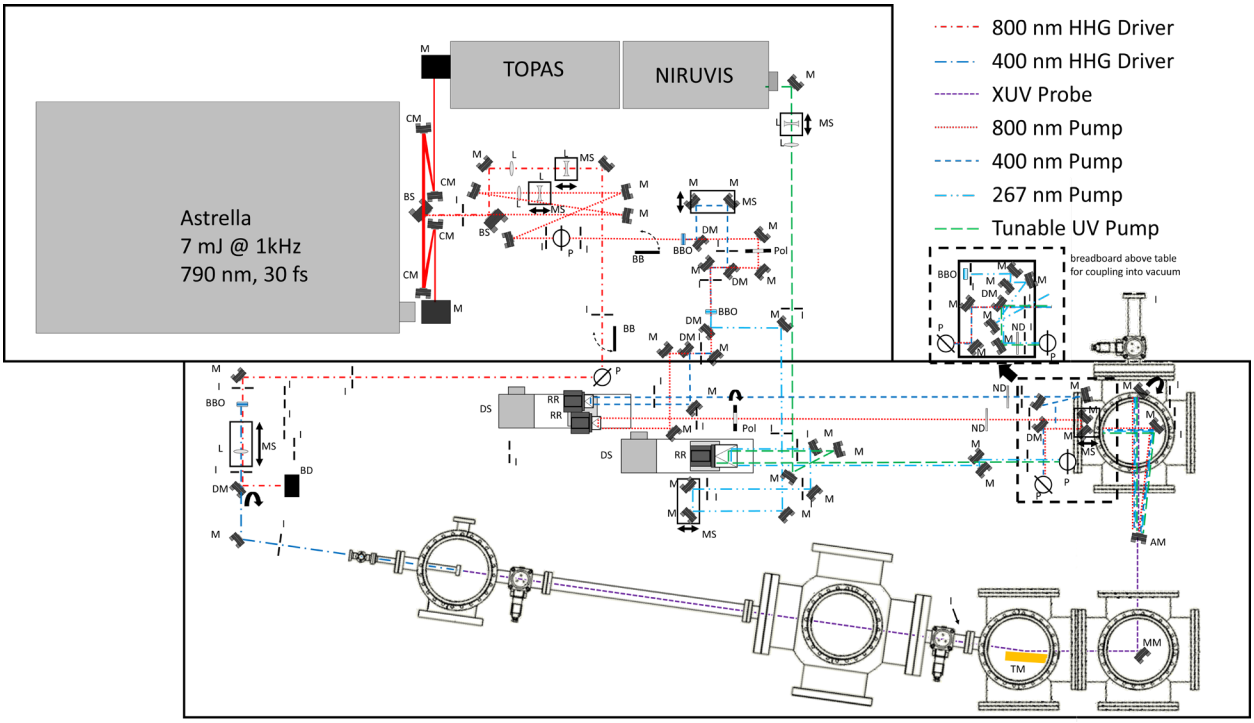

Figure 2.1 – Detailed table layout showing all the relevant components of the ultrafast laser optical setup. Relevant components are as follows: mirror (M), beamsplitter (BS), curved mirror (CM), iris (I), lens (L), periscope (P), beam block (BB), manual stage (MS), delay stage (DS), polarizer (Pol), dichroic mirror (DM), ß-barium borate crystal (BBO), retroreflector (RR), beam dump (BD), neutral density filter (ND), toroidal mirror (TM), multilayer mirror (MM), annular mirror (AM).

2.2.1 The Ultrafast Amplifier

The femtosecond Ti:Sapphire laser system used in this experiment is a commercially available Astrella USP turn-key laser system from Coherent, Inc.. This system consists of a Vitara™-S Ti:Sapphire oscillator pumped by a Verdi™-G5 optically pumped semiconductor (OPS) laser, a Revolution Nd:YLF pump laser, a regenerative amplifier, and a stretcher/compressor. This laser, typically referred to as a "turnkey" or "closed-box" system, is designed to minimize user input by maximizing the thermal and mechanical stability of the various components. To effect this, only the amplifier cavity and steering optics between the various components are accessible by the user; the Verdi, Vitara, Revolution, and stretcher/compressor are all hermetically sealed by the manufacturer and cannot be accessed by the user without voiding the manufacturer warranty and service agreements. The system has proven to be extremely reliable, maintaining stable operation with minimal power loss even with at times faulty, high-loss Pockels cells and a burnt lithium triborate (LBO) in the Revolution pump laser. The thermal and mechanical stability characteristics make this laser ideal for the liquid microjet spectroscopy experiment; the laser can maintain overlap between pump, probe, and liquid microjet over several hours without active beam stabilization and only needing slight adjustment to touch up overlap after data collection runs. Additionally, it reproducibly maintains pump-probe overlap day to day even when turning the laser off and back on the next day, significantly simplifying day to day work in the lab.

The process of generating femtosecond pulses in the Astrella starts with the Verdi™-G5, a continuous-wave (CW) OPS laser [3]. This laser consists of a semiconductor quantum well lasing medium pumped by a laser diode pump module emitting light at 808 nm driven by a ~25-26 A current. The optical cavity output is then frequency doubled in an LBO crystal to 532 nm to give a highly stable CW output used to pump the Vitara-S oscillator lasing medium. This laser is operated at the minimum output power needed to maintain stable mode locking of the Vitara™-S, nominally just over 3 W.[1] The Vitara™-S is a passively mode-locked Ti:Sapphire Oscillator utilizing Kerr lens mode locking for the stable generation of a 40 fs output with an ~90 nm full width at half maximum (FWHM) at 80 MHz. This femtosecond pulse can then be amplified through chirped pulse amplification (CPA) [4, 5]. This process, first demonstrated by Strickland and Mourou [6], is the basis for essentially all lasers used to generate high peak power ultrashort laser pulses

[1] As the total operating time on the Verdi-G5 and Vitara-S have gone up, the set value of the output power has needed to be increased slightly from 2.99 W to 3.13 W. The measured output power is 3.09 W with a set power of 3.13 W. The likely cause of this is increased wear of the optical components inside the oscillator cavity, decreased efficiency of the optically pumped semiconductor lasing medium in the Verdi-G5, and/or an inaccurate reading from the internal power meter.

today. In CPA, the seed is temporally broadened by adding chirp to the pulse (in the case of the Astrella in a grating-based stretcher)[2] before it seeds the amplifier cavity. In the Astrella, a z-scheme regenerative amplifier consisting of plano mirrors at the ends of the "z", positive meniscus lens' at the corners of the "z" with the front side 800 high-reflection (HR) coated, the back side 527 anti-reflection (AR) coated, and radii of curvature chosen to focus both the reflected 800 nm cavity beam and transmitted 527 Nd:YLF beam into the Ti:Sapphire crystal at the mid-point of the "z". In the cavity beamline are two Pockels cells and a wave-plate for rotating and maintaining the polarization of the beam, injecting a seed pulse, and extracting the amplified pulse which is pulled out of the z-scheme by a polarizing beam splitter. The amplified pulse is then expanded in a reflective geometry telescope and then passes through a transmissive cylindrical lens telescope to correct the astigmatism before being compressed by the same grating-based optical layout as the stretching of the seed pulse.[3] The resulting 1 kHz, 7 W output has an approximate bandwidth of 35 nm at FWHM centered at 797 nm, corresponding to a 28 fs transform limit and typical pulse duration of between 30 and 35 fs FWHM.[4]

The 7 W output of the Astrella is divided into three distinct beamlines using transmissive beamsplitters. The full 7 W, 11 mm beam is first expanded to 23 mm to minimize nonlinear dispersive effects in transmissive optics. This expanded beam is split into two by an 85/15 R/T beamsplitter, with the 1.05 W transmitted beam being telescoped to the 13 mm input diameter required for the TOPAS-Prime OPA system. The reflected 5.95 W is then split further by an 80/20 R/T beamsplitter, with the 4.76 W reflected beam reduced to 10 mm in diameter in a transmissive telescope and directed towards the semi-infinite gas cell (SIGC) to drive the high harmonic generation (HHG) process. The 1.2 W transmitted beam is reduced to 8 mm in diameter in a separate transmissive telescope and optically upconverted in BBOs to the second, third, and optionally the fourth harmonic of 800 nm.

2.2.2 Second Harmonic and Sum Frequency Generation

Converting the light generated in the Astrella to wavelengths across the electromagnetic spectrum is an extremely important part of the experiment as the generated light at 800 nm is useful in a very limited set of circumstances. The ability to tune the femtosecond output over a broad range of wavelengths from the IR to the UV is therefore necessary to perform most experiments. A straightforward

[2] The stretcher optical layout is ~60% efficient in transmitting the seed pulse from the oscillator.

[3] The compressor path is substantially more efficient than the equivalent stretcher path, at 75-80% transmission.

[4] These pulse durations vary slightly depending on the experimental setup and wavelengths ultimately used for the pump as a small amount of chirp is added in the compressor to compensate for chirp accumulated from transmissive optics in the beamline.

means of accomplishing at least the upconversion of the 800 nm output to the UV can be accomplished through second harmonic generation (SHG) and sum frequency generation (SFG) in a nonlinear optical medium [7]. To understand these processes, the interaction between the electric field of the incident laser pulse(s) and the induced polarization in the material must be considered. The polarization, or the average induced dipole moment of a material, can be represented as a power series with respect to the electric field as described by Equation 2.1:

$$\tilde{P}(t) = \epsilon_0\left[\chi^{(1)}\tilde{E}(t) + \chi^{(2)}\tilde{E}^2(t) + \chi^{(3)}\tilde{E}^3(t) + \chi^{(4)}\tilde{E}^4(t) + \cdots\right] \tag{2.1}$$

where $\tilde{P}(t)$ is the total polarization, ϵ_0 is the permittivity of free space, $\chi^{(n)}$ is the nth order optical susceptibility, and $\tilde{E}(t)$ is the electric field. Typical materials used to accomplish this, such as β-barium borate (BBO) and lithium triborate (LBO), are both non-centrosymmetric but also have a large second order susceptibility $\left(\chi^{(2)}\right)$ that facilitates the nonlinear process. The total electric field can then be represented as a sum of the oscillatory components with amplitude E_i. For sum frequency generation this involves two components of the incident field, E_1 and E_2, as shown in Equation 2.2.

$$\tilde{E}(t) = E_1(t)e^{-i\omega_1 t} + E_2(t)e^{-i\omega_2 t} + c.c. \tag{2.2}$$

Inputting this into the second order term of the polarization expansion shown in Eq. 2.1, one obtains the second order nonlinear polarization given in Equation 2.3.

$$\tilde{P}^{(2)}(t) = \epsilon_0\chi^{(2)}\left[{E_1}^2(t)e^{-i2\omega_1 t} + E_2(t)e^{-i2\omega_2 t} + 2E_1(t)E_2(t)e^{-i(\omega_1+\omega_2)t} + 2E_1(t)E_2(t)e^{-i(\omega_1-\omega_2)t} + c.c.\right] + 2\epsilon_0\chi^{(2)}[E_1E_1^* + E_2E_2^*] \tag{2.3}$$

From here, we can pick out the terms relevant to the processes we are interested in, where SFG derives from the $\omega_1 + \omega_2$ containing terms, DFG derives from the $\omega_1 - \omega_2$ containing terms, and SHG derives from the $2\omega_1$ and $2\omega_2$ containing terms. While this treatment makes many simplifications (such as considering the influence of the light simply as a time-varying electric field rather than a propagating wave with a polarization direction, vectored propagation axis, amplitude that varies in both space and time, and a depletable intensity, considering the medium to be lossless and dispersion-less with instantaneous response) it does demonstrate that the SHG and SFG processes rely on the square of the electric field strength and requires a material with a large $\chi^{(2)}$ to be as efficient as possible. While more extensive derivations can be found in many several resources [8, 9], the full derivation is not necessarily relevant to the use of the nonlinear crystals for optical upconversion and only the important consequences of the full derivations are

presented here. First, the SHG and SFG processes are two photon processes so the efficiency of the process increases substantially with increased incident field intensity, though practical limitations such as crystal thickness and the damage threshold of the optic set an upper limit to this. Second, the conditions described in Equations 2.4 and 2.5 must be met.

$$\omega_1 + \omega_2 = \omega_3 \tag{2.4}$$

$$\vec{k}_1 + \vec{k}_2 = \vec{k}_3 \tag{2.5}$$

Here, ω_i is the frequency of each mixing component and $\vec{k}_i$ is the associated wave vector of each mixing component. All wave-mixing geometries used to generate harmonics of the fundamental output of the laser were collinear, and therefore Equation 2.5 can be rewritten as Equation 2.6 [7]:

$$\frac{n_1}{\lambda_1} + \frac{n_2}{\lambda_2} = \frac{n_3}{\lambda_3} \tag{2.6}$$

where n_i is the refractive index of the medium and λ_i is the wavelength of each mixing component. This condition, known as the phase-matching condition, can be satisfied in a birefringent material where the refractive index depends on both the polarization axis and direction of propagation of the light. From this, the crystal angle necessary for the mixing process and the relative polarization of the input beams follow. In BBO, this is accomplished at a crystal angle of 29.2° for SHG utilizing Type I phase matching where two incident 800 nm photons with polarization aligned with the ordinary axis of the crystal are converted to one 400 nm photon with polarization aligned with the extraordinary axis of the crystal. In BBO, conversion to 266 nm and 200 nm light is possible through SFG using Type I phase matching can be accomplished at crystal angles of 44.3° and 64.7° crystal angles, respectively. A typical optical layout to generate the third and optionally the fourth harmonic is shown in Figure 2.2.

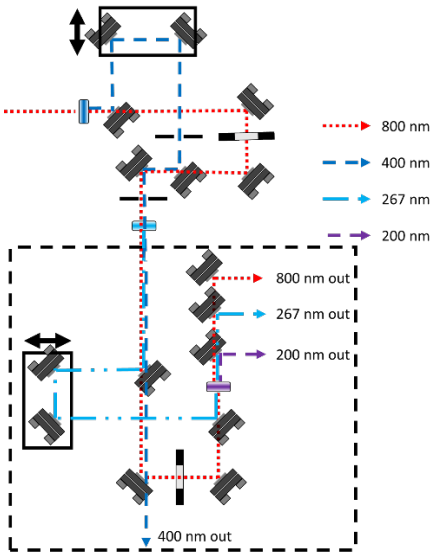

Figure 2.2 – Quadrupler layout with the 4ω leg shown in the box removed when 267 nm is being used as the probe wavelength.

Another important consideration that follows from Equation 2.6 is that the phase-matching condition needs to be met for all frequency components of input pulses. Practically, this means that for femtosecond pulses the group velocity delay (GVD)[5] of the material makes it such that only thin crystals can be used to generate short upconverted pulses. In this work, BBO crystals with thicknesses in the range of 80-500 μm were used to generate the second, third, and fourth harmonics as shown in Figure 2.2. It was observed that SHG was ~35% efficient (~400 mW), THG was ~8% efficient (~60 mW), and FHG was ~1% efficient (~3 mW) when FHG was employed, though these efficiencies are dependent on the thickness of the crystal and so the thinner crystals typically employed to maintain shorter pulses lead to poorer conversion efficiency.

2.2.3 Optical Parametric Amplification

The optical parametric amplification approach utilized in the TOPAS-Prime system used in lab to generate tunable UV light is a multi-stage system of parametric amplification and optical upconversion using ~1 W of the 800 nm output of the Astrella. This is accomplished through non-linear processes in materials with substantial third-order susceptibilities $\left(\chi^{(3)}\right)$ as well as materials with large second-order $\left(\chi^{(2)}\right)$ in conjunction [8, 9] to initially generate tunable IR light that can then be amplified in DFG and upconverted through SFG and SHG processes. The TOPAS

[5] GVD is the temporal broadening of an ultrafast pulse due to wavelength-dependent variability in velocity in transparent media of the different frequency components making up the pulse.

does not rely on optical parametric generation (also known as parametric fluorescence) that is common in many OPA systems. Generating the signal and idler beams by spontaneous emission is generally less efficient than through the parametric amplification of a white light continuum (WLC) component, as is used in the TOPAS-Prime. Here a small fraction of the beam is focused into a sapphire plate, sapphire having a $\chi^{(3)}$ appreciable enough for a small portion of the 30 fs TOPAS input to undergo filamentation and self-phase modulation due to the optical Kerr effect. With the correct focusing conditions, higher order terms of the refractive index shown in Equation 2.7 become relevant.

$$n \propto n_0 + \frac{\chi^{(3)}}{n_0}|\boldsymbol{E}_\omega|^2 \tag{2.7}$$

Here, n is the total refractive index, n_0 is the linear refractive index, $\chi^{(3)}$ is the third order optical susceptibility, and $\boldsymbol{E}_\omega$ is the electric field amplitude from the driving field. Under these conditions, the index of refraction varies appreciably across the gaussian spatial profile of the input beam, leading to self-focusing into a single filament.[6] Under these conditions, the input pulse is broadened spectrally through self-phase modulation, resulting in a WLC with wavelength components from the visible to beyond 1600 nm, the infrared portion being the important portion needed for the following steps.

From here, the IR light in the 1100-1600 nm range is amplified through optical parametric amplification, a special case of DFG in which an intense pump beam is used to amplify the weaker signal beam and generating an idler beam with frequency satisfying Equation 2.4, where the signal and idler would correspond to $\omega_1 + \omega_2$. In the case of the TOPAS-Prime, this occurs in two stages to generate a final combined ~320 mW of signal and idler. The signal and a "fresh" portion of the 800 nm input are mixed in a BBO to generate tunable visible light through SFG which is then doubled in a BBO to generate the tunable UV light spanning 235 – 265 nm used in some of the experiments detailed later in this dissertation. A detailed explanation of the alignment procedure of the TOPAS along with diagrams showing the beam path through the various stages are given in Appendix C.

[6] In the TOPAS-Prime it is crucial to get a single filament for white-light generation for best stability, if the input beam has too large a diameter and too high an intensity, multiple filaments can be generated the following optical parametric amplification stages will be noticeably less stable.

2.2.4 High Harmonic Generation

Arguably the most important factor in any photoelectron spectroscopy experiment is the ability to ionize an analyte of interest in a manner as unperturbed by Franck-Condon (FC) factors as possible to collect a sample that is representative of the dynamics in whatever population of interest. The easiest way to accomplish this is to simply use a probe pulse several eV higher in energy than the binding energy of the state you are observing. For most solvated analytes and liquids [10], this means having a probe energy of ~10-12 eV at a minimum to readily photoionize valence electrons from the ground electronic state or from any possible excited state. To achieve probe energies of this magnitude, it was decided to build a high-harmonic generation beamline based on a semi-infinite gas cell [11]. Most of the planning and design of this beamline was done by H. L. Williams, and any design specifics not found here can be found in her dissertation [1]. The implementation of these designs and integration into the existing photoelectron spectrometer setup such that time-resolved photoelectron spectra of solvated species can be readily and reproducibly collected has been the primary undertaking of this dissertation.

The generation of XUV harmonics can be driven with any wavelength from the IR to the UV so long as it is of sufficient intensity to substantially distort the coulombic potential of an atom [12-17]. In this experiment, harmonics are generated by a driving field centered at 400 nm. In the testing and optimization phase of implementing an XUV probe in the experiment, 800 nm was used to initially generate harmonics to test alignment and the extremes of potential gas cell conditions. Generating harmonics with 400 nm results in substantially higher flux for low energy harmonics due to the $\sim\lambda^{-4} - \lambda^{-5}$ wavelength scaling [18-20] and simplifies harmonic selection by lowering the cut-off energy resulting in fewer harmonics. Additionally, driving harmonics using a 400 nm driver is advantageous as harmonics are spaced by $2\omega_0$, making harmonic selection significantly more manageable. Future iterations of the experiment will likely employ either an 800 nm or 1300 nm[7] driving field though this will not be discussed here.

Currently, ~4.5 W of the 800 nm output of the Astrella is directed towards the gas cell, first being doubled in a BBO crystal[8] to 0.7 – 1.1 W of 400 nm light through SHG. This light is focused by a 1 m focal length lens (Eksma Optics, 110-1245ET)

[7] Generated by a TOPAS-HE driven by 4.5-5 mJ of the 800 nm fundamental.

[8] Several crystal thicknesses and suppliers have been used for this purpose. Crystal thicknesses from 200 μm to 1 mm have been used and suppliers include Eksma Optics, Edmund Optics, Wisoptic, and Crystec. Thinner crystals generate lower overall power but result in a temporally shorter driving field while thicker crystals result in higher average power and longer pulses. Initial testing was done with a 1 mm thick crystal but we have gradually transitioned to consistently using a 200 μm to generate the 400 nm driver due to the shorter temporal duration of the resulting driver.

mounted in a 5-axis kinematic mount (Thorlabs, K5X1) and linear translation stage (Newport, 436) on which the kinematic mount is fixed. The remaining 800 nm fundamental is filtered out using a 1 mm thick dichroic mirror (Edmund Optics, #69-202) to minimize nonlinear effects due to the high intensity of the beam at this point. The turning mirrors used to adjust the near-field and far-field alignment are dual band HRs (Eksma Optics, 052-4080), with low-GDD coatings for both 400 and 800 nm to accommodate a wider range of focusing and doubling layouts. The quality of the focal spot size at the exit of the gas cell evaluated and optimized to obtain the smallest diameter and best gaussian shape by imaging the focus with a monochrome camera (Edmund Optics, EO-1312-GL LE) just outside the gas cell with the chamber at atmospheric pressure and adjusting the lens position and angle relative to the input beam. Once optimized, the linear translation stage is moved a distance back corresponding to the distance from the camera sensor to the gas cell exit when the focus is being imaged. The possibility of utilizing a concave mirror to focus the driving beam instead of a transmissive lens was considered initially when evaluating the performance of the harmonic generation process as concave mirrors largely eliminate aberrations limiting focal diameter. It was determined using a reflective lens would only increase the generation efficiency if the harmonic generation was optimized at the focus of the driver and would add substantial complexity to the alignment as moving the focal position would certainly change the alignment into the gas cell.

The gas cell assembly, shown in Figure 2.3, consists of a 27.6 cm long tube 1" in diameter with a 1.33" CF flange on one end and a custom end cap for securing replaceable disks. Welded at the midpoint of this tube is a 2.75" CF flange used to mount the gas cell to a vacuum chamber to differentially pump the region outside the gas cell. The gas cell is extended by attaching two 1.33" CF tees (Duniway, TE-0133) and two 1.33" CF full nipples (Duniway, NP-0133) to the 1.33" CF flange at the end of the gas cell. This extends the SIGC to a total length of 60 cm from window to end cap. This is done to minimize nonlinear effects within and burning of the fused silica window. The atmosphere side of the SIGC is sealed by a 0.75" diameter, 1 mm thick fused silica window (CVI Laser Optics, PW1-0704-UV) through which the driving laser beam transmits and is affixed to the 1.33" CF flange at the end of the gas cell using a Viton CF gasket (Duniway, VG-0133-5) and a custom Teflon flange. The opposite end is sealed by a pair of 0.75" diameter, 0.005" thick stainless steel disks cut from a sheet of foil (McMaster-Carr, 3254K93) and tightened into a Viton o-ring (Sealing Devices Inc., 2-032) to form a vacuum-tight seal.

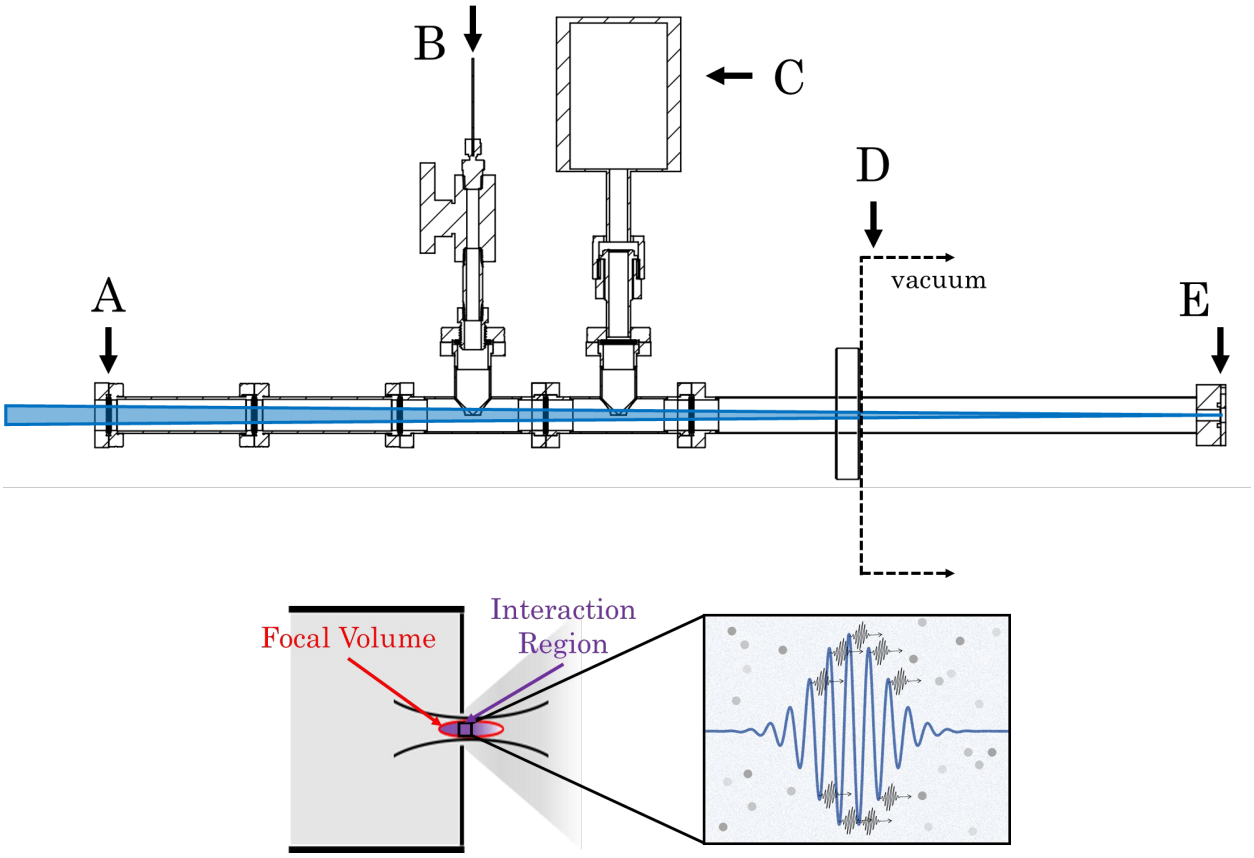

Figure 2.3 – Top: Semi-infinite gas cell assembly with driving laser beam path shown and important components labeled as follows A) entrance window, B) gas inlet, C) Baratron pressure gauge, D) transition from atmosphere to vacuum outside gas cell formed by a conflat flange, and E) drilled foil creating an abrupt transition from the gas cell pressure to high-vacuum. Bottom: Schematic of HHG occurring at the end of the gas cell, with the focal volume centered slightly outside the SIGC and the interaction region primarily to the left-most side of the focal volume. The XUV light being generated at the peak of each cycle of the intense driving field in this interaction region is shown in the expanded view. Adapted from [21].

The gas cell is initially evacuated using a rotary vane vacuum pump (Pfeiffer, DUO 11 M) that maintains vacuum in the gas manifold through which the SIGC gas is supplied to minimize volatile contaminants. When generating 21.7 eV harmonics, the gas cell is filled to 6 Torr with ultra-pure Kr gas (99.9999% purity) and the pressure maintained with a low-flow metering valve (Swagelok, SS-SS2-VH). Pressure is monitored by a Baratron gauge (MKS Instruments, 622C13TBE) mounted on the 1.33" CF tee between the flow metering valve and 2.75" CF flange, and pressure is read out on a pressure meter (MKS Instruments, 660C12). This allows for stable and reproducible gas cell conditions for harmonic generation.

Maximum harmonic flux is achieved by setting the focal position of the driving laser ~1 cm beyond the end of the gas cell. With the focus at this position, the driving beam drills a hole in the stainless steel ~250 micron in diameter which serves as an opening that allows the harmonics to exit the gas cell. Due to slight variations in pointing day to day, this hole eventually increases in size until low (10^{-4} Torr) pressures can no longer be maintained in this region of the beamline, at which point the stainless steel disks must be replaced. This happens every 3-4 weeks and simply requires venting that chamber, loosening all 4 screws on the end cap, removing the bottom screw to allow the spent disks to fall out, replacing this screw and removing the top screw and placing two new disks in, and finally tightening the screws until the o-ring forms a vacuum-tight seal with the disks.

The vacuum chamber into which the harmonics exit is maintained at high vacuum, on the order of 10^{-4} Torr, to minimize flux lost to reabsorption. This is accomplished using a 1000 L/s turbomolecular pump (Leybold, 1000C) backed by a rotary vane mechanical pump (Edwards, E2M18). The gas load for this turbomolecular pump is still substantially higher than anywhere else in the experiment thus requires cooling at the limit of the conductance through the internal cooling tubing. This region is separated from the remainder of the beamline by a 2.75" CF gate valve (MDC Precision, 303001-01) and a 2.75" blank copper gasket with a 0.1875" hole drilled through the center. This hole is sized to match the size of the driving beam at this point plus a small margin for alignment error. Even if the driving beam clips slightly, the XUV is expected to be approximately 1/3 the size of the driving beam so it is highly unlikely the XUV will clip. This gasket serves as a differential pumping aperture, preventing most of the gas exiting the SIGC from propagating into other regions of the XUV beamline.

Notably, it was observed this HHG configuration generated substantially more harmonic flux than could reasonably be used in a given experiment. Using the full flux generated resulted in substantial broadening of photoelectron signals due to space-charge broadening. To remedy this, an iris was adjusted to reduce the driving field intensity until the generated harmonic flux was such that the photoelectron signal showed visibly distinct solvent peaks. Typically, this amounted to 10-20% the harmonic flux that was generated with the full driving laser field intensity.

2.2.5 Measuring and Steering XUV Harmonics

The manipulation of the XUV beam must be done under high vacuum to minimize reabsorption, so the entirety of the XUV beamline is kept at 10^{-6} – 10^{-7} Torr. This is accomplished with a series of four 10" CF 6–way crosses each pumped on by an

individual turbomolecular pump and separated by gate valves, either pneumatic (MDC Precision, 303001-01) or manual (MDC Precision, 302006).

The first chamber in the XUV beamline is the beam analyzer and filter chamber. This chamber, a 10" CF 6-way cross, is modified with two CF half nipples above the horizontal portions of the cross along the XUV propagation axis. These allow for linear feedthroughs (MDC, BLM-133-6) holding filter holders to be mounted on the chamber allowing for filters to be changed while still under vacuum. Given the fragile nature of the filters, this is crucial to save time replacing damaged foils. There are 4 positions for filters on the current filter mount, though typically only 3 will be used and the 4th position left open in case the driving beam alignment needs to be checked while still under vacuum. The chamber is pumped out by a turbomolecular pump (Leybold, 450i) backed by a rotary vane mechanical pump (Pfeiffer, Duo 11 M). The pumping speed of the backing pump is reduced by a butterfly valve (Kurt J. Lesker Company, KBV010MAQF25) to minimize the likelihood of damage to the foils when roughing out the chamber. The XUV chambers and optics are shown in Figure 2.4.

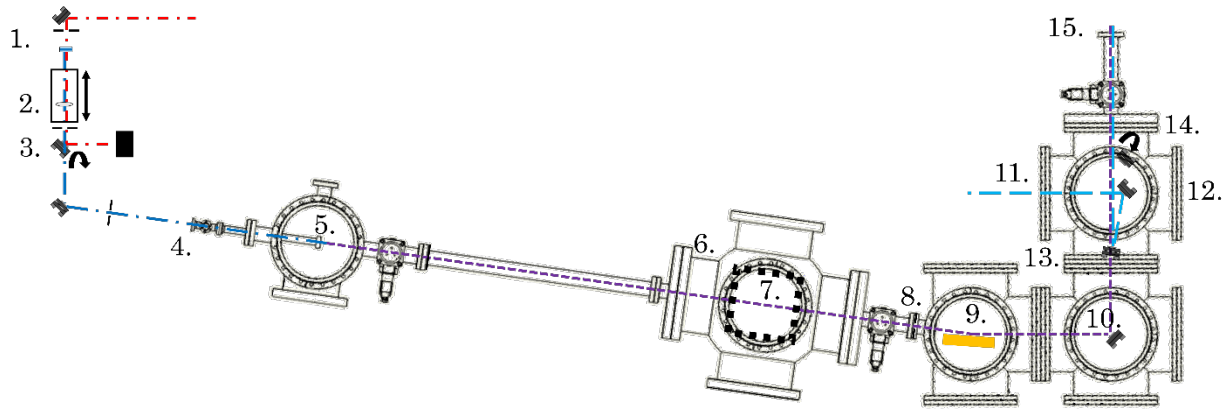

Figure 2.4 – The XUV beamline. Relevant components are as follows: 1. BBO crystal used to double the driving laser, 2. 1.0 m thin plano-convex lens for focusing into the gas cell. 3. Thin dichroic mirror for separating residual 800 nm from the 400 nm driver. 4. Thin fused-silica entrance window to the SIGC. 5. Exit of the SIGC into the surrounding chamber. 6. 200 nm thick aluminum filter. 7. Beam analyzer. 8. Beamline alignment pinhole. 9. Toroidal mirror. 10. Multilayer mirror. 11. Pump beam entrance window. 12. Picomotor-actuated alignment mirror for pump beam steering. 13. Annular mirror. 14. Pickoff mirror on flip mount for coupling pump and XUV driver beams out of vacuum. 15. Entrance to interaction region.

To separate the driving laser beam from the XUV harmonics, a thin aluminum foil is employed. This filter is 200 nm thick and backed by a Ni mesh with 86%

transmission (Lebow Company, 0.2Al-M-L1.0). At this thickness, aluminum transmits 10% of 15.5 eV light, 64% of 21.7 eV light (the desired harmonic), and 62% of 27.9 eV and 34.1 eV light. The driving beam is largely reflected and dispersed back into the vacuum chamber and does not continue to propagate along with the XUV beam.

Once separated from the driver, a home-built spectrometer can be moved into the beamline to qualitatively analyze the harmonics being produced in the SIGC. This spectrometer, replicated from the design of Gessner [22], consists of two entrance tubes, an entrance slit (Lenox Laser, A-SLIT-3/8-DISC mounted, 50 μm x 3 mm), a SiN_x nanograting (LumArray, 100 nm periodicity), and an imaging-grade set of 2" chevron-stacked microchannel plates (MCPs) and phosphor screen detector. The incident beam transmits through one of the two entrance tubes, one transmitting directly to the MCP detector to monitor total flux and one to the slit before the nanograting. The XUV transmitted through the slit is then incident on the nanograting at an angle normal to the grating plane. The entrance tube to the slit eliminates background signal from scattered light and the slit ensures diffracted harmonics are spatially isolated on the detector. The SiN_x nanograting consists of 1.0 mm × 4.5 mm windows [23, 24]. In the windows, supports 0.17 μm wide with periodicity of 1.5 μm run perpendicular to the nanograting. The nanograting is lithographically developed from a 200 nm thick SiN_x membrane, resulting in a grid of free-standing 44 nm wide bars with a periodicity of 100 nm. This nanograting will separate the XUV light by wavelength with angular spacing for first order diffraction given by Equation 2.8:

$$\theta = sin^{-1}\left(\frac{n\lambda}{d}\right) \tag{2.8}$$

where θ is the diffraction angle, n is the diffraction order, λ is the diffracted wavelength, and d is the periodicity of the grating. For the relevant harmonics generated by a 400 nm and 800 nm driving fields, the diffraction angles are given in Table 2.1.

When the wide range of angles is considered, the detection angle must be optimized for a given harmonic. In our case, the MCPs are positioned approximately 3 cm from the nanograting at a 30° offset from the incident XUV on the nanograting. The assembly is shown in Figure 2.5. The entire assembly is mounted on a 2" translation stage (Newport, 436 unanodized) actuated by a 2" travel actuator (MDC Precision, 660006) and mounted to a custom 10" CF flange (Pfeiffer Vacuum, 1000-000N) with a custom coupling and mounting bracket, the drawings for which are given in Appendix B.

800 nm Harmonics		400 nm Harmonics	
Harmonic Energy (eV)	Diffraction Angle	Harmonic Energy (eV)	Diffraction Angle
17.1 (11th)	46.5°	15.5 (5th)	53.1°
20.2 (13th)	37.9°	21.7 (7th)	34.8°
23.3 (15th)	32.1°	27.9 (9th)	26.4°
26.4 (17th)	28.0°	34.1 (11th)	21.3°
29.5 (19th)	24.9°	40.3 (13th)	17.9°
32.6 (21st)	22.4°		
35.7 (23rd)	20.3°		
38.8 (25th)	18.6°		
41.9 (27th)	17.2°		
45.0 (29th)	16.0°		
48.1 (31st)	14.9°		

Table 2.1 – Diffraction angle from the 100 nm nanograting for relevant harmonics generated by an 800 nm driving field and a 400 nm driving field.

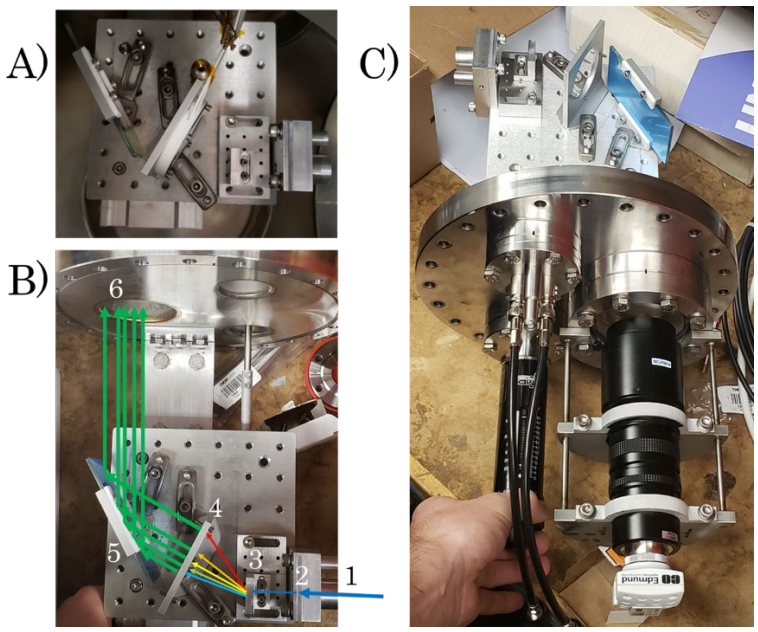

Figure 2.5 – A) Spectrometer assembly. B) Full beam analyzer flange assembly. C) Schematic diagram of spectrometer operation with relevant components labeled. 1) entrance tube, 2) 50 μm slit, 3) 100 nm transmissive nanograting, 4) MCP/phosphor screen detector assembly, 5) silver mirror, 6) window to camera.

This spectrometer measures relative intensity of harmonics with the only losses due to the filter employed. While advantageous for understanding the HHG process, proper alignment of the grating and assignment of the harmonics is practically quite difficult. With a 400 nm driving field, only 2-3 harmonics can be imaged by the phosphor screen effectively due to space limitations requiring the MCPs to be

several centimeters from the nanograting. As such, it has been found the photon flux and harmonic distribution is much more easily determined using photoelectron yields and total flux measured by a XUV photodiode just before the interaction region. This method has the advantage of optimizing not only the HHG conditions but the total harmonic flux on target and saves time compared to aligning the spectrometer. While this works well for low-order harmonics with good reflectivity off a gold mirror at a 45° AOI, it likely will not work nearly as well for harmonics above 50 eV where the reflectivity of a gold mirror at this angle is in the single digit percentages compared to ~30% in the 20-30 eV range. As such, the spectrometer is not frequently used but remains available to use if higher-order harmonics are needed for the experiment.

When aligned well, it was possible to diffractively image the individual harmonics generated in the semi-infinite gas cell (SIGC) immediately after the 200 nm Al filter. A typical image taken using the spectrometer is shown in Figure 2.6. It is noteworthy that the 5th harmonic of 400 nm is not observed. When these images were taken, the aluminum foils had been exposed to atmospheric conditions for an extended period of time. This led to oxidation of the Al filter surface, suppressing the 5th harmonic at 15.5 eV. In the image, the 7th and 9th harmonic are readily apparent.

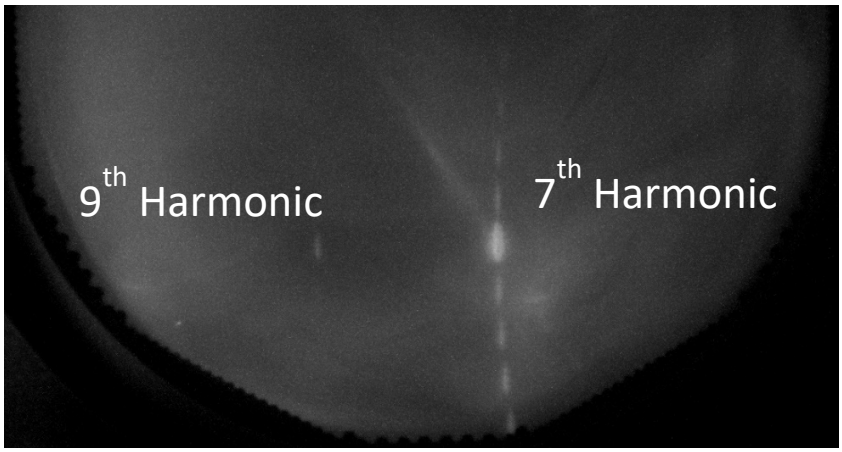

Figure 2.6 – The image captured using the beam analyzer to measure the harmonic spectrum.

By interpreting this image in the fashion described by Kornilov et al. [22], we find that the 7th harmonic is approximately an order of magnitude more intense than the 9th, and the energetic width of the signal is 250 ± 50 meV. This agrees well with the photoelectron spectra collected using atomic systems as the target. Unfortunately, the difficulty in aligning this spectrometer made it unreliable for day-to-day beam diagnostics. It was found that the photoelectron spectrometer was substantially more sensitive to small signals such as the minute amount of the 11th harmonic of

400 nm generated. To this end, optimization of harmonic flux was preferentially done by using the photoelectron spectrometer.

After filtering out the driving laser, the XUV propagates along the beamline to a toroidal mirror. This mirror is held in a custom holder mounted on a rotational stage (Newport, 07SI26049) and a stack of linear translation stages (Newport, 07SI25008) to move the mirror in the XY-plane. The holder, originally presented in the dissertation of B. A. Erickson [2], has been modified to add Z-axis and adjustability for rotation about the axis normal to the surface of the mirror. Drawings detailing these changes are included in Appendix B. The toroidal mirror is used at a distance 2 times the focal length[9] to image the region in which the harmonics are generated an equivalent distance away. Adjusting this mirror is very complex, and instructions for aligning this mirror are included in Appendix C. The toroidal mirror mount is contained in a modified 10" CF 5-way cross with a 2.75" CF half nipple welded parallel to the table surface at an 8° offset from being orthogonal to the other flanges. This flange serves as an excellent point of alignment for the XUV before the toroidal mirror, which is best accomplished using a blank 2.75" CF blank gasket with a 0.125" hole at the center point. This chamber is mounted on a custom stand consisting of a 10" CF blank flange welded to a 10" OD stainless steel tube cut to length to elevate the chamber such that the center of the chamber is at the height of the beam (~10.75" from the surface of the table). This chamber is pumped on by a turbomolecular pump (Leybold, 450i) backed by a rotary vane mechanical pump (Edwards, E2M28) with a manual valve (Kurt J. Lesker Company, SA0100MVQF) used to throttle the pumping speed of the mechanical pump.

After the toroidal mirror, the beam is incident on a multilayer mirror used to simultaneously turn the beam 90° and select a single harmonic. This ensures that photoelectron signal collected during any given experiment does not contain contributions from multiple harmonics which would convolute interpretation of and potentially obscure signals from any transient signals. Due to the high energy of the beam and the AOI, a mirror had to be specially designed to selectively reflect the desired harmonic with high reflectivity. This is accomplished with a multilayer mirror designed by Eric Gullikson who works at the Center for X-Ray Optics at LBNL. The measured angle-dependent reflectivity of the mirror currently in use is shown in Figure 2.7. Notably, the multilayer mirror is slightly more reflective than a gold mirror for the 7th harmonic of 400 nm with a reflectivity of 35%, with reflectivity at the 5th and 9th harmonic of 400 nm of 4% and 2%, respectively.

[9] The toroidal mirror, which is 160 mm × 30 mm × 20 mm, has radii of curvature R_1 = 12322.8 mm ± 1% and R_2 = 93.6 mm ± 1%. This corresponds to an on-axis focal length of 889 mm at the operational angle. This was a point of great consternation, as the actual focal length was determined to be f = 992 mm, ~10% greater than the focal length it was spec'd to be.

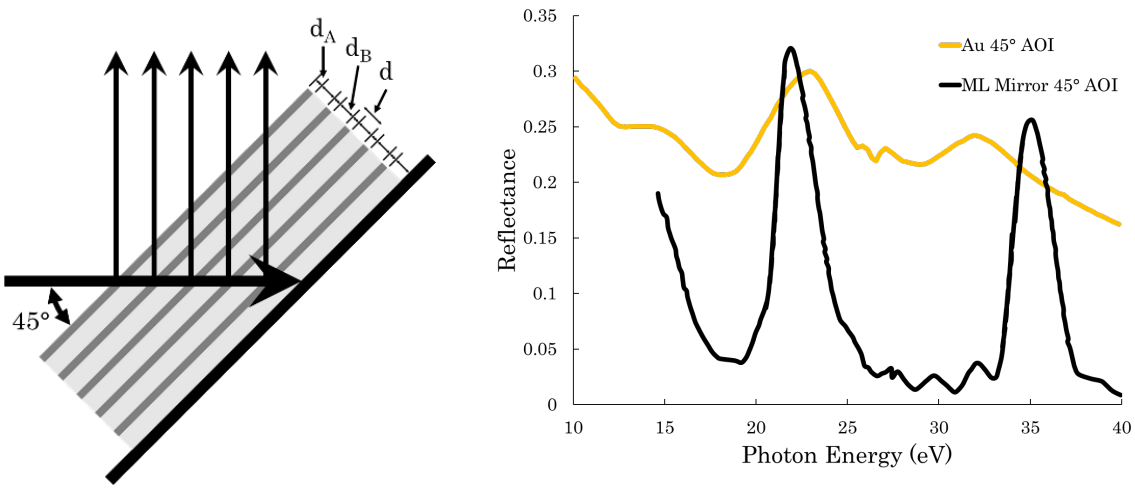

Figure 2.7 – Left: Schematic diagram of the multilayer mirror, showing the incident XUV beam at a 45° AOI and the resultant partial reflections of XUV light off each layer boundary. Adapted from [25]. Right: Calculated reflectance of XUV light off of a thick gold mirror and a multilayer mirror designed to selectively reflect 21.7 eV and minimize reflectivity of 27.9 eV.

The mirror is composed of 5 layers each of alternating SiC and Mg, with a 52 nm total layer thickness and a layer thickness ratio $\Gamma = 0.1$. These layers are deposited on a Si wafer with thin alternating SiC layers reflecting progressively more of the incident XUV. The layer thicknesses and Γ are tuned specifically to optimize the reflection of the 7th harmonic (21.7 eV, 57 nm) while minimizing the reflectivity of the 5th and 9th harmonics (15.5 eV, 80 nm; 27.9 eV, 44 nm) to eliminate their contributions in the photoelectron spectra. An example of the effect the multilayer mirror has on photoelectron spectra is shown in Figure 2.8. The multilayer mirror is mounted in a piezoelectric motor-actuated optic mount (Newport, 8821-AC-UHV) which is connected to the same controller that actuates all the picomotors in the experiment. The motorized control allows for extremely fine alignment of the XUV probe while maintaining constant alignment into the gas cell.

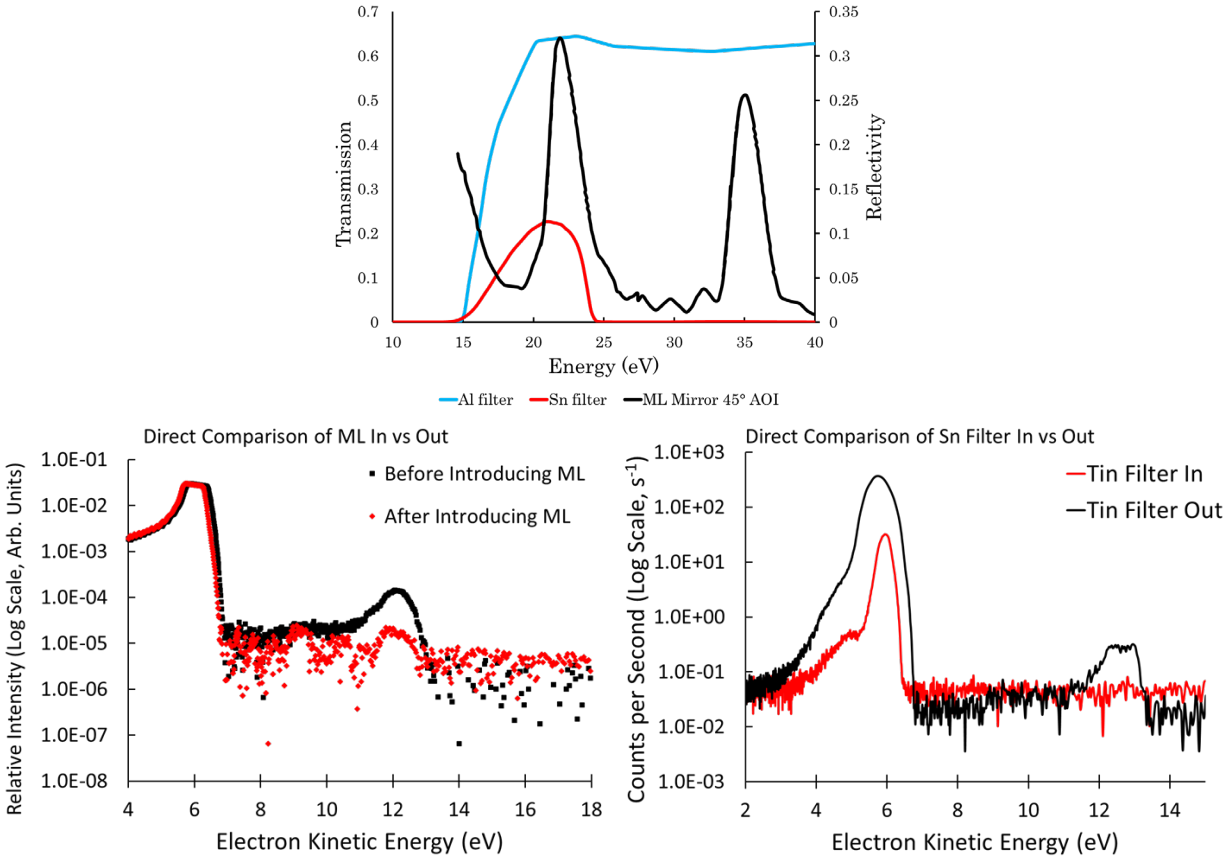

Figure 2.8 – (top) Transmission of 200 μm Al and Sn filters and reflectivity of the multilayer mirror for reference. (bottom left) Effect of replacing the gold mirror with the multilayer mirror. (bottom right) Spectra obtained after further filtering the harmonic spectra with a tin filter immediately after the multilayer mirror.

Recently, it was observed that the multilayer mirror alone was not sufficient to fully eliminate the contributions from the 9th harmonic. To rectify this, a 200 nm Sn filter was added after the multilayer mirror to fully suppress this contribution, as shown in Figure 2.8. This thickness of Sn readily suppresses the 9th harmonic (0.014% transmission at 27.9 eV) while still maintaining good 7th harmonic transmission (22% at 21.7 eV). This filter is mounted in a piezoelectric motorized filter mount (Thorlabs, ELL9K). This filter mount is made for 1" diameter optics, so the Lebow L1.0-size filters, with a 17 mm O.D., are first secured in a threaded mounting adapter (Thorlabs, AD17T). This was found to be a much more effective solution compared to filling the chambers after the Al filter with Ne, which would require such high pressures that they would prevent the turbomolecular pumps from operating. It was estimated that all the chambers from the toroidal mirror to the liquid jet (~2 m path length) would need to be filled to a pressure of over 100 mTorr of Ne to have the same effect as a 200 nm Sn filter. The portion of the optical layout including the toroidal mirror, multilayer mirror, tin filter, and annular mirror is shown in Figure 2.9.

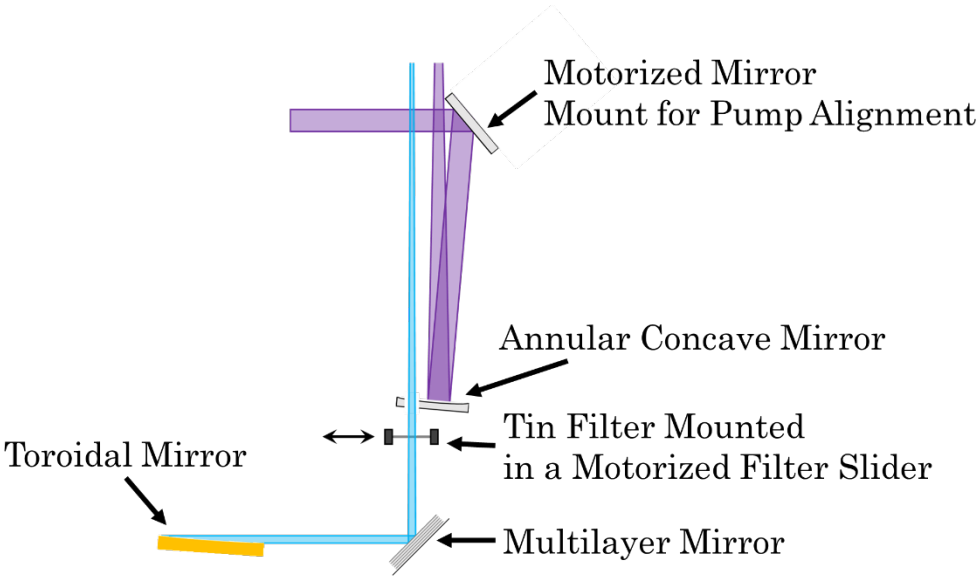

Figure 2.9 – Optical layout under vacuum in the XUV beamline including all components from the toroidal mirror to the annular mirror. Relevant components are labeled in the figure.

To account for this filter being in vs not, the attenuation of the HHG driving beam is adjusted to maximize signal intensity while still maintaining distinct solvent peaks. The Sn filter is not used for filtering out the driving beam as Sn filters have a reputation for being particularly fragile and burning/melting at the intensities we use to drive harmonics and are more than double the price of the Al filters, making this combination both an economical and effective solution to filtering out both the driving field and 9th harmonic completely.

The multilayer mirror and Sn filter are housed in a 10" CF 6-way cross connected directly to the 10" chamber housing the toroidal mirror and is pumped out by the same turbomolecular and rotary vane pump. Like the chamber housing the toroidal mirror, the center of the chamber housing the multilayer mirror is brought up to the XUV beam height using a 10" CF blank flange welded to a 10" OD stainless steel tube cut to length to elevate the chamber accordingly. Additionally, the optics are mounted on a breadboard (Thorlabs, MBR6U) to essentially elevate the base of the chamber to minimize the length of optical post necessary for mounting the optics. Finally, this chamber and the following chamber are separated by a 6" CF manual gate valve (MDC Precision, 302006).

The final optic in the XUV beamline, an annular mirror, is not used for manipulating the XUV beam but rather overlapping it with the pump pulse at a minimal crossing angle, approximately 0.5°. This annular mirror is highly customized, originating as a concave window (Eksma, 010-0225E) before having a

hole drilled through at a 5° angle. Several substrates with varying hole size were fabricated, but the current optic uses a 5 mm diameter hole offset from the edge by ~4 mm on the coated side. The coating of the mirror was done after the optic had been cleaned thoroughly to remove adhesive and lubricant used in the fabrication. Once cleaned, the mirror substrates were sent to Lattice Electro Optics where a protected UV enhanced aluminum coating was added to the curved side of the substrates. This coating is damage resistant and offers a >85% reflectivity across the whole range of pump wavelengths we utilize (specifically 200-800 nm). The mirror is used to simultaneously focus the pump beam, being placed as precisely to 1 m from the interaction region as possible, resulting in UV spot sizes of ~100 μm. This corrects for the aberrations and broadening of the pulse from using 2 m transmissive lenses [26], which was unavoidable due to space constraints and wavelength-dependent focal positions of transmissive lenses. In the near future, the use of a translation stage under the annular mirror is planned to enable maximization of the pump-probe overlap by controllably changing the focal position of the annular mirror. The annular mirror and all other optics in the annular mirror chamber are mounted on a 4" × 12" optical breadboard (Thorlabs, MB412). The pump beam is coupled into vacuum through a 2 mm CaF_2 window (Crystran, CAFP25.4-2U) with custom spacer mounted in a 2.75" CF flange for 5 mm windows (Thorlabs, VC224).

In addition to the annular mirror, a motorized kinematic mount (Newport, 8821) directing the 800 nm, 400 nm, 267 nm, or TUV light to the annular mirror allows for fine alignment control of the pump beam. Additionally, a flip mount allows to couple the pump beam and low-power XUV driver beam while at atmospheric pressure or under vacuum. Another useful diagnostic tool in this chamber is a calibrated XUV photodiode (OptoDiode Corp, AXUV100G). The responsivity of this photodiode is well known, having been tested at Physikalisch-Technische Bundesanstalt and confirmed independently using calculations from groups at LBL and NIST [27]. This high degree of certainty for the photodiode itself meant that it only needed to be referenced to a known UV flux at a given wavelength and at comparable fluences to account for the circuitry connecting the photodiode to the oscilloscope used to measure the photodiode waveform. The wavelength-dependent responsivity of the photodiode is shown in Figure 2.10

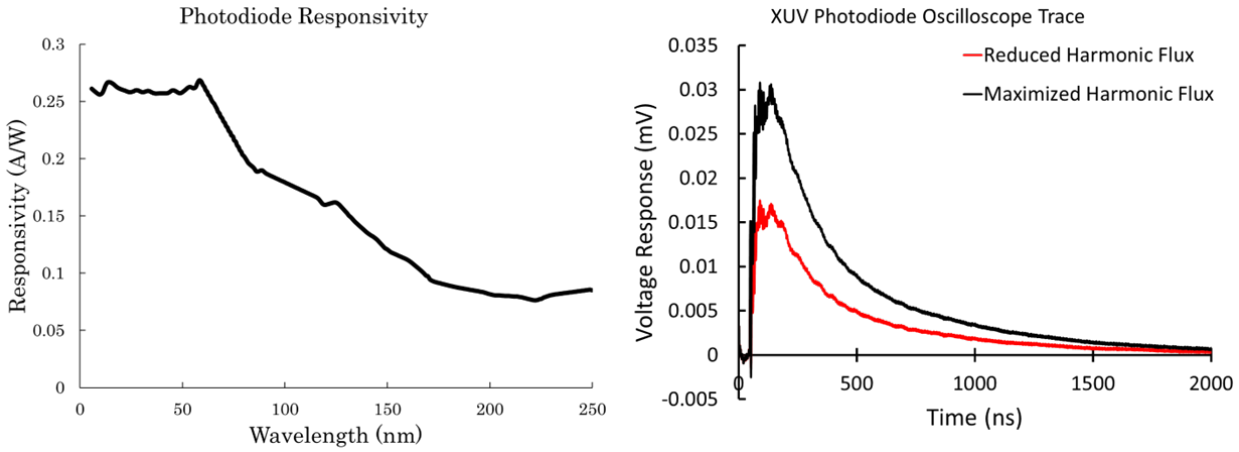

Figure 2.10 – (left) XUV responsivity of AXUV100G and (right) typical oscilloscope trace for XUV measurement using the photodiode.

After calibrating the photodiode using 250 nm UV light with continuous pulsed powers in the 200 μW to 900 μW range known to a precision of at least 1.5%, the XUV total flux before the interaction region was measured. A typical oscilloscope trace for an XUV photodiode measurement is shown in Figure 2.10. By measuring the flux just before the interaction region and accounting for sources of loss, specifically a gold mirror at 45° AOI, a gold mirror at 4° AOI, and a 200 nm Al filter, to arrive at an approximate 100 nJ/pulse (this was done before the multilayer mirror and Sn filters were used).[10] This would equate to a conversion efficiency of ~1.0×10^{-4}, which agrees well with conversion efficiencies obtained from similar experiments [28]. This measurement was done when optimizing total flux from the HHG source was the main goal of the experiment, now the typical energy is 10-20 nJ/pulse in a single harmonic as the multilayer mirror makes it nearly impossible to estimate the flux in neighboring harmonics. This flux is further cut down to an estimated flux in the range of 2-5 nJ/pulse for any given experiment.

The gate valves on either side of this chamber allow for it to be vented while keeping the remainder of the vacuum system under high vacuum, enabling the flip mount to be put in place and the chamber pumped back down to low pressure within an hour of starting the venting process. The chamber is currently pumped down using a magnetically levitated turbomolecular pump (Pfeiffer, ATP 1603 M) on loan from the SEVI project while a replacement pump (Shimadzu Industrial, TMP-1003 LMC) is serviced. The transition to magnetically levitated pumps was

[10] This is determined by the well-known reflectivity and transmission of these optical components. The relative intensities of each harmonic are measured in the photoelectron spectrometer using a $Xe_{(g)}$ target such that the relative cross section at each harmonic energy is approximately the same. The relative transmissions for each harmonic are 2.2% for the 5th harmonic, 16.3% for the 7th harmonic, 11.6% for the 9th harmonic, and 12.0% for the 11th harmonic.

necessitated by the wearing of bearing on an old ceramic bearing pump making the pump-probe overlap dependence on pump vibrations readily apparent. This was confirmed by monitoring pump-probe overlap with the pump on vs off, with nearly half an order of magnitude improvement in pump-probe overlap stability gained while the pump was off. Introducing the magnetically levitated pump yielded a pump-probe overlap stability comparable to what was observed with the ceramic bearing pump turned off.

Overlapping the pump and XUV probe both spatially and temporally is practically quite difficult but theoretically simple. First, the lengths of the optical paths the XUV and pump beams propagate along must be measured to make sure the temporal overlap is within the travel distance of the stage. Once this is confirmed, the overlap of the XUV driver and pump beams should be checked over the full travel range of the delay stage using the flip mirror inside the annular mirror chamber and a pinhole outside. Then, a BBO of appropriate angle and thickness can be substituted for the pinhole and the delay stage moved in small increments until the appropriate wave-mixing signal is observed. Once all pump wavelengths have been optimized in this fashion, the flip mirror can be flipped down and overlap optimized between XUV and pump under vacuum. This is accomplished stepwise, with 800 nm overlap optimized using LAPE taking advantage of the wavelength scaling of LAPE. Then 267 nm – 800 nm, TUV – 800 nm, and 267 nm – 400 nm overlap optimized using two-color multiphoton ionization of either $H_2O_{(g)}$ or $Xe_{(g)}$. Finally, overlap of all pump beams with the XUV can be optimized through LAPE. This stepwise process is something that can be done under all foreseeable experimental conditions.

2.3 Liquid Microjets and Flatjets for Photoelectron Spectroscopy

A general requirement of photoelectron spectroscopy is that the photoelectrons emitted from a sample be detected with minimal distortion to the initially generated distribution of photoelectrons, as this allows for accurate determination of photoelectron binding energy (eBE) which is characteristic to the electronic state of the atom or molecule from which the electron originated [29]. A common and problematic cause of this distortion is inelastic scattering, in which the photoelectrons lose energy through collisions with molecules along the path from sample to detector thereby broadening and shifting the measured eKE [30]. The simplest solution to this problem is to minimize the effect of inelastic scattering by operating under experimental conditions where the distance from sample to detector is less than the mean free path of the electron. The mean free path is given

by Equation 2.9, in which λ is the mean free path, c is the ratio of the electron and gas velocities, ρ is the vapor density, and σ is the collisional cross section [31-33].

$$\lambda = (c \cdot \rho \cdot \sigma)^{-1} \tag{2.9}$$

For electrons emitted from liquids, this entails minimizing the amount of water vapor between liquid surface and detector through use of a microscopic liquid source and differential pumping. The liquid microjet was first demonstrated in 1988 as a means of satisfying these conditions, generating a stream of free-flowing liquid in vacuum only a few 10s of microns in diameter [31]. At these diameters, the Knudsen condition, $\lambda > d$ where λ is the mean free path of the liquid vapor at equilibrium and d is the diameter of the liquid microjet, are satisfied such that evaporation from the surface of the microjet is essentially collision-less. For liquid water, this can only be accomplished for liquid microjets with $d \approx 10\,\mu m$. While water microjets with diameters on the order of 20-75 μm (and more recently liquid flatjets) don't necessarily satisfy the Knudsen condition, the mean free path of the emitted electrons still benefits from a reduced density of water vapor between the surface of the microjet and the entrance of the detector. Introducing these minute amounts of liquid allows ambient pressures on the order of 10^{-4} – 10^{-5} Torr in the chamber containing the liquid source which is maintained by moderate pumping using a combination of cryogenically cooled surfaces and turbomolecular pumps. Finally, separating the ToF detector region from the liquid source with a skimmer of diameter ranging from 400 to 900 μm further reduces the ambient pressure in the detector region to 10^{-7} – 10^{-6} Torr, increasing the mean free path of the photoelectrons to the order of meters.

2.3.1 The Liquid Microjet Technique

Practical implementations of generating liquid microjets revolve around a central theme, forcing liquid through an orifice of the desired liquid microjet diameter whether it be a platinum plate with a pinhole [31], a pulled capillary [33], or a fused-silica capillary [34]. Our liquid jet setup, based on the design originally developed by the Saykally group at UC Berkeley, is extensively discussed in the dissertation of Alex Shreve. An example of this design is shown in Figure 2.11 (a) in operation at atmosphere and in Figure 2.11 (b) in operation under vacuum. In short, it features a ~8 mm section of fused-silica capillary of varying internal diameter (15-75 μm ID, 363 μm OD, Polymicro Tight-Tolerance VS) secured inside a ~6 mm section of polyether ether ketone (PEEK) tubing (0.015" ID, 1/16" OD, VICI/Valco Instruments Co. Inc.) by compressing both in a 1/16" Swagelok tube fitting (Swagelok, SS-100-6). The capillary segments are homemade, cut from a reel of

several meters of capillary stock using a rotating diamond blade (Agilent, 5183-4669) creating reproducibly flush, burr-free cuts.

The capillary assembly is attached to a cylindrical 0.5" diameter inline filter housing assembly (Idex Heath & Science, A-314) containing a 2 μm stainless steel or PEEK filter frit (Idex Health & Science, A-100/A-706). The inline filter assembly serves two purposes. First, it acts as a last point of filtration to minimize particulate buildup within the capillary. This prevents asymmetric flow through the capillary, an important consideration as asymmetric flow can lead to changes in the direction the liquid travels after exiting the capillary thereby decreasing the jet stability. The inline filter also serves as the point at which the liquid microjet assembly is held by the new mounting assembly introduced in 2020. This filter assembly and liquid microjet, mounted in vacuum, is connected to a syringe pump (Teledyne Isco, 500D) by a ~10' segment of PEEK tubing identical to what is used to secure the capillary. This tubing passes through a KF to Ultra-Torr adapter (Idealvac, P109141) serving as a vacuum feedthrough and broken into smaller segments by unions (Swagelok, SS-100-6) and inline filter assemblies (Idex Health & Science, A-431) at points convenient for facilitating flushing of the pump and tubing.

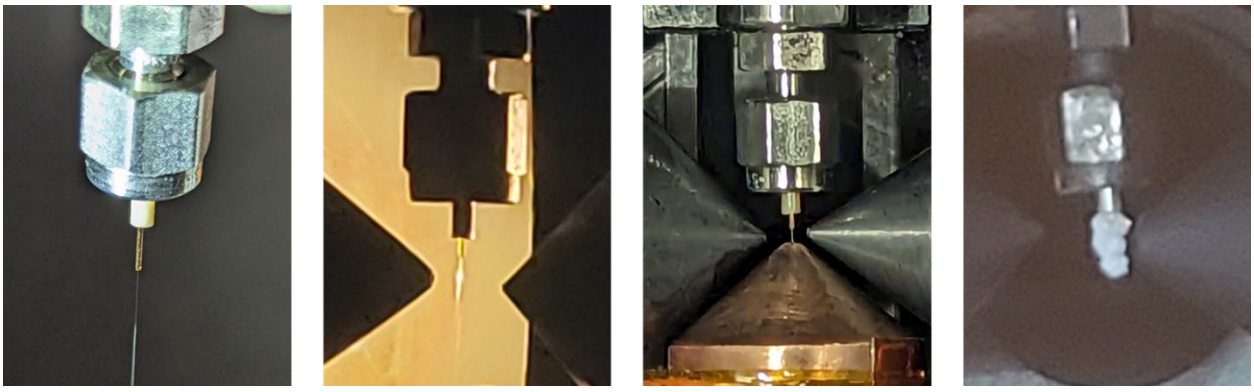

Figure 2.11 – From left to right: Liquid microjet running at atmosphere, running at high-vacuum without a catcher, running at high-vacuum with a catcher, and frozen liquid microjet.

The syringe pump was used for all experiments included in this dissertation but is in the process of being replaced by a low-pulsation, biocompatible HPLC pump (Shimadzu Scientific Instruments, LC – 40i) at the time of writing. This new pump will enable recirculation of samples, extended up-time, and enhanced stability of microjet generation. To generate liquid microjets, the pump parameters are first determined on the benchtop at atmosphere. This involves adjusting the flow rate or backing pressure until flow conditions have been found that maximize the length of laminar flow. Laminar flow length is characterized by shining a light on the liquid microjet and identifying the point at which the jet begins to scatter the light, this

being the point at which the liquid microjet transitions from laminar to turbulent flow. Typical flow rates depend both on the diameter of the microjet being generated and the solution. For nucleobase solutions through a 20 μm capillary, flow rates of 0.20 mL/min were found to produce the most stable microjets. For 30 μm microjets, flow rates of 0.70 – 0.90 mL/min resulted in the best stability. While these are substantially different flow rates, the microjet velocity is consistently 10 – 20 m/s with backing pressures from 80 – 100 atm.

In vacuum, jet instability at flow rates determined under atmospheric conditions is occasionally observed; this is frequently observed for solutions of poorly soluble analytes where the concentration nears saturation especially when salt is included in the solution. This instability manifests as visible flickering of the microjet or salt accumulation around the tip of catcher; practically this can be quickly remedied by increasing or decreasing the flow rate in 0.05 mL/min increments until the microjet stabilizes or freezes out. Frozen jets, as exampled in Figure 2.11 (d), occur due to the evaporative cooling ubiquitous for liquids in a vacuum. The magnitude of cooling and length at which breakup occurs in cylindrical jets can be represented as a function of a few fundamental variables and empirically derived expressions have been developed by others [35] and are given by Equations 2.10 and 2.11.

$$\frac{\mathrm{dT}}{\mathrm{dz}} = -\left(\frac{P_{vap}(T)}{r_{jet}}\right)\left(\frac{1}{v_{jet}}\right)\left(\frac{\Delta H_{vap}(T)}{C_P(T)\rho(T)}\right)\sqrt{\frac{32m}{\pi RT}} \tag{2.10}$$

$$L_{breakup} \approx d_{jet}\sqrt{\frac{\rho d_{jet} v_{jet}^2}{\gamma}}\left(1 + \frac{3\eta}{\sqrt{\rho\gamma d_{jet}}}\right)\left(7.68 - \frac{2.66\eta}{\sqrt{\rho\gamma d_{jet}}}\right) \tag{2.11}$$

Here T is the solvent temperature at distance z from the fused-silica capillary, P_{vap} is the vapor pressure of the solvent, r_{jet} is the microjet radius immediately after exiting the fused-silica, v_{jet} is the jet velocity, ΔH_{vap} is the enthalpy of vaporization, C_P is the solvent heat capacity, ρ is the density of the solvent, m is the solvent molecule mass, R is the ideal gas constant, γ is the surface tension of the solvent, and η is the solution viscosity. For a 30 μm liquid microjet running at 0.8 mL/min, the temperature at the point it intersects the detection axis (~1 mm below the fused-silica capillary) is 275 K and the temperature at the breakup length, 2.34 mm below the fused-silica capillary, is 264.4 K.

2.3.2 Liquid Flatjets for Photoelectron Spectroscopy

While liquid microjets have been utilized to great success enabling the study of pure liquids and solutions using gas-phase techniques, some inherent limitations exist

with regard to maintaining stable spatial overlap between the focused laser beam and liquid microjet as well as multiphoton and space charge effects. A potential solution to these problems is the liquid flat-jet, a series of orthogonally alternating sheets of relatively flat liquid generated when two liquid microjets are collided at an appropriate crossing angle and flow rate [36]. Early experiments involving flat-jets involved colliding individual cylindrical jets orthogonally [37]. This proves challenging as the jets need to be aligned precisely, the apparatus for accomplishing this requiring a substantial amount of space. Additionally, flow through each cylindrical jet typically needs to be adjusted independently to account for slight differences in flow rate through each individual microjet to maintain symmetric and stable generation of the liquid sheets. These limitations made it previously intractable to implement a flat jet into this experiment.

Recently, advances in microfluidics technology have made it possible to solve these problems by generating flat-jets using microfluidic chips containing three etched channels in borosilicate glass [36]. These three channels are supplied through two inlets, one supplying two outer channels which converge at the tip with ~50 x 55 μm^2 channel dimensions, and one supplying a central channel flowing directly to the tip with ~20 x 25 μm^2 channel dimensions [38]. This chip can be operated in two configurations, both reliably and reproducibly generating liquid flat-jets. The first is in a colliding jet geometry; here the central channel is blocked and liquid is only supplied to the upper inlet to the outer channels. These channels, being in a fixed position relative to one another, do not require independent alignment. Additionally, as they are supplied by the same inlet and the liquid passes through identical channels to the chip tip, no independent adjustment of the flow is necessary. An example of a flat jet operating in a colliding jet geometry under vacuum is shown in Figure 2.12 (b). The one downside to this is the increased flow requirements needed to operate the chip in this configuration. The typical flow rate used to stably generate at least a single sheet while avoiding substantial breakup below the sheets is ~2.5 mL/min. The alternative configuration to this is to use the chip as a gas dynamic virtual nozzle, in which liquid is supplied to the central channel to generate a cylindrical jet approximately 25 μm in diameter and gas is supplied to the outer channels to compress the cylindrical jet at the tip of the chip to form the sheets. A flat jet generated in this fashion is shown operating at atmosphere in Figure 2.12 (a)

Figure 2.12 – Liquid flat jet running (left) at atmospheric pressure and (right) under low vacuum.

It is estimated the implementation of a flat jet in the experiment will increase the S/N achievable by nearly a factor of 5 corresponding to the increase in signal associated with overlapping the full diameter of the probe with the sample. This is primarily because the best focusing that has been achievable for the XUV probe is a focal diameter with a FWHM of 50–75 μm. Consequently, under the best attainable focusing conditions, the largest portion of the XUV probe that can intersect a 30 μm liquid microjet is 52%, though a more realistic estimate would be closer to 40%. This can increase the impact of jet instability; a slight 10 μm change in microjet position, on the order of what is seen over the course of a typical experiment, would lead to a 9% change in the intensity of XUV light probing the sample. Further, photoelectrons generated on the side of the microjet facing the magnet will, for the most part, be emitted away from the detector and will therefore not be steered into the ToF region. This reduces the useful portion of the XUV focus to 20-25% of the total beam size. With a flat jet, the size of the liquid sample would be an order of magnitude larger than both the pump and probe focal diameters and a majority of photoelectrons emitted from the liquid surface will be steered into the ToF region, eliminating this problem. Finally, it is expected the peak pump intensity required to generate observable excited state signal would be lowered by increasing the area over which excited state signal is created, creating a comparable excited state population with a lower peak intensity. This would lead to reduced space–charge shifting and broadening of the solution–phase peaks by reducing multiphoton ionization from the pump beam.

As the surface area of a flatjet is substantially greater than that of a cylindrical jet, it is advantageous to cool the solution to a few °C above the freezing point just before passing through the vacuum feedthrough [39]. As the PEEK tubing is

thermally insulating, stainless steel tubing must be coiled and submerged in a bath for effective heat transfer to occur. A coil 3" in diameter consisting of 12 turns of 0.125" stainless steel tubing was made to submerge in a solvent bath. The solvent bath consists of an outer reservoir containing the solvent used for the experiment and a cold finger suspended in the outer reservoir containing a methanol/water bath that can be cooled by dry ice. The temperature of this bath can be easily controlled by adjusting the methanol/water ratio in the inner reservoir and the large path length through the stainless steel tubing results in thermal equilibration of the inner solution with the outer solvent. The solution is immediately transferred back to PEEK tubing after exiting the bath to minimize temperature rise between the bath and jet, though at the time of writing this dissertation the exact temperature rise between the bath exit and flat-jet assembly has not been determined.

2.3.3 Liquid Jet Mount and Catcher

A crucial part in any experiment is ensuring consistent and reproducible alignment between sample, probe, and detector. With the upgraded XUV beamline, it was found that more precise and stable jet manipulation was required. As detailed in the dissertation of A. T. Shreve [34], the original design employed a XYZ-motion platform consisting of a micrometer-actuated XY stage and a linear shift mechanism. This came with advantages such as being able to precisely measure the displacement of the jet while it was under vacuum. The disadvantage of this design was the ~18" long 0.25" diameter stainless steel tube that was used to suspend the liquid microjet assembly in vacuum from the top of the 3-axis manipulator as well as the difficulty in reproducibly mounting the assembly to the KF to CF adapter at the top of the manipulator. This led to difficulties maintaining stable overlap as shifting of the micrometer-actuated stages and KF mount would lead to the jet drifting over the course of measurements in addition to instabilities due to minor vibrations being amplified by the long tube from which the jet was suspended. For UV/UV experiments, this design was more than adequate as the focal diameters of the UV beams were approximately an order of magnitude larger than the microjets. With the new XUV probe focal diameter being a fraction of the old UV probe focal diameter, a new microjet mounting and manipulation apparatus was required.

When designing the new apparatus, the main goals were primarily to improve the instantaneous stability of the jet while also designing a highly adaptable apparatus to facilitate future experimental improvements, both anticipated and unanticipated. Drawings for all fabricated components incorporated into this redesigned mount are given in Appendix B. To accomplish this reduction in instantaneous stability, the XYZ-motion components were moved inside the 6-way CF cross encompassing the interaction region to eliminate the need to suspend the jet assembly from the top of the chamber. This makes it intractable to control the stages manually, so the motion

assembly consists of two linear stages with 1" apertures (Newport, 426A) mounted directly to the center of a 10" to 2.75" zero length reducer CF flange on the vacuum side. Stage manipulation in vacuum is accomplished by 1" travel linear piezoelectric actuators (Newport, 8302) controlled by an 8-channel controller/driver (Newport, 8742-8-KIT) in conjunction with the Picomotor Application GUI supplied by Newport. These picomotors have a minimum motion increment of 30 nm and a travel speed of 1 mm/min which is a much higher motion resolution than the previous manual micrometer-actuated stage but a much slower travel speed. These stages allow for the movement of the full mounting apparatus in the XY-plane. A custom mounting plate is attached to the larger stages and a compact XYZ-stack of 0.5" travel stages (Newport, 9062-XYZ-PPP) is mounted to this plate about 3" from the center of the chamber. These stages are actuated by 0.5" travel picomotors (Newport, 8301NF) and controlled by the same controller/driver and GUI as the other picomotors. These stages allow for the independent alignment of the microjet assembly along three axes relative to any other components mounted on the custom mounting plate. All these picomotors are connected to a 2 x 5 array of BNC feedthroughs on the side of the 10" CF flange the stages are affixed to, with independent driver signal pins for each piezoelectric motor and a common ground. The CF flange additionally has a 2.75" half-nipple for additional electronics feedthroughs if all the 4 spare feedthroughs break or if any other electronic or fluid feedthroughs are required for future experiments.

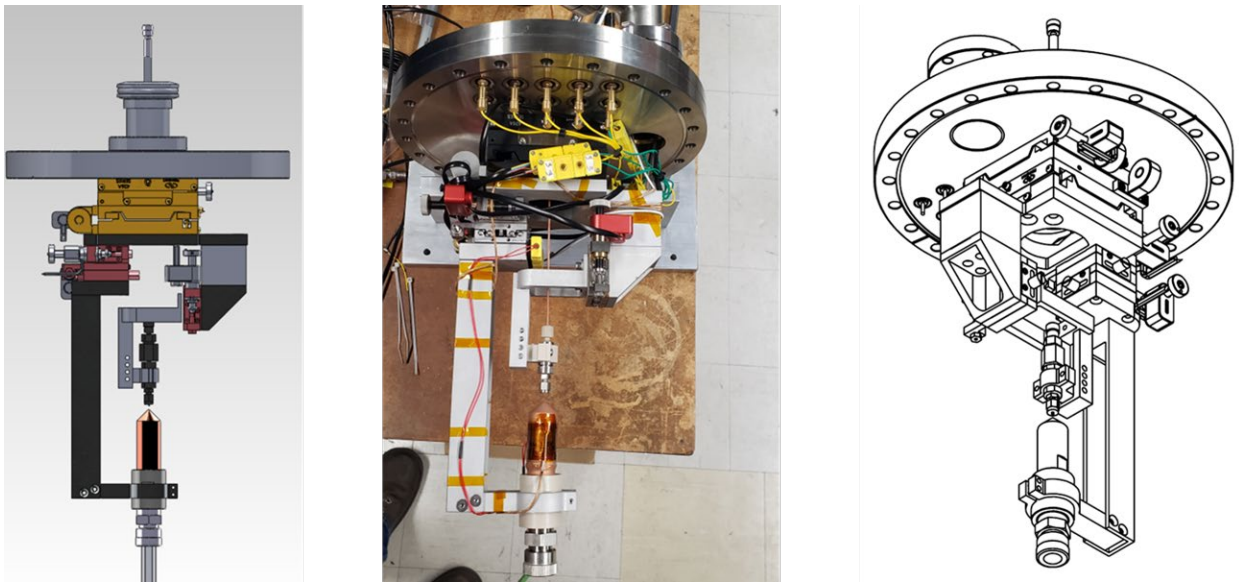

Figure 2.13 – Liquid jet motion and catcher apparatus. Left: false color image of the CAD assembly. Middle: Fully assembled apparatus. Left: Black and white view of the assembly machine drawing.

The mount was designed to incorporate mounting and feedthroughs for an optional heated catcher. Heated catchers have been implemented in other groups who've demonstrated a substantial decrease in ambient pressure in the interaction region containing the liquid microjet as well as a substantial decrease in effects from electrokinetic charging of the microjet [40, 41]. The mounting points for the arm that extends below the plane formed by the laser beam and detector axes are directly on the custom adapter plate opposite the stages for independent microjet alignment. This right-angle mounting arm stretches the distance from the mounting plate to ~4" below the laser-detector plane and is essentially a u-channel bar with a hollowed-out space the laser beams propagate through. This opposite end of the bar connects to a 1.2" ID circular clamp for mounting the catcher with easy access to the screw so the catcher can be introduced/removed/adjusted without needing to remove the apparatus from the vacuum chamber. The original catcher design used and displayed in the dissertation of Blake Erickson is a soldered copper tube assembly with a tip tapered at a 45° angle and a 500 μm orifice. The tube is 1.7" long and 0.84" OD, used to accommodate an adhesive-mount flexible DC heater (1" x 2", 10 W, 24 V DC, McMaster-Carr, 7945T62) and a surface-mount thermocouple (adhesive-back, Type K, McMaster-Carr, 3648K34). The bottom is a 0.5" NPT threaded fitting that mates with the rest of the catcher assembly and has an 8-32 tap hole on the side for connecting an electrode or grounding wire. All three pieces are silver soldered together. The silver soldering connection proved problematic as the linearity of the piece is not perfect and required particular positioning when introduced in the mount such that the 8-32 tap hole is facing away from the chamber door and then torque applied to the catcher assembly by pulling the bottom toward the chamber door and by pushing the tip away from the chamber door. While this catcher worked sufficiently well for what it was needed for, it was also certainly a prototype with room for improvement.

The current catcher, designed with both ease of fabrication, general utility, and improved performance in mind, has proved to be a marked improvement over the old design. It consists of two pieces, a piece of 0.84" OD aluminum tubing ~2" long with factory produced 0.5" NPT threading on one side and 5/8-18 female threading on the opposite end. The aluminum tubing accommodates the same heater and thermocouple as the old design. The second piece is a beryllium copper cone with matching threading to mate to the aluminum tube. The cone is tapered at a 60° angle with a 1 mm OD and 800 μm ID tip; this was done to improve the ease of positioning the catcher relative to the magnet tip and the skimmer.[11] This also simplified boring out the inside of the catcher, a commercially available set of

[11] The skimmer is tapered at 57° and the magnet tip at 45°. The prototype design, tapered at 45° but rounded off at the top, would frequently bump into the magnet or occasionally the skimmer as it is best positioned just below the bottom of the skimmer entrance. As the magnet is not always perfectly centered relative to the skimmer it would complicate alignment as the catcher could get too close and make contact.

countersink drill bits were used as opposed to the lathe tooling used for the custom 62° interior angles on the skimmers. This simplified construction allowed for multiple duplicate tips to be made, enabling the daily replacement of the catcher tip to simplify cleaning after data collection. Adding to the versatility of the new catcher tips, the ID of the tip can be readily decreased if desired by suspending tungsten wire of the desired tip ID on the centerline of the catcher. The tip can then be heated and a small amount of lead or tin solder applied to the inner opening of the catcher tip. Once cool, the tungsten wire can be removed carefully from the solder in the same direction as the liquid jet would flow and a new ID the diameter of the tungsten wire will be obtained [42].

The catchers, both old and new, are kept at 50-80°C depending on the solution being run. This is optimized by monitoring jet stability and chamber pressure as a function of temperature. The ideal temperature is found by increasing the temperature until the pressure in the vacuum chamber begins to climb, then decreasing by ~5°C. Occasionally, the temperature needs to be increased beyond this point to increase jet stability though this should be done in small increments with time in between temperature increases to allow for the temperature to equilibrate.

The catcher threads into the top of a PEEK 0.5" NPT coupling that serves as an electrical break, thermal break, and mounting point for the 1.2" circular clamp arm that is used to suspend the catcher and couple to the XY-stages. A stainless steel 0.5" NPT to Ultra-Torr adapter (Swagelok, SS-8-UT-1-8, modified to be bored-through) threads into the bottom of this PEEK coupling to which the flexible PVC plastic tubing (McMaster-Carr, 5233K58) that removes fluid from vacuum is attached. The NPT to Ultra-Torr fitting is modified in-house to be bored-through and has an added 8-32 tapped hole for attaching a grounding cable. It is crucial all the components in the assembly are properly grounded unless intended to be held at a controlled floating potential to prevent charge buildup which can lead to shifting and distortion of the photoelectron signal. More about this can be found in Chapter 4.

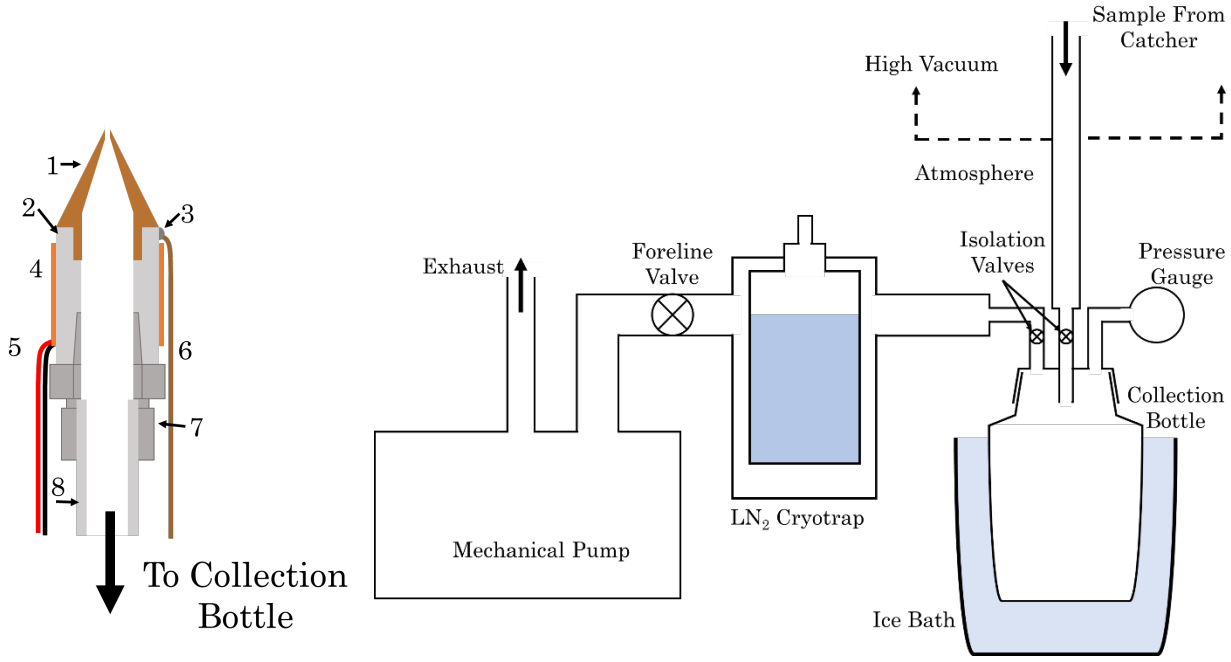

Figure 2.14 – Catcher apparatus components. (left) Catcher diagram showing the (1) removable copper tip with 500 μm tip I.D., (2) aluminum thread adapter, (3) type-K surface-mount thermocouple, (4) 24 V DC-powered adhesive-mount heating tape, (5) wire leads connecting the heater to a Kepco variable DC power supply, (6) wire lead connecting to heater controller, (7) NPT to Ultra-Torr adapter, (8) ½" tubing in which sample is carried to the collection bottle. (right) Schematic diagram of the catcher apparatus outside vacuum in which sample is collected in the collection bottle surrounded by an ice bath to reduce the sample vapor pressure. Sample vapor is removed to maintain low pressures using a cryotrap combined with a mechanical pump.

The remainder of the catcher apparatus accommodates fluid and electrical feedthroughs. Because of the difficulty in adjusting or replacing wiring, backup electrical hookups for a heater and thermocouple are in place parallel to the wiring harness used to supply power and monitor temperature in the top of the catcher assembly. The extra heater power supply and thermocouple connection can optionally be used to employ a detachable heating assembly for the bottom half of the catcher assembly. The upper and lower metallic components are separated by a PEEK coupling that was intended to allow the upper and lower components to be independently grounded or held at a floating potential. PEEK is also a thermal insulator, causing the coupling to also act as a thermal break preventing the catcher arm from acting as a heat sink.[12] Consequently, if the jet is misaligned slightly or

[12] The heater must be a DC heater as the AC heaters tested were observed to induce an oscillating shift and distortion of the photoelectron signal corresponding to the heater turning on and off. This

breaking apart and impinging on the top or sides of the stainless steel 0.5" NPT to Ultra-Torr adapter, the lack of heat transfer into adapter to balance the evaporative cooling on the surface leads to ice buildup and eventual clogging of the catcher. Another solution to this problem, developed in parallel with the heating solution, was to push the PVC tubing up until it abuts the bottom of the conical catcher component. As the PVC is smooth and hydrophobic, the liquid (typically water) lacks a point to nucleate and just runs down the sides into the collection bottle rather than freezing. By placing it further up, no reasonable instability or change in pointing of the jet can lead to liquid collecting on the metallic components so it also solves the issue of solution freezing within the catcher and clogging it. Fortuitously, this solution doesn't require heating, so lower ultimate pressure can be attained employing this solution rather than the solution involving extra heating.

Vacuum feedthroughs are used to supply power to the heater(s) in vacuum and read the temperature. Thermocouple feedthroughs on a 2.75" CF flange (Kurt J. Lesker, TFT2KY00003) and BNC feedthroughs on a 2.75" CF flange (Kurt J. Lesker, IFTBG042033) are attached to a CF 2.75" 4-way cross (Duniway, CR-0275). BNC feedthroughs are used for power supplied to the heater(s) and for supplying potential for any components needing to be held at a fixed, non-zero potential in an experiment. These feedthrough flanges are attached to a CF 2.75" 4-way cross, which is in turn connected to a CF 4.5" tee that is fixed to the bottom 10" CF flange of the interaction region. The PVC tubing passes through a bored-through 0.5" NPT to 0.5" Ultra-Torr adapter at the bottom of the 4.5" CF tee. It then connects to a collection bottle using a series of Ultra-Torr and Swagelok fittings, a valve, and a custom welded tube to GL45 adapter cap. The collection bottle can be kept in a bath or simply kept at room temperature depending on the solution used. The solvent bottle and, by extension, PVC tubing and catcher assembly are pumped on by a Edwards E2M8 oil-sealed rotary vane pump with a liquid nitrogen trap (MDC Precision, 434011) in line to remove as much water vapor as possible. Rough pumping is a crucial component of the catcher assembly, it reduces the increase in pressure in the catcher assembly from evaporation of solvent in the collection bottle. It has been observed that too little pumping on the catcher bottle can lead to pressure increases in the catcher assembly significant enough to lead to appreciable backflow through the catcher tip. Substantial backflow causes the jet to swing wildly, inevitably leading to the jet freezing out. It is also possible to pump too much on the collection bottle. Too much pumping is evidenced by the solvent boiling in the bottle and icicles growing from the inlet tube to the catcher. This can lead to ice blocking the inlet tube as well as filling the liquid nitrogen trap with ice. To strike a balance between these two extremes, it is necessary to use a combination of valves and conductance limiting tubing to reach stable roughing conditions for the catcher assembly.

---

also precludes the possibility of using an AC heater in conjunction with a Variac®, as this would just induce a static shift and distortion of the photoelectron signal. DC

The temperature of components is monitored by connecting the thermocouples in vacuum to a home-built temperature controller box. Central to this construction is a process temperature controller (Omron Automation and Safety, E5GC-QX1A6M-000) that uses a PID temperature control loop to maintain the set temperature. This temperature controller outputs a control voltage for a solid state relay (TE Potter & Brumfield, SSRDC-200D12) that switches the 24V DC power supply. Power to the heater is supplied by a Kepco DC power supply (Kepco, ATE25-10M) set to 24 V and power to the remainder of the temperature control box power is supplied by wall voltage.

Finally, the jet alignment is monitored by cameras mounted above the laser-detector plane at 45° angles relative to the detector axis and the jet axis. The ability to resolve small changes in jet alignment on the micron level is crucial to maintaining good alignment. To this end, a 6.3 MP USB camera operating at 60 FPS (The Imaging Source, DFK 37AUX226) and a 5 MP USB camera operating at 6 FPS (The Imaging Source, DFK 72BUC02) are both attached to macro video lenses (Navitar, Zoom 7000) and focused such that the camera images a ~9 mm × 6 mm region at the center of the chamber. In this region, the tip of the skimmer, tip of the magnet, microjet or flat-jet assembly, and catcher tip are all visible and well resolved. At this magnification, 1 pixel on the camera corresponds to between 2 and 3 μm. While it is still difficult to image the microjet due to the transparency of the laminar flow region, it is still possible to align it sufficiently well with this magnification. The windows for these cameras were added by modifying the original custom 10" 6-way cross by adding 2.75" CF half nipples to the side opposite the detector region, to which 2.75" CF viewports (Accu-Glass Products, Inc., 112667) and custom camera mounts are attached. To add these CF half nipples, the chamber had to be rotated around the detector axis 90° so the 4.625" CF half nipple through which the magnet alignment picomotors connect to the driver is below the laser-detector plane and not where the cameras need to be mounted. Unfortunately, this means that the 10" CF flanges above and below the interaction region are now rotatable rather than fixed, complicating the process of mounting the flanges the jet motion components and the magnet stage are attached to as the rotation of the flange is no longer fixed. The rationale behind this compromise was essentially that the flanges are infrequently removed and replaced but the jet is aligned daily so this trade-off saves time overall. These two viewpoints make it possible to accurately align the jet along the detector axis and laser axis even though they are rotated 45° relative to the axes the jet is being aligned along.

2.3.4 Electron Scattering and Probe Depth Considerations

An important consideration in this experiment is the effect of scattering on photoelectrons generated by photons of varying energy. This scattering is dependent

on the electron kinetic energy and is therefore difficult to predict in a disordered medium such as water [43]. Scattering occurs in both the liquid phase and gas phase, with inelastic scattering being the main concern for photoelectron spectroscopy as this alters the kinetic energy of photoelectrons reporting on the binding energy of the state from which they originated. The effects of scattering are characterized by either the inelastic mean free path (IMFP) or electron attenuation length (EAL) [44]. The IMFP is taken as the distance it takes for the original population I_0 of the photoelectrons at a specific energy to be reduced to $\frac{1}{e}I_0$ or $\sim 0.368\, I_0$ due to scattering events that result in a loss of kinetic energy. The EAL is comparable to this, defined for solution-phase scattering as the distance at which the number of photoelectrons emitted is $\frac{1}{e}$ or ~0.368 the number generated. This quantity takes into account the elastic scattering events in addition to the inelastic. The distinction between these two quantities being that inelastic scattering does not always prevent the electron from being detected, so the IMFP is generally smaller than the EAL. When considering electron scattering, it is convenient to consider the scattering events between photoelectron generation and emission to vacuum and scattering events between emission to vacuum and detection separately.

To consider the effects of scattering in the gas phase, the density and distribution of particles the photoelectrons interact with must be determined. The probability of scattering, defined as a change in incident photoelectron intensity per unit distance, depends on the scattering cross section and number density of particles along the photoelectron path, which can be represented as shown in Equation 2.12 [32, 45].

$$dI = -I_e \cdot \sigma_{e^- \cdot H_2O}(E) \cdot \left(\frac{P_{H_2O}(z)}{k_b T}\right) dz \tag{2.12}$$

Here, the change in intensity is given as dI, the total energy-dependent scattering cross section for electrons and water is given as $\sigma_{e^- \cdot H_2O}(E)$, and the density of water, which is assumed to be the only particle the electrons interact with, can be given as $\left(\frac{P_{H_2O}}{k_b T}\right)$ assuming an ideal gas.

From Equation 2.12, it is apparent that the probability of electron scattering is directly proportional to the pressure of water vapor. The pressure of the water vapor can be approximated at any point by considering the vapor pressure of the liquid microjet at the point it crosses the detection axis, any apertures along the electron detection path, and the ambient pressure in any given region. The vapor pressure of the liquid microjet is determined by the identity of the solvent and the temperature of the liquid microjet. For pure water, the vapor pressure varies from 75.6 Torr at 25°C to 4.58 Torr at 0.1°C so an accurate determination of temperature at the

interaction point using Equation 2.10 is important [46]. For a typical experiment, the concentration of solutes is very small so the vapor pressure of pure water can be taken as the vapor pressure of the solution. Using Equation 2.10, the temperature of the microjet is shown to drop to approximately 15°C by the time it crosses through the detector-laser plane, corresponding to a vapor pressure of ~13 Torr. The microjet can be approximated as a line-source of water vapor, meaning the pressure decrease as a function of distance from the center of the microjet, r, is approximately P_0/r. In the absence of any apertures the MFP for 10 eV eKE electrons, given by $\sigma_{e^-\cdot H_2O}(E) \cdot \left(\frac{P_{H_2O}}{k_b T}\right)$, would be on the order of 1.6 cm. As this is substantially less than the ~70 cm ToF spectrometer length, a differential pumping aperture must be employed. Skimmers with internal diameters ranging from 400 μm to 900 μm are employed to decrease the density of vapor along the ToF axis and maintain lower ambient pressures in this region overall by limiting conductance of vapor into the detector region from the interaction region. Additionally, the skimmer acts as a point source for vapor along the detector axis, causing the vapor density to decrease as P_0'/r^2, where P_0' is determined by $P_0/r_{skimmer}$ where $r_{skimmer}$ is the distance from microjet surface to skimmer. By placing this skimmer ~1 mm away from the liquid microjet, the MFP of the electron at 10 eV eKE is extended to the order of meters, far greater than the length of the ToF spectrometer thereby minimizing any scattering effects on electrons in vacuum.

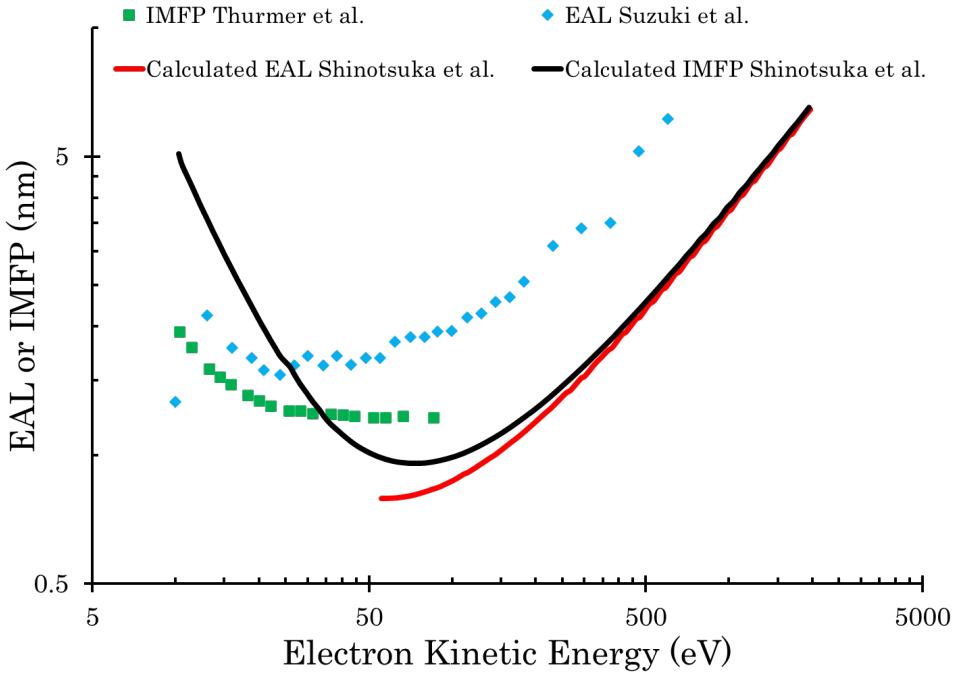

Figure 2.15 – Calculated and measured energy dependence of the inelastic mean free path and electron attenuation length for electrons generated in liquid water.

Blue diamonds are measured EAL values reproduced from [47]. Green squares are measured IMFP values reproduced from [48]. Solid black and red lines are calculated IMFP and EAL values reproduced from [44].

In solution, scattering can't be avoided and has a much more substantial impact on photoelectrons due to the increased density of water.[13] In this experiment, inelastic scattering is the limiting factor when considering the probe depth attainable. At 21.7 eV, the molecular absorption cross section for water is 2×10^{-17} cm^2 [49] leading to an attenuation depth of 15 nm. As water is essentially transparent in the UV (the cross section is on the order of 1×10^{-25} cm^2 [50, 51]), the incident UV pump is only appreciably attenuated by solutes of interest and can be approximated as constant. The energy-dependent EAL and IMFP values for electrons in liquid water have been both calculated and measured on numerous occasions, with results reproduced in Figure 2.15. Electrons from molecules of interest ionized at this XUV wavelength (57 nm) have eKE between 10 – 20 eV and will therefore have IMFP and EAL measured to be ~1.2 and ~2 nm respectively [47, 48], substantially less than the depth the excitation and probe pulses penetrate to. Because of this scattering, the dynamics we can observe are predominantly limited to molecules near the surface, but a water monolayer is only on the order of 2.5 – 3 Å thick. A majority of analytes within the EAL of the surface will therefore be surrounded by at least one solvation shell of water molecules, if not more, and as such can be considered solvated. Together, this means most photoelectrons collected from photoexcited solute molecules are indeed representative of the dynamics in the bulk. However, the eKEs measured for these photoelectrons will have some degree of shifting and broadening due to inelastic scattering, the degree to which is determined by the eKE of the photoelectrons. As recent studies have shown [30, 43, 52-56], inelastic scattering becomes a non-negligible factor in the shape and position of photoelectron peaks with eKE less than ~20 eV, though this effect is asymptotic. The magnitude of the shift is only on the order of 10s of meV for photoelectrons with eKE in the 20 – 12.5 eV range, and on the order of 100s of meV for photoelectrons with eKE less than 12.5 eV [30]. Given a 21.7 eV probe and solutes with binding energies in the range of 8 – 9 eV for the ground electronic state, inelastic scattering can largely be ignored except when trying to attain the highest degree of accuracy in the measurement of eBE for a given analyte. Finally, surface signal can represent ~12% of observed signal if the solute is equally likely to be found at the interface as in bulk solution.[14] While this seems large, typical, soluble analytes will likely have surface concentrations lower than bulk as solvation is typically a favorable process. However, for analytes that are poorly soluble, the surface concentration can be

[13] The density of water is 4.4×10^{23} molecules/m^3 for water vapor at the surface of the microjet and 3.3×10^{28} molecules/m^3 for liquid water at 298 K.

[14] This is determined by calculating the volume of region between 0 and 3 Å from the surface and an exponential decay of signal vs distance from the surface given by the EAL.

higher than bulk, leading to an increase in the contribution from analytes at the liquid-vacuum interface.

2.3.5 Streaming Potentials in Liquid Microjets

As cylindrical jets are generated by forcing liquid through a thin capillary, what's known as an electrokinetic charging of the microjet occurs. This is due to charge separation present at the interface between fused silica capillary and liquid solution, forming a charged double layer of H+/OH- for pure water [57]. When solution passes through the capillary under laminar flow conditions, the flow velocity near the capillary – liquid interface goes to zero, resulting in a separation of charge when the liquid separates from the capillary and a net charging of the liquid surface. The streaming potential of a liquid microjet can described by Equation 2.13 [58]:

$$\Phi_{stream} = -\frac{1}{2\pi\varepsilon_0}\frac{I_{stream}}{v_{jet}}\ln\left(\frac{d_{jet}}{2}\right) \tag{2.13}$$

where Φ_{stream} is the surface potential generated, I_{stream} is the streaming current, v_{jet} is the jet velocity, and d_{jet} is the jet diameter. The streaming potential of liquid microjets depends largely on flow velocity and solute ion concentration. Practically, the streaming potential of a microjet is minimized by adding salt, typically sodium chloride, to a concentration of ~50 mM [59]. While this minimizes the streaming potential, it doesn't necessarily eliminate it. A potential on the order of ~0.1 V is typical and can be readily corrected when retrieving accurate binding energies. To correct for the streaming potential in previous works, the shift induced by the potential on the photoelectrons generated through three-photon photodetachment of Xe to Xe^+ ($^2P_{3/2}$) was measured as a function of the microjet to Xenon jet distance. By fitting this to Equation 2.14, the streaming potential can be determined [60].

$$eKE(z) = eKE(Xe) - \frac{L}{L+z}\Phi_{stream} \tag{2.14}$$

Here, $eKE(z)$ is the distance-dependent kinetic energy of electrons generated by Xe to Xe^+ ($^2P_{3/2}$) photoionization, $eKE(Xe)$ is the field-free kinetic energy of electrons generated by Xe to Xe^+ ($^2P_{3/2}$) photoionization, L is the distance to the spectrometer entrance (assumed to be at the instrument ground), and z is the distance from the microjet to photoionization point. By measuring $eKE(z)$ at varying l, Φ_{stream} can be determined.

With the implementation of an XUV probe, the measurement of streaming potentials now no longer requires the use of a $Xe_{(g)}$ effusive jet. Instead, gaseous solvent molecules resulting from evaporation from the surface of the microjet can be used as a reference. The binding energy for photoionization of gaseous water from the $1b_1$ orbital is well known (12.621 ± 0.008 eV [61]) so the same procedure for determining streaming potential can be followed.

The streaming potential is largely a surface effect, generated by charge separation of the electric double-layer formed at the capillary interface. As such, the potential is generated at the surface and decays as $1/r$ into bulk. Because the photoelectrons observed in this experiment are generated 1 – 2 nm from the liquid – vacuum interface, it is a reasonable assumption that the ~100 meV potential is constant for photoelectrons generated in a typical experiment in which the liquid microjet is frozen in .

2.3.6 Applying a Bias Voltage to Liquid Jets

An increasingly common method for the accurate determination of the vertical ionization energy and work function for a given solution by separating liquid signal from gas is to apply a biasing potential to the liquid source. By applying a biasing potential, the measured eKE for the liquid is shifted by a value slightly less than the biasing potential due to characteristic internal resistance differences between the voltage source and solution. In our case, voltage is supplied by a Kepco DC voltage supply (Kepco, ATE 15-6M) with the positive electrode referenced to ground. The negative electrode is connected to a BNC feedthrough using a shielded RG-58/u cable, and the vacuum-side of the feedthrough is connected to the inline filter assembly (Idex Health & Science, A-314) holding the microjet by an 18 AWG copper wire with vacuum-compatible insulation.

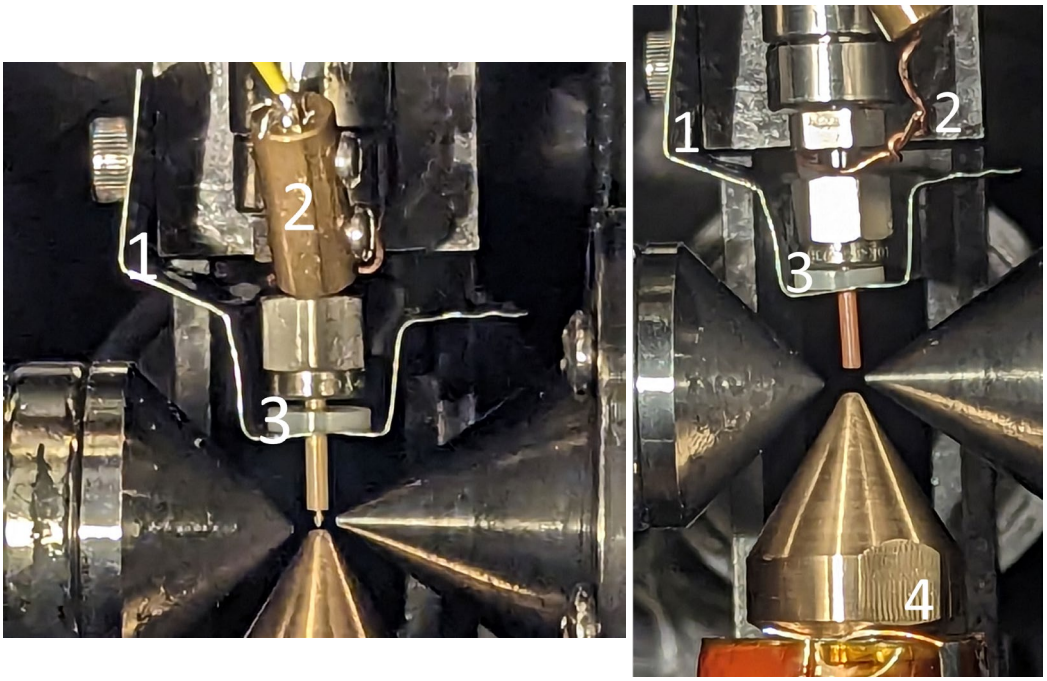

Figure 2.16 – Images of the microjet assembly used to apply biasing potential to liquid microjets. In these images are the (1) formed stainless steel shielding electrode eliminating stray fields originating from the microjet filter assembly in the interaction region, (2) the Ceramaseal fitting connecting the wire carrying potential from the Kepco voltage supply to the copper wire wound round the filter assembly serving as an electrode connection, and (3) an electrically insulating washer isolating the microjet assembly from the shielding electrode. In the right image, (4) one of the grounding wires maintaining the instrument ground potential throughout the interaction region is also visible.

When applying voltage to the liquid jet assembly, it was not immediately obvious what components in the interaction region would need to be held at an identical potential or grounded, so the magnet and catcher were similarly connected to the same voltage supply *via* identical but separate feedthroughs to isolate, ground, or apply voltage to each of these components. By monitoring shifts in $Ar_{(g)}$ photoelectron spectra taken with a 21.7 eV probe, it was found that applying potential to all components resulted in the most shifting of $Ar_{(g)}$ signal. Applying potential to the filter assembly alone resulted in the least shifting of the $Ar_{(g)}$ signal, and the shifting of gaseous signal was essentially eliminated by adding a stainless steel electrode[15] held at the instrument ground to shield the interaction region from the potential applied to the liquid jet assembly [30].

$$eKE = h\nu - eBE - \Phi_{Stream} - \gamma V_{applied} \tag{2.15}$$

[15] This electrode was handmade, but the approximate dimensions for it are given in the drawing given in Appendix B.

The kinetic energy of photoelectrons generated from solution is given by Equation 2.15. Here, γ is a factor experimentally determined by varying $V_{applied}$ to account for the voltage drop due to resistance differences between liquid and electrode. The behavior of $\gamma V_{applied}$ and Φ_{Stream} are identical when considering their radial behavior beyond the liquid – vacuum interface, but it should be noted that Φ_{Stream} only affects the surface region in which photoelectrons are generated while $\gamma V_{applied}$ affects the entire solution. Due to the radial behavior of the potential applied to the liquid but extending into vacuum, photoelectron signals from gas-phase water in the vapor jacket of the liquid jet will be smeared out considerably. For a sufficiently large potential, the $1/r$ behavior of the potential will result in an appreciably large difference in measured eKE for water vapor photoionized at the water – vacuum interface as opposed to water vapor photoionized by the outermost portions of the probe pulse. This would mean that contributions from gaseous signals would be shifted and broadened into the baseline for sufficiently large applied voltages.

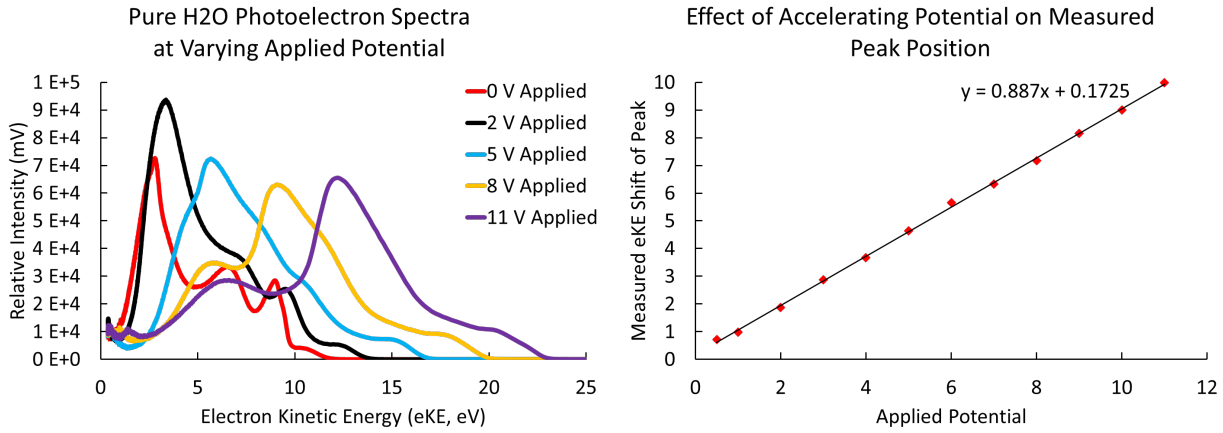

Figure 2.17 – The effect of applying a potential to the liquid microjet accelerating photoelectrons generated in solution to higher eKE. The raw spectra (left) show a substantial broadening of peaks and static shifting of the secondary electron background with the shifting $1b_1$ peak. (right) The measured shift in the liquid water $1b_1$ peak relative to the applied potential. The shift is linear relative to the applied potential and reduced by ~10%.

In practice, this did result in a linear, static shift of photoelectron spectra from solvated species relative to gaseous signals which were broadened substantially. However, this also resulted in broadening of the photoelectron spectra of solvated species making it difficult to identify and fit the various contributions to the spectra. Additionally, it did not solve the issue that spurred this line of experimental modification – contributions from photoionization of water (both liquid and gas) from higher-order harmonics. As such, biasing of the jet is currently not employed but the implemented electrical connections and electrodes are still available if biasing is revisited in the future.

2.3.7 Space-charge Effect

In the interaction region, the pump and probe generated as described in Section 2.2 are nearly collinear and both orthogonally coincident with the liquid source as described in Section 2.3. Both pump and probe generate photoelectrons, the pump through multiphoton ionization and the probe through one photon ionization. To generate sufficient excited state signal that can be observed using a few μW of XUV flux, laser intensities well in excess of the ~50-100 μW powers that were typical in UV-UV experiments. At the 1-2 mW intensities used in liquid experiments, several undesirable effects are observed, principally among them the space-charge effect. This effect can be broken down into two general categories: electron-electron interactions and electron-cation interactions [62]. The electron-electron interaction is straightforward, when many photoelectrons are generated in the experiment they interact as they travel through the flight tube. This repulsive interaction leads to shifting and spreading of the energetic distribution of photoelectrons. Homogenous broadening occurs when large probe fluences lead to a large enough quantity of electrons of comparable eKE such that electrons from the same electronic state interact with each other. This repulsion leads to an equal but opposite change for electrons on the fast and slow sides of a given peak, leading to homogenous broadening. The electron-electron interactions leading to broadening also include the interaction of fast photoelectrons generated by the XUV probe and slow photoelectrons generated by the UV pump. If the XUV probe is temporally delayed relative to the UV pump (as is the case with all positive delays in TRPES scans), the photoelectrons generated by the XUV probe pass through the photoelectrons generated by the UV pump leading to a decrease in kinetic energy for the fast photoelectrons generated by the XUV probe and an increase in kinetic energy for photoelectrons generated by the UV pump. At negative delays, the interaction between electrons slightly increases the eKE of XUV-generated photoelectrons, though the magnitude of the change in eKE is less than at positive delays as the faster XUV-generated photoelectrons interact with the slower UV-generated photoelectrons to a lesser degree as the two clouds of photoelectrons don't overlap in space at negative delays whereas they temporarily overlap spatially at positive delays.

The electron-cation space-charge effect slows down XUV-generated photoelectrons, with substantial decreases in eKE at positive delays and minimal decrease in eKE at negative delays. The simplest case to consider is negative delays. This is because the XUV probe is typically set to a low enough fluence to not shift the eKE considerably. As such, electron-cation interactions result only from cations generated by the UV-pump, which comes after the probe at negative delays. As the field from electrons generated by the UV-pump is nearly equivalent to the field from cations generated by the UV-pump, the electron-electron and electron-cation space-

charge effects essentially offset each other and can largely be ignored at negative delays. At positive delays, the XUV-generated photoelectrons interact with cations generated through photoionization with both the pump and the probe. This leads to a decrease in eKE of the XUV-generated photoelectrons that decreases exponentially with cation dissipation in solution.

Other undesirable effects include ponderomotive, AC stark shift, and plasma formation [63, 64]. These effects typically only occur at pump powers of greater than 10 mW, and as such are not observed in typical experiments. Even in gas-phase experiments, it is typically not observed except when pump and probe conditions are chosen such that these effects are intentionally included in an experiment.

2.4 Photoelectron Spectrometer

The magnetic bottle time-of-flight photoelectron spectrometer consists of regions where photoelectrons are generated, separated by energy, and detected. The majority of the spectrometer is original to the design of A. T. Shreve [34] and prior modifications by M. H. Elkins [65], H. L. Williams [1], and B. A. Erickson [2] can be found in their respective theses. Central to the spectrometer is the interaction region, in which the detector axis, laser axis, and liquid jet axes all intersect and in which photoelectrons are generated, and the time-of-flight (ToF) spectrometer, into which the photoelectrons are steered and separated by energy before being detected by a microchannel plate, the signals from which are amplified and converted to a digital waveform. Notable changes from previous descriptions of the spectrometer include addition of an angular degree of freedom to the magnet, redesigned skimmers for sampling photoelectrons, a newly implemented decelerator, and preamplification of MCP signals.

2.4.1 Interaction Region

The magnetic bottle ToF spectrometer is separated into two general regions: the interaction region and the flight tube. The interaction region consists of two 10" CF chambers, a 6 way cross and a 4-way cross. The 4-way cross serves the purpose of housing all pumping elements, including 600 L/s of total turbomolecular pumping speed (Leybold, Turbovac 151 C; Leybold, Turbovac 450i) backed by a rotary vane mechanical pump (Edwards, E2M18) and a cryo-pumping surface with ~1300 cm^2 total pumping surface area. The cryo-pumping surface is the primary means of maintaining low ultimate pressures in the interaction region, the pumping speed of which can be calculated by Equation 2.16 [66, 67].

$$S_{th} = A_K \cdot S_A \cdot \alpha \cdot \left(1 - \frac{P_{end}}{P}\right) \tag{2.16}$$

Here, S_{th} is the theoretical pumping speed of the cryo-surface, A_K is the size of the surface, S_A is the pumping speed of a given gas per unit area of the surface, P_{end} is the ultimate pressure attainable, and P is the chamber pressure. As the surface is in direct contact with a liquid nitrogen reservoir, it is assumed the surface temperature is ~77 K which is sufficiently below the freezing point of water so the sticking coefficient α can be assumed to be 1. Additionally, the ultimate pressure of the chamber is substantially lower than the pressure at which cryo-pumping is initiated, so the final term in Equation 2.16 can be assumed to be 1 as well. Given the cryogenically cold area is known, the final unknown is S_A, can be determined by the gas temperature and molar mass as shown in Equation 2.17:

$$S_A = \sqrt{\frac{R \cdot T_g}{2\pi \cdot M}} \tag{2.17}$$

where R is the ideal gas constant, T_g is the gas temperature, and M is the molar mass of the gas being cryo-pumped from the chamber. For water in the interaction region, S_A is approximately 14.68 L/s$\cdot$ cm^2 making the maximum theoretical pumping speed of the cryo-pump ~19,000 L/s. These pumps, in conjunction with the catcher discussed in Section 2.3.3, are capably of maintaining ambient pressures in the interaction region of 5.0 10^{-5} Torr.

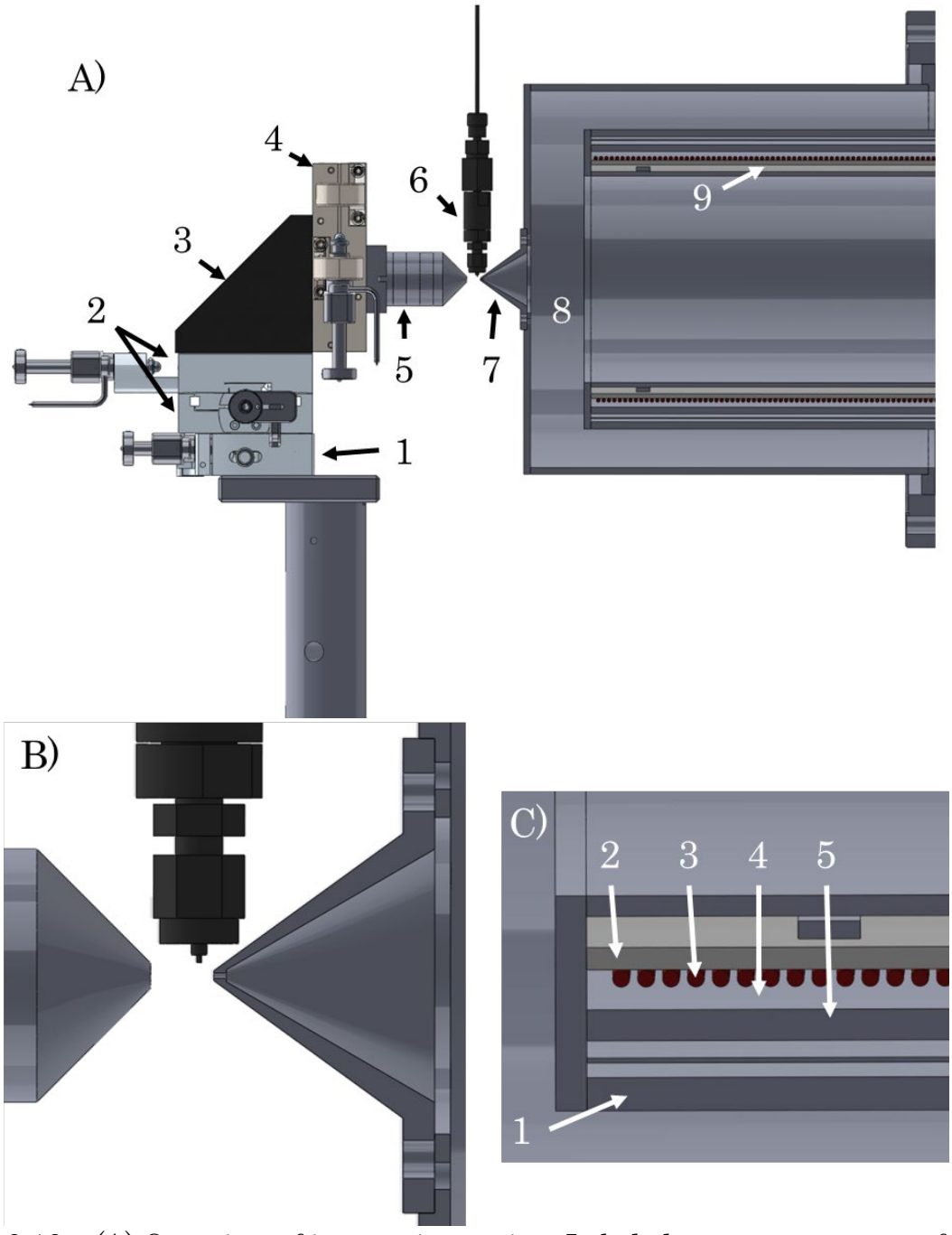

Figure 2.18 – (A) Overview of interaction region. Labeled components are as follows: (1) rotation stage, (2) stages manipulating magnet x- and y-axes, (3) 90° mounting adapter, (4) z-axis magnet manipulation stage, (5) magnet stack, (6) liquid microjet assembly, (7) skimmer, (8) ToF drift region, and (9) solenoid assembly. (B) Zoomed-in view of the interaction region, with a cut-through view of the skimmer design shown. (C) Enhanced view of the solenoid assembly with the (1) concentric tubes extending into detector allowing solenoid to be kept at atmosphere, (2) inner solenoid mount with grooves for solenoid wires, (3) solenoid wires, (4) plastic solenoid cover for electrical isolation, and (5) mu-metal magnetic detector shielding.

The final major components in the interaction region include the magnet assembly and skimmer dividing this region from the ToF region. The magnet assembly sits on a custom breadboard detailed in A. T. Shreve's dissertation [34]. To this assembly is mounted a customized rotation stage (Newport, RS65) with a piezoelectric motor (Newport, 8301NF) in place of the vernier micrometer typically installed. This component is new to the assembly; as the chamber had to be rotated to mount cameras for aligning the liquid jet – catcher assembly, the magnet could no longer be guaranteed to be parallel to the detector axis so this degree of freedom had to be added to the magnet assembly. To this rotation stage is an XYZ-stack equivalent to what's been previously described but with stages substituted for low-profile equivalents to account for the extra height of the rotation stage. The magnet stack is mounted as shown previously, with one notable difference being the addition of a grounding wire to keep the magnet stack at the instrument ground or at a set voltage. The stack consists of four neodymium magnets (McMaster-Carr, 5862K253) capped with a soft iron cone (Ed Fagan, HyperCo 50A) tapered at a 45° angle to a 500 μm diameter blunted tip. This blunted tip design creates a higher intensity magnetic field in the interaction region, on the order of 0.5 T as opposed to ~0.4 T [68].

The skimmer currently used has been redesigned from the previously described. Previous iterations were tapered to a knife-edge at the tip leaving nearly no material there, making the tip extremely fragile and prone to collapse and ablation. When aligning the pump beam using the high laser intensities needed to generate LAPE signal, the beam frequently clipped the skimmer leading to a notch etched through the tip of the skimmer through the gradual ablation of the skimmer. To solve this, a skimmer with substantially more material at the tip was designed and fabricated, drawings of this skimmer can be found in Appendix B. In short, the design is essentially identical to the old design, with the exception of the angle of the outer taper to the tip, leaving a 1 mm tip diameter, and the angle of the inner taper to the tip, leaving a ~500 μm long channel at the diameter of the skimmer opening.[16] Additionally, the angle of the inner taper was set such that it could be machined using commercially available countersinks, greatly decreasing the fabrication time by a factor of 3-4 relative to the time required to fabricate a skimmer with a knife-edge.

2.4.2 Magnetic Bottle Time-of-Flight Spectrometer

The magnetic bottle spectrometer includes components in both the interaction region and the ToF region. The magnetic bottle technique is crucial for this experiment to work, as nearly 50% of ejected photoelectrons can be steered into the

[16] Two skimmers were made using this design, one with a 400 μm ID and one with a 500 μm ID.

ToF region [69, 70]. This is accomplished through an intense, divergent magnetic field in the interaction region created by a stack of neodymium magnets and soft iron cone that shapes the magnetic field lines.

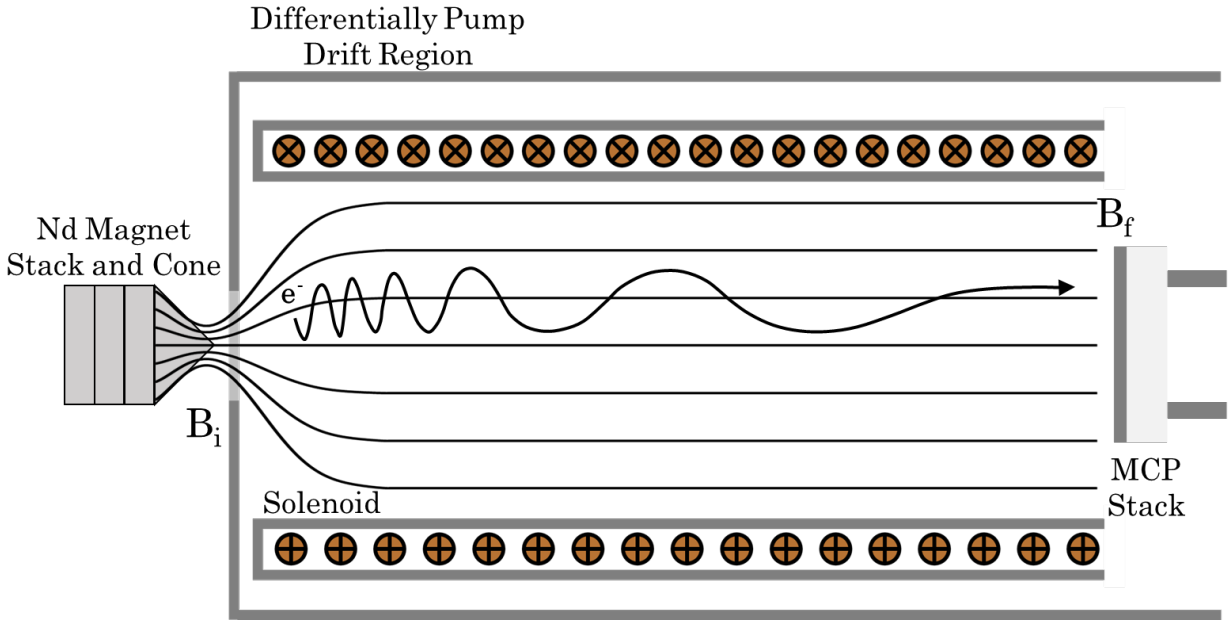

Figure 2.19 – Schematic representation of the magnetic fields generated by the neodymium stack, soft iron cone, and solenoid present in the magnetic bottle time-of-flight region. The trajectory of an electron propagating in this field is shown.

The use of an iron cone results in a magnetic field with field strength as high as 1.1 T at the tip of the cone for a cone that comes to a tip. This field is reduced to ~0.4 T over the distance from cone to liquid microjet. At the interaction point where the laser is crossed with the liquid microjet, the generated photoelectrons interact with this divergent magnetic field. This resultant force on the photoelectrons from the magnetic field is known as the Lorentz force, $\boldsymbol{F}$, and is described by Equation 2.18:

$$\boldsymbol{F} = q(\boldsymbol{E} + \boldsymbol{v} \times \boldsymbol{B}) \tag{2.18}$$

where q is the charge of an electron, $\boldsymbol{E}$ is the electric field vector, $\boldsymbol{v}$ is the vector velocity of the photoelectron, and $\boldsymbol{B}$ is the magnetic field vector. For a static magnetic field in the absence of an electric field, the Lorentz force acts on the electrons perpendicularly to the field lines, causing the electrons to spiral about them with frequency given by Equation 2.19 and cyclotron radius given by Equation 2.20.

$$\omega_i = \frac{q_e B_i}{m_e} \tag{2.19}$$

$$r_i = v \cdot \frac{\sin(\theta_i)}{\omega_i} \tag{2.20}$$

For a divergent field, the decreasing magnetic field amplitude and corresponding off-axis components lead to conversion of orthogonal velocity components to parallel velocity components with respect to the magnetic field axis. When combined with a weak magnetic field parallel to the detection axis generated by a solenoid the photoelectrons are parallelized, with off-axis velocity components almost completely converted to on-axis velocity.

As this process requires a velocity component parallel to the detection axis, only electrons with unit velocity within the hemisphere on the ToF side of the liquid jet will be guided into the ToF region. As such, slightly less than 50% of photoelectrons generated will be detected assuming an isotropic distribution. These electrons are rapidly parallelized, and it can be assumed that they are separated according to kinetic energy characterized by flight length and time alone according to Equation 2.21.

$$eKE = \frac{1}{2} m_e \left(\frac{l^2}{(t - t_0)^2} \right) \tag{2.21}$$

This assumption holds so long as the angular and transverse motion can be considered independently. This is the case when the initial magnetic field magnitude, B_i, is substantially larger than the final magnetic field magnitude, B_f. Under this assumption, the angular momentum is conserved and "non-adiabatic" effects leading to spectral broadening and spatial asymmetry are absent [69]. As the cyclotron radius is inversely proportional to the magnetic field strength, the ratio of initial (r_i) and final (r_f) photoelectron spatial distributions can be determined by the ratio of initial and final magnetic field strengths as given by Equation 2.22.

$$\frac{r_f}{r_i} = \left(\frac{B_i}{B_f} \right)^{0.5} \tag{2.22}$$

Here, the initial magnetic field strength is determined by numerical simulations of the field created by the neodymium magnet stack and soft iron cone with a blunted tip used in the current assembly using the Finite Element Method Magnetics (FEMM) software and is approximately 0.75 T at the blunted tip of the magnet and

0.36 T at the point the photoelectrons are generated. The final magnetic field strength is given by Ampere's Law applied to solenoids, as given by Equation 2.23.

$$B = \frac{\mu}{\mu_0} nI \tag{2.23}$$

For copper wire, $\frac{\mu}{\mu_0}$ is ~1. Therefore, the field strength generated along the ~66 cm long solenoid, consisting of 14 AWG copper wire coiled at 10 TPI (~4 turns per cm), is approximately 8 G for a 2 A current supplied by a Kepco DC power supply (Kepco, ATE 6-10M). Assuming the initial radius for the spatial distribution of the photoelectrons is equivalent to the XUV focal radius, the photoelectron distribution would be approximately 70 μm at the skimmer and 0.75 mm at the detector.

Given the cyclotron radius depends directly on the initial direction of the velocity vector relative to the magnetic field, the trajectory of electrons with equivalent eKE would not be identical. To assess the impact of this difference in path-lengths, others have carried out numerical simulations to determine the difference in arrival time for an isotropic distribution of photoelectrons under comparable conditions. Their simulations returned an upper limit of $\frac{\Delta t}{t} = 0.56\%$ for isotropic distributions of photoelectrons [69]. Given that the fundamental limitation in determining electron arrival time for this experiment is the pulse width for electron counts amplified by the MCPs, this uncertainty only becomes comparable to the detector uncertainty for electrons with ToF of ~900 ns.[17] Even in this regime, the inherent width of signals from liquids means this limitation is not a limiting factor even for slow photoelectrons in a given LJ-TRPES experiment. This all assumes proper alignment of the magnetic bottle; if the neodymium magnet stack or solenoid are misaligned, the misalignment drastically increases the non-adiabatic effects resulting in visible broadening of the spatial distribution as imaged on the phosphor screen and substantially broadened peaks in the ToF spectrum.

2.4.3 Calibrating the Spectrometer

Proper alignment and calibration of the spectrometer must be performed any time the magnet is moved, intentionally or otherwise. While the alignment is straightforward (accomplished by simply minimizing the linewidth of a given photoelectron peak), calibration is not always as simple. The existing "go-to" system for calibrating the spectrometer was to observe multiphoton ionization of $Xe_{(g)}$. The $Xe \rightarrow Xe^+$ ionization process is resonantly enhanced, proceeding first through a 2-

[17] This assumes a 5 ns detector uncertainty. The detector uncertainty was taken to be the width of the peak resulting from amplification of a single electron.

photon excitation centered around ~247 nm and then ionizing to either $Xe^+(^2P_{3/2})$ or $Xe^+(^2P_{1/2})$ [71].[18] Using the well-known ionization energies to these states and spectra collected at several wavelengths above and below 247 nm, a calibration curve can be created from which the ToF parameters l and t_0 are extracted.

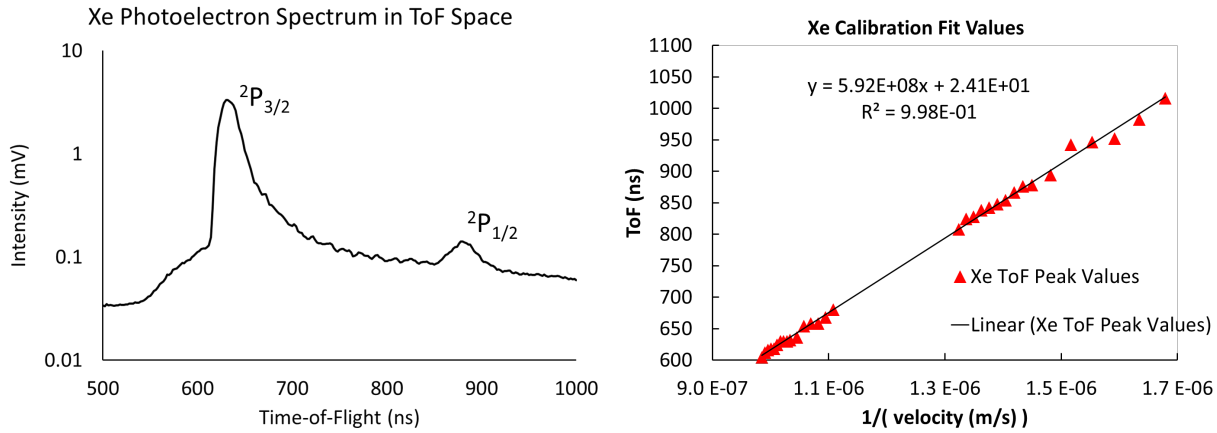

Figure 2.20 – Typical photoelectron spectrum of Xe photoionization used to determine the kinetic energy of the spin-orbit split peaks at a given measured tunable UV wavelength, in this case 251 nm. The position of these peaks in ToF space are recorded for a wide range of tunable UV wavelengths above and below the resonance at 247 nm and plotted as shown on the right. By plotting these points with measured ToF on the y-axis and expected inverse velocity on the x-axis, fitting a trendline yields a fit slope corresponding to the length parameter of the spectrometer and a fit intercept corresponding to the t_0 parameter of the spectrometer.

While this process of shifting the center wavelength about a resonant optical transition works extremely well for $Xe_{(g)}$ ionization, systems like $Ar_{(g)}$ do not benefit from resonant enhancement within our UV tuning range.[19] However, the onset of LAPE is attainable for available 800 nm, 400 nm, and 266 nm pump intensities. Employing LAPE using minimum pump and XUV probe intensities such that detrimental effects of high-intensity light are avoided creates a symmetric, well-defined patterns of satellite peaks a well-known spacing above and below a main peak resulting from ionization of a gas with well-known binding energy.[20] Using this, both the precise energy of the XUV probe and the ToF parameters can be retrieved. This fitting has better results when multiple harmonics are present in the XUV probe, allowing for less uncertainty in all degrees of freedom after fitting.

[18] The ionization energy of Xe to $Xe^+(^2P_{3/2})$ and $Xe^+(^2P_{1/2})$ are 12.1298 eV and 13.4363 eV, respectively.
[19] Comparable excitations in $Ar_{(g)}$ and $Kr_{(g)}$ would require 2-photon excitation around 180 nm and 210 nm, respectively.
[20] Most commonly used are $Ar_{(g)}$ or $H_2O_{(g)}$, with ionization energies of 15.7596 and 12.61 eV, respectively.

Setting XUV generation conditions such that flux at higher order harmonics is increased for calibration also has the advantage of guaranteeing the accuracy of the calibration in the eKE range excited state signals for a typical LJ-TRPES experiment would be observed.

Other systems can be used to roughly calibrate the spectrometer, with $H_2O_{(g)}$ being principle among them. While multiphoton ionization of water vapor leads to very broad peaks, XUV photoionization leads to a narrow photoelectron peak from the $1b_1$ orbital [72].[21] This peak is prominent in any spectra taken when the liquid microjet is in the interaction region, whether the laser is impinging on it or not.

2.4.4 Photoelectron Decelerator

An issue that has become apparent as the experiment has progressed to ever higher probe energies is the limitation of the ToF energy resolution. The energy resolution of a ToF spectrometer goes as $\Delta E \propto E^{3/2}$, so at sufficiently high eKE the resolution of the spectrometer is on par with the natural linewidths of the features. For the current iteration of the spectrometer, photoelectrons with 20 eV eKE will have a ~0.5-1.0 eV energy space resolution.[22] Future implementations of this experiment will likely include core-level ionization using probe energies on the order of 100-200 eV which would have uncertainties on the order of 2-3 eV, substantially greater than any natural linewidths that would be expected.

Two possible solutions exist to resolve this issue: the length of the ToF region could be extended until the desired energy resolution is obtained, or the kinetic energy of all photoelectrons reduced by a fixed amount before entering the ToF region. While extending the length of the ToF region may seem most advantageous, it is practically difficult as the existing solenoid cannot be simply extended the way one would bolt on a CF cross to extend the chamber length. As this would also lead to added difficulty ensuring a parallel and homogeneous solenoid field, increased complication maintaining low pressures, and space limitations preventing substantial increase in length, it was decided the introduction of decelerating optics would be the more appropriate path forward.

[21] Ionization from the $3a_1$ and $1b_2$ are not useful calibration points as they are broad due to a multitude of vibronic levels present in the photoelectron spectrum.
[22] This assumes a 5 ns ToF uncertainty determined by measuring the FWHM of dark counts. This is also highly dependent on calibration.

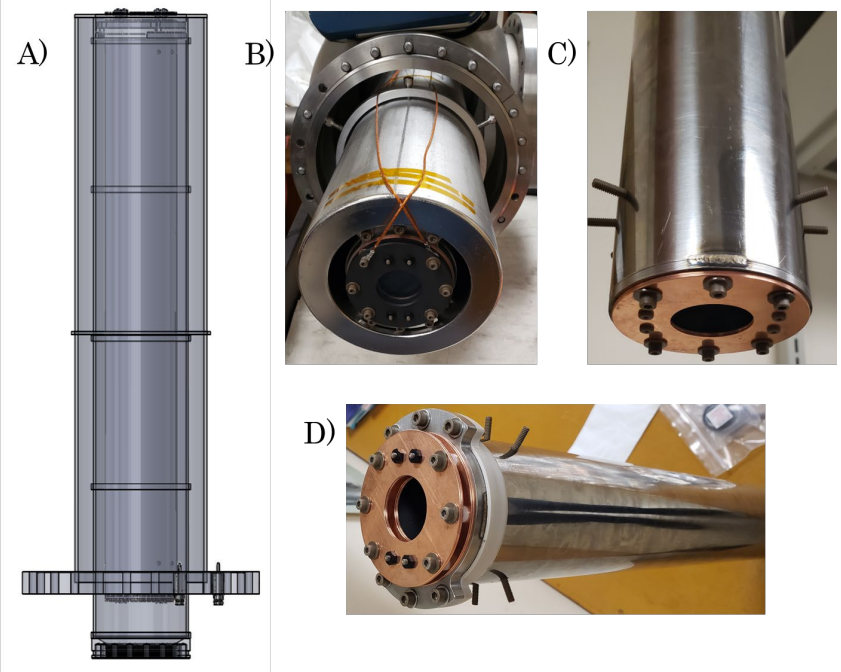

Figure 2.21 – Various views of the decelerator assembly. A) Semi-transparent schematic of the CAD assembly. B) Decelerator nested in the detector. C) Back end of the decelerator assembly facing the MCP stack. D) Front end of the decelerator assembly facing the interaction region.

The decelerator assembly is shown in Figure 2.21. It consists of three electrode assemblies each consisting of a 117.6 LPI mesh (Precision Eforming, MN49) sandwiched between copper mounting plates. Two electrode assemblies at the entrance of the ToF region are kept a set distance apart using nylon spacers and affixed to a 3" diameter polished stainless steel drift tube. The front electrode is kept at the instrument ground to screen the interaction region from the floating potential of the drift tube. The electrode in electrical contact with the drift region is held at a fixed negative potential using a Kepco DC power supply (Kepco, ATE 25-10M) with the positive electrode referenced to ground. The third electrode assembly is secured to the end of the drift tube nearest the detector, screening the drift tube from the positive potential on the front of the MCP assembly. Finally, the drift tube is electrically isolated from the rest of the instrument using a PEEK collar and is made parallel to the ToF axis using a set of screws on the rear of the drift tube.

For current experiments with a 21.7 eV probe, the decelerator was tested at voltages of -10 V. It was observed that the peaks were appropriately decelerated to a point, but the peaks broadened disproportionately with what would be expected due to ToF considerations alone, and decreased in amplitude disproportionately with what would be expected due to the Jacobian factor. From this, it is likely the decelerator was not perfectly orthogonal to the magnetic field. This would manifest

similarly to a misaligned magnetic bottle, as was observed. The alignment was never perfected due to time constraints, but proper implementation of the decelerator assembly should be possible and will likely be implemented in the near future.

2.4.5 Detector Assembly

The final component in the photoelectron spectrometer is the detector assembly. Photoelectrons are guided to chevron-stacked MCPs (Photonis, Long Life MCP 25/12/10/12 I 40:1 TC; Hamamatsu, F1552-011F) with a bias voltage of 2.25 kV applied across the stack. These MCPs consist of highly resistive (~50 MΩ) material with many channels 10 μm in diameter spanning the distance between each face of the plate at a 12° bias angle. The MCPs are electron multipliers; if an electron strikes the inside surface of a channel, a cascade of secondary electrons is initiated, propagating through the channel until exiting at the opposite end. Due to the large bias voltage applied across the plate (~1.1 kV), the incident particle (in this experiment electrons) is multiplied, amplifying the original single electron signal. To aid in detection of low eKE photoelectrons, the front face of the MCP stack is kept at a 50 V floating potential. To prevent this electric field from penetrating into the ToF drift region, a ground nickel mesh is placed directly in front of the MCP stack. The MCPs in a chevron stack lead to amplification of single electrons by a factor of $10^6 – 10^7$. Behind the MCPs is a type P-43 phosphor screen (Beam Imaging Solutions, 25-008) that is held at 3.35 kV. The combination of the MCPs and phosphor screen, held in a commercial housing (Beam Imaging Solutions, BOS-25-OPT1), lead to a ~10^7 amplification of single electrons.

The high voltage supply (Bertan, 205B-05R) connects to the back of the back MCP through a 50 kΩ and 1 MΩ resistors. A 2200 pF capacitor capacitively couples the high voltage supply to ground to dampen any AC components from the voltage supply. Voltage drops across the MCPs, which are electrically contacted using a thin electrode placed between the MCPs. A 10 MΩ voltage divider runs parallel to the MCPs, with the voltage after this resistor kept at 50 V using a Zener diode coupled to ground. The 50 V voltage is supplied to the front of the front MCP using a 1 MΩ resistor. The phosphor screen is supplied by an additional high voltage supply, with this voltage coupled to the phosphor screen through a 1 MΩ resistor. Signal is capacitively coupled off the back MCP using a 1 nF capacitor. This was decided as the signal coupled off the phosphor screen had substantially larger amplitude ringing than the back MCP. It should be noted that all electronic components except the voltage supplies and the 1 MΩ phosphor screen resistor have been moved into the space between the feedthroughs and the phosphor screen on the vacuum side of the CF flange on which the MCPs are mounted. This was done to minimize ringing;

the FWHM of a single electron count was reduced from 8 ns to 5 ns with nearly no ringing (at most 10% the magnitude of the main peak).

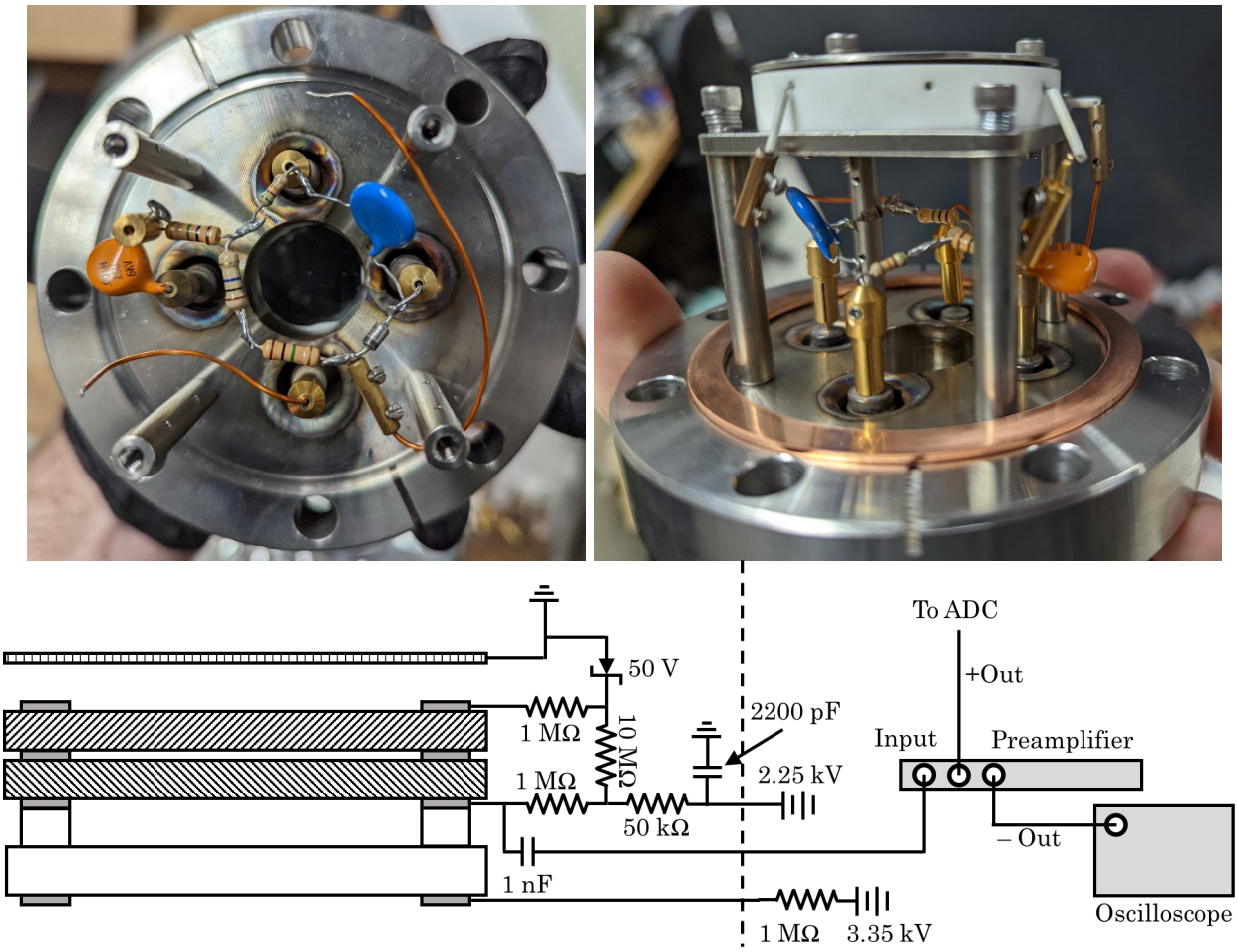

Figure 2.22 – MCP detector and circuit. (top left) Portion of the MCP voltage supply circuit inside of vacuum. (top right) Same circuit shown with MCP connections and assembly in place. (bottom) Schematic diagram of the MCP voltage supply and detection circuit.

Signals are transmitted out of vacuum through a 12" BNC cable (C D International Technology, BDBD-58-2 W2323) to variable gain preamplifier (Stanford Research Systems, SR446). The gain of the preamplifier is typically set to anywhere in the range from 10.0 to 40.0. The preamplifier has a built-in output filter, which is typically set to 200 MHz to remove high-frequency components of the amplified MCP output. The amplified signal is then transmitted to an ADC digitizer card (Acqiris, U5309A) installed in the lab computer. This digitizer is an 8-bit ADC, converting the signal out of the preamplifier into voltage vs. time. The digitizer card has a minimum full-scale range of 500 mV, meaning the analog voltage from the preamplifier can only be divided into ~1 mV bins. This is why it is extremely

advantageous to use the preamplifier, the amplified signal can be more finely divided using this minimum voltage range, increasing signal resolution and decreasing electronic noise from the card relative to the signal.

2.5 Data Collection and Processing

Data is collected using home-written LabVIEW software integrating commercial sub-vi's from suppliers of the various components. This software does, to a small degree, treat the raw data by correcting for fluctuations in the baseline signal level and applying a DC thresholding filter to remove noise in the baseline on a shot-to-shot basis. This data, time-resolved or not, is then sorted and stored in a .csv file. The data can then be transferred to MATLAB, where all the post-processing code has been written. Here, the data is background subtracted, baseline corrected, and corrected for any space-charge effects and known sources of interference. From here, the data can be analyzed and meaningful lifetimes and spectral components extracted.

2.5.1 LabVIEW Data Collection Software

All data is collected through LabVIEW, which has contributions that can be found in the theses of A. T. Shreve [34], H. L. Williams [1], and B. A. Erickson [2]. Many updates to the code were made parallel to the work Erickson did to integrate the subVIs to collect data using the ADC card to simultaneously improve background subtraction, collection speed, and baseline noise while removing systematic errors by randomizing delays and actively correcting baseline variations. The overall explanation of how the code works and description of upgrades predating this dissertation can be found in the theses mentioned above. A more detailed description of the code is given in Appendix A including figures showing the code itself.

Due to flooding in lab and inadequate data backups, the source code for the LabVIEW executables was lost. This meant all improvements made by Williams were not available and had to be duplicated. Fortunately, this was done in short order due to the documentation in her dissertation. In this process, useful controls were added to change the wait time for the servo motors moving the beam-blocks. This allowed for the XUV driver to be blocked rather than the XUV itself, simplifying initial testing and development of an XUV probe for time-resolved spectroscopy. The XUV was seen to require ~10 s to reach equilibrated conditions once the driver has been unblocked, so a wait time of 12,000 ms was set as the default. Parallel to this re-creation of the code for one-color background scans,

specifically the code for actuating the servo-controlled beam blocks, code for actuating rapidly opening and closing optical shutters (Vincent Associates, Uniblitz VS25; Vincent Associates, Uniblitz CS45) both in and out of vacuum was added. These shutters have substantially improved opening times compared to the servo-actuated shutters, with 20 ms and 6 ms opening times in atmosphere and vacuum, respectively. These backgrounds can be actuated using the denotations "D", "E", or "F" in the configuration table corresponding to closing the shutter on channel 1, 2, or 3 on the shutter driver (Vincent Associates, VMM-D3). The servo-actuated beam-blocks can still be actuated using the denotations "A", "B", and "C" as was the case before. The denotation "G" has also been added as a case where all shutters and beam blocks are opened.

The randomization of delay order and optional background spectra taken after every delay were also added as features in the new LabVIEW code. The two features are implemented in the same block of code, as the table must be broken into component portions and rebuilt for both the randomization and background subtraction features. To accomplish this, controls denoting whether a single background or two backgrounds will be taken after each delay and, if only one of two backgrounds after each delay is taken, different controls indicating whether the first or second background is taken after each delay are used. Regardless of how many and which backgrounds are taken after every delay, the number of backgrounds and delays are first counted and the rows for taking data and rows for taking backgrounds are separated into separate tables. A column of random numbers the length of the data table is appended to the data table, which is then sorted by increasing value of the values in the appended column. Background rows can then be added after each data delay according to the selected controls, and the final table constructed with checks to make sure the total number of rows after reconstruction of the table matches the expected value. This table is what is then used to collect data. After the data is collected, the spectra taken for each background and each delay are separated into data and background .csv files, which are then exported for post-processing.

Recently, it was observed that the baseline of the analog-to-digital converter (ADC) card fluctuated by as much as ~1% the full scale range (FSR) of the card. This was determined to be an issue of the on-board fan turning on and off to maintain the set temperature of 65°C. To account for this, a firmware update was installed to maintain a fan speed of 50% the maximum speed, rather than alternately running at 100% and 0% the maximum speed to maintain the set temperature. This still left some instability in the card temperature which manifested as an unstable baseline. This was corrected by adding an active baseline correction routine to the code. This is accomplished by subtracting the average of a signal-free portion of the spectrum from the next scan after every 1000 shots accumulated. The signal-free portion of the spectrum must be selected with care; typically, the region from 50-150 ns ToF is

a good choice but if substantial photon scattering creates signal in this region the region before the photon scattering signal can be used by adjusting the trigger delay and increasing the total ToF range acquired.

Finally, the thresholding routine briefly described in the dissertation of Blake Erickson was improved. In the version described previously, the digitize spectrum was converted into an array of either 1s or 0s depending on if the signal intensity is above the set threshold. While this is good in theory, in practice it did not have the desired effect as it equated signals substantially above the threshold with the sporadic noise that was just barely above the threshold. At the heart of the problem was the bin size for the digitizer, a single bit corresponds to 1 mV signal at the smallest FSR available. As the single electron counts from the detector are on the order of 3-7 mV, the lower end of the single-count distribution is cut off when the threshold is set to eliminate variations in the digitizer baseline which are 2-3 bits. To collect the most signal, the threshold needed to be set to approximately 4-5 mV, which eliminates all but the most extreme fluctuations in the digitizer baseline but also eliminates up to 50% of single-count signal. To counteract this, a "DC" thresholding scheme was set up such that the thresholded spectrum consisting of 0s and 1s is multiplied by the original spectrum, resulting in both the signals and noise maintaining their original intensity, as the noise is substantially lower in intensity than the signal a larger portion of the single-count distribution can be captured while keeping a comparable baseline level, resulting in an increased S/N. This is discussed further in Appendix A. As shown in Figure 2.23, The "Digital" thresholding scheme gives an approximate S/N increase of 1.5 orders of magnitude while the "DC" thresholding scheme gives an approximate S/N increase of 3 orders of magnitude for weak signals by decreasing the noise while maintaining comparable signal levels.

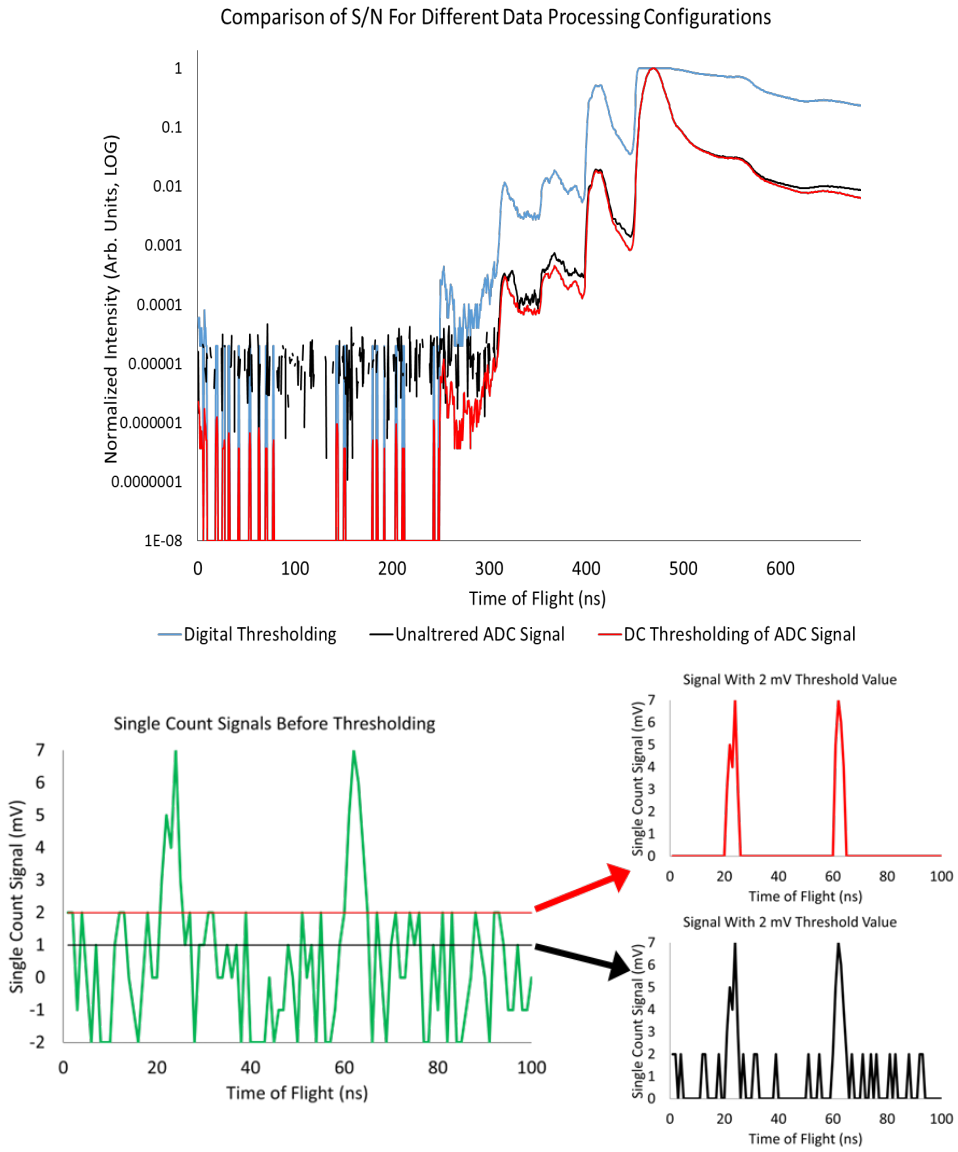

Figure 2.23 – (top) Demonstration of the "Digital" and "DC" thresholding noise reduction algorithms implemented. (bottom) A graphical representation of the action the DC thresholding noise reduction algorithm has on the single shot spectrum.

2.5.2 Post-Processing of Spectra

After data is exported from LabVIEW and before it can be fit, some small amount of processing is required. This process has been detailed extensively in the theses of both Elkins and Williams, so only a short summary and details of some notable changes will be detailed here. First, data is imported into MATLAB and converted to eKE space using constants extracted from calibration data. Then backgrounds

are subtracted, a baseline fit, and the background subtracted data is baseline corrected. The data is then corrected for the Jacobian factor from the ToF to eKE conversion. At this point the data processing differs from previous iterations. The shift due to space-charge effects is removed by fitting the $H_2O_{(l)}$ peak to a gaussian and shifting the spectra so the centers of the peak retrieved from the fit at each time delay are aligned [41]. From here, the data can be smoothed and fit as normal.

2.5.3 Data Analysis Methods

Data analysis methods used to retrieve signal decay lifetimes, relative amplitudes, and cross-correlation vary depending on the degree to which spectral features overlap. For well-separated signals, the lane integration method is well suited for fitting the time-resolved signals. As the name suggests, a range of eKEs that encompasses the signal of interest while avoiding other features is determined and the entirety of the signal within the lane is integrated at each time delay. From here, the data can be fit to an appropriate function such as a monoexponential decay convolved with the instrument response function (IRF) as shown in Equation 2.24 [73].

$$f(t-t_0) = \frac{I_0}{2} \cdot e^{\left(\frac{\sigma^2}{2\tau^2} - \frac{(t-t_0)}{\tau}\right)} \cdot \left(\mathrm{erf}\left(\frac{(t-t_0)}{\sigma\sqrt{2}} - \frac{\sigma}{\tau\sqrt{2}}\right) + 1\right) \tag{2.24}$$

Here, t_0 denotes the time at which the pump and probe overlap, I_0 is the feature amplitude, σ is the cross-correlation of the pump and probe pulses, and τ is the lifetime of the feature being fit. It is important to remember that this will give best results for signals that don't shift outside of the chosen lane or for lanes that do not include contributions from other features. As this is often not the case for features present in a typical LJ-TRPES experiment, the lane integration method is typically only used for roughly fitting features present in liquid experiments and for experiments involving gas-phase determination of the cross-correlation. More about this can be found in the theses of Elkins [65] and Williams [1].

An alternative to lane integration is global lifetime analysis (GLA) [73-75], a powerful tool for separating spectral components with different lifetimes but significant overlap in eKE. While this is a useful tool for fitting overlapping components, it requires the entire TRPES data set simultaneously with as many decay components required to accurately fit the dynamics. This can often be a computationally intensive process requiring good initial values for fitting parameters. This process depends on a few basic assumptions: that the entire data set can be broken into independent components dependent only on energy ($S_i(eKE)$) and time ($S_i(t)$), that the temporal component can be represented as a sum of

monoexponentials convolved with the IRF, and that energy components don't change shape or position. If these assumptions hold, the data set can be fit to Equation 2.25.

$$S(eKE,t) = \sum_{i=1}^{j} \sigma_j \cdot S_i(eKE) \cdot S_i(t) = \sum_{m=1}^{n} DAS_{\tau_m}(eKE) \cdot \left[e^{-\frac{t}{\tau_m}} * L(t-t_0) \right] \quad (2.25)$$

Here, j is the total number of features fit, σ_j is a weighting factor accounting for relative cross sections, $DAS_{\tau_m}(eKE)$ is the energy-dependent decay associated spectrum for decay component with lifetime τ_m, and $e^{-\frac{t}{\tau_m}} * L(t-t_0)$ is the exponential decay convolved with the IRF, $L(z-t)$. This fit function, initialized with as few τ_m as needed to adequately describe the dynamics, is iteratively fit to the data until it converges. As discussed in the Elkins' dissertation [65], $S(eKE,t)$ can be alternatively represented with the energy-dependent component modeled as a sum of gaussians with the shifting center and width varying in time as a monoexponential shift from initial to final values. This is particularly useful in instances where normal GLA analysis breaks down due to substantial energetic relaxation of a single spectral component. This is common in cases where conical intersections transfer population to a region on the potential surface well above the vibrational ground state, resulting in substantial shifting in eKE with vibrational cooling. Finally, 95% confidence intervals can be determined by calculating χ^2 values at the best fit lifetimes arrived at from the GLA fitting and at test lifetimes distributed about the best fit lifetimes. This process is discussed in detail in Elkins' dissertation.

2.6 References

[1] Williams, H. L. Ultrafast Dynamics of Adenine Derivatives Studied by Time-Resolved Photoelectron Spectroscopy in Water Microjets. Ph.D., University of California, Berkeley, United States -- California, 2017.

[2] Erickson, B. A. Extending Time-Resolved Photoelectron Spectroscopy to the Extreme Ultraviolet. Ph.D., University of California, Berkeley, Proquest, 2021.

[3] Juan, L. A. C.; Stuart, D. B.; Alexander, Z.; John, P. C.; Andrea, L. C.; Murray, K. R.; Luis, S. High-power optically pumped semiconductor lasers. In *Proc.SPIE*, 2004; Vol. 5332, pp 143-150. DOI: 10.1117/12.549003.

[4] Strickland, D. Chirped Pulse Amplification. In *Handbook of Laser Technology and Applications*; Guo, C., Singh, S. C., Eds.; Vol. 1; CRC Press, 2021; p 10.

[5] Maine, P.; Strickland, D.; Bado, P.; Pessot, M.; Mourou, G. Generation of ultrahigh peak power pulses by chirped pulse amplification. *IEEE J. Quantum Elect.* **1988**, *24* (2), 398-403. DOI: 10.1109/3.137.

[6] Strickland, D.; Mourou, G. Compression of amplified chirped optical pulses. *Opt. Commun.* **1985**, *55* (6), 447-449. DOI: 10.1016/0030-4018(85)90151-8.

[7] Salin, F. How to Manipulate and Change the Characteristics of Laser Pulses. In *Femtosecond Laser Pulses*, 2 ed.; Rulliere, C. Ed.; Springer, 2005; pp 175-194.

[8] Boyd, R. W. *Nonlinear Optics 3rd ed.*; Academic Press, 2008.

[9] Sutherland, R. L. *Handbook of Nonlinear Optics*; Marcel Dekker, Inc., 2003.

[10] Seidel, R.; Winter, B.; Bradforth, S. E. Valence Electronic Structure of Aqueous Solutions: Insights from Photoelectron Spectroscopy. *Annu. Rev. Phys. Chem.* **2016**, *67* (1), 283-305. DOI: 10.1146/annurev-physchem-040513-103715.

[11] Brichta, J. P.; Wong, M. C. H.; Bertrand, J. B.; Bandulet, H. C.; Rayner, D. M.; Bhardwaj, V. R. Comparison and real-time monitoring of high-order harmonic generation in different sources. *Phys. Rev. A* **2009**, *79* (3), 033404. DOI: 10.1103/PhysRevA.79.033404.

[12] Lewenstein, M.; Balcou, P.; Ivanov, M. Y.; L'Huillier, A.; Corkum, P. B. Theory of high-harmonic generation by low-frequency laser fields. *Phys. Rev. A* **1994**, *49* (3), 2117-2132. DOI: 10.1103/PhysRevA.49.2117.

[13] Krausz, F.; Ivanov, M. Attosecond Physics. *Rev. Mod. Phys.* **2009**, *81*, 163.

[14] Krause, J. L.; Schafer, K. J.; Kulander, K. C. High-order harmonic generation from atoms and ions in the high intensity regime. *Phys. Rev. Lett.* **1992**, *68* (24), 3535-3538. DOI: 10.1103/PhysRevLett.68.3535.

[15] Corkum, P. B.; Krausz, F. Attosecond science. *Nat. Phys.* **2007**, *3* (6), 381-387. DOI: 10.1038/nphys620.

[16] Corkum, P. B. Plasma perspective on strong field multiphoton ionization. *Phys. Rev. Lett.* **1993**, *71* (13), 1994-1997. DOI: 10.1103/PhysRevLett.71.1994.

[17] Becker, W.; Lohr, A.; Kleber, M. Light at the end of the tunnel: two- and three-step models in intense-field laser-atom physics. *Quantum Semiclass. Opt.* **1995**, *7* (3), 423. DOI: 10.1088/1355-5111/7/3/017.

[18] Falcão-Filho, E. L.; Gkortsas, V. M.; Gordon, A.; Kärtner, F. X. Analytic scaling analysis of high harmonic generation conversion efficiency. *Opt. Express* **2009**, *17* (13), 11217-11229. DOI: 10.1364/OE.17.011217.

[19] Shiner, A. D.; Trallero-Herrero, C.; Kajumba, N.; Bandulet, H. C.; Comtois, D.; Légaré, F.; Giguère, M.; Kieffer, J. C.; Corkum, P. B.; Villeneuve, D. M. Wavelength Scaling of High Harmonic Generation Efficiency. *Phys. Rev. Lett.* **2009**, *103* (7), 073902. DOI: 10.1103/PhysRevLett.103.073902.

[20] Marceau, C.; Hammond, T. J.; Naumov, A. Y.; Corkum, P. B.; Villeneuve, D. M. Wavelength scaling of high harmonic generation for 267 nm, 400 nm and 800 nm driving laser pulses. *J. Phys. Commun* **2017**, *1* (1), 015009. DOI: 10.1088/2399-6528/aa74f6.

[21] Steingrube, D. S.; Vockerodt, T.; Schulz, E.; Morgner, U.; Kovačev, M. Phase matching of high-order harmonics in a semi-infinite gas cell. *Phys. Rev. A* **2009**, *80* (4), 043819. DOI: 10.1103/PhysRevA.80.043819.

[22] Kornilov, O.; Wilcox, R.; Gessner, O. Nanograting-based compact vacuum ultraviolet spectrometer and beam profiler for in situ characterization of high-order harmonic generation light sources. *Rev. Sci. Instrum.* **2010**, *81* (6). DOI: 10.1063/1.3443575.

[23] Savas, T. A.; Shah, S. N.; Schattenburg, M. L.; Carter, J. M.; Smith, H. I. Achromatic interferometric lithography for 100-nm-period gratings and grids. *J. Vac. Sci. Technol. B* **1995**, *13* (6), 2732-2735. DOI: 10.1116/1.588255.

[24] Savas, T. A.; Schattenburg, M. L.; Carter, J. M.; Smith, H. I. Large-area achromatic interferometric lithography for 100 nm period gratings and grids. *J. Vac. Sci. Technol. B* **1996**, *14* (6), 4167-4170. DOI: 10.1116/1.588613.

[25] Henke, B. L.; Gullikson, E. M.; Davis, J. C. X-Ray Interactions: Photoabsorption, Scattering, Transmission, and Reflection at E = 50-30,000 eV, Z = 1-92. *Atomic Data and Nuclear Data Tables* **1993**, *54* (2), 181-342. DOI: 10.1006/adnd.1993.1013.

[26] Dereniak, E. L.; Dereniak, T. D. *Geometrical and Trigonometric Optics*; Cambridge University Press, 2008. DOI: 10.1017/CBO9780511755637.

[27] Gullikson, E. M.; Korde, R.; Canfield, L. R.; Vest, R. E. Stable silicon photodiodes for absolute intensity measurements in the VUV and soft X-ray regions. *J. Electron Spectrosc. and Rel. Phenom.* **1996**, *80*, 313-316. DOI: 10.1016/0368-2048(96)02983-0.

[28] Comby, A.; Descamps, D.; Beauvarlet, S.; Gonzalez, A.; Guichard, F.; Petit, S.; Zaouter, Y.; Mairesse, Y. Cascaded harmonic generation from a fiber laser: a milliwatt XUV source. *Opt. Express* **2019**, *27* (15), 20383-20396. DOI: 10.1364/OE.27.020383.

[29] Stolow, A.; Bragg, A. E.; Neumark, D. M. Femtosecond Time-Resolved Photoelectron Spectroscopy. *Chem. Rev.* **2004**, *104* (4), 1719-1758. DOI: 10.1021/cr020683w.

[30] Thurmer, S.; Malerz, S.; Trinter, F.; Hergenhahn, U.; Lee, C.; Neumark, D. M.; Meijer, G.; Winter, B.; Wilkinson, I. Accurate vertical ionization energy and work function determinations of liquid water and aqueous solutions. *Chem. Sci.* **2021**, *12* (31), 10558-10582. DOI: 10.1039/d1sc01908b.

[31] Faubel, M.; Schlemmer, S.; Toennies, J. P. A molecular beam study of the evaporation of water from a liquid jet. *Z. Phys. D: At., Mol. Clusters* **1988**, *10*, 269-277. DOI: 10.1007/BF01384861.

[32] McQuarrie, D. A.; Simon, J. D. *Physical chemistry: a molecular approach*; University Science Books, 1997.

[33] Wilson, K. R.; Rude, B. S.; Smith, J.; Cappa, C.; Co, D. T.; Schaller, R. D.; Larsson, M.; Catalano, T.; Saykally, R. J.; A., B.; M., D.; S., P. P.; H., W. A.; J., A.-N.; J., B. Investigation of volatile liquid surfaces by synchrotron x-ray spectroscopy of liquid microjets. *Rev. Sci. Instrum.* **2004**, *75* (3), 725-736. DOI: 10.1063/1.1645656.

[34] Shreve, A. T. Photoelectron Spectroscopy of Solvated Electrons in Liquid Microjets. Ph.D., University of California, Berkeley, United States -- California, 2012.

[35] Faust, J. A.; Nathanson, G. M. Microjets and coated wheels: versatile tools for exploring collisions and reactions at gas–liquid interfaces. *Chem. Soc. Rev.* **2016**, *45* (13), 3609-3620. DOI: 10.1039/C6CS00079G.

[36] Koralek, J. D.; Kim, J. B.; Brůža, P.; Curry, C. B.; Chen, Z.; Bechtel, H. A.; Cordones, A. A.; Sperling, P.; Toleikis, S.; Kern, J. F.; Moeller, S. P.; Glenzer, S. H.; DePonte, D. P. Generation and characterization of ultrathin free-flowing liquid sheets. *Nat. Commun* **2018**, *9* (1), 1353. DOI: 10.1038/s41467-018-03696-w.

[37] Ekimova, M.; Quevedo, W.; Faubel, M.; Wernet, P.; Nibbering, E. T. J. A liquid flatjet system for solution phase soft-x-ray spectroscopy. *Struct. Dyn* **2015**, *2* (5). DOI: 10.1063/1.4928715.

[38] Lee, C.; Pohl, M. N.; Ramphal, I. A.; Yang, W.; Winter, B.; Abel, B.; Neumark, D. M. Evaporation and Molecular Beam Scattering from a Flat Liquid Jet. *J. Phys. Chem. A* **2022**, *126* (21), 3373-3383. DOI: 10.1021/acs.jpca.2c01174.

[39] Lee, C. Gas Liquid Interface Studied by Molecular Beam Scattering From a Liquid Flat Jet. Ph.D., University of California, Berkeley, United States -- California, 2022.

[40] Riley, J. W.; Wang, B.; Parkes, M. A.; Fielding, H. H. Design and characterization of a recirculating liquid-microjet photoelectron spectrometer for multiphoton ultraviolet photoelectron spectroscopy. *Rev Sci Instrum* **2019**, *90* (8), 083104. DOI: 10.1063/1.5099040 From NLM PubMed-not-MEDLINE.

[41] Hummert, J.; Reitsma, G.; Mayer, N.; Ikonnikov, E.; Eckstein, M.; Kornilov, O. Femtosecond Extreme Ultraviolet Photoelectron Spectroscopy of Organic Molecules in Aqueous Solution. *J. Phys. Chem. Lett.* **2018**, *9* (22), 6649-6655. DOI: 10.1021/acs.jpclett.8b02937.

[42] Atkinson, R. D. E. Soldering Tungsten. *Nature* **1930**, *126* (3168), 97-97. DOI: 10.1038/126097b0.

[43] Luckhaus, D.; Yamamoto, Y.-i.; Suzuki, T.; Signorell, R. Genuine binding energy of the hydrated electron. *Sci. Adv* **2017**, *3* (4), e1603224. DOI: 10.1126/sciadv.1603224.

[44] Shinotsuka, H.; Da, B.; Tanuma, S.; Yoshikawa, H.; Powell, C. J.; Penn, D. R. Calculations of electron inelastic mean free paths. XI. Data for liquid water for energies from 50 eV to 30 keV. *Surf. Interface Anal.* **2017**, *49* (4), 238-252. DOI: 10.1002/sia.6123.

[45] Szmytkowski, C. Absolute total cross sections for electron-water vapour scattering. *Chem. Phys. Lett.* **1987**, *136* (3), 363-367. DOI: 10.1016/0009-2614(87)80267-1.

[46] Wagner, W.; Pruß, A. The IAPWS Formulation 1995 for the Thermodynamic Properties of Ordinary Water Substance for General and Scientific Use. *J. Phys. Chem. Ref. Data* **2002**, *31* (2), 387-535. DOI: 10.1063/1.1461829.

[47] Suzuki, Y.-I.; Nishizawa, K.; Kurahashi, N.; Suzuki, T. Effective attenuation length of an electron in liquid water between 10 and 600 eV. *Phys Rev E* **2014**, *90* (1), 010302. DOI: 10.1103/PhysRevE.90.010302.

[48] Thürmer, S.; Seidel, R.; Faubel, M.; Eberhardt, W.; Hemminger, J. C.; Bradforth, S. E.; Winter, B. Photoelectron Angular Distributions from Liquid Water: Effects of Electron Scattering. *Phys. Rev. Lett.* **2013**, *111* (17), 173005. DOI: 10.1103/PhysRevLett.111.173005.

[49] Chan, W. F.; Cooper, G.; Brion, C. E. The electronic spectrum of water in the discrete and continuum regions. Absolute optical oscillator strengths for photoabsorption (6–200 eV). *Chem. Phys.* **1993**, *178* (1), 387-400. DOI: 10.1016/0301-0104(93)85078-M.

[50] Wang, Z.-C.; Yin, B.; Min, Q.; Zhu, L. Temperature-dependence of the near-UV absorption of water vapor in the 290–350nm range. *J. Quant. Spectrosc. Radiat. Transf.* **2022**, *286*, 108204. DOI: 10.1016/j.jqsrt.2022.108204.

[51] Ranjan, S.; Schwieterman, E. W.; Harman, C.; Fateev, A.; Sousa-Silva, C.; Seager, S.; Hu, R. Photochemistry of Anoxic Abiotic Habitable Planet Atmospheres: Impact of New H2O Cross Sections. *Astrophys. J.* **2020**, *896* (2), 148. DOI: 10.3847/1538-4357/ab9363.

[52] Signorell, R.; Winter, B. Photoionization of the aqueous phase: clusters, droplets and liquid jets. *Phys. Chem. Chem. Phys.* **2022**, *24* (22), 13438-13460. DOI: 10.1039/D2CP00164K.

[53] Scholz, M. S.; Fortune, W. G.; Tau, O.; Fielding, H. H. Accurate Vertical Ionization Energy of Water and Retrieval of True Ultraviolet Photoelectron Spectra of Aqueous Solutions. *J. Phys. Chem. Lett.* **2022**, *13* (30), 6889-6895. DOI: 10.1021/acs.jpclett.2c01768.

[54] Yamamoto, Y.-i.; Ishiyama, T.; Morita, A.; Suzuki, T. Exploration of Gas–Liquid Interfaces for Liquid Water and Methanol Using Extreme Ultraviolet

Laser Photoemission Spectroscopy. *J. Phys. Chem. B* **2021**, *125* (37), 10514-10526. DOI: 10.1021/acs.jpcb.1c04765.

[55] Nishitani, J.; Yamamoto, Y.-i.; West, C. W.; Karashima, S.; Suzuki, T. Binding energy of solvated electrons and retrieval of true UV photoelectron spectra of liquids. *Sci. Adv* **2019**, *5* (8), eaaw6896. DOI: 10.1126/sciadv.aaw6896.

[56] Nishitani, J.; West, C. W.; Suzuki, T. Angle-resolved photoemission spectroscopy of liquid water at 29.5 eV. *Struct. Dyn* **2017**, *4* (4), 044014. DOI: 10.1063/1.4979857.

[57] Faubel, M. Early Microjet Experimentation with Liquid Water in Vacuum. *Accts. Chem. Res.* **2023**, *56* (6), 625-630. DOI: 10.1021/acs.accounts.2c00739.

[58] Holstein, W. L.; Hayes, L. J.; Robinson, E. M. C.; Laurence, G. S.; Buntine, M. A. Aspects of Electrokinetic Charging in Liquid Microjets. *J. Phys. Chem. B* **1999**, *103* (15), 3035-3042. DOI: 10.1021/jp984336v.

[59] Nishitani, J.; Karashima, S.; West, C. W.; Suzuki, T. Surface potential of liquid microjet investigated using extreme ultraviolet photoelectron spectroscopy. *J. Chem. Phys.* **2020**, *152* (14). DOI: 10.1063/5.0005930.

[60] Tang, Y.; Suzuki, Y.-i.; Shen, H.; Sekiguchi, K.; Kurahashi, N.; Nishizawa, K.; Zuo, P.; Suzuki, T. Time-resolved photoelectron spectroscopy of bulk liquids at ultra-low kinetic energy. *Chem. Phys. Lett.* **2010**, *494* (1), 111-116. DOI: 10.1016/j.cplett.2010.05.084.

[61] Truong, S. Y.; Yencha, A. J.; Juarez, A. M.; Cavanagh, S. J.; Bolognesi, P.; King, G. C. Threshold photoelectron spectroscopy of H2O and D2O over the photon energy range 12–40eV. *Chem. Phys.* **2009**, *355* (2), 183-193. DOI: 10.1016/j.chemphys.2008.12.009.

[62] Oloff, L. P.; Oura, M.; Rossnagel, K.; Chainani, A.; Matsunami, M.; Eguchi, R.; Kiss, T.; Nakatani, Y.; Yamaguchi, T.; Miyawaki, J.; Taguchi, M.; Yamagami, K.; Togashi, T.; Katayama, T.; Ogawa, K.; Yabashi, M.; Ishikawa, T. Time-resolved HAXPES at SACLA: probe and pump pulse-induced space-charge effects. *New J. Phys.* **2014**, *16* (12), 123045. DOI: 10.1088/1367-2630/16/12/123045.

[63] Faubel, M.; Siefermann, K. R.; Liu, Y.; Abel, B. Ultrafast Soft X-ray Photoelectron Spectroscopy at Liquid Water Microjets. *Accts. Chem. Res.* **2012**, *45* (1), 120-130. DOI: 10.1021/ar200154w.

[64] Link, O.; Lugovoy, E.; Siefermann, K.; Liu, Y.; Faubel, M.; Abel, B. Ultrafast electronic spectroscopy for chemical analysis near liquid water interfaces: concepts and applications. *Appl. Phys. A* **2009**, *96* (1), 117-135. DOI: 10.1007/s00339-009-5179-1.

[65] Elkins, M. H. Dynamics of Electron Relaxation Studied Using Time-Resolved Photoelectron Spectroscopy in Liquid Microjets. Ph.D., University of California, Berkeley, United States -- California, 2015.

[66] Haefer, R. A. Cryogenic vacuum techniques. *J. Phys. E* **1981**, *14* (3), 273. DOI: 10.1088/0022-3735/14/3/002.

[67] *Fundamentals of Vacuum Technology*; Oerlikon Leybold Vacuum, 2016.

[68] Kurahashi, N.; Thürmer, S.; Liu, S. Y.; Yamamoto, Y.-i.; Karashima, S.; Bhattacharya, A.; Ogi, Y.; Horio, T.; Suzuki, T. Design and characterization of a magnetic bottle electron spectrometer for time-resolved extreme UV and X-ray photoemission spectroscopy of liquid microjets. *Struct. Dyn* **2021**, *8* (3). DOI: 10.1063/4.0000107.

[69] Kruit, P.; Read, F. H. Magnetic field paralleliser for 2π electron-spectrometer and electron-image magnifier. *J. Phys. E* **1983**, *16* (4), 313. DOI: 10.1088/0022-3735/16/4/016.

[70] Rijs, A. M.; Backus, E. H. G.; de Lange, C. A.; Westwood, N. P. C.; Janssen, M. H. M. 'Magnetic bottle' spectrometer as a versatile tool for laser photoelectron spectroscopy. *J. Electron Spectrosc. and Rel. Phenom.* **2000**, *112* (1), 151-162. DOI: 10.1016/S0368-2048(00)00209-7.

[71] Saloman, E. B. Energy Levels and Observed Spectral Lines of Xenon, XeI through XeLIV. *J. Phys. Chem. Ref. Data* **2004**, *33* (3), 765-921. DOI: 10.1063/1.1649348.

[72] Brundle, C. R.; Turner, D. W.; Price, W. C. High resolution molecular photoelectron spectroscopy II. Water and deuterium oxide. *Proc. R. Soc. London Ser. A Math. Phys. Sci.* **1968**, *307* (1488), 27-36. DOI: doi:10.1098/rspa.1968.0172.

[73] van Stokkum, I. H. M.; Larsen, D. S.; van Grondelle, R. Global and target analysis of time-resolved spectra. *Biochim. Biophys. Acta Bioenerg.* **2004**, *1657* (2), 82-104. DOI: 10.1016/j.bbabio.2004.04.011.

[74] Hendler, R. W.; Shrager, R. I. Deconvolutions based on singular value decomposition and the pseudoinverse: a guide for beginners. *J. Biochem. Biophys. Methods* **1994**, *28* (1), 1-33. DOI: 10.1016/0165-022X(94)90061-2.

[75] Marciniak, H.; Lochbrunner, S. On the interpretation of decay associated spectra in the presence of time dependent spectral shifts. *Chem. Phys. Lett.* **2014**, *609*, 184-188. DOI: 10.1016/j.cplett.2014.05.006.

Chapter 3 – Nonadiabatic Dynamics Studied by Liquid-Jet Time-Resolved Photoelectron Spectroscopy

The content and figures of this chapter are adapted with permission from:

Z. N. Heim, D. M. Neumark, Nonadiabatic Dynamics Studied by Liquid-Jet Time-Resolved Photoelectron Spectroscopy. *Acc. Chem. Res.*, **55,** 3652 (2022).

3.1 Overview

The development of the liquid microjet technique by Faubel and co-workers has enabled the investigation of high vapor pressure liquids and solutions utilizing high-vacuum methods. One such method is photoelectron spectroscopy (PES), which allows one to probe the electronic properties of a sample through ionization in a state-specific manner. Liquid microjets consisting of pure solvents and solute-solvent systems have been studied with great success utilizing PES and its time-resolved corollary, TRPES. Here we discuss progress made over recent years in understanding the solvation and excited state dynamics of the solvated electron and nucleic acid constituents (NACs) using these methods, as well as the prospect for their future.

The solvated electron is of particular interest in liquid microjet experiments as it represents the simplest solute system. Despite this simplicity, there were still many unresolved questions about its binding energy and excited state relaxation dynamics

that are ideal problems for liquid microjet PES. In the work discussed in this chapter, accurate binding energies were measured for the solvated electron in multiple high vapor pressure solvents. The advantages of liquid jet PES were further highlighted in the femtosecond excited state relaxation studies on the solvated electron in water where a 75 ± 20 fs lifetime attributable to internal conversion from the excited p-state to a hot ground state was measured, supporting a nonadiabatic relaxation mechanism.

Nucleic acid constituents represent a class of important solutes with several unresolved questions that the liquid microjet PES method is uniquely suited to address. As TRPES is capable of tracking dynamics with state-specificity, it is ideal for instances where there are multiple excited states potentially involved in the dynamics. Time-resolved studies of NAC relaxation after excitation using ultraviolet light identified relaxation lifetimes from multiple excited states. The state-specific nature of the TRPES method allowed us to identify the lack of any signal attributable to the nπ* state in thymine derived NACs. The femtosecond time resolution of the technique also aided in identifying differences between the excited state lifetimes of thymidine and thymidine monophosphate. These have been interpreted, aided by molecular dynamics simulations, as an influence of conformational differences leading to a longer excited state lifetime in thymidine monophosphate.

Finally, we discuss advances in tabletop light sources extending into the extreme ultraviolet and soft x-ray regimes that allow expansion of liquid jet TRPES to full valence and potentially core level studies of solutes and pure liquids in liquid microjets. As most solutes have ground state binding energies in the range of 10 eV, observation of both excited state decay and ground state recovery using ultraviolet pump-ultraviolet probe TRPES has been intractable. With high-harmonic generation light sources, it will be possible to not only observe full relaxation pathways for valence level dynamics but to also track dynamics with element specificity by probing core levels of the solute of interest.

3.2 Introduction

The development of vacuum-compatible liquid water microjets, first reported in 1988 [1], has greatly expanded the range of chemical physics experiments that can be performed on water and other volatile solvents. Liquid jets enable one to apply very powerful tools based on photoelectron spectroscopy to properties and dynamics of volatile solvents and the solutes dissolved within. Photoelectron spectroscopy (PES) is a well-established technique in which a sample is ionized, and the resulting electron kinetic energy distribution is measured. It is typically used to determine electron binding energies and the electronic properties of gases and solids, but its application to liquids were restricted to those with exceedingly low vapor pressures[2] owing to the high vacuum requirements of a photoelectron spectrometer. By applying PES to liquid microjets in a vacuum, it has been possible to investigate the electronic properties of pure volatile liquids [3-6] and solutes [7-9]. One photon PES measurements of binding energies have been used to characterize the electronic structure of both pure liquids [6, 10] and solutes [11-13], elucidating shifts in the binding energy in both solutes and individual solvent molecules due to interactions with surrounding solvent. Experiments of this type represent an active frontier in modern physical chemistry; in addition to providing a novel probe of structure and energetics within liquids, they link gas phase studies of isolated molecules and clusters to chemical dynamics in the liquid phase.

A powerful variant of PES used in many areas of chemical dynamics is time-resolved photoelectron spectroscopy (TRPES). TRPES is a pump-probe technique that is capable of following the dynamical evolution of a excited state wavepacket [14]. The overall experimental scheme is as follows:

$$A \xrightarrow{h\nu_{pu}} A^* \xrightarrow{\Delta t, h\nu_{pr}} A^+ + e^- \qquad (3.1)$$

In Scheme 3.1, a femtosecond pump pulse ($h\nu_{pu}$) photoexcites the system of interest (A), which then evolves in time (Dt) before being ionized to a resultant cationic state (A^+) by a femtosecond pulse ($h\nu_{pr}$) that probes the evolution of the excited system (A*). The pump-induced dynamics are encoded in the resulting photoelectron kinetic energy distribution, which is measured as a function of pump-probe delay. TRPES is particularly sensitive to non-adiabatic transitions, since the various electronic states that participate in the dynamics tend to have distinct electron binding energies. With pulses of sufficiently short duration and appropriate wavelengths, TRPES can be used to track the complete relaxation process of a given excited state from initial excitation through any intermediates that are populated en route to the ground state. TRPES has been shown to have significant advantages including high sensitivity

stemming from exceptional intrinsic collection and detection efficiencies [15] and allowing the direct observation of the transient electronic states responsible for driving the ultrafast dynamics of interest [8]. For these reasons, TRPES has for many years been an excellent tool for the study of dynamics in both neutral and anionic gas phase molecules and clusters [14, 16], as well as the photophysics and photochemistry of metal and semiconductor surfaces [17, 18]. With the advent of liquid jet technology, it is now possible to apply TRPES to investigate the dynamics of electronically excited solutes in bulk liquid [19-22], thereby adding a powerful new tool that complements time-resolved techniques such as transient absorption [23-25] and nonlinear spectroscopies [26-28] that have been used to investigate liquids for many years.

While liquid jet TRPES (LJ-TRPES) carries with it advantages intrinsic to the PES technique, there are also limitations one must be cognizant of when interpreting these spectra. For example, experiments and simulations show that the inelastic mean free path of these photoelectrons ranges from 1-3 nm, depending on their kinetic energy [29]. Under these circumstances, one must consider whether photoelectrons are created at the liquid-vacuum interface or within the bulk liquid [30]. In addition, a TRPES experiment is only capable of observing dynamics involving electronic states in which the probe photon energy is sufficient to photoionize/photodetach from a given region of a potential surface [14]. As such, insufficient probe photon energies can lead to a TRPES experiment being blind to certain electronic states relevant to the complete relaxation dynamics of the system and can even artificially shorten the observed lifetimes of electronic states with binding energies that fall outside of the observable range during the relaxation process [31]. This limitation has been a major motivating factor behind extending the probe photon energy range of LJ-TRPES experiments into the XUV using high-harmonic generation.

Applications of TRPES using liquid jets (LJ-TRPES) considered here include the investigation of the solvated electron, a benchmark condensed phase solute, and exploration of the role that the solvent plays in the non-adiabatic relaxation dynamics of nucleic acid constituents (NACs). The ground and excited states of the solvated electron have been well studied in a variety of solvents using electron spin resonance, transient absorption, and PES in an effort to understand both its ground state structure and excited state relaxation dynamics [32]. However, extraction of the p→s internal conversion (IC) lifetime from transient absorption experiments is ambiguous [33, 34], while LJ-TRPES yields a clear IC lifetime that is critical in assessing the mechanism for electronic relaxation of the hydrated electron [20]. The work on NACs in motivated by experiments in the gas phase and in aqueous solution showing that excited state lifetimes after ultraviolet excitation are typically well under 1 ps [35, 36]. As a result, relaxation to the ground state can occur more rapidly than excited state dissociation [36], leading to high photostability of DNA and its constituents. Using a bottom-up approach, LJ-TRPES can in principle map out the complete set of

electronic states that participate in this mechanism and thus complement previous experimental and theoretical work on NAC dynamics. To reach its full potential, however, the probe photon energy used in LJ-TRPES experiments must be extended to be able to ionize the intermediate and ground electronic states that play a role in the overall relaxation mechanism. This consideration motivates the last section of this chapter in which the beamline used to generate femtosecond extreme ultraviolet (XUV) pulses is described.

3.3 Experimental Apparatus

The liquid microjet apparatus used for carrying out the photoelectron spectroscopy studies discussed here has been modified since originally described [37, 38] but at its core remains the same. The design of the liquid microjet is based on the design developed by Wilson [39] and similar to the type pioneered by Faubel [40]. In brief, the microjet is formed by forcing a solution through an approximately 10 mm long segment of fused silica capillary with an inner diameter ranging from 10 to 30 μm at pressures of 40 to 120 atm. These microjet diameters are necessary to collect photoelectrons while minimizing inelastic scattering in the surrounding vapor [6].

The liquid microjet assembly, shown in Fig. 1, is affixed to a three-axis piezoelectric actuator allowing it to be positioned 1 mm above the intersection of the detector and laser axes. After passing through the interaction region, the jet can be frozen in a cryogenically cold vessel at the bottom of the interaction region or captured in a heated copper catcher similar to those implemented by Hummert et al. [21] and Riley et al. [41] The catcher, which is attached to the same mounting apparatus as the jet, is kept approximately 1 cm below the jet and can be translated independent of the jet for alignment purposes. The jet passes through a 500 μm aperture in the catcher, which is kept at 75°C, and flows into a bottle in an ice bath that is evacuated to a few Torr. Catching the liquid as opposed to freezing it has been shown to be advantageous as it mitigates the effects of electrokinetic charging on the photoelectron spectrum [41] in addition to lowering the measured chamber pressure by nearly an order of magnitude.

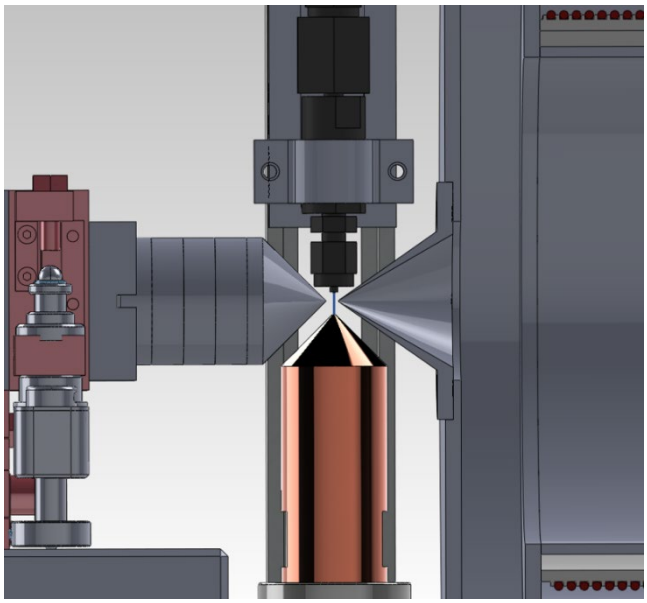

Figure 3.1 – Schematic diagram of the interaction region where the femtosecond pump and probe pulses cross the liquid jet (from above) and subsequent photoelectrons are steered through a skimmer into the differentially pumped MB-TOF detector region (right) by a strong permanent magnet stack (left). Remaining sample is collected in the heated copper catcher (below).

Early work on liquid microjets in the Neumark group [37, 42] utilized ultraviolet light generated by frequency quadrupling or quintupling the output of a nanosecond Nd:YAG laser which could then be used to excite and photoionize solutes of interest within the duration of a single ~35 ns duration laser pulse. More recent explicitly time-resolved iterations of the experiment [20, 22, 38, 43, 44] have utilized femtosecond pulses from a Ti:Sapphire oscillator/amplifier, the output of which can then be frequency doubled, tripled, and quadrupled or directed into an optical parametric amplifier to obtain ultraviolet pump and probe pulses with energies as high as 6.20 eV. To achieve even higher probe photon energies, we have built a beamline employing high-harmonic generation to selectively generate 21.7 eV photons (see Section 3.3). The femtosecond pulses are delayed relative to one another and then cross the liquid microjet, emitting photoelectrons. The photoelectrons are collected and energy-analyzed using a magnetic bottle time-of-flight spectrometer and microchannel plate detector [45].

3.4 Results and Discussion

3.4.1 Ultrafast Dynamics of Solvated Electrons

The solvated electron was the first system to be extensively studied by LJ-TRPES experiments. This species is of fundamental interest in solution chemistry, as a reducing agent in organic chemistry, a product in the radiolysis of water, and in the attachment to and subsequent damage of DNA [46]. Its dynamics after photoexcitation have been investigated with an impressive array of experimental [32] and theoretical [47] methods. From the perspective of gas phase chemistry, water cluster anions $(H_2O)_n^-$ have been studied using one-photon [48] and time-resolved PES [46], electronic spectroscopy [49, 50], and vibrational spectroscopy [51, 52], with one goal being to understand the relationship of these finite systems to the bulk hydrated electron. LJ-TRPES experiments offer a unique and explicit link between the cluster and aqueous phase environments of an excess electron in water. The primary focus of these experiments has been to determine the vertical detachment energy of the hydrated electron and to probe its relaxation dynamics after photoexcitation.

In solution, solvated electrons can be readily generated from a variety of simple solutes such as iodide or ferrocyanide upon UV excitation of charge-transfer-to-solvent (CTTS) transitions [53], adding to the simplicity of these studies. Initial LJ-PES investigations by Siefermann et al. [54], Tang et al. [55], Lübcke et al. [56], and Shreve et al. [37] yielded values ranging from 3.3-3.6 eV for the binding energy of the bulk solvated electron, in good agreement with the values extrapolated from measurements of internally solvated electrons in water cluster anion studies [46, 48]. These initial LJ-PES measurements of the solvated electron binding energy remain in good agreement with recent measurements yielding a value of 3.7 ± 0.1 eV that include corrections for factors such as energy dependent scattering cross sections [30]. These corrections, while not applied to the work presented in this chapter, are becoming increasingly important in LJ-PES studies for accurate determination of electron binding energies where increasingly wider ranges of probe energies can be applied to the same system. Recent investigations of the solvated electron with probe energies ranging from 3.6 to 13.6 eV have highlighted both the accuracy these corrections, retrieving the same 3.7 eV vertical binding energy from a data set with uncorrected vertical binding energies ranging from 3.3 to 4.5 eV [30].

Further studies on solvated electrons have demonstrated the utility of LJ-TRPES to elucidate the time-resolved dynamics of these species. In aqueous solution, the solvated electron can be excited to a manifold of p-states through excitation in the near-infrared and has been shown through optical spectroscopy to relax back to the

ground s-state with three time constants ranging from 50 fs to 1 ps [34, 57]. The interpretation of these time constants in terms of the overall relaxation mechanism has been ambiguous. Two mechanisms have been invoked, the nonadiabatic and adiabatic mechanisms [47]. These can in principle be distinguished by measuring the time constant for p→s internal conversion, which is on the order of 50 fs in the nonadiabatic model and 400 fs in the adiabatic model. In size-selected water cluster anions, TRPES was used to measure this IC lifetime; the extrapolation of these lifetimes to the bulk limit yielded a value of ~60 fs, strongly favoring the nonadiabatic model for relaxation [46]. However, given the uncertainty in how electrons bind to finite water clusters and how the electron binding motif affects the excited state lifetime [58], it seemed prudent to carry out TRPES in bulk water.

Using LJ-TRPES, experiments have been carried out as shown schematically in Figure 3.2 [20]. Solvated electrons are generated from CTTS excitation of iodide at 240 nm after which an 800 nm pump pulse excites solvated electrons to the p-state and subsequent dynamics are tracked by a 267 nm probe pulse and can be assigned unambiguously based on their respective binding energies. These experiments have also been used to observe the initial thermalization and recombination of electrons initially generated by the CTTS excitation prior to excitation [38]. In Figure 3.2, signal at a binding energy of 2.2 ± 0.2 eV is assigned to the p-state and relaxes with a time constant of 75 ± 20 fs [20]. This excited state population transfers to a region nearly 1 eV higher in binding energy, assigned to hot ground state signal, which then thermalizes with τ = 410 ± 40 fs. This study solidifies the nonadiabatic mechanistic picture of solvated electron relaxation as it directly observes the p-state relaxation, resolving differing interpretations of TA experiments. A subsequent investigation by Karashima et al. [59] using time- and angle-resolved photoemission from a liquid microjet showed that the first component of the relaxation process, with a lifetime of 60 fs, was associated with anisotropic photoemission while the second component and ground state corresponded to isotropic photoemission. The evolving angular distribution reflects the change in orbital symmetry going from the excited p-state manifold to the ground s-state, supporting the assignment of the fast component in the excited state relaxation mechanism to a nonadiabatic transition from the excited state to a hot ground state. These results motivated similar LJ-TRPES experiments carried out on the solvated electron in D_2O [43] and methanol [38], with resulting measurements of the internal conversion lifetime and solvent isotope effect also consistent with a nonadiabatic mechanism.

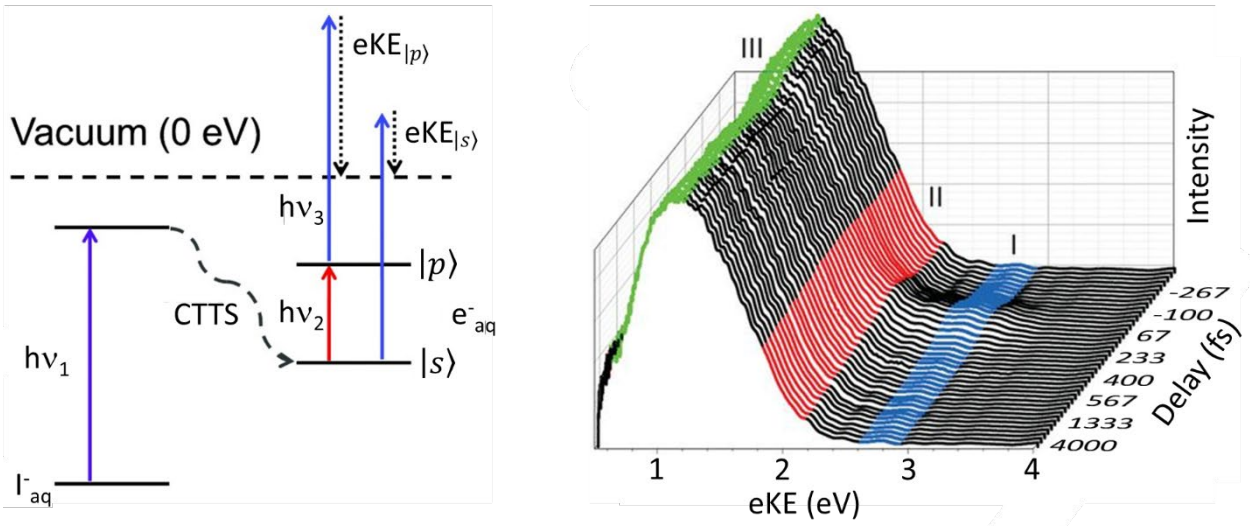

Figure 3.2 – Left: Energy level diagram showing the states relevant to three pulse experiments in which solvated electrons are generated by CTTS excitation ($h\nu_1$) and the p-state relaxation dynamics are studied using an 800 nm pump ($h\nu_2$) and a 267 nm probe ($h\nu_3$). Right: LJ-TRPES spectra showing excited state relaxation of the solvated electron after 800 nm irradiation. Reprinted in part and adapted from [20]. Copyright 2013 American Association for the Advancement of Science.

3.4.2 Ultrafast Excited State Dynamics in NACs

Nucleic acid constituents (NACs) have been studied widely [36] owing to their importance in biology as well as their complex photochemistry. NACs absorb light in the UV-C region with large absorption bands near 270 nm and 200 nm attributed to ππ* transitions [60]. These wavelengths are typically destructive as the energy imparted on the molecule is on the order of typical bond dissociation energies [35]. Despite this, NACs have a remarkable photostability owing to ultrafast relaxation that efficiently funnels the excess electronic energy from the excited state into vibrational energy on the ground electronic surface, which can then be dissipated to the surrounding medium [36, 61]. The underlying mechanism has been studied in solution using transient absorption (TA) and fluorescence upconversion (FU) [35, 36, 61]. TRPES has been applied to this problem in both gas phase [31, 62-64] and liquid jet [22, 44, 65-67] experiments using UV pump and probe pulses. As was the case for hydrated electrons, a comparison of TRPES experiments in the gas phase and aqueous solution offers a unique opportunity to carry out complementary experiments of the same system in two very different environments.

The relaxation dynamics of NACs rely heavily on the relative position of the various possible excited states that could be involved [68], most notably the lowest energy $^1\pi\pi^*$, $^1n\pi^*$, and $^3\pi\pi^*$ states, shown schematically in Figure 3.3 for aqueous thymine.

In the gas phase, excitation in the 270 nm band of isolated NACs populates the $^1\pi\pi^*$ state, which is energetically above both the $^1n\pi^*$ and $^3\pi\pi^*$ states, allowing for population of these states as the molecule undergoes relaxation. In aqueous solution, this $^1\pi\pi^*$ state is stabilized relative to the nearby $^1n\pi^*$ state, as illustrated in Fig. 3, putting it at comparable if not lower energy [65]. The $^3\pi\pi^*$ state would also be stabilized in a comparable fashion. The relaxation pathways possible involving these states involve passage through a conical intersection (CI) from the $S_1(^1\pi\pi^*)$ state to the ground state, internal conversion to the $^1n\pi^*$ state, or intersystem crossing (ISC) to the $^3\pi\pi^*$ state shown in Figure 3.3.

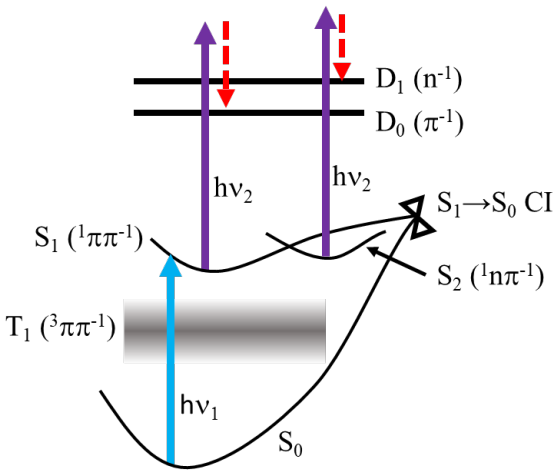

Figure 3.3 – Schematic representation of the relevant electronic states involved of aqueous T, Thd, and TMP related to the relaxation dynamics after UV excitation.

In solution, TA experiments indicate notably different relaxation mechanisms for thymine and adenine derived NACs. In adenine, the relaxation was shown to involve only direct internal conversion through a CI from the S_1 excited state to the ground electronic state with no evidence of any contributions from intermediate excited states [69]. In thymine-derived NACs, TA experiments found a delay for ground state recovery that was attributed to intermediate excited states involved in the relaxation dynamics from the initially populated $^1\pi\pi^*$ state [70, 71]. Early studies attributed this delay to a long-lived intermediate $^1n\pi^*$ state through which stepwise IC to the ground state occurred [70]. This assignment has been called into question by more recent TA studies, in which time-resolved UV/Vis and IR spectroscopy experiments of thymine and TMP were performed [71]. In the gas phase, TRPES experiments were carried out to observe the relaxation dynamics of isolated nucleobases [64, 72, 73]. These studies show adenine and pyrimidine bases both have rapid transfer of population out of the initially populated $^1\pi\pi^*$ state within <100 fs to an intermediate electronic state [64, 72]. Later work was done employing a higher energy probe capable of capturing a more complete picture of the relaxation process, as earlier studies lacked sufficient probe energy to observe dynamics beyond ~1 ps. That study

showed that the $^3\pi\pi^*$ state was populated from the $^1n\pi^*$ state in isolated thymine with a rise time of approximately 3.5 ps [73]. These observations of rapid transfer of population to the $^1n\pi^*$ state in gas phase TRPES experiments and the possible involvement of excited states other the $^1\pi\pi^*$ state in solution serve as motivation to perform comparable TRPES experiments in aqueous solution.

Initial experiments using liquid microjet TRPES to study NACs were performed by Buchner et al, who observed femtosecond relaxation lifetimes of adenine, adenosine [67], thymine, thymidine [65], and guanosine [66] using a tunable UV (238 to 248 nm) and 267 nm pump-probe scheme. For adenosine and adenine, they presented the first direct observation of the evolution of excited NACs along a potential surface using femtosecond TRPES. This work not only determined the lifetimes of the solvated NACs, but also tracked the average kinetic energy of electrons from the excited state as a function of time to infer dynamics of the population on the excited state surface itself. These studies were then extended in our laboratory using a pump-probe scheme utilizing similar tunable UV pump pulses and 200 nm rather than 267 nm probe pulses [22, 44, 65, 67]. This scheme extended the maximum probe energy by 1 eV in an effort to observe as much of the dynamics as possible, as relaxation along the excited state surface or population of a lower-lying intermediate state could increase the ionization energy of the evolving system beyond the lower probe photon energy. We applied this pump probe scheme to adenosine (Ado), thymine (T), and thymidine (Thd) in addition to adenosine monophosphate (AMP) and thymidine monophosphate (TMP). Extending the LJ-TRPES studies to include the nucleotides AMP and TMP was important to further the bottom-up approach to understanding the dynamics in macromolecular DNA after radiation absorption. Key results are as follows.

3.4.2.1 Relaxation from the $S_1(^1\pi\pi^*)$ Excited State

Figure 3.4 shows LJ-TRPES results for T and TMP at pump and probe energies of 4.74 and 6.20 eV, respectively. As discussed above, the relaxation dynamics from the $S_1(^1\pi\pi^*)$ state in aqueous T, Thd, and TMP have been hotly debated, with uncertainty surrounding the involvement of the lowest lying $^1n\pi^*$state in the relaxation from an initially prepared $^1\pi\pi^*$ state absorbing at ~260 nm [36]. LJ-TRPES studies of T, Thd, and TMP find lifetimes for the $S_1 \rightarrow S_0$ relaxation in T and Thd at 4.74 eV pump energy to be 360 fs and 390 fs respectively, in excellent agreement with previous LJ-TRPES experiments and slightly shorter than but comparable to TA and FU experiments. The corresponding lifetime in TMP is considerably longer, 870 fs, as can be seen by comparing Figs. 4a and 4b. Moreover, no excited state signal is observed beyond 4 ps, as shown in Figure 3.4(c) for T, even with the 6.2 eV probe energies employed. This observation adds further evidence that the $^1n\pi^*$ state has no significant involvement in the relaxation dynamics of aqueous T, Thd, and TMP. This state has been observed in the gas-phase with a lifetime of ~10 ps and has a measured vertical

ionization energy of 6.5 eV [73]. Given these values, one could expect signal from the $^1n\pi^*$ state to appear with ~1 eV eKE given solvent stabilization of the resulting cationic state after photoionization. Lacking any persistent signal in this spectral region, the involvement of the $^1n\pi^*$ in the solution phase relaxation dynamics of thymine compounds is highly unlikely. Instead, it is possible the persistent signal seen in TA experiments is attributable to the $^3\pi\pi^*$ state, as predictions for the binding energy of this state lie anywhere from 0.6 eV above to 0.6 eV below the probe energy available in this experiment which would at best be near the lower detection limit of the detector used.

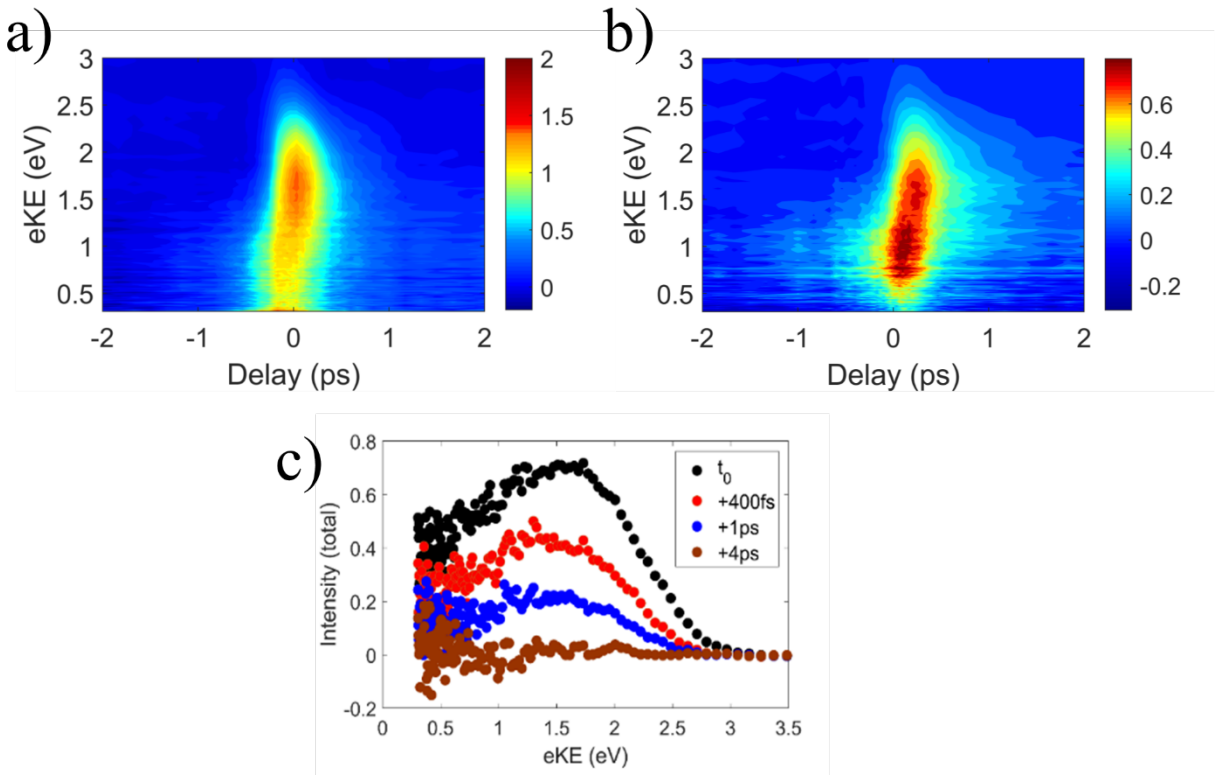

Figure 3.4 – TRPE spectra of (a) thymine and (b) TMP showing 5.17 eV pump/6.20 eV probe data at positive delays. (c) Static spectra at given delays for thymine show no identifiable signal past 4 ps. Reproduced in part from [22]. Copyright 2019 American Chemical Society.

In LJ-TRPES experiments of aqueous Ado and AMP using the same TUV pump to excite to the $S_1(^1\pi\pi^*)$ state, monoexponential excited state lifetimes on the order of 220 fs to 250 fs were found [44], in general agreement with previous work [67]. Photoelectron spectra showed no delay dependent energy shifting of the excited state population, emphasizing the rapid timescales on which these dynamics occur. In addition, the $S_1 \rightarrow S_0$ lifetimes observed at the highest TUV pump energy of 4.97 eV was essentially identical to the lifetime observed when exciting at 4.69 eV, in contrast

to previous work where the lifetime at 4.66 eV pump and 5.0 eV probe energies is approximately double the retrieved lifetime with those pump and probe energies switched [44, 67]. The difference in probe energy here is key; the previous study used a 4.66 eV probe while this work used a 6.2 eV probe. The additional 1.54 eV probe energy allowed observation of the full excited state wavepacket and retrieval of an accurate lifetime not artificially shortened by excited state population relaxing to a portion of the excited state surface that could not be readily ionized at 4.66 eV.

3.4.2.2 Differences in Nucleotide Relaxation Lifetimes

Our experiments on TMP show that the lifetime of the $S_1(^1\pi\pi^*)$ state is nearly double that of T and Thd. While this trend had been observed previously in TA and FU experiments, no explanation for the substantial increase in lifetime had been proposed. To this end, molecular dynamics simulations were performed, finding the dominant conformation of aqueous Thd to be the syn-conformer whereas the dominant TMP conformation was the anti-conformer, shown in 1(a) and 2(b) of Figure 3.5, respectively [22]. These conformational differences are important since the conical intersections responsible for the rapid relaxation to the ground state involve distortions of the pyrimidine ring. The effects of these ground state conformational differences on the dynamics of the photoexcited species are currently under theoretical investigation.

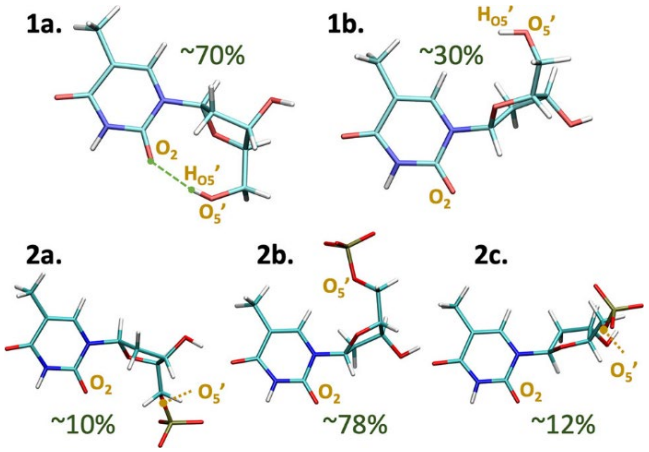

Figure 3.5 – Main conformers of Thd (1a and 1b) and TMP (2a, 2b, and 2c) determined by percentage occupation in a MM trajectory calculation. Reproduced from [22]. Copyright 2019 American Chemical Society.

3.5 Future Prospects of Using Femtosecond XUV Probes

TRPES is capable, in principle, of tracking the complete relaxation pathway of a photoexcited system from the initially excited electronic state down to its ground state. The extent to which one can do this is determined by the probe photon energy and the type of system under study. In negative ion TRPES experiments, electron affinities are typically 5 eV or less. Hence, ground state negative ions can be photodetached by readily accessible UV femtosecond laser pulses generated by standard nonlinear optical methods. TRPES using femtosecond probe pulses at 7.9 eV produced by four-wave mixing has also recently been reported [74]. However, the ionization potentials of neutral molecules in the gas phase and in solution can be 10 eV or higher. Hence, the ability to generate femtosecond probe pulses in the extreme ultraviolet (XUV) region of the electromagnetic spectrum will significantly enhance the dynamical range of TRPES, as has been demonstrated in gas phase experiments using both table-top laser systems [75, 76] and free electron lasers [73, 77, 78].

Advances in optical physics have brought about the high-harmonic generation (HHG) technique, in which high energy harmonics of a driving laser field can be generated by focusing the intense laser field into a diffuse gaseous medium [79]. These harmonics can be generated on a tabletop setup such as that shown in Figure 3.6 utilizing the same types of lasers typically used in TRPES experiments, so HHG is well suited for overcoming the aforementioned probe energy limitations, as was first demonstrated by Leone and co-workers on gas phase Br_2 [75]. HHG sources for PES require relatively narrowband femtosecond pulses with energy resolution of the order of 10s to 100s of meV so as to minimize the width of photoelectron energy distributions from a given electronic state [80]. To this effect, XUV beamlines employing HHG yielding discrete harmonics and either multilayer mirrors or time-compensating extreme ultraviolet (XUV) monochromators [21, 81-83] have been built. These afford temporal durations of XUV pulses on the order of 10s of femtoseconds while bandwidth in the range of 200-500 meV is attainable. Various implementations of this approach have yielded femtosecond high-harmonic sources with isolated harmonics ranging from 7 eV [83] to 100 eV [84].

LJ-TRPES using XUV probe pulses presents its own special challenges. Most notably, any time-resolved dynamics resulting from photoexcitation and photoionization of solute molecules competes with very strong signals from one-photon ionization of water, for which the vertical ionization energy is 11.33 eV [85]. Nonetheless, several such experiments have already been performed, ranging from fundamental processes in pure liquids to solute dynamics in systems such as the solvated electron [8], organic chromophores [21, 86], and organometallic complexes [87]. These studies of increasingly complex molecules illustrate the trend towards

larger systems that can be effectively studied by the LJ-TRPES method given the advances in light sources and detector technology.

An additional challenge in implementing XUV probe pulses is that of probe depth considerations, as these relate directly to whether electrons detected in these LJ-PES experiments carry information about the dynamics of solute molecules solvated in bulk solution or at the vacuum-water interface. Detailed simulations have been performed to determine the degree to which inelastic and elastic scattering impact probe depth. These simulations show that for a photoelectron emitted with 35 eV kinetic energy, near the minimum inelastic mean free path for electrons in liquid water [29], approximately half of the ejected photoelectrons originate deeper than 3 water monolayers inside the liquid jets and could be considered bulk [30]. Given these results, it can be assumed most LJ-TRPES experiments can indeed probe bulk solute dynamics with minimal influence from signal originating from the vacuum-liquid interface, though choosing to probe solutions at this minimum would yield signals heavily influenced by the interface and could be exploited to selectively study solutes at the interface. Using HHG to generate discrete harmonics in the XUV allows for studying dynamics at varying probe depths simply by selecting a different harmonic, allowing both the refinement of energy dependent scattering corrections by improving measurements of energy dependent scattering cross sections and preferentially probe bulk and interfacial dynamics.

The setup in our laboratory to carry out XUV TRPES on liquid jets is shown in Figure 3.6. Here, 400 nm light is used to generate harmonics in a semi-infinite gas cell [88]. Driving harmonics with 400 nm affords both a wide harmonic spacing of 6.2 eV and has the advantage of higher HHG conversion efficiencies, as the efficiency scales with driving laser wavelength as approximately λ^{-5}- λ^{-6}, though this also reduces the highest attainable photon energies [89, 90]. Harmonic generation parameters in the semi-infinite gas cell, highlighted in Fig 3.6(d), are optimized to maximize flux in the 7th harmonic of 400 nm (21.7 eV) and minimize contributions from higher energy harmonics. The 7th harmonic is isolated using a multilayer mirror developed by the Center for X-ray Optics at Lawrence Berkeley National Laboratory designed to suppress the 5th and 9th harmonics while efficiently reflecting the 7th harmonic at a 45 angle of incidence as shown in Fig 6(h). This selection is done in conjunction with an oxidized aluminum foil that both blocks the driving laser light and suppresses the 5th harmonic at 15.5 eV. This design maximizes harmonic flux at the liquid jet by minimizing the optics necessary to select and refocus a single harmonic, with only 3 optics in the harmonic beamline prior to pump-probe recombination using an annular mirror shown in Fig 6(i).

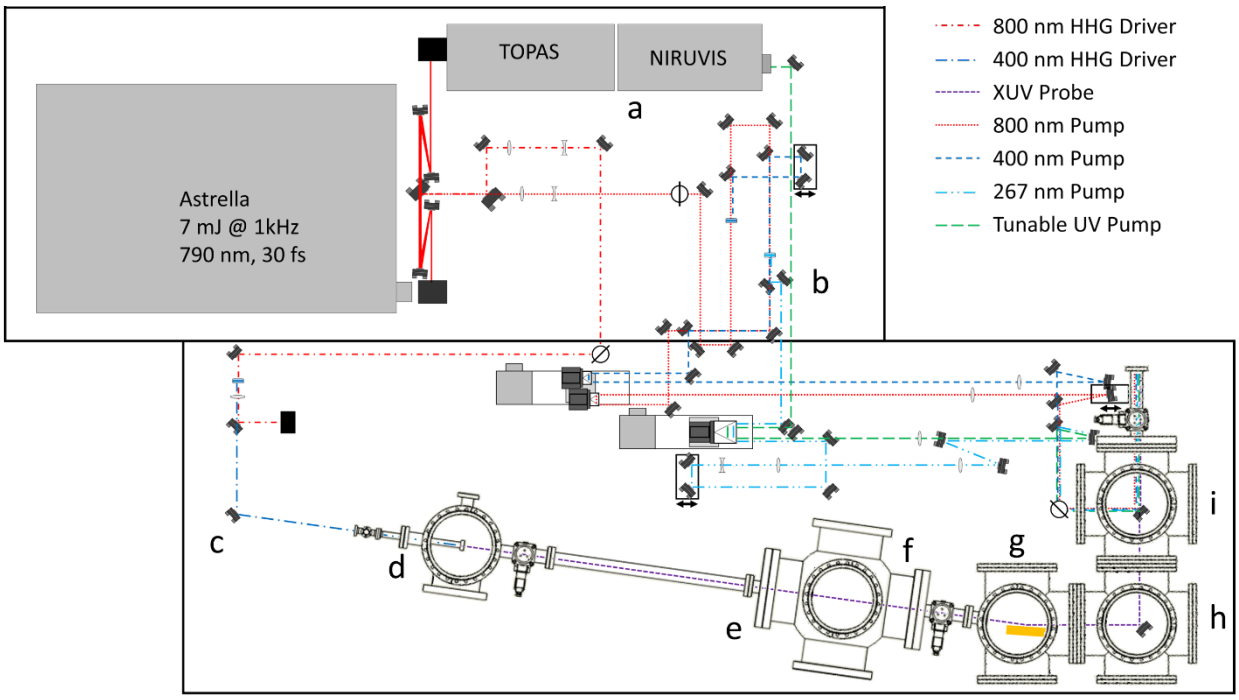

Figure 3.6 – Optical layout used to generate pump and probe pulses in our XUV LJ-TRPES project. The layout consists of a) an OPA, b) a BBO-based third harmonic generation setup, and c) a HHG beamline consisting of d) a semi-infinite gas cell, e) a 200 nm thick Al filter, f) a beam analyzer for spectral characterization, g) a toroidal mirror, h) a multilayer mirror, and i) an annular mirror.

Initial experiments will focus on using probe pulses at 21.7 eV to perform valence ionization of photoexcited neutral and ionic solutes. In the near future, we plan to extend our photon energy range into the soft x-ray regimes in order to take advantage of the elemental specificity offered by core-level PES in liquids [11].

3.6 Concluding Remarks

In this chapter, the ultrafast dynamics of the solvated electron as well as thymine- and adenine-derived nucleic acid constituents as studied by liquid jet time-resolved photoelectron spectroscopy are summarized. These experiments, aimed at developing a greater understanding of the role solvent plays in relaxation dynamics, form the basis for insight into the initial dynamics relevant to DNA damage both indirectly by free electrons in solution and by direct absorption of ultraviolet light. The generation and relaxation of the solvated electron was investigated in H_2O, D_2O, and MeOH. In these studies, it was shown that an initially excited charge-transfer-to-solvent transition readily generates free electrons that persist for nanoseconds. When these

electrons are photoexcited, p→s internal conversion occurs on a ~100 fs timescale in all three solvents. This timescale is consistent with the so-called nonadiabatic relaxation mechanism for solvated electrons. Additionally, experiments interrogating the relaxation dynamics of thymine- and adenine-derived NACs from the $S_1(^1\pi\pi^*)$ state allowed measurement and comparison of lifetimes associated with these states across the different NACs. The thymine- and adenine-derived NACs both show no evidence for intermediate states in relaxation from the $S_1(^1\pi\pi^*)$ state. The thymine NAC studies revealed a substantially longer lifetime for the S_1 excited state in TMP compared to T and Thd; the source of this discrepancy was attributed to conformational changes from Thd to TMP that could impact the excited state relaxation pathway. Finally, new tabletop XUV light sources will enable carrying out LJ-TRPES experiments on a much wider variety of solutes and afford access to more information in an experiment through ionization of all valence states of a solute.

3.7 References

[1] Faubel, M.; Schlemmer, S.; Toennies, J. P. A molecular beam study of the evaporation of water from a liquid jet. *Z. Phys. D: At., Mol. Clusters* **1988**, *10*, 269-277. DOI: 10.1007/BF01384861.

[2] Siegbahn, H. Electron spectroscopy for chemical analysis of liquids and solutions. *J. Phys. Chem.* **1985**, *89* (6), 897-909. DOI: 10.1021/j100252a005.

[3] Yamamoto, Y.-i.; Ishiyama, T.; Morita, A.; Suzuki, T. Exploration of Gas–Liquid Interfaces for Liquid Water and Methanol Using Extreme Ultraviolet Laser Photoemission Spectroscopy. *J. Phys. Chem. B* **2021**, *125* (37), 10514-10526. DOI: 10.1021/acs.jpcb.1c04765.

[4] Longetti, L.; Randulová, M.; Ojeda, J.; Mewes, L.; Miseikis, L.; Grilj, J.; Sanchez-Gonzalez, A.; Witting, T.; Siegel, T.; Diveki, Z.; van Mourik, F.; Chapman, R.; Cacho, C.; Yap, S.; Tisch, J. W. G.; Springate, E.; Marangos, J. P.; Slavíček, P.; Arrell, C. A.; Chergui, M. Photoemission from non-polar aromatic molecules in the gas and liquid phase. *Phys. Chem. Chem. Phys.* **2020**, *22* (7), 3965-3974, 10.1039/C9CP06799J. DOI: 10.1039/C9CP06799J.

[5] Nishitani, J.; West, C. W.; Suzuki, T. Angle-resolved photoemission spectroscopy of liquid water at 29.5 eV. *Struct. Dyn* **2017**, *4* (4), 044014. DOI: 10.1063/1.4979857.

[6] Faubel, M.; Steiner, B.; Toennies, J. P. Photoelectron Spectroscopy of Liquid Water, some Alcohols, and Pure Nonane in Free Micro Jets. *J. Chem. Phys.* **1997**, *106* (22), 9013-9031. DOI: 10.1063/1.474034.

[7] Buttersack, T.; Mason, P. E.; McMullen, R. S.; Schewe, H. C.; Martinek, T.; Brezina, K.; Crhan, M.; Gomez, A.; Hein, D.; Wartner, G.; Seidel, R.; Ali, H.;

Thürmer, S.; Marsalek, O.; Winter, B.; Bradforth, S. E.; Jungwirth, P. Photoelectron spectra of alkali metal-ammonia microjets: From blue electrolyte to bronze metal. *Science* **2020**, *368* (6495), 1086-1091. DOI: 10.1126/science.aaz7607.

[8] Nishitani, J.; Yamamoto, Y.-i.; West, C. W.; Karashima, S.; Suzuki, T. Binding energy of solvated electrons and retrieval of true UV photoelectron spectra of liquids. *Sci. Adv* **2019**, *5* (8), eaaw6896. DOI: 10.1126/sciadv.aaw6896.

[9] Tau, O.; Henley, A.; Boichenko, A. N.; Kleshchina, N. N.; Riley, R.; Wang, B.; Winning, D.; Lewin, R.; Parkin, I. P.; Ward, J. M.; Hailes, H. C.; Bochenkova, A. V.; Fielding, H. H. Liquid-microjet photoelectron spectroscopy of the green fluorescent protein chromophore. *Nat. Commun* **2022**, *13* (1), 507. DOI: 10.1038/s41467-022-28155-5.

[10] Schewe, H. C.; Brezina, K.; Kostal, V.; Mason, P. E.; Buttersack, T.; Stemer, D. M.; Seidel, R.; Quevedo, W.; Trinter, F.; Winter, B.; Jungwirth, P. Photoelectron Spectroscopy of Benzene in the Liquid Phase and Dissolved in Liquid Ammonia. *J. Phys. Chem. B* **2022**, *126* (1), 229-238. DOI: 10.1021/acs.jpcb.1c08172.

[11] Winter, B.; Weber, R.; Hertel, I. V.; Faubel, M.; Jungwirth, P.; Brown, E. C.; Bradforth, S. E. Electron binding energies of aqueous alkali and halide ions: EUV photoelectron spectroscopy of liquid solutions and combined ab initio and molecular dynamics calculations. *J. Am. Chem. Soc.* **2005**, *127* (19), 7203-7214. DOI: 10.1021/ja042908l.

[12] Winter, B.; Faubel, M. Photoemission from Liquid Aqueous Solutions. *Chem. Rev.* **2006**, *106* (4), 1176-1211. DOI: 10.1021/cr040381p.

[13] Seidel, R.; Thürmer, S.; Winter, B. Photoelectron Spectroscopy Meets Aqueous Solution: Studies from a Vacuum Liquid Microjet. *J. Phys. Chem. Lett.* **2011**, *2* (6), 633-641. DOI: 10.1021/jz101636y.

[14] Stolow, A.; Bragg, A. E.; Neumark, D. M. Femtosecond Time-Resolved Photoelectron Spectroscopy. *Chem. Rev.* **2004**, *104* (4), 1719-1758. DOI: 10.1021/cr020683w.

[15] Buchner, F.; Schultz, T.; Lübcke, A. Solvated electrons at the water-air interface: Surface versus bulk signal in low kinetic energy photoelectron spectroscopy. *Phys. Chem. Chem. Phys.* **2012**, *14* (16), 58375842. DOI: 10.1039/C2CP23305C.

[16] Fielding, H. H.; Worth, G. A. Using time-resolved photoelectron spectroscopy to unravel the electronic relaxation dynamics of photoexcited molecules. *Chem. Soc. Rev.* **2018**, *47* (2), 309-321. DOI: 10.1039/C7CS00627F.

[17] Siefermann, K. R.; Pemmaraju, C. D.; Neppl, S.; Shavorskiy, A.; Cordones, A. A.; Vura-Weis, J.; Slaughter, D. S.; Sturm, F. P.; Weise, F.; Bluhm, H.; Strader, M. L.; Cho, H.; Lin, M.-F.; Bacellar, C.; Khurmi, C.; Guo, J.; Coslovich, G.;

Robinson, J. S.; Kaindl, R. A.; Schoenlein, R. W.; Belkacem, A.; Neumark, D. M.; Leone, S. R.; Nordlund, D.; Ogasawara, H.; Krupin, O.; Turner, J. J.; Schlotter, W. F.; Holmes, M. R.; Messerschmidt, M.; Minitti, M. P.; Gul, S.; Zhang, J. Z.; Huse, N.; Prendergast, D.; Gessner, O. Atomic-Scale Perspective of Ultrafast Charge Transfer at a Dye–Semiconductor Interface. *J. Phys. Chem. Lett.* **2014**, *5* (15), 2753-2759. DOI: 10.1021/jz501264x.

[18] Neppl, S.; Gessner, O. Time-resolved X-ray photoelectron spectroscopy techniques for the study of interfacial charge dynamics. *J. Electron Spectrosc. and Rel. Phenom.* **2015**, *200*, 64-77. DOI: 10.1016/j.elspec.2015.03.002.

[19] Buchner, F.; Lübcke, A.; Heine, N.; Schultz, T. Time-resolved photoelectron spectroscopy of liquids. *Rev. Sci. Instrum.* **2010**, *81* (11), 113107. DOI: 10.1063/1.3499240.

[20] Elkins, M. H.; Williams, H. L.; Shreve, A. T.; Neumark, D. M. Relaxation Mechanism of the Hydrated Electron. *Science* **2013**, *342* (6165), 1496-1499. DOI: 10.1126/science.1246291.

[21] Hummert, J.; Reitsma, G.; Mayer, N.; Ikonnikov, E.; Eckstein, M.; Kornilov, O. Femtosecond Extreme Ultraviolet Photoelectron Spectroscopy of Organic Molecules in Aqueous Solution. *J. Phys. Chem. Lett.* **2018**, *9* (22), 6649-6655. DOI: 10.1021/acs.jpclett.8b02937.

[22] Erickson, B. A.; Heim, Z. N.; Pieri, E.; Liu, E.; Martinez, T. J.; Neumark, D. M. Relaxation Dynamics of Hydrated Thymine, Thymidine, and Thymidine Monophosphate Probed by Liquid Jet Time-Resolved Photoelectron Spectroscopy. *J. Phys. Chem. A* **2019**, *123* (50), 10676-10684. DOI: 10.1021/acs.jpca.9b08258.

[23] Kumpulainen, T.; Lang, B.; Rosspeintner, A.; Vauthey, E. Ultrafast Elementary Photochemical Processes of Organic Molecules in Liquid Solution. *Chem. Rev.* **2017**, *117* (16), 10826-10939. DOI: 10.1021/acs.chemrev.6b00491.

[24] Berera, R.; van Grondelle, R.; Kennis, J. T. M. Ultrafast transient absorption spectroscopy: principles and application to photosynthetic systems. *Photosynthesis Research* **2009**, *101* (2), 105-118. DOI: 10.1007/s11120-009-9454-y.

[25] Kovalenko, S. A.; Schanz, R.; Hennig, H.; Ernsting, N. P. Cooling dynamics of an optically excited molecular probe in solution from femtosecond broadband transient absorption spectroscopy. *J. Chem. Phys.* **2001**, *115* (7), 3256-3273. DOI: 10.1063/1.1380696 (acccessed 2022/08/29).

[26] Auböck, G.; Consani, C.; van Mourik, F.; Chergui, M. Ultrabroadband femtosecond two-dimensional ultraviolet transient absorption. *Opt. Lett.* **2012**, *37* (12), 2337-2339. DOI: 10.1364/OL.37.002337.

[27] Khalil, M.; Demirdöven, N.; Tokmakoff, A. Coherent 2D IR Spectroscopy: Molecular Structure and Dynamics in Solution. *J. Phys. Chem. A* **2003**, *107* (27), 5258-5279. DOI: 10.1021/jp0219247.

[28] Hybl, J. D.; Ferro, A. A.; Jonas, D. M. Two-dimensional Fourier transform electronic spectroscopy. *J. Chem. Phys.* **2001**, *115* (14), 6606-6622. DOI: 10.1063/1.1398579.

[29] Seidel, R.; Winter, B.; Bradforth, S. E. Valence Electronic Structure of Aqueous Solutions: Insights from Photoelectron Spectroscopy. *Annu. Rev. Phys. Chem.* **2016**, *67* (1), 283-305. DOI: 10.1146/annurev-physchem-040513-103715.

[30] Luckhaus, D.; Yamamoto, Y.-i.; Suzuki, T.; Signorell, R. Genuine binding energy of the hydrated electron. *Sci. Adv* **2017**, *3* (4), e1603224. DOI: 10.1126/sciadv.1603224.

[31] Hudock, H. R.; Levine, B. G.; Thompson, A. L.; Satzger, H.; Townsend, D.; Gador, N.; Ullrich, S.; Stolow, A.; Martínez, T. J. Ab Initio Molecular Dynamics and Time-Resolved Photoelectron Spectroscopy of Electronically Excited Uracil and Thymine. *J. Phys. Chem. A* **2007**, *111* (34), 8500-8508. DOI: 10.1021/jp0723665.

[32] Herbert, J. M.; Coons, M. P. The Hydrated Electron. *Annu. Rev. Phys. Chem.* **2017**, *68* (1), 447-472. DOI: 10.1146/annurev-physchem-052516-050816.

[33] Yokoyama, K.; Silva, C.; Son, D. H.; Walhout, P. K.; Barbara, P. F. Detailed Investigation of the Femtosecond Pump−Probe Spectroscopy of the Hydrated Electron. *J. Phys. Chem. A* **1998**, *102* (35), 6957-6966. DOI: 10.1021/jp981809p.

[34] Pshenichnikov, M. S.; Baltuška, A.; Wiersma, D. A. Hydrated-electron population dynamics. *Chem. Phys. Lett.* **2004**, *389* (1), 171-175. DOI: 10.1016/j.cplett.2004.03.107.

[35] Schreier, W. J.; Gilch, P.; Zinth, W. Early Events of DNA Photodamage. *Annu. Rev. Phys. Chem.* **2015**, *66* (1), 497-519. DOI: 10.1146/annurev-physchem-040214-121821.

[36] Middleton, C. T.; Harpe, K. d. L.; Su, C.; Law, Y. K.; Crespo-Hernández, C. E.; Kohler, B. DNA Excited-State Dynamics: From Single Bases to the Double Helix. *Annu. Rev. Phys. Chem.* **2009**, *60* (1), 217-239. DOI: 10.1146/annurev.physchem.59.032607.093719.

[37] Shreve, A. T.; Yen, T. A.; Neumark, D. M. Photoelectron spectroscopy of hydrated electrons. *Chem. Phys. Lett.* **2010**, *493* (4), 216-219. DOI: 10.1016/j.cplett.2010.05.059.

[38] Elkins, M. H.; Williams, H. L.; Neumark, D. M. Dynamics of electron solvation in methanol: Excited state relaxation and generation by charge-transfer-to-solvent. *J. Chem. Phys.* **2015**, *142* (23), 234501. DOI: 10.1063/1.4922441 (acccessed 2022/06/16).

[39] Wilson, K. R.; Rude, B. S.; Smith, J.; Cappa, C.; Co, D. T.; Schaller, R. D.; Larsson, M.; Catalano, T.; Saykally, R. J. Investigation of volatile liquid surfaces by synchrotron x-ray spectroscopy of liquid microjets. *Rev. Sci. Instrum.* **2004**, *75* (3), 725-736. DOI: 10.1063/1.1645656.

[40] Faubel, M.; Steiner, B.; Toennies, J. P. Measurement of He I photoelectron spectra of liquid water, formamide and ethylene glycol in fast-flowing microjets. *J. Electron Spectrosc. Relat. Phenom.* **1998**, *95* (2-3), 159-169. DOI: 10.1016/S0368-2048(98)00208-4.

[41] Riley, J. W.; Wang, B.; Parkes, M. A.; Fielding, H. H. Design and characterization of a recirculating liquid-microjet photoelectron spectrometer for multiphoton ultraviolet photoelectron spectroscopy. *Rev. Sci. Instrum.* **2019**, *90* (8), 083104. DOI: 10.1063/1.5099040.

[42] Shreve, A. T.; Elkins, M. H.; Neumark, D. M. Photoelectron spectroscopy of solvated electrons in alcohol and acetonitrile microjets. *Chem. Sci.* **2013**, *4* (4), 1633-1639. DOI: 10.1039/C3SC22063J.

[43] Elkins, M. H.; Williams, H. L.; Neumark, D. M. Isotope effect on hydrated electron relaxation dynamics studied with time-resolved liquid jet photoelectron spectroscopy. *J. Chem. Phys.* **2016**, *144* (18), 184503. DOI: 10.1063/1.4948546.

[44] Williams, H. L.; Erickson, B. A.; Neumark, D. M. Time-resolved photoelectron spectroscopy of adenosine and adenosine monophosphate photodeactivation dynamics in water microjets. *J. Chem. Phys.* **2018**, *148* (19), 194303. DOI: 10.1063/1.5027258.

[45] Kruit, P.; Read, F. H. Magnetic Field Paralleliser for 2PI Electron-Spectrometer and Electron-Image Magnifier. *J. Phys. E: Sci. Instrum.* **1983**, *16* (4), 313-324.

[46] Young, R. M.; Neumark, D. M. Dynamics of Solvated Electrons in Clusters. *Chem. Rev.* **2012**, *112* (11), 5553-5577. DOI: 10.1021/cr300042h.

[47] Turi, L.; Rossky, P. J. Theoretical Studies of Spectroscopy and Dynamics of Hydrated Electrons. *Chem. Rev.* **2012**, *112* (11), 5641-5674. DOI: 10.1021/cr300144z.

[48] Coe, J. V.; Lee, G. H.; Eaton, J. G.; Arnold, S. T.; Sarkas, H. W.; Bowen, K. H.; Ludewigt, C.; Haberland, H.; Worsnop, D. R. Photoelectron spectroscopy of hydrated electron cluster anions, (H2O)−n=2–69. *J. Chem. Phys.* **1990**, *92* (6), 3980-3982. DOI: 10.1063/1.457805.

[49] Ayotte, P.; Johnson, M. A. Electronic absorption spectra of size-selected hydrated electron clusters: (H2O)n−, n=6–50. *J. Chem. Phys.* **1997**, *106* (2), 811-814. DOI: 10.1063/1.473167.

[50] Herburger, A.; Barwa, E.; Ončák, M.; Heller, J.; van der Linde, C.; Neumark, D. M.; Beyer, M. K. Probing the Structural Evolution of the Hydrated Electron in Water Cluster Anions (H2O)n–, n ≤ 200, by Electronic Absorption Spectroscopy. *J. Am. Chem. Soc.* **2019**, *141* (45), 18000-18003. DOI: 10.1021/jacs.9b10347.

[51] Hammer, N. I.; Shin, J.-W.; Headrick, J. M.; Diken, E. G.; Roscioli, J. R.; Weddle, G. H.; Johnson, M. A. How Do Small Water Clusters Bind an Excess Electron? *Science* **2004**, *306* (5696), 675-679. DOI: 10.1126/science.1102792.

[52] Asmis, K. R.; Santambrogio, G.; Zhou, J.; Garand, E.; Headrick, J.; Goebbert, D.; Johnson, M. A.; Neumark, D. M. Vibrational spectroscopy of hydrated electron clusters(H2O)15–50− via infrared multiple photon dissociation. *J. Chem. Phys.* **2007**, *126* (19), 191105. DOI: 10.1063/1.2741508.

[53] Hart, E. J.; Boag, J. W. Absorption Spectrum of the Hydrated Electron in Water and in Aqueous Solutions. *J. Am. Chem. Soc.* **1962**, *84* (21), 4090-4095. DOI: 10.1021/ja00880a025.

[54] Siefermann, K. R.; Liu, Y.; Lugovoy, E.; Link, O.; Faubel, M.; Buck, U.; Winter, B.; Abel, B. Binding energies, lifetimes and implications of bulk and interface solvated electrons in water. *Nature Chem.* **2010**, *2*, 274-279. DOI: 10.1038/nchem.580.

[55] Tang, Y.; Suzuki, Y.-i.; Shen, H.; Sekiguchi, K.; Kurahashi, N.; Nishizawa, K.; Zuo, P.; Suzuki, T. Time-resolved photoelectron spectroscopy of bulk liquids at ultra-low kinetic energy. *Chem. Phys. Lett.* **2010**, *494* (1), 111-116. DOI: 10.1016/j.cplett.2010.05.084.

[56] Lübcke, A.; Buchner, F.; Heine, N.; Hertel, I. V.; Schultz, T. Time-resolved photoelectron spectroscopy of solvated electrons in aqueous NaI solution. *Phys. Chem. Chem. Phys.* **2010**, *12*, 14629. DOI: 10.1039/C0CP00847H.

[57] Assel, M.; Laenen, R.; Laubereau, A. Femtosecond solvation dynamics of solvated electrons in neat water. *Chem. Phys. Lett.* **2000**, *317* (1), 13-22. DOI: 10.1016/S0009-2614(99)01369-X.

[58] Borgis, D.; Rossky, P. J.; Turi, L. Electronic Excited State Lifetimes of Anionic Water Clusters: Dependence on Charge Solvation Motif. *J Phys Chem Lett* **2017**, *8* (10), 2304-2309. DOI: 10.1021/acs.jpclett.7b00555.

[59] Karashima, S.; Yamamoto, Y.-i.; Suzuki, T. Resolving Nonadiabatic Dynamics of Hydrated Electrons Using Ultrafast Photoemission Anisotropy. *Phys. Rev. Lett.* **2016**, *116* (13), 137601. DOI: 10.1103/PhysRevLett.116.137601.

[60] Voet, D.; Gratzer, W. B.; Cox, R. A.; Doty, P. Absorption spectra of nucleotides, polynucleotides, and nucleic acids in the far ultraviolet. *Biopolymers* **1963**, *1* (3), 193-208. DOI: 10.1002/bip.360010302.

[61] Pecourt, J.-M. L.; Peon, J.; Kohler, B. DNA Excited-State Dynamics: Ultrafast Internal Conversion and Vibrational Cooling in a Series of Nucleosides. *J. Am. Chem. Soc.* **2001**, *123* (42), 10370-10378. DOI: 10.1021/ja0161453.

[62] Evans, N. L.; Ullrich, S. Wavelength Dependence of Electronic Relaxation in Isolated Adenine Using UV Femtosecond Time-Resolved Photoelectron Spectroscopy. *J. Phys. Chem. A* **2010**, *114* (42), 11225-11230. DOI: 10.1021/jp1029097.

[63] Satzger, H.; Townsend, D.; Zgierski, M. Z.; Patchkovskii, S.; Ullrich, S.; Stolow, A. Primary processes underlying the photostability of isolated DNA bases: Adenine. *PNAS* **2006**, *103* (27), 10196-10201. DOI: 10.1073/pnas.0602663103.

[64] Ullrich, S.; Schultz, T.; Zgierski, M. Z.; Stolow, A. Electronic relaxation dynamics in DNA and RNA bases studied by time-resolved photoelectron spectroscopy. *Phys. Chem. Chem. Phys.* **2004**, *6* (10), 2796-2801, 10.1039/B316324E. DOI: 10.1039/B316324E.

[65] Buchner, F.; Nakayama, A.; Yamazaki, S.; Ritze, H. H.; Lübcke, A. Excited-State Relaxation of Hydrated Thymine and Thymidine Measured by Liquid-Jet Photoelectron Spectroscopy: Experiment and Simulation. *J. Am. Chem. Soc.* **2015**, *137* (8), 2931-2938. DOI: 10.1021/ja511108u.

[66] Buchner, F.; Heggen, B.; Ritze, H.-H.; Thiel, W.; Lübcke, A. Excited-state dynamics of guanosine in aqueous solution revealed by time-resolved photoelectron spectroscopy: Experiment and theory. *Phys. Chem. Chem. Phys.* **2015**, *17* (47), 31978-31987. DOI: 10.1039/C5CP04394H.

[67] Buchner, F.; Ritze, H. H.; Lahl, J.; Lübcke, A. Time-resolved Photoelectron Spectroscopy of Adenine and Adenosine in Aqueous Solution. *Phys. Chem. Chem. Phys.* **2013**, *15* (27), 11402-11408. DOI: 10.1039/C3CP51057C.

[68] Improta, R.; Santoro, F.; Blancafort, L. Quantum Mechanical Studies on the Photophysics and the Photochemistry of Nucleic Acids and Nucleobases. *Chem. Rev.* **2016**, *116* (6), 3540-3593. DOI: 10.1021/acs.chemrev.5b00444.

[69] Cohen, B.; Hare, P. M.; Kohler, B. Ultrafast Excited-State Dynamics of Adenine and Monomethylated Adenines in Solution: Implications for the Nonradiative Decay Mechanism. *J. Am. Chem. Soc.* **2003**, *125* (44), 13594-13601. DOI: 10.1021/ja035628z.

[70] Hare, P. M.; Crespo-Hernández, C. E.; Kohler, B. Internal conversion to the electronic ground state occurs via two distinct pathways for pyrimidine bases in aqueous solution. *PNAS* **2007**, *104* (2), 435-440. DOI: 10.1073/pnas.0608055104.

[71] Pilles, B. M.; Maerz, B.; Chen, J.; Bucher, D. B.; Gilch, P.; Kohler, B.; Zinth, W.; Fingerhut, B. P.; Schreier, W. J. Decay Pathways of Thymine Revisited. *J. Phys. Chem. A* **2018**, *122* (21), 4819-4828. DOI: 10.1021/acs.jpca.8b02050.

[72] Canuel, C.; Mons, M.; Piuzzi, F.; Tardivel, B.; Dimicoli, I.; Elhanine, M. Excited states dynamics of DNA and RNA bases: Characterization of a stepwise deactivation pathway in the gas phase. *J. Chem. Phys.* **2005**, *122* (7), 074316. DOI: 10.1063/1.1850469 (acccessed 2022/07/13).

[73] Wolf, T. J. A.; Parrish, R. M.; Myhre, R. H.; Martínez, T. J.; Koch, H.; Gühr, M. Observation of Ultrafast Intersystem Crossing in Thymine by Extreme Ultraviolet Time-Resolved Photoelectron Spectroscopy. *J. Phys. Chem. A* **2019**, *123* (32), 6897-6903. DOI: 10.1021/acs.jpca.9b05573.

[74] Liu, Y.; Chakraborty, P.; Matsika, S.; Weinacht, T. Excited state dynamics of cis,cis-1,3-cyclooctadiene: UV pump VUV probe time-resolved photoelectron spectroscopy. *J. Chem. Phys.* **2020**, *153* (7), 074301. DOI: 10.1063/5.0006920.

[75] Nugent-Glandorf, L.; Scheer, M.; Samuels, D. A.; Mulhisen, A. M.; Grant, E. R.; Yang, X. M.; Bierbaum, V. M.; Leone, S. R. Ultrafast time-resolved soft x-ray photoelectron spectroscopy of dissociating Br_2. *Phys. Rev. Lett.* **2001**, *87* (19), 193002.

[76] Warne, E. M.; Downes-Ward, B.; Woodhouse, J.; Parkes, M. A.; Springate, E.; Pearcy, P. A. J.; Zhang, Y.; Karras, G.; Wyatt, A. S.; Chapman, R. T.; Minns, R. S. Photodissociation dynamics of methyl iodide probed using femtosecond extreme ultraviolet photoelectron spectroscopy. *Phys. Chem. Chem. Phys.* **2020**, *22* (44), 25695-25703. DOI: 10.1039/D0CP03478A.

[77] Braußе, F.; Goldsztejn, G.; Amini, K.; Boll, R.; Bari, S.; Bomme, C.; Brouard, M.; Burt, M.; de Miranda, B. C.; Düsterer, S.; Erk, B.; Géléoc, M.; Geneaux, R.; Gentleman, A. S.; Guillemin, R.; Ismail, I.; Johnsson, P.; Journel, L.; Kierspel, T.; Köckert, H.; Küpper, J.; Lablanquie, P.; Lahl, J.; Lee, J. W. L.; Mackenzie, S. R.; Maclot, S.; Manschwetus, B.; Mereshchenko, A. S.; Mullins, T.; Olshin, P. K.; Palaudoux, J.; Patchkovskii, S.; Penent, F.; Piancastelli, M. N.; Rompotis, D.; Ruchon, T.; Rudenko, A.; Savelyev, E.; Schirmel, N.; Techert, S.; Travnikova, O.; Trippel, S.; Underwood, J. G.; Vallance, C.; Wiese, J.; Simon, M.; Holland, D. M. P.; Marchenko, T.; Rouzée, A.; Rolles, D. Time-resolved inner-shell photoelectron spectroscopy: From a bound molecule to an isolated atom. *Phys. Rev. A* **2018**, *97* (4), 043429. DOI: 10.1103/PhysRevA.97.043429.

[78] Mayer, D.; Lever, F.; Picconi, D.; Metje, J.; Alisauskas, S.; Calegari, F.; Düsterer, S.; Ehlert, C.; Feifel, R.; Niebuhr, M.; Manschwetus, B.; Kuhlmann, M.; Mazza, T.; Robinson, M. S.; Squibb, R. J.; Trabattoni, A.; Wallner, M.; Saalfrank, P.; Wolf, T. J. A.; Gühr, M. Following excited-state chemical shifts in molecular ultrafast x-ray photoelectron spectroscopy. *Nat. Commun* **2022**, *13* (1), 198. DOI: 10.1038/s41467-021-27908-y.

[79] Corkum, P. B. Plasma perspective on strong field multiphoton ionization. *Phys. Rev. Lett.* **1993**, *71* (13), 1994-1997. DOI: 10.1103/PhysRevLett.71.1994.

[80] Schuurman, M. S.; Blanchet, V. Time-resolved photoelectron spectroscopy: the continuing evolution of a mature technique. *Phys. Chem. Chem. Phys.* **2022**, *24* (34), 20012-20024. DOI: 10.1039/D1CP05885A.

[81] Poletto, L.; Frassetto, F. Time-preserving grating monochromators for ultrafast extreme-ultraviolet pulses. *Appl. Opt.* **2010**, *49* (28), 5465-5473. DOI: 10.1364/AO.49.005465.

[82] Ojeda, J.; Arrell, C. A.; Longetti, L.; Chergui, M.; Helbing, J. Charge-transfer and Impulsive Electronic-to-vibrational Energy Conversion in Ferricyanide: Ultrafast Photoelectron and Transient Infrared Studies. *Phys. Chem. Chem. Phys.* **2017**, *19* (26), 17052-17062. DOI: 10.1039/C7CP03337K.

[83] Ban, L.; Yoder, B. L.; Signorell, R. Size-Resolved Electron Solvation in Neutral Water Clusters. *J. Phys. Chem. A* **2021**, *125* (24), 5326-5334. DOI: 10.1021/acs.jpca.1c03631.

[84] Ojeda, J.; Arrell, C. A.; Grilj, J.; Frassetto, F.; Mewes, L.; Zhang, H.; Mourik, F. v.; Poletto, L.; Chergui, M. Harmonium: A pulse preserving source of monochromatic extreme ultraviolet (30–110 eV) radiation for ultrafast photoelectron spectroscopy of liquids. *Struct. Dyn* **2016**, *3* (2), 023602. DOI: 10.1063/1.4933008.

[85] Thurmer, S.; Malerz, S.; Trinter, F.; Hergenhahn, U.; Lee, C.; Neumark, D. M.; Meijer, G.; Winter, B.; Wilkinson, I. Accurate vertical ionization energy and work function determinations of liquid water and aqueous solutions. *Chem. Sci.* **2021**, *12* (31), 10558-10582. DOI: 10.1039/d1sc01908b.

[86] West, C. W.; Nishitani, J.; Higashimura, C.; Suzuki, T. Extreme ultraviolet time-resolved photoelectron spectroscopy of aqueous aniline solution: enhanced surface concentration and pump-induced space charge effect. *Mol. Phys.* **2021**, *119* (1-2), e1748240. DOI: 10.1080/00268976.2020.1748240.

[87] Longetti, L.; Barillot, T. R.; Puppin, M.; Ojeda, J.; Poletto, L.; van Mourik, F.; Arrell, C. A.; Chergui, M. Ultrafast photoelectron spectroscopy of photoexcited aqueous ferrioxalate. *Phys. Chem. Chem. Phys.* **2021**, *23* (44), 25308-25316, 10.1039/D1CP02872C. DOI: 10.1039/D1CP02872C.

[88] Sutherland, J. R.; Christensen, E. L.; Powers, N. D.; Rhynard, S. E.; Painter, J. C.; Peatross, J. High harmonic generation in a semi-infinite gas cell. *Opt. Express* **2004**, *12* (19), 4430-4436. DOI: 10.1364/OPEX.12.004430.

[89] Falcão-Filho, E. L.; Gkortsas, V. M.; Gordon, A.; Kärtner, F. X. Analytic scaling analysis of high harmonic generation conversion efficiency. *Opt. Express* **2009**, *17* (13), 11217-11229. DOI: 10.1364/OE.17.011217.

[90] Harth, A.; Guo, C.; Cheng, Y.-C.; Losquin, A.; Miranda, M.; Mikaelsson, S.; Heyl, C. M.; Prochnow, O.; Ahrens, J.; Morgner, U.; L'Huillier, A.; Arnold, C.

L. Compact 200 kHz HHG source driven by a few-cycle OPCPA. *Journal of Optics* **2017**, *20* (1), 014007. DOI: 10.1088/2040-8986/aa9b04.

Chapter 4 – Implementation and Initial TRPES Results Using an XUV Probe

4.1 Overview

The XUV beamline described in Chapter 2 has been used as the probe for studying a wide variety of systems presented in this dissertation, both gaseous and solvated, using photoelectron spectroscopy. The XUV generated in the experiment has been characterized using multiple methods to measure the total flux, harmonic linewidth, total spectral composition, and spatial characteristics of the XUV probe employed in the following experiments.

The XUV probe has been used to measure the photoelectron spectra of several noble gases and water vapor. These spectra are crucial in the calibration, characterization, and troubleshooting of the XUV probe. Typically, argon gas is used to optimize the flux and alignment of the XUV beamline while water vapor is used for in situ fine-tuning of flux and alignment when between scans of liquid samples.

Pump – probe and LAPE scans have been taken at pump wavelengths of 800 nm, 400 nm, and 267 nm on gaseous systems including argon, xenon, H_2O vapor, and methyl iodide. Both pump – probe and LAPE signals in argon and xenon have been observed using both an XUV probe and through two-color multiphoton ionization. These systems have served as a useful tool for characterizing the spatiotemporal properties of the pump and probe pulses as well as a proof-of-concept for the collection of photoelectron spectra using an XUV probe.

Similarly, the XUV probe alone has been used to collect photoelectron spectra of solvated systems including neat water, aqueous iodide, the chromophore metanil yellow, the organometallic complex hexacyanoferrate, and the nucleosides uridine, thymidine, and adenosine. Due to the complicated nature of collecting time-resolved spectra, only LAPE spectra of neat water and pump – probe spectra of the nucleobases thymine and adenine, and the nucleosides uridine, thymidine, and adenosine have been collected. Preliminary time-resolved results for these systems are presented in this chapter.

4.2 Characterizing the XUV Probe

The fundamental characteristics of the XUV probe generated in this experiment are determined by employing a series of methods including using an XUV photodiode, a diffractive imaging spectrometer, and of course the photoelectron spectrometer itself. Initial measurements of XUV light were taken using the photoelectron spectrometer due to the high efficiency of detecting charged particles, though poor alignment meant the first reliable measurements were taken using the calibrated XUV photodiode and the beam analyzer. The results of characterization of the XUV probe using these various methods that have not already been discussed in Chapter 2 are presented here.

4.2.1 Photoelectron Spectra Collected to Characterize Harmonics

Due to the sensitivity of detectors for charged particles, using the magnetic bottle photoelectron spectrometer to characterize the harmonics generated as they pertained to the experiment was the most convenient and sensitive method for determining the total harmonic spectrum at the interaction region. Naturally, this method is limited by the photon energy-dependent beamline transmission so a true representation of the harmonics produced in the SIGC is not attainable but this limitation is negligible for the purposes of optimization.

We first generated harmonics using an 800 nm pulsed driving field on the order of 1-2 W continuous power in an argon gas medium. The harmonics generated were used to ionize an effusive jet of argon gas. Argon is a convenient target as it has an ionization energy of 15.76 eV [1] and a spin-orbit splitting in the cation between the $^2P^\circ_{3/2}$ and $^2P^\circ_{1/2}$ levels of 0.18 eV [2]. This spin-orbit splitting is smaller than the bandwidth of the XUV harmonics used to ionize the argon, so only a single peak with energetic width approximately equivalent to the energetic width of the harmonic is

observed.[A] An initial harmonic spectrum is shown in Figure 4.1. These harmonics were generated using 1.75 W of 800 nm for the driving field.

Use of a 400 nm pulsed driving field is advantageous as it increases the spacing between harmonics from 3.1 eV to 6.2 eV, facilitating the isolation of a single harmonic for photoelectron spectroscopy. This also had the advantage of reducing the cutoff energy such that only the 5^{th}, 7^{th}, 9^{th}, and occasionally 11^{th} harmonics of the 400 nm pulsed driving field were generated, simplifying isolation of a single harmonic considerably. Fortuitously, we found that the distribution of harmonics in the harmonic spectrum observed was such that the 7^{th} harmonic made up more than 90% of the total harmonic flux measured by using the photoelectron spectrometer. The spectra resulting from ionization of either argon or xenon using harmonics generated using a 400 nm pulsed driving field are shown in Figure 4.2. In the spectra of xenon photoionization, the 5^{th} harmonic is visible whereas it isn't in the argon spectra as the ionization energy of xenon is 12.13 eV [3]. Additionally, the spin-orbit splitting of the $^2P^\circ_{3/2}$ and $^2P^\circ_{1/2}$ levels Xe^+ is 1.31 eV [4], making it readily resolvable with the energetic width of the harmonics generated as shown in Figure 4.2.

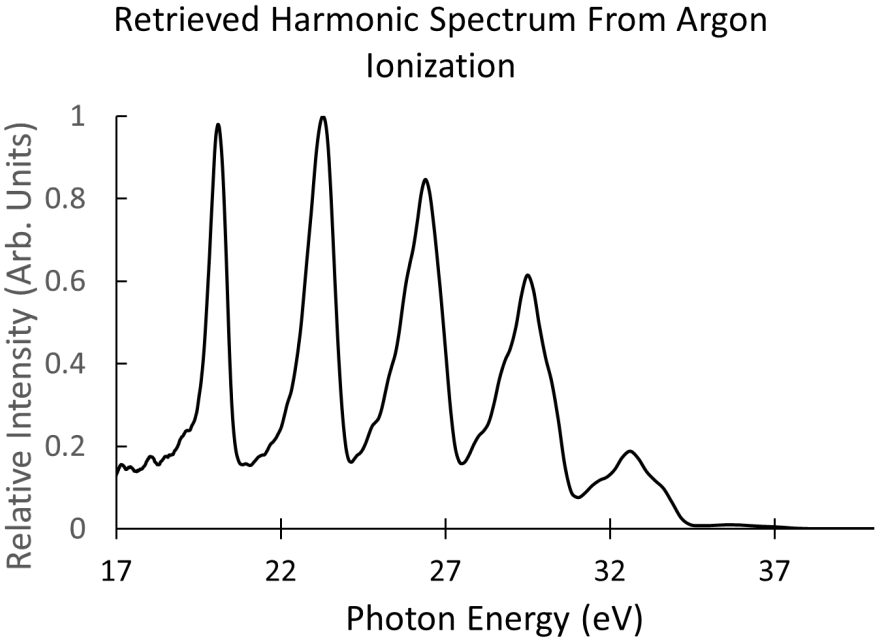

Figure 4.1 – Harmonic spectrum generated using 800 nm. The harmonic spectrum in photon energy is retrieved from measuring the eKE spectrum and adding the binding energy of argon, 15.76 eV, to the eKE values to arrive at the photon energy.

[A] This does not take into account the energy resolution of the ToF spectrometer, which scales as $eKE^{3/2}$.

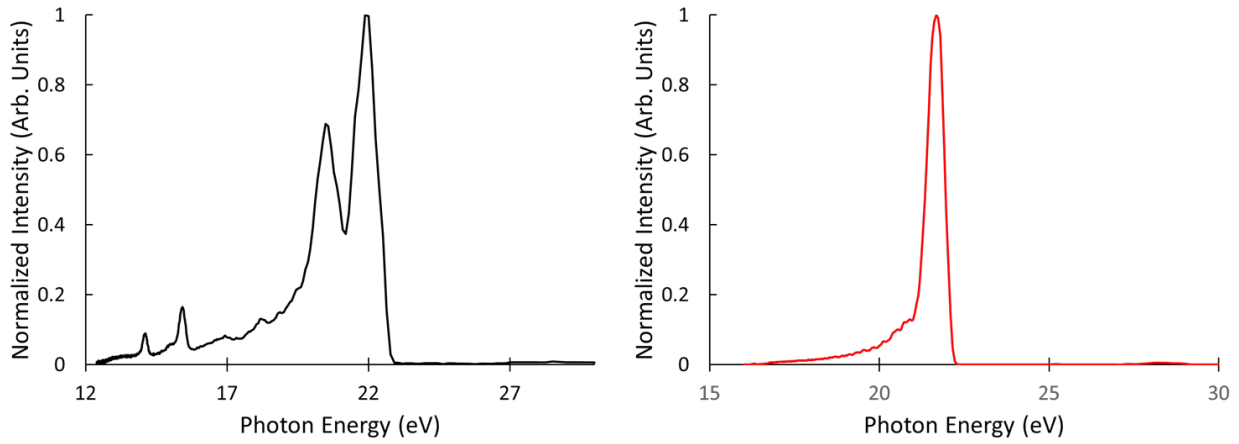

Figure 4.2 – 400 nm harmonic spectrum retrieved from ionization of (left) xenon and (right) argon gas.

The spectra in Figure 4.2 were taken without any specific means of harmonic selection employed in the beamline. To spectrally isolate the 7th harmonic, a multilayer mirror is employed to preferentially reflect the 7th harmonic while minimizing reflectance of the 5th and 9th harmonics as discussed in Chapter 2. Additionally, a tin filter can be employed to further isolate the 7th harmonic. Photoelectron spectra of argon gas in these various configurations are given in Figure 4.5. The 7th harmonic has an intensity approximately 4-5 orders of magnitude greater than that of the 9th harmonic (the primary source of interference in a given experiment) when both the multilayer mirror and tin filter are employed. From this, it is clear the 7th harmonic is properly isolated, as has been shown earlier in Figure 2.7. The FWHM of the isolated harmonic under conditions where space-charge broadening is negligible has been measured to be 350 ± 20 meV, in reasonable agreement with the 250 meV value determined using the nanograting spectrometer.

4.2.2 Spatial Characterization

With the introduction of motorized mirror mounts for aligning both the XUV and the annular mirror, the spatial dimensions and overlap of the pump and probe in the interaction region can be determined. The size of the pump focus is first measured by placing a camera at the interaction point in the sample chamber with the chamber open to atmosphere. A typical image of the pump focus with scale determined by pixel dimension for reference is shown in Figure 4.3. This also serves as a means by which the number of actuations of the piezoelectric motors controlling the pointing of each optic. This mapping has been determined to be 100 turns = 130 μm for the current placement of the annular mirror.

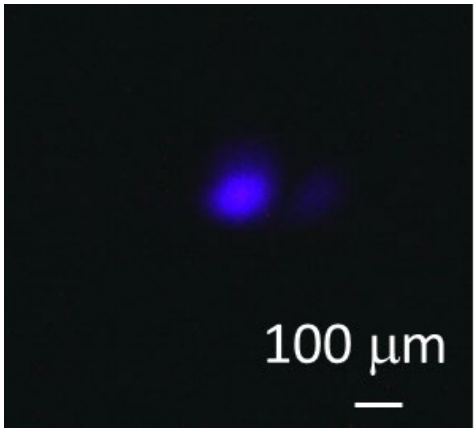

Figure 4.3 – An image taken of the 400 nm pump beam using a CMOS camera sensor with scale for reference.

With the size of the pump beam known, the size of the pump-probe overlap can be determined by a linear pump-probe process such as LAPE. Given both beam profiles are gaussian, the pump-probe overlap will be gaussian and described by a convolution of the pump and probe gaussians. The convolution of two gaussians is shown in Equations 4.1 and 4.2.

$$f_{pump} = \frac{1}{\sigma_{pump}\sqrt{2\pi}} e^{-\frac{(x-\mu_{pump})^2}{2\,\sigma_{pump}^2}}, \; g_{probe} = \frac{1}{\sigma_{probe}\sqrt{2\pi}} e^{-\frac{(x-\mu_{probe})^2}{2\,\sigma_{probe}^2}} \tag{4.1}$$

$$A_{conv} = f_{pump} * g_{probe} = \frac{1}{\sqrt{2\pi\left(\sigma_{pump}^2+\sigma_{probe}^2\right)}} e^{-\frac{\left(x-\left(\mu_{pump}+\mu_{probe}\right)\right)^2}{2\left(\sigma_{probe}^2+\sigma_{probe}^2\right)}} \tag{4.2}$$

Here, f_{pump} is the gaussian describing the pump laser profile in one dimension with mean μ_{pump} and standard deviation σ_{pump}, and g_{probe} is the gaussian describing the probe laser profile in one dimension with mean μ_{probe} and standard deviation σ_{probe}. The convolution of these gaussians, A_{conv}, is a gaussian with mean $\mu_{pump} + \mu_{probe}$ and standard deviation $\sqrt{\left(\sigma_{pump}^2 + \sigma_{probe}^2\right)}$, also referred to as the cross correlation. When μ_{pump} and σ_{pump} are known and with μ_{probe} set to 0, the size of the probe beam σ_{probe} can be determined. A typical scan in both horizontal and vertical axes is shown in Figure 4.4. From these scans, horizontal and vertical FWHM[B] of the convolution are 150 µm and 167 µm, respectively.

[B] Note that $FWHM = 2\sqrt{2\ln(2)}\,\sigma = 2.355\sigma$ for a gaussian.

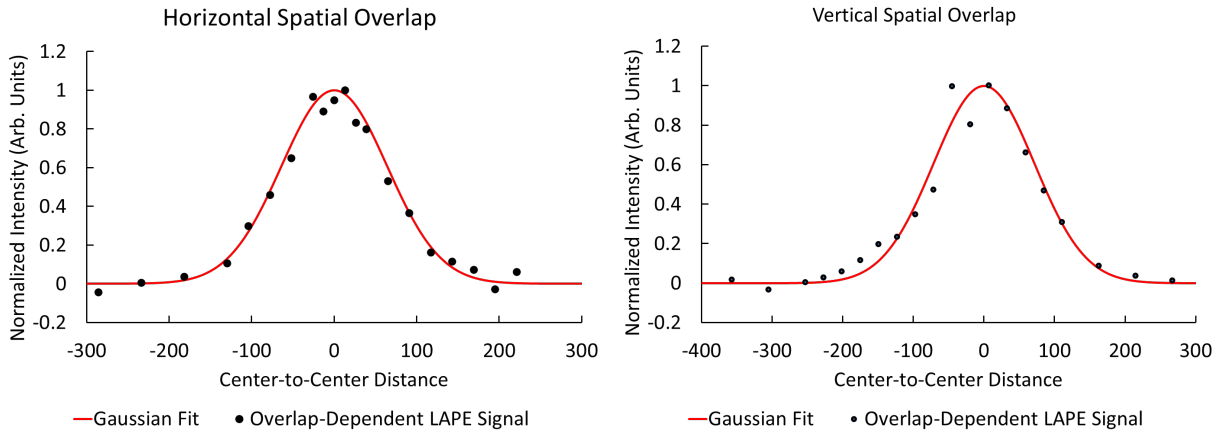

Figure 4.4 – (left) Horizontal axis scan of pump-probe overlap. (right) Vertical axis scan of pump-probe overlap.

4.3 Photoelectron Spectra of Gaseous Species

Throughout the process of implementing the XUV beamline, a variety of fundamental systems have been studied to demonstrate the functionality of the XUV probe. Gaseous molecular species were the logical next step in using the XUV probe to collect static photoelectron spectra. Due to its prominence in photoelectron spectroscopy of solvated species, static PES of $H_2O_{(g)}$ have been collected with the highest resolution attainable with our femtosecond XUV probe. Moving on from taking static spectra, LAPE spectra of $Ar_{(g)}$ and $H_2O_{(g)}$ and pump – probe spectra of $CH_3I_{(g)}$ have been collected.

4.3.1 Water Vapor

The presence of water vapor in the photoelectron spectra of solvated species is an extremely useful feature that can be used as an energetic reference. Static photoelectron spectra of water vapor ionized using a 21.7 eV probe exhibits three distinct peaks corresponding to ionization from the $1b_1$, $3a_1$, and $1b_2$ molecular orbitals of water with VIEs of 12.61 eV, 14.73 eV, and 18.55 eV, respectively. The static photoelectron spectra of $H_2O_{(g)}$ taken using the femtosecond XUV probe is shown in Figure 4.5 with a high-resolution spectrum displaying vibrational fine structure for reference.

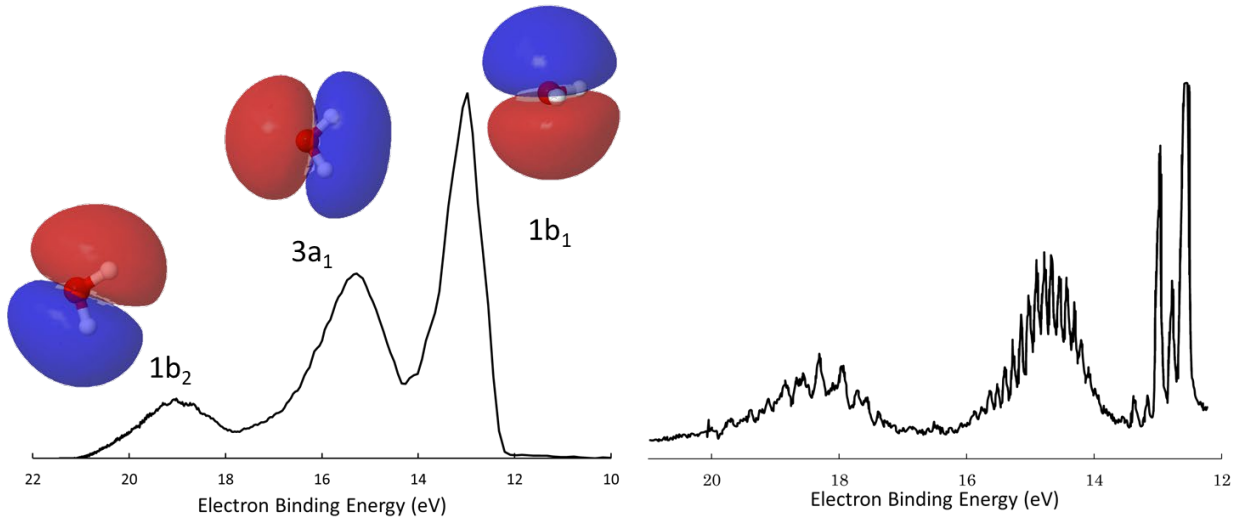

Figure 4.5 – Left: Static photoelectron spectra of $H_2O_{(g)}$ collected using the femtosecond XUV probe with peaks labeled with the corresponding molecular orbital, which is also depicted. Right: High-resolution photoelectron spectrum of $H_2O_{(g)}$ adapted from [5] for comparison.

The $1b_1$ peak is especially useful as an internal energetic reference due to its narrow natural linewidth and large relative intensity. This peak is used to shift spectra such that it sits at 9.1 eV eKE. This method is reliable as the gas phase signals, originating from samples with low number densities, are less susceptible to the space charge effects discussed in Chapter 2 that substantially impact liquid signals and remains stationary and narrow relative to other signals in the photoelectron spectrum [6].

4.3.2 LAPE in $Ar_{(g)}$ and $H_2O_{(g)}$

The first time-resolved signal taken utilizing the XUV probe was LAPE spectra taken using an 800 nm dressing field. The wavelength scaling of LAPE, which goes as λ^{-4} [7-9], makes the amplitude of the sidebands at $\pm n\hbar\omega$, where n is an integer and ω is the dressing field frequency, most intense for IR dressing fields .[C] LAPE spectra were also readily observed using a 400 nm dressing field once a system for overlapping the 400 nm and 800 nm pulses in a pinhole at the interaction point was devised. It was only recently and with great effort that LAPE spectra using a 267 nm dressing field was observed. Using an iterative scheme in which 800 nm LAPE signal is found for one-photon ionization of an $Ar_{(g)}$ target using the XUV probe and then 800 nm LAPE

[C] Normalized for dressing field intensity, the amplitude of sidebands generated using a 400 nm dressing field is smaller than the amplitude of sidebands generated using an 800 nm dressing field by a factor of 2^{-4}. Similarly, the amplitude of sidebands generated using a 267 nm dressing field is smaller than the amplitude of sidebands generated using an 800 nm dressing field by a factor of 3^{-4}.

found for 267 nm MPI signal of $Ar_{(g)}$, the overlap between the 267 nm pump and XUV probe can be found by extension. The LAPE spectra taken using an 800 nm, 400 nm, and 267 nm dressing fields are shown in Figure 4.6.

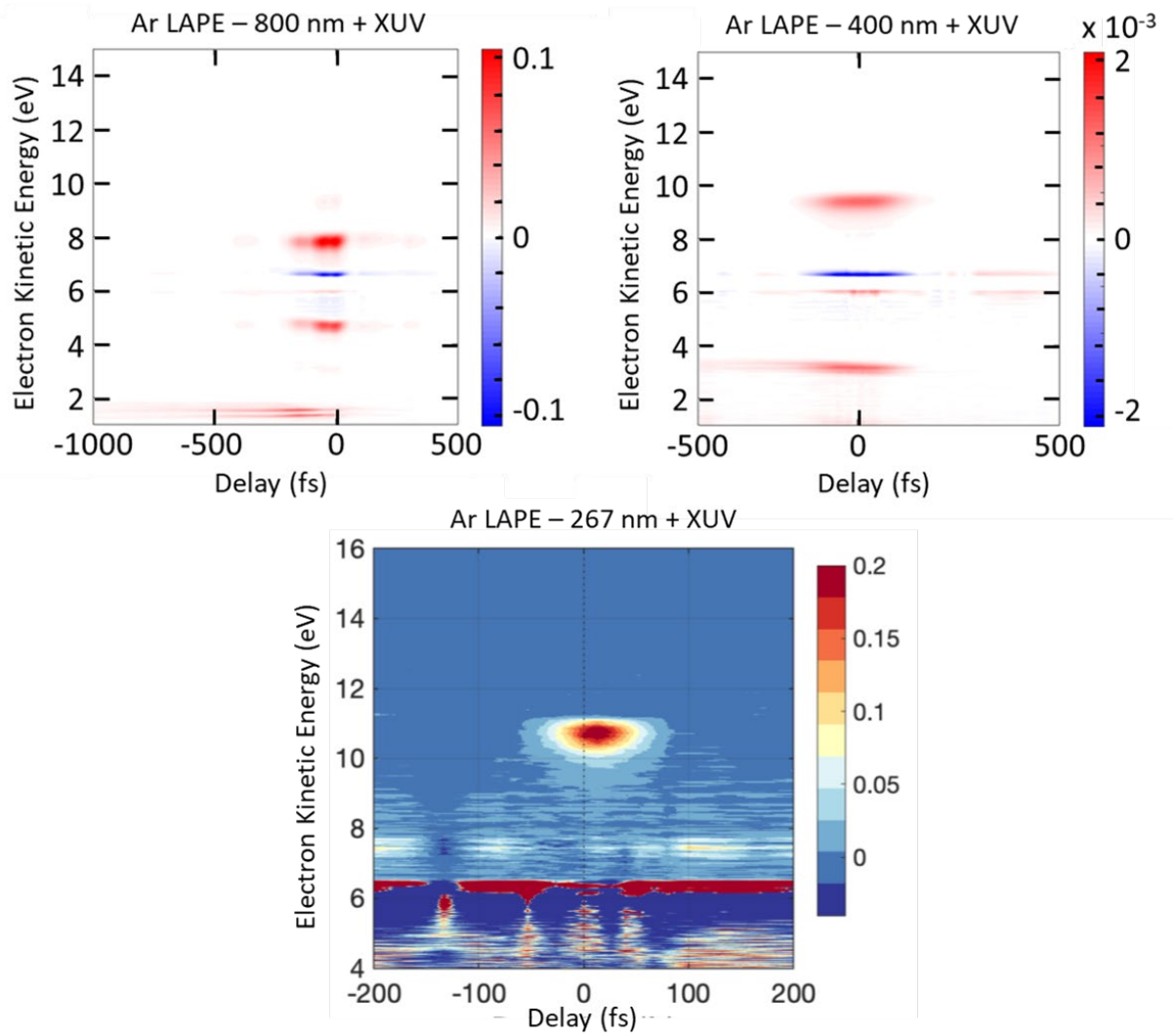

Figure 4.6 – Argon LAPE spectra taken using (top left) a 800 nm dressing field, (top right) a 400 nm dressing field, and (bottom center) a 267 nm dressing field.

Here, the red peaks at 8 eV eKE and 5 eV eKE in 4.9(a), 9.2 eV and 3 eV eKE in 4.9(b), and at 11 eV eKE in 4.9(c) indicate signals corresponding to the satellite peaks generated through LAPE. In Figure 4.6 (a) and 4.6 (b), long-lived signal can be seen at negative delays corresponding to XUV-pump, 800/400 nm probe signal of argon Rydberg states. The states are thought to be the 6d/8s levels in the $^2P_{1/2}$ series and either the 8d/10s or 9d/11s levels in the $^2P_{3/2}$ series [10].

The large photoionization cross section of $Ar_{(g)}$ at 21.7 eV (57.1 nm) of 36×10^{-18} cm^{-2} [11] relative to similar gaseous systems such as water vapor which has a cross section of 21.6×10^{-18} cm^{-2} [12] makes it an ideal system to utilize to measure the temporal cross-correlation of the instrument. Using the LAPE signal, which is linearly dependent on dressing field intensity for the first order sideband, the cross-correlation has been found for all three dressing field wavelengths and fit to a gaussian of the form given in Equation 4.2. Cross-correlation measurements at the different dressing field wavelengths are given in Figure 4.17.

As we cannot easily measure the autocorrelation of the dressing fields after they've been introduced into vacuum, it is difficult to retrieve the width of the pump and probe component gaussians making up the cross-correlation gaussian fit to the LAPE signal. A rough estimate of the individual pump and probe temporal widths can be arrived at by measuring the temporal duration of the 800 nm dressing field using frequency-resolved optical gating (FROG) in a GRENOUILLE device. Once this pulse duration is known, the remaining pulse durations can be extracted from the LAPE cross-correlation scans as long as the assumption that the 800 nm pulse duration is not substantially different at the interaction point compared to where it is measured on the table. Since the 800 nm beam passes through ~10 mm of fused silica and CaF_2 transmissive optics between where the FROG trace is measured and the photoelectron spectrometer, the duration of the 800 nm pulse at the interaction region is estimated to be 10 fs longer than measured to account for the GVD leading to stretching of the pulse duration.

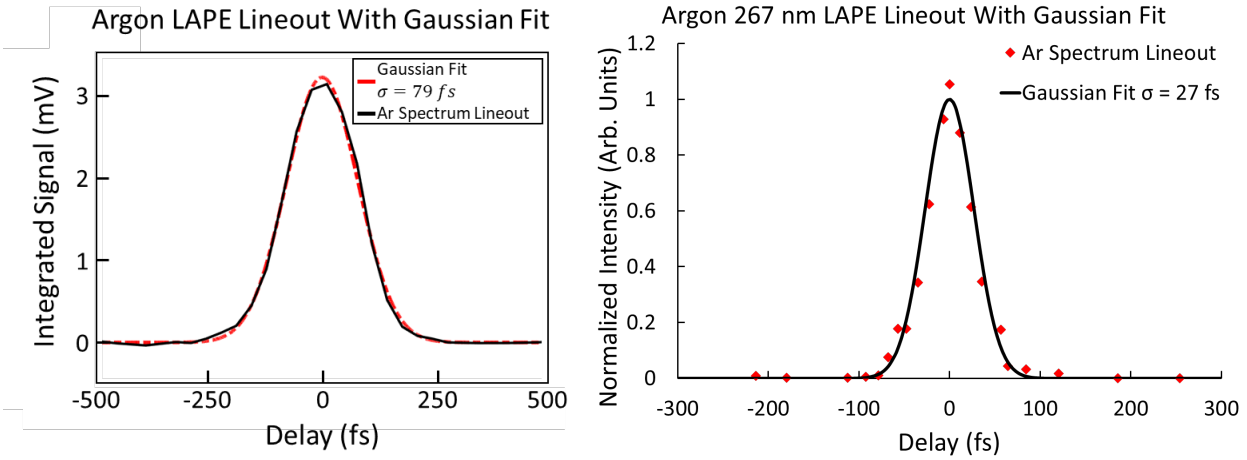

Figure 4.7 – Integrated eKE lanes for the $+\hbar\omega$ LAPE peaks for $Ar_{(g)}$ photoionized using a 21.7 eV probe and (left) 400 nm and (right) 267 nm dressing fields.

The shorter pulse duration observed for the 267 nm dressing field is a consequence of that beamline only transmitting through the 2 mm CaF_2 window to couple into vacuum, otherwise all other optics are reflective. Given the 800 and 400 are

transmitted through anywhere from 10 mm to 20 mm of fused silica or calcium fluoride these pulses are substantially broadened relative to the 267 nm pulse. Between scans, the spatiotemporal overlap between pump and probe occasionally needs to be reoptimized to account for the slight drift over the course of the 1-2 hour long scan. Due to the intrinsically broad features of solution-phase spectra, it is prohibitively difficult to reoptimize overlap using either excited state or LAPE signals from liquid signals. By moving the jet ~200 μm away from the ToF entrance while keeping the pump and probe steering fixed, spatiotemporal overlap can be found and optimized using the water vapor evaporating off the surface of a liquid microjet as a target. This has proved to be an invaluable tool for in situ diagnostics of pointing and temporal stability. A typical LAPE spectrum of $H_2O_{(g)}$ is shown in Figure 4.8.

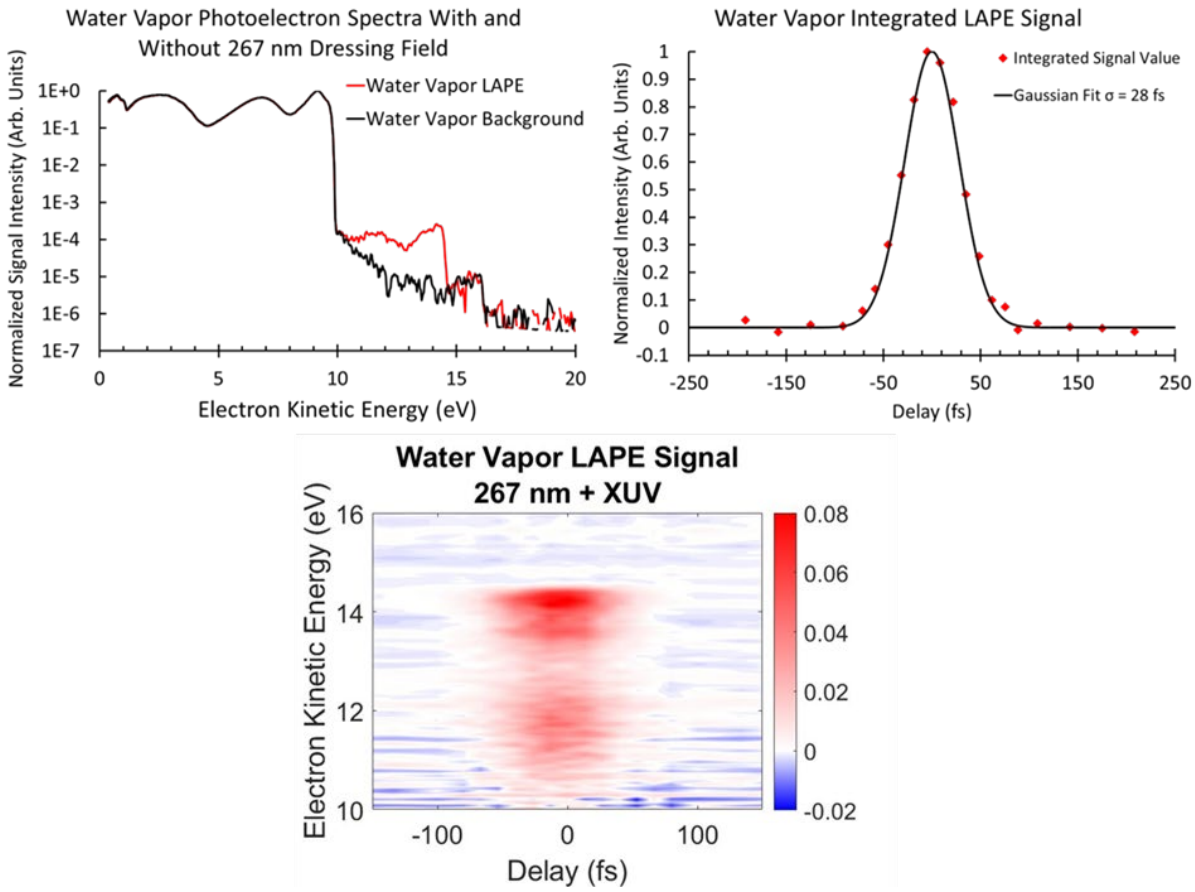

Figure 4.8 – $H_2O_{(g)}$ LAPE signal generated using a 267 nm dressing field and an XUV probe using water vapor evaporating off the surface of a liquid microjet. (top left) Lineouts showing water vapor LAPE signal and the XUV-only background. (top right) Temporal profile of the LAPE signal integrated over 10 eV to 15 eV eKE. (bottom) Contour plot showing the water vapor LAPE signal.

4.3.3 Methyl Iodide TRPES as a Test System

As a first demonstration of using our newly implemented XUV beamline as a probe for TRPES experiments studying excited state dynamics, the excited state photodissociation dynamics of methyl iodide was chosen as a test system. Having a vapor pressure of 400 Torr at room temperature, it was possible to use the same sample-delivery system as used in $Ar_{(g)}$ experiments by attaching a liquid sample reservoir held at 298 K, thereby simplifying finding excited state signal. Methyl iodide, CH_3I, is a very well understood system having been studied in detail by femtosecond TRPES [13, 14] and by femtosecond [15, 16] and attosecond [17] TA.

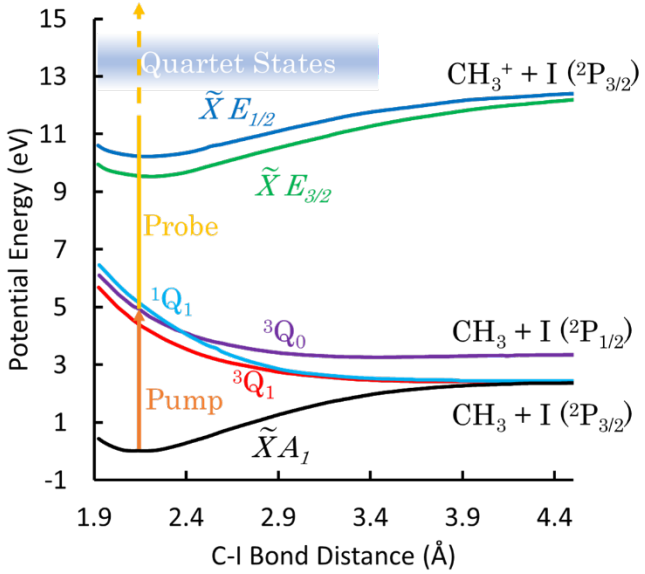

Figure 4.9 – Methyl iodide potential surfaces of the various electronic states involved in the TRPES experiment taken as one-dimensional cuts along the C – I bond distance. Adapted from [14]. As the quartet states have not been calculated previously, their approximate position is denoted with the blue rectangle.

Absorption of the 267 nm pump pulse leads to creation of an excited state wavepacket along the repulsive $^3Q_0$ surface in methyl iodide. This excitation transfers an electron from the iodine nonbonding orbital to the C-I σ^* orbital, leading to dissociation of the C-I bond within 100 fs. As the excited-state wavepacket evolves along the $^3Q_0$ surface, part of the excited state population passes through a conical intersection to the $^1Q_1$ surface in 15 fs [17], a timescale too rapid to observe outside of the cross-correlation of the pump and probe (FWHM = 64 fs). As such, all that is observed is the appearance and disappearance of excited state signal, which consists of a peak at 5-6 eV eBE corresponding to ionization to the $\tilde{X}^2E_{3/2}$ and $\tilde{X}^2E_{1/2}$ cationic states and a peak at 7-8 eV eBE corresponding to excited-state ionization to quartet states in the cation [14].

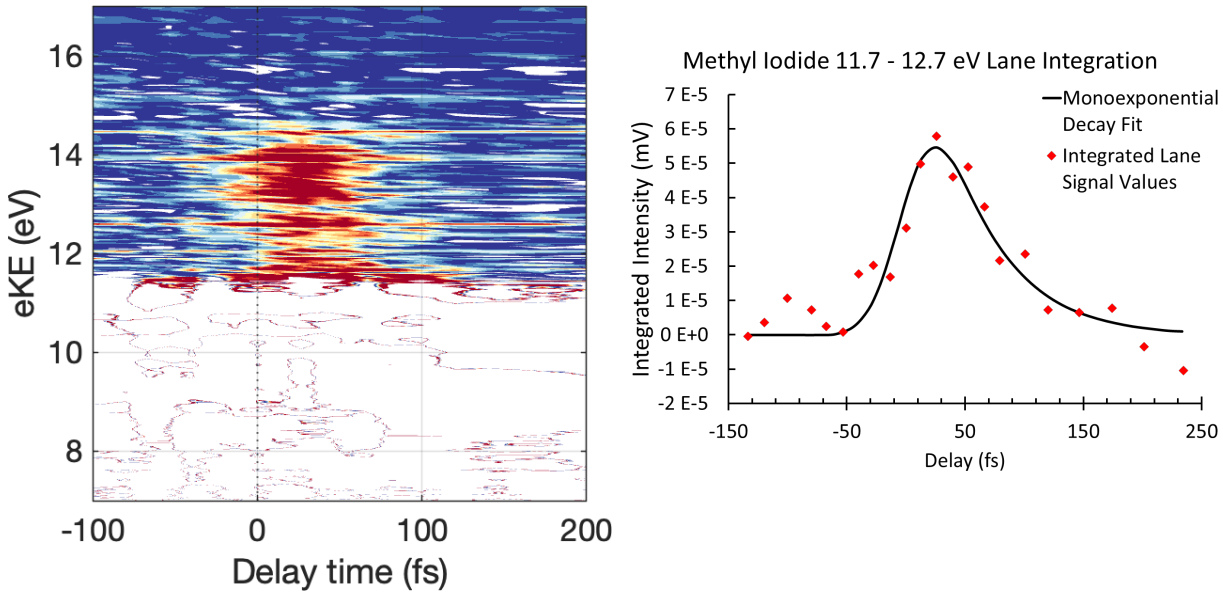

Figure 4.10– Methyl iodide excited state decay subsequent to excitation at 267 nm. (left) Contour plot showing the full exctied state signal. (right) Lane integration and monoexponential decay fit to the integrated signal.

The spectrum taken is shown in Figure 4.10. The previous findings are adequately reproduced; we observe a sub-100 fs lifetime and reproduce the shifting of the excited state signal to higher binding energy [13]. By reproducing the observation of this excited state transient signal, which is three orders of magnitude less intense than the main photoionization signal and at eKEs spanning 13 – 17 eV, the functionality of the XUV probe for TRPES is successfully demonstrated.

4.4 Photoelectron Spectra of Solvated Species Studied

The ultimate purpose of implementing the XUV probe is to increase the range of states that can be photoionized, thereby increasing the observable dynamics in solvated species. Moving forward from gas phase systems, static spectra of neat water and iodide were taken in order to fine tune the experiment for studying solvated species. The first time-resolved spectra of a solution phase system were LAPE spectra of water. Moving onward to studying dynamics of dilute solutes in water, TRPES spectra of several NACs were taken. The most recently observed, adenosine and adenine, are studied for the first time using an XUV probe.

4.4.1 Static PES of $H_2O_{(l)}$ and I^-

The first solvated species studied by us using LJ-PES with an XUV probe were water and hydrated iodide. To collect liquid water PES data with the effects of electrokinetic charging minimized without additional signals, a small amount of sodium chloride is added. The sodium cation has a eBE of 35.4 eV for $Na^+(2p)$ photoemission in water, putting it well outside the window of ionizable species in this experiment [18].The chloride anion has a eBE of 9.6 eV for $Cl^-(3p)$ photoemission, approximately equivalent to that of the liquid water $1b_1$ peak which has a eBE of 11.16 eV [18, 19]. Given the NaCl concentration is at least 3 orders of magnitude less than that of liquid water, it can be assumed the presence of salt is negligible and does not contribute to $H_2O_{(l)}$ PES.

A typical photoelectron spectrum of $H_2O_{(l)}$ is shown in Figure 4.11. Due to the presence of the vapor jacket surrounding the liquid microjet, signal attributable to water vapor is omnipresent in solution phase spectra. As such, a typical photoelectron spectrum of $H_2O_{(g)}$ is also shown. Immediately apparent is the substantial increase in peak width when comparing the $1b_{1(g)}$ and $1b_{1(l)}$ peaks. This is a result of the increased number of energetically accessible microenvironments experienced by solvated species resulting in broad natural linewidths. Further, the solution phase water photoionization peaks are shifted by approximately 1.5 eV relative to the analogous peaks in the gas phase water spectrum. This is a result of the stabilization of the final cationic states in solution relative to the gas phase as discussed in Section 1.2 in Chapter 1. Finally, the retrieved binding energies of the liquid water photoelectron peaks agree well with literature values of 11.2, 13.5, and 17.3 eV for the $1b_1$, $3a_1$, and 1b peaks, respectively [19].

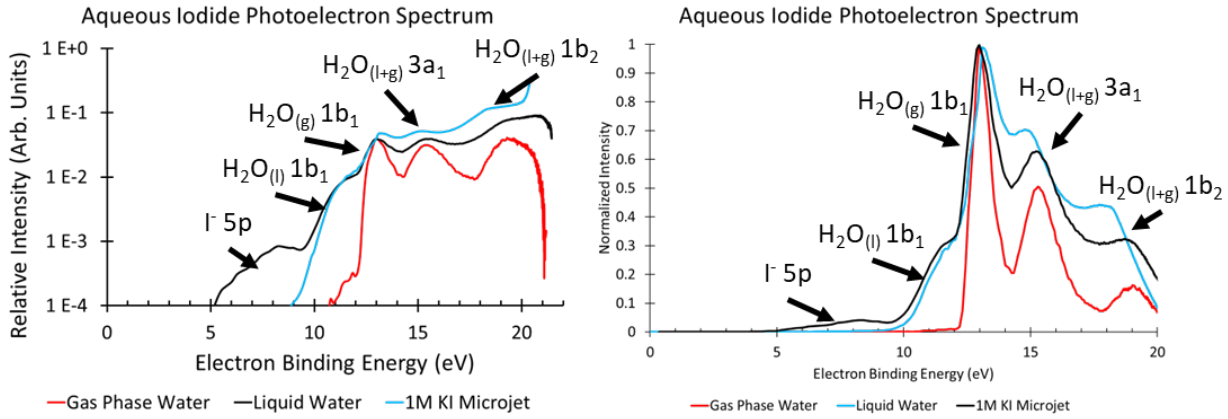

Figure 4.11 – Combined spectra showing the XUV photoelectron spectra for water vapor (red), liquid water (blue), and potassium iodide solution (black). Two identical data sets are given, one with the Jacobian factor applied (left) and one without (right) to help emphasize the peaks at higher binding energy.

Moving forward from pure water, a 1 M solution of potassium iodide was introduced into the spectrometer. Iodide is a common solute frequently present both LJ-PES and LJ-TRPES due to it being highly soluble and having an strong CTTS transition accessible by irradiation at 240 nm. In aqueous solution, iodide has been shown to exhibit photoelectron peaks at 7.7 eV and 8.8 eV eBE corresponding to $I^-(5p)$ photoemission. A spectrum taken of aqueous iodide solution using the newly implemented XUV probe, shown in Figure 4.11, exhibits a single broad peak spanning several eV eKE. This is attributed to a combination of the large natural width of these peaks, measured to be ~1 eV [18], and the reduced energy resolution of the ToF detector in the high eKE region. Regardless, the signal qualitatively matches what has been observed previously, demonstrating the functionality of the apparatus for studying solutes in aqueous solution.

4.4.2 LAPE Spectra from Solutions

As was the case with gas phase systems, the first time-resolved photoelectron spectra of a liquid system taken were LAPE spectra. LAPE has previously been observed in LJ-TRPES spectra at a variety of wavelengths, including 800 nm [9], 400 nm [20], and 267 nm [21]. We've similarly been able to observe this effect in liquid water spectra taken at those same wavelengths; spectra taken using an 800 nm and 267 nm dressing fields are shown in Figure 4.12. The spectra shown here readily reproduce those taken by other groups. Depending on the intensity and wavelength of the dressing field, the LAPE signal in the LJ-TRPES spectra consists of at least one order of sidebands above and below each peak making up the corresponding XUV-only spectrum. Due to the relative spacing of the peaks from gaseous and liquid water photoionization, LAPE spectra commonly only displayed prominent signal at eKEs greater than the $1b_{1(l)}$ water peak at 10.5 eV due to interference of LAPE signals from neighboring water photoionization peaks.

This effect has consistently been observed in spectra taken intending to measure excited state signal rather than LAPE signal. Due to this, the LAPE signal from liquid water peaks will need to be fit and subtracted so as to not obscure short time excited state dynamics. In doing this, the cross-correlation and energetic width of the LAPE peak must be determined. This makes the LAPE peaks a useful diagnostic tool, even in spectra where only excited state signal is desired.

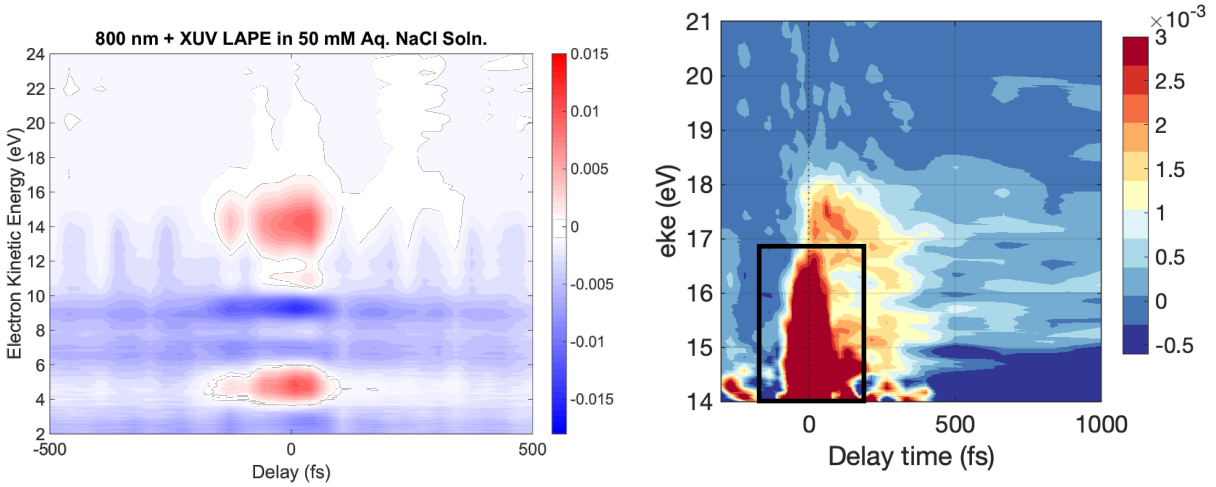

Figure 4.12 – LAPE spectra of water shown using a (left) 800 nm dressing field and (right) 267 nm dressing field. Note the contour plot in the 267 nm LAPE spectrum also shows excited state signal due to the presence of solute, so the LAPE specifically is highlighted within the box.

4.4.3 LJ-TRPES of Several NACs

The totality of upgrades to the spectrometer apparatus were carried out ultimately to perform experiments measuring the complete array of UV-induced dynamics in NACs from initial excitation to ground state recovery. These experiments expand upon the UV pump/UV probe experiments previously performed on this project studying the excited state dynamics in the thymine-derived [22] and adenine-derived [23] NACs [24]. Current progress toward this end has involved measuring the LJ-TRPES spectra of the pyrimidine nucleosides uridine and thymine and the purine NACs adenine and adenosine.

Understanding of the relaxation pathway of thymine-derived NACs has been fairly contentious until recently. Studies employing transient absorption (TA) [25, 26] and fluorescence upconversion (FU) [27, 28] to measure the excited state decay subsequent to UV absorption have identified at least two distinct excited states, assigned as the $^1\pi\pi^*$ and $^1n\pi^*$ states, involved in the relaxation mechanism, as shown in Figure 4.13.

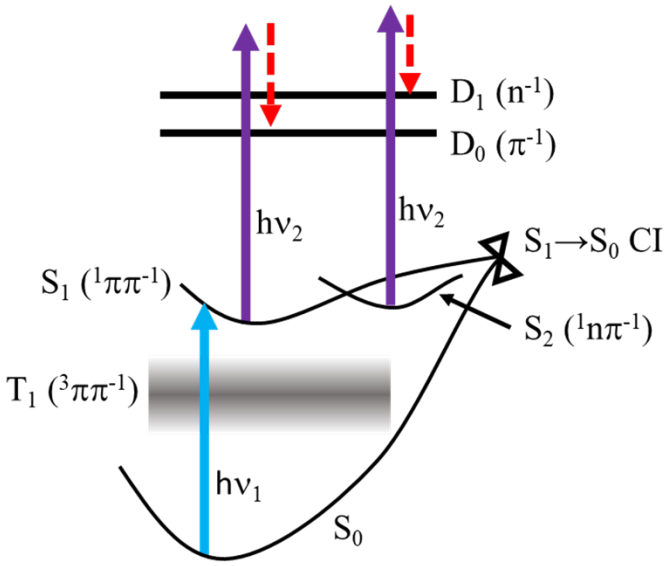

Figure 4.13 – The proposed relaxation mechanism for the thymine-derived NACs.

Recent studies have gone farther, identifying long-lived signals in the relaxation process ascribed to either the $^3\pi\pi^*$ or $^3n\pi^*$ states populated through ISC. Previous studies employing LJ-TRPES with probe energies in the 4.6-6.2 eV range did not observe any signals attributable to states other than the $^1\pi\pi^*$ state initially populated. Recently, Miura et al. [21] employed a near identical LJ-TRPES experiment to that described in this dissertation to study several pyrimidine NACs including uridine and thymine. This study was able to elucidate the involvement of the $^1n\pi^*$ state in the excited state relaxation mechanism for the first time using LJ-TRPES, as well as provides a useful point of comparison for our studies. The LJ-TRPES spectra of a 150 mM uridine sample and a 15 mM thymine sample taken using a 21.7 eV probe are shown in Figure 4.14.

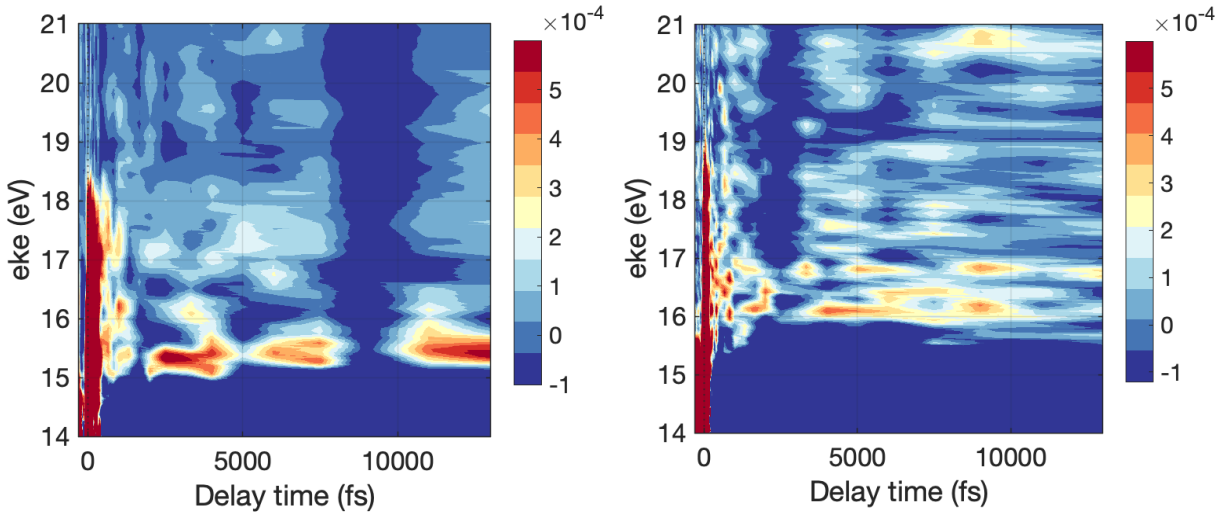

Figure 4.14 – Contour plots depicting the TRPES excited state dynamics of (left) thymine and (right) uridine after photoexcitation at 267 nm.

In both the uridine and thymidine LJ-TRPES spectra, three important features are present. First, a prominent signal at t_0 spanning 14 to 16.5 eV eKE is assigned to the first order LAPE sideband of the $H_2O_{(l)}$ $1b_1$ peak. This signal allows us to retrieve a cross-correlation of ~60 fs FWHM for the thymidine experiment and ~70 fs for the uridine experiment. Second, a weaker signal in the 16 to 17 eV eKE region is observed. This is assignable as excited state signal arising from the $^1\pi\pi^*$ state, relaxing with a measured lifetime of ~200 fs for thymidine and ~150 fs for uridine in good agreement with previous measurements [21]. Finally, a long lived signal is observed in the 15-16 eV eKE region persisting beyond the 10 ps observation window of this experiment. This signal is tentatively assigned to the $^1n\pi^*$ state and matches closely to what was observed in the experiment of Miura et al. [21].

A recent study has demonstrated the utility of replacing cylindrical liquid microjets with a liquid flatjet formed by colliding two cylindrical jets and using the flat leaves as sample targets for static photoelectron spectroscopic studies of the solution delivered by the crossed cylindrical jets [29]. Given their success substantially increasing the liquid signal intensity relative to signal coming from the vapor jacket in their static scans, we were motivated to extend this to time-resolved studies. The first attempt at adding a flat jet sample delivery setup to the TRPES experiment was done using the micronit sheet nozzles in a gas dynamic virtual nozzle configuration with a 15 mM thymine sample delivered through the center channel and ~10 psia He delivered through the side channels forming liquid sheets with the first sheet ~500 micron wide. The spectra collected in this experiment are given in Figure 4.18.

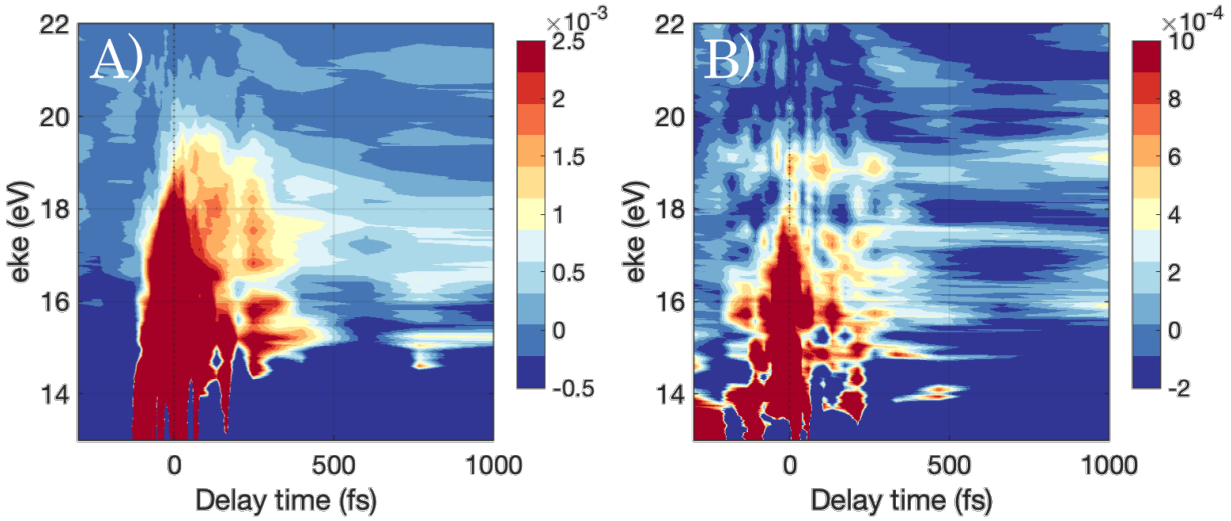

Figure 4.15 – Direct comparison between transient signal levels in comparable experiments observing ultrafast relaxation of 15 mM thymine solutions with (A) a liquid flat jet sample delivery setup and (B) a 30 μm liquid microjet sample delivery setup. Both spectra were taken using 900 mW of 267 nm pump power, XUV power set such that the water signal is 5 mV, and 50k laser shots averaged per time delay.

The TRPE spectra taken have been compared to spectra taken using a 30 μm microjet target. From the spectra taken, the advantages of the larger target size are immediately evident. With the same pump and probe fluences, the transient signal acquired using a flat jet delivery system is nearly an order of magnitude greater than the corresponding signal acquired using a 30 μm microjet target. This tracks well with the estimated differences in signal collected on geometric considerations alone as laid out in Chapter 2. Additionally, the instability leading to large fluctuations in signal between each delay point evident in the spectra taken with a microjet is largely eliminated. The ultimate reason for this is likely a combination of factors including mitigation of pointing instability with the larger target size, greater area probed increasing the total signal, and elimination of jet instability considerations, though this has yet to be experimentally determined. Given the substantial improvements in S/N achieved using a flat jet instead of a cylindrical jet, future studies will likely all involve using the flat jet as the sample delivery method.

To confirm that the long-lived signal observed in LJ-TRPES spectra of uridine and thymidine was not an artifact of the correction for space-charge shifting of the time-resolved signal, adenosine was observed by LJ-TRPES using the 21.7 eV probe for the first time. To maintain consistency between initial LJ-TRPES experiments showing long-lived signal and these control experiments, the following experiments were performed using 30 μm cylindrical jets as the sample delivery method. Adenosine has previously been studied by TA [30-32], FU [33-36], and UV pump/UV probe LJ-TRPES [37, 38]. All previous studies show complete relaxation of the $^1\pi\pi^*$ excited

state generated by photoexcitation at 267 nm directly to the ground electronic state with a lifetime of ~300 fs with no evidence for relaxation through a long-lived intermediate excited state as is the case in thymidine and uridine. The LJ-TRPES spectrum obtained from a 7 mM solution of adenosine is shown in Figure 4.16. As expected, the complete excited state population relaxes to the ground electronic state with a lifetime of 200 fs with no evidence of a long-lived intermediate.

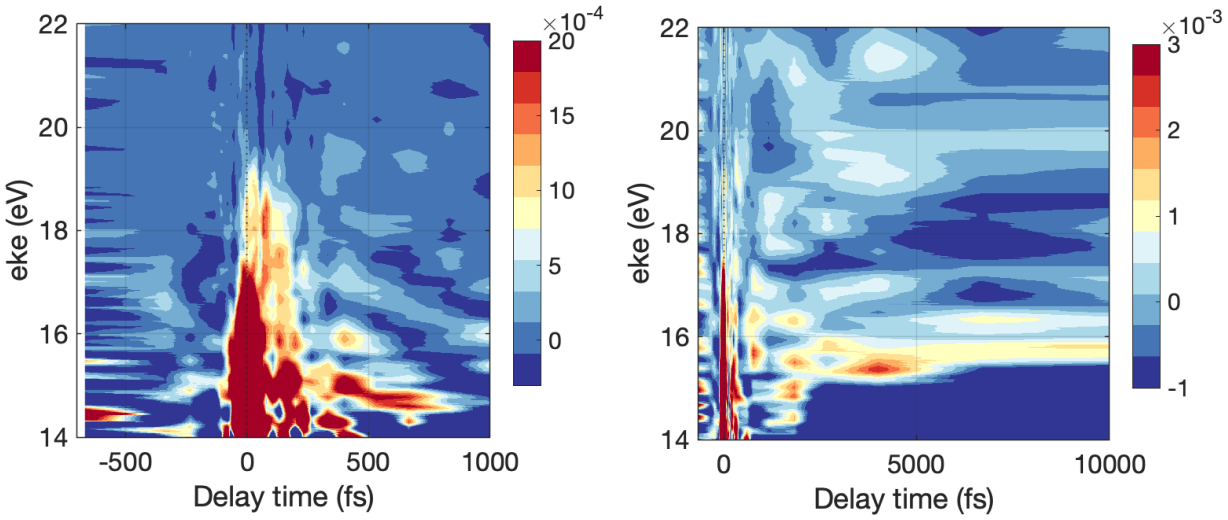

Figure 4.16 – (left) Contour plot of the time-resolved excited state signal in adenosine subsequent to excitation at 267 nm. (right) Contour plot of the time-resolved excited state signal in adenine subsequent to excitation at 267 nm.

The nucleobase adenine has also been studied by LJ-TRPES for the first time using an XUV probe. In the previous LJ-TRPES experiment employing a tunable UV probe ranging from 4.65 to 5.2 eV [38], the correlated increase in lifetime with increasing probe energy suggests the measured lifetime is artificially shortened due to insufficient probe energy required to access the full FC window as the excited state population relaxes on the $^1\pi\pi^*$ surface. The XUV probe employed in this experiment ensures the full FC window can be accessed along the entirety of the relaxation process. Due to jet instability resulting from the poor solubility of adenine, only a limited preliminary dataset has been measured and is presented here. The LJ-TRPES spectrum is shown in Figure 4.16. The rough excited state lifetime of the mixture of 7H and 9H tautomers of adenine attributable to $^1\pi\pi^* \rightarrow S_0$ relaxation is on the order of 350 fs. This lifetime is slightly longer than the value previously measured, but is only an estimate given that the poor signal quality in adenine makes it difficult to confidently fit the decay lifetime. Further measurements of both adenine and adenosine will be required to increase the certainty of the lifetimes reported here which will be presented in a publication planned for the near future.

4.5 Conclusion and Outlook

The experimental capability to follow the full range of dynamical processes in solution phase systems subsequent to photoexcitation on femtosecond to picosecond timescales has been a long sought after goal. Through implementation of a femtosecond XUV source coupled to a liquid microjet photoelectron spectrometer, this goal has largely been achieved as demonstrated here. Time-resolved photoelectron spectra of both liquids and solutes have been collected, demonstrating the functionality of this newly upgraded experiment.

As a part of this effort, a variety of nucleic acid constituents have been studied to demonstrate the technique. Adenine and adenosine have been studied here for the first time using the LJ-TRPES technique coupled to an XUV probe. The observed relaxation dynamics of adenosine reproduce those previously measured using a 6.2 eV probe. Aqueous adenine was observed for the first time by LJ-TRPES using a probe definitively of sufficient energy so as to not artificially shorten the measured relaxation lifetime.

Throughout the process of developing the project to the point that publication-quality data can begin being collected, many useful tools have been implemented to facilitate this data collection. Optimization using LAPE at dressing field wavelengths from the NIR to the UV has been relied on heavily and has proved to be invaluable. Additionally, PES of gas phase targets in general has proven to be a useful diagnostic tool due to the reproducibility of these systems and ease of setting up and switching between gas phase PES experiments.

In the near future, completing the collection LJ-TRPES data employing an XUV probe for the purine family of nucleic acid constituents, which have not been studied using an XUV probe, would be the next logical step. These NACs not only have 200-300 fs excited state lifetimes, but also must be studied before moving on to larger NACs. Moving on from single isolated NACs, slight modification to the experiment to implement a recirculating sample delivery system would enable precious (expensive) samples of oligonucleotides to be studied. These UV pump/XUV probe experiments would ideally be able to distinguish between and measure the relative contributions of the isolated excimer, delocalized exciton, and charge transfer states to the relaxation pathway [34, 39-41]. Of particular interest would be determining the difference in dynamics between oligonucleotides of different lengths and sequences to elucidate the effect of DNA and RNA secondary structure on excited state dynamics and even potentially photolesion formation.

4.6 References

[1] Velchev, I.; Hogervorst, W.; Ubachs, W. Precision VUV spectroscopy of Ar I at 105 nm. *J. Phys. B* **1999**, *32* (17), L511. DOI: 10.1088/0953-4075/32/17/105.

[2] Saloman, E. B. Energy levels and observed spectral lines of ionized argon, ArII through ArXVIII. *J. Phys. Chem. Ref. Data* **2010**, *39* (3). DOI: 10.1063/1.3337661.

[3] Saloman, E. B. Energy Levels and Observed Spectral Lines of Xenon, XeI through XeLIV. *J. Phys. Chem. Ref. Data* **2004**, *33* (3), 765-921. DOI: 10.1063/1.1649348.

[4] Jørgen, E. H.; Willy, P. Revised analysis of singly ionized xenon, Xe II. *Phys. Scr.* **1987**, *36* (4), 602. DOI: 10.1088/0031-8949/36/4/005.

[5] Brundle, C. R.; Turner, D. W.; Price, W. C. High resolution molecular photoelectron spectroscopy II. Water and deuterium oxide. *Proc. R. Soc. London Ser. A Math. Phys. Sci.* **1968**, *307* (1488), 27-36. DOI: 10.1098/rspa.1968.0172.

[6] Thurmer, S.; Malerz, S.; Trinter, F.; Hergenhahn, U.; Lee, C.; Neumark, D. M.; Meijer, G.; Winter, B.; Wilkinson, I. Accurate vertical ionization energy and work function determinations of liquid water and aqueous solutions. *Chem. Sci.* **2021**, *12* (31), 10558-10582. DOI: 10.1039/d1sc01908b.

[7] Madsen, L. B. Strong-field approximation in laser-assisted dynamics. *Am. J. Phys.* **2005**, *73* (1), 57-62. DOI: 10.1119/1.1796791.

[8] Glover, T. E.; Schoenlein, R. W.; Chin, A. H.; Shank, C. V. Observation of Laser Assisted Photoelectric Effect and Femtosecond High Order Harmonic Radiation. *Phys. Rev. Lett.* **1996**, *76* (14), 2468-2471. DOI: 10.1103/PhysRevLett.76.2468.

[9] Arrell, C. A.; Ojeda, J.; Mewes, L.; Grilj, J.; Frassetto, F.; Poletto, L.; van Mourik, F.; Chergui, M. Laser-Assisted Photoelectric Effect from Liquids. *Phys. Rev. Lett.* **2016**, *117* (14), 143001. DOI: 10.1103/PhysRevLett.117.143001.

[10] Cao, W.; Warrick, E. R.; Neumark, D. M.; Leone, S. R. Attosecond transient absorption of argon atoms in the vacuum ultraviolet region: line energy shifts versus coherent population transfer. *New J. Phys.* **2016**, *18* (1), 013041. DOI: 10.1088/1367-2630/18/1/013041.

[11] West, J. B.; Marr, G. V.; Series, G. W. The absolute photoionization cross sections of helium, neon, argon and krypton in the extreme vacuum ultraviolet region of the spectrum. *Proceedings of the Royal Society of London. A. Mathematical and Physical Sciences* **1976**, *349* (1658), 397-421. DOI: 10.1098/rspa.1976.0081.

[12] Haddad, G. N.; Samson, J. A. R. Total absorption and photoionization cross sections of water vapor between 100 and 1000 Å. *J. Chem. Phys.* **1986**, *84* (12), 6623-6626. DOI: 10.1063/1.450715.

[13] Warne, E. M.; Downes-Ward, B.; Woodhouse, J.; Parkes, M. A.; Springate, E.; Pearcy, P. A. J.; Zhang, Y.; Karras, G.; Wyatt, A. S.; Chapman, R. T.; Minns, R. S. Photodissociation dynamics of methyl iodide probed using femtosecond extreme ultraviolet photoelectron spectroscopy. *Phys. Chem. Chem. Phys.* **2020**, *22* (44), 25695-25703. DOI: 10.1039/D0CP03478A.

[14] Downes-Ward, B.; Warne, E. M.; Woodhouse, J.; Parkes, M. A.; Springate, E.; Pearcy, P. A. J.; Zhang, Y.; Karras, G.; Wyatt, A. S.; Chapman, R. T.; Minns, R. S. Photodissociation dynamics of methyl iodide across the A-band probed by femtosecond extreme ultraviolet photoelectron spectroscopy. *J. Phys. B* **2021**, *54* (13), 134003. DOI: 10.1088/1361-6455/ac08f3.

[15] Chang, K. F.; Reduzzi, M.; Wang, H.; Poullain, S. M.; Kobayashi, Y.; Barreau, L.; Prendergast, D.; Neumark, D. M.; Leone, S. R. Revealing electronic state-switching at conical intersections in alkyl iodides by ultrafast XUV transient absorption spectroscopy. *Nat. Commun* **2020**, *11* (1), 4042. DOI: 10.1038/s41467-020-17745-w.

[16] Attar, A. R.; Bhattacherjee, A.; Leone, S. R. Direct Observation of the Transition-State Region in the Photodissociation of CH3I by Femtosecond Extreme Ultraviolet Transient Absorption Spectroscopy. *J. Phys. Chem. Lett.* **2015**, *6* (24), 5072-5077. DOI: 10.1021/acs.jpclett.5b02489.

[17] Chang, K. F.; Wang, H.; Poullain, S. M.; González-Vázquez, J.; Bañares, L.; Prendergast, D.; Neumark, D. M.; Leone, S. R. Conical intersection and coherent vibrational dynamics in alkyl iodides captured by attosecond transient absorption spectroscopy. *J. Chem. Phys.* **2022**, *156* (11). DOI: 10.1063/5.0086775.

[18] Weber, R.; Winter, B.; Schmidt, P. M.; Widdra, W.; Hertel, I. V.; Dittmar, M.; Faubel, M. Photoemission from aqueous alkali-metal-iodide salt solutions using EUV synchrotron radiation. *J. Phys. Chem. B* **2004**, *108*, 4729. DOI: 10.1021/jp030776x.

[19] Winter, B.; Weber, R.; Widdra, W.; Dittmar, M.; Faubel, M.; Hertel, I. V. Full Valence Band Photoemission from Liquid Water Using EUV Synchrotron Radiation. *J. Phys. Chem. A* **2004**, *108*, 2625. DOI: 10.1021/jp030263q.

[20] Hummert, J.; Reitsma, G.; Mayer, N.; Ikonnikov, E.; Eckstein, M.; Kornilov, O. Femtosecond Extreme Ultraviolet Photoelectron Spectroscopy of Organic Molecules in Aqueous Solution. *J. Phys. Chem. Lett.* **2018**, *9* (22), 6649-6655. DOI: 10.1021/acs.jpclett.8b02937.

[21] Miura, Y.; Yamamoto, Y.-i.; Karashima, S.; Orimo, N.; Hara, A.; Fukuoka, K.; Ishiyama, T.; Suzuki, T. Formation of Long-Lived Dark States during Electronic Relaxation of Pyrimidine Nucleobases Studied Using Extreme

Ultraviolet Time-Resolved Photoelectron Spectroscopy. *J. Am. Chem. Soc.* **2023**, *145* (6), 3369-3381. DOI: 10.1021/jacs.2c09803.

[22] Erickson, B. A.; Heim, Z. N.; Pieri, E.; Liu, E.; Martinez, T. J.; Neumark, D. M. Relaxation Dynamics of Hydrated Thymine, Thymidine, and Thymidine Monophosphate Probed by Liquid Jet Time-Resolved Photoelectron Spectroscopy. *J. Phys. Chem. A* **2019**, *123* (50), 10676-10684. DOI: 10.1021/acs.jpca.9b08258.

[23] Williams, H. L.; Erickson, B. A.; Neumark, D. M. Time-resolved photoelectron spectroscopy of adenosine and adenosine monophosphate photodeactivation dynamics in water microjets. *J. Chem. Phys.* **2018**, *148*, 194303. DOI: 10.1063/1.5027258.

[24] Heim, Z. N.; Neumark, D. M. Nonadiabatic Dynamics Studied by Liquid-Jet Time-Resolved Photoelectron Spectroscopy. *Accts. Chem. Res.* **2022**, *55* (24), 3652-3662. DOI: 10.1021/acs.accounts.2c00609.

[25] Xue, B.; Yabushita, A.; Kobayashi, T. Ultrafast dynamics of uracil and thymine studied using a sub-10 fs deep ultraviolet laser. *Phys. Chem. Chem. Phys.* **2016**, *18* (25), 17044-17053, 10.1039/C5CP07861J. DOI: 10.1039/C5CP07861J.

[26] Pilles, B. M.; Maerz, B.; Chen, J.; Bucher, D. B.; Gilch, P.; Kohler, B.; Zinth, W.; Fingerhut, B. P.; Schreier, W. J. Decay Pathways of Thymine Revisited. *J. Phys. Chem. A* **2018**, *122* (21), 4819-4828. DOI: 10.1021/acs.jpca.8b02050.

[27] Gustavsson, T.; Sharonov, A.; Markovitsi, D. Thymine, thymidine and thymidine 5′-monophosphate studied by femtosecond fluorescence upconversion spectroscopy. *Chem. Phys. Lett.* **2002**, *351* (3), 195-200. DOI: 10.1016/S0009-2614(01)01375-6.

[28] Gustavsson, T.; Bányász, Á.; Sarkar, N.; Markovitsi, D.; Improta, R. Assessing solvent effects on the singlet excited state lifetime of uracil derivatives: A femtosecond fluorescence upconversion study in alcohols and D2O. *Chem. Phys.* **2008**, *350* (1), 186-192. DOI: 10.1016/j.chemphys.2008.02.032.

[29] Stemer, D.; Buttersack, T.; Haak, H.; Malerz, S.; Schewe, H. C.; Trinter, F.; Mudryk, K.; Pugini, M.; Credidio, B.; Seidel, R.; Hergenhahn, U.; Meijer, G.; Thürmer, S.; Winter, B. Photoelectron spectroscopy from a liquid flatjet. *J. Chem. Phys.* **2023**, *158* (23). DOI: 10.1063/5.0155182 (acccessed 8/5/2023).

[30] Röttger, K.; Marroux, H. J. B.; Böhnke, H.; Morris, D. T. J.; Voice, A. T.; Temps, F.; Roberts, G. M.; Orr-Ewing, A. J. Probing the excited state relaxation dynamics of pyrimidine nucleosides in chloroform solution. *Faraday Disc.* **2016**, *194* (0), 683-708. DOI: 10.1039/C6FD00068A.

[31] Pecourt, J.-M. L.; Peon, J.; Kohler, B. DNA Excited-State Dynamics: Ultrafast Internal Conversion and Vibrational Cooling in a Series of

Nucleosides. *J. Am. Chem. Soc.* **2001**, *123* (42), 10370-10378. DOI: 10.1021/ja0161453.

[32] Cohen, B.; Hare, P. M.; Kohler, B. Ultrafast Excited-State Dynamics of Adenine and Monomethylated Adenines in Solution: Implications for the Nonradiative Decay Mechanism. *J. Am. Chem. Soc.* **2003**, *125* (44), 13594-13601. DOI: 10.1021/ja035628z.

[33] Peon, J.; Zewail, A. H. DNA/RNA nucleotides and nucleosides: direct measurement of excited-state lifetimes by femtosecond fluorescence up-conversion. *Chem. Phys. Lett.* **2001**, *348* (3), 255-262. DOI: 10.1016/S0009-2614(01)01128-9.

[34] Kwok, W.-M.; Ma, C.; Phillips, D. L. Femtosecond Time- and Wavelength-Resolved Fluorescence and Absorption Spectroscopic Study of the Excited States of Adenosine and an Adenine Oligomer. *J. Am. Chem. Soc.* **2006**, *128* (36), 11894-11905. DOI: 10.1021/ja0622002.

[35] Gustavsson, T.; Sharonov, A.; Onidas, D.; Markovitsi, D. Adenine, deoxyadenosine and deoxyadenosine 5′-monophosphate studied by femtosecond fluorescence upconversion spectroscopy. *Chem. Phys. Lett.* **2002**, *356* (1), 49-54. DOI: 10.1016/S0009-2614(02)00290-7.

[36] Gustavsson, T.; Sarkar, N.; Vayá, I.; Jiménez, M. C.; Markovitsi, D.; Improta, R. A joint experimental/theoretical study of the ultrafast excited state deactivation of deoxyadenosine and 9-methyladenine in water and acetonitrile. *Photochem. Photobiol. Sci.* **2013**, *12* (8), 1375-1386. DOI: 10.1039/c3pp50060h.

[37] Williams, H. L.; Erickson, B. A.; Neumark, D. M. Time-resolved photoelectron spectroscopy of adenosine and adenosine monophosphate photodeactivation dynamics in water microjets. *J. Chem. Phys.* **2018**, *148* (19), 194303. DOI: 10.1063/1.5027258.

[38] Buchner, F.; Ritze, H. H.; Lahl, J.; Lübcke, A. Time-resolved Photoelectron Spectroscopy of Adenine and Adenosine in Aqueous Solution. *Phys. Chem. Chem. Phys.* **2013**, *15* (27), 11402-11408. DOI: 10.1039/C3CP51057C.

[39] Improta, R. Vertical Ionization Energies computed for dApdA dinucleotide in solution in the ground and in the excited state. A preliminary Report. 2021.

[40] Rössle, S.; Friedrichs, J.; Frank, I. The Formation of DNA Photodamage: The Role of Exciton Localization. *ChemPhysChem* **2010**, *11* (9), 2011-2015. DOI: 10.1002/cphc.201000081.

[41] Improta, R.; Barone, V. Interplay between “Neutral” and “Charge-Transfer” Excimers Rules the Excited State Decay in Adenine-Rich Polynucleotides. *Angew. Chem. Int. Ed.* **2011**, *50* (50), 12016-12019. DOI: 10.1002/anie.201104382.

Appendix A – LabVIEW Code Updates

A.1 Overview

The data acquired in this experiment is collected through code written in LabVIEW. The LabVIEW code is divided into two programs, one for static data collection and one for time-resolved data collection. The code integrates subVIs for operating the ADC card, delay stages, shutters, and Arduino controller. Given the complexity of the code, there exist contributions from many graduate students so I will only focus on the contributions implemented within the scope of this dissertation.

A.2 Changes to Static Collection Code

The static code operates functionally identically to how it is described in the thesis of B. A. Erickson [1], with added features including improved thresholding, invertibility of the spectra collected to easily accommodate differing detection coupling schemes, and added functionality to control the sampling rate. The thresholding algorithm has proved crucial to detecting the most minute signals by eliminating the electronic noise from the ADC, leaving just the single count signals to be averaged. In Figure A.1, a typical single count spectrum is given with the considerable electronic noise shown. This noise is a result of the ADC being an 8-bit digitizer with an effective FSR of 250 mV, leading to fluctuations in the digital baseline, on the order of ±1 bit, to be of comparable magnitude to the single counts coupled off the MCPs, which have a distribution of 3-7 mV for 99% of the counts observed. By choosing the threshold value to eliminate 95% of the electronic noise (~2 bits), the single count signals can be measured and averaged without being washed out into the baseline fluctuations of the digitizer card.

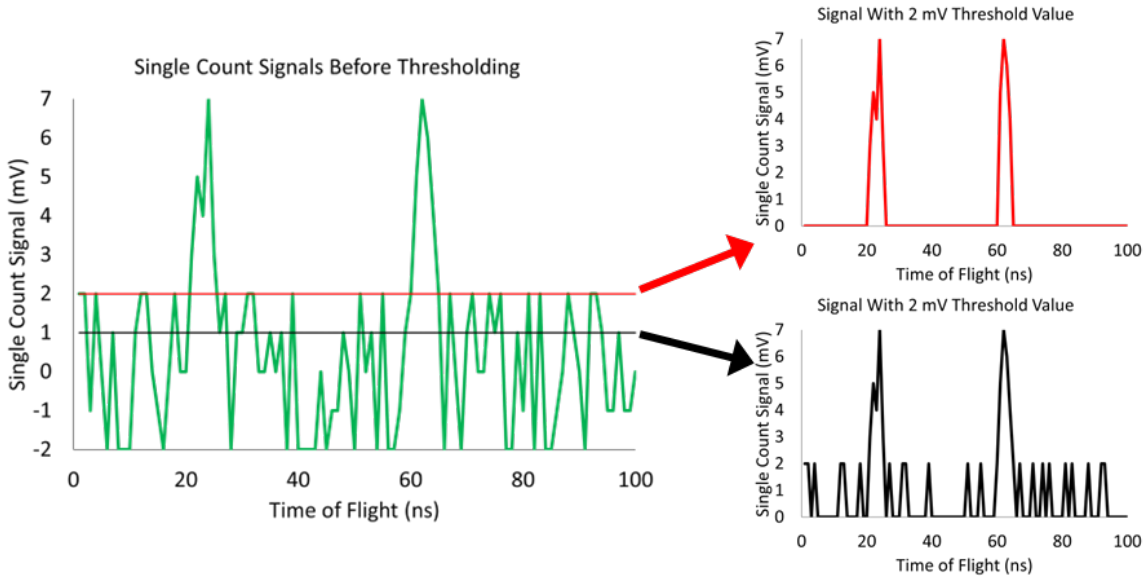

Figure A.1 – Effect that the thresholding algorithm has on single count spectra. Left: figure shows a typical single shot spectrum (green) with signal from two single electron detection events above a baseline of typical electronic noise in the ADC card with the thresholding levels (black = 1 mV, red = 2 mV) to arrive at the spectra to the right shown. Top Right: Spectrum retrieved by setting a threshold value of 2 mV, eliminating all baseline fluctuations from the ADC card. Bottom Right: Spectrum retrieved by setting a threshold value of 1 mV, eliminating all but the most extreme noise.

The complete static photoelectron spectrum retrieval code is shown in Figure A.2. Briefly, the code initializes the ADC card and inputs the relevant settings to the card so the appropriate acquisition mode is set. When this is set, the code pulls a single shot spectrum from the card each time it receives a trigger signal from the SDG box. In the 1.0 ms it takes to receive another trigger, the code scans the entire spectrum sent from the card and creates an array of 1s and 0s the same dimension of the spectrum depending on if each point scanned is greater than or less than the threshold value (greater than threshold value results in 1, less than results in 0). This array, referred to as the counting spectrum, is then multiplied by the original spectrum from the ADC card, yielding what we refer to as a DC thresholded spectrum. The three different spectra are averaged across the total number of shots taken in 1k intervals to account for card limitations and saved to a .csv file with the highest precision attainable to prevent errors associated with the code rounding small values.

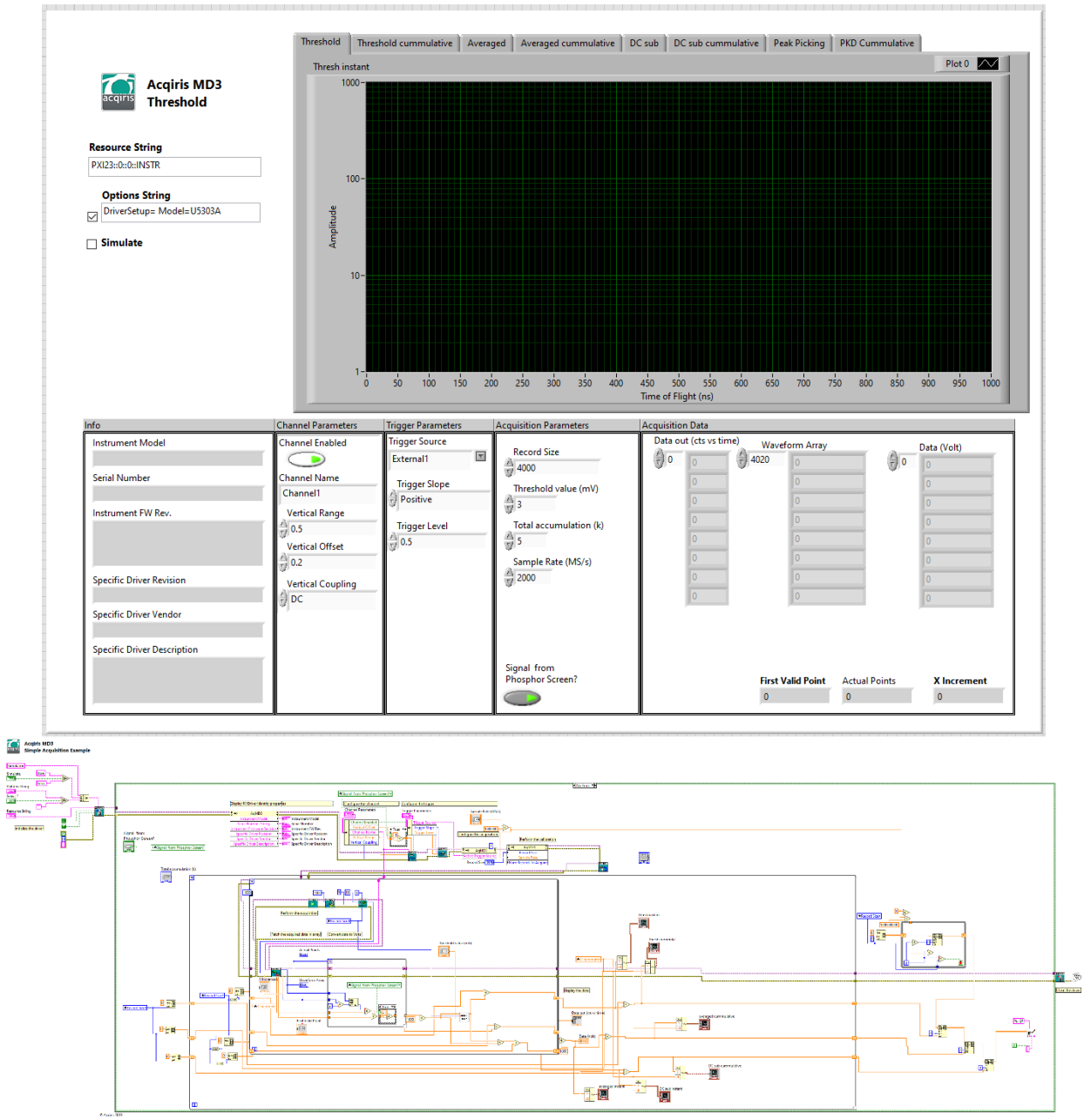

Figure A.2 – Top: Front panel of the static averaging photoelectron spectrum retrieval code. Bottom: Block diagram showing the relevant subVI functionality to initialize the ADC card, loop through spectrum retrieval, thresholding, and averaging, and save collected data.

The relevant algorithm for thresholding described here is shown in Figure A.3. Other improvements include controllability to invert the spectral output of the ADC card. This allows the thresholding algorithm to function appropriately regardless of if the signal is being coupled off the back MCP or phosphor screen. Finally, the ability to modify the sample rate is added to allow for longer total ToF times to be collected (for

example 8000 ns instead of 2000) while still allowing the thresholding algorithm to complete within the 1 ms between shots.

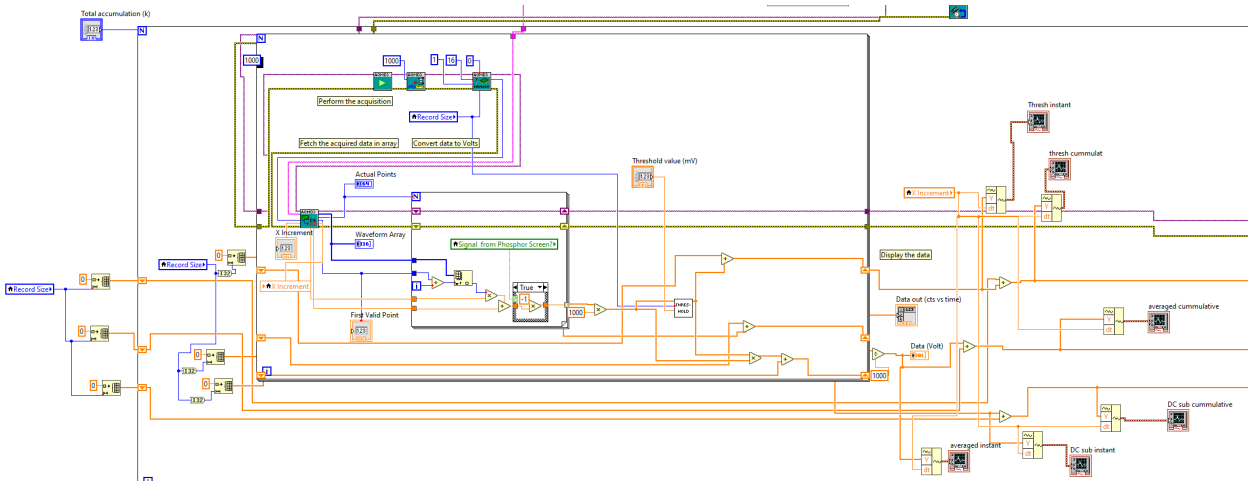

Figure A.3 – The modified portion of the LabVIEW code for DC thresholding.

A.3 Changes to Time-Resolved Data Collection Code

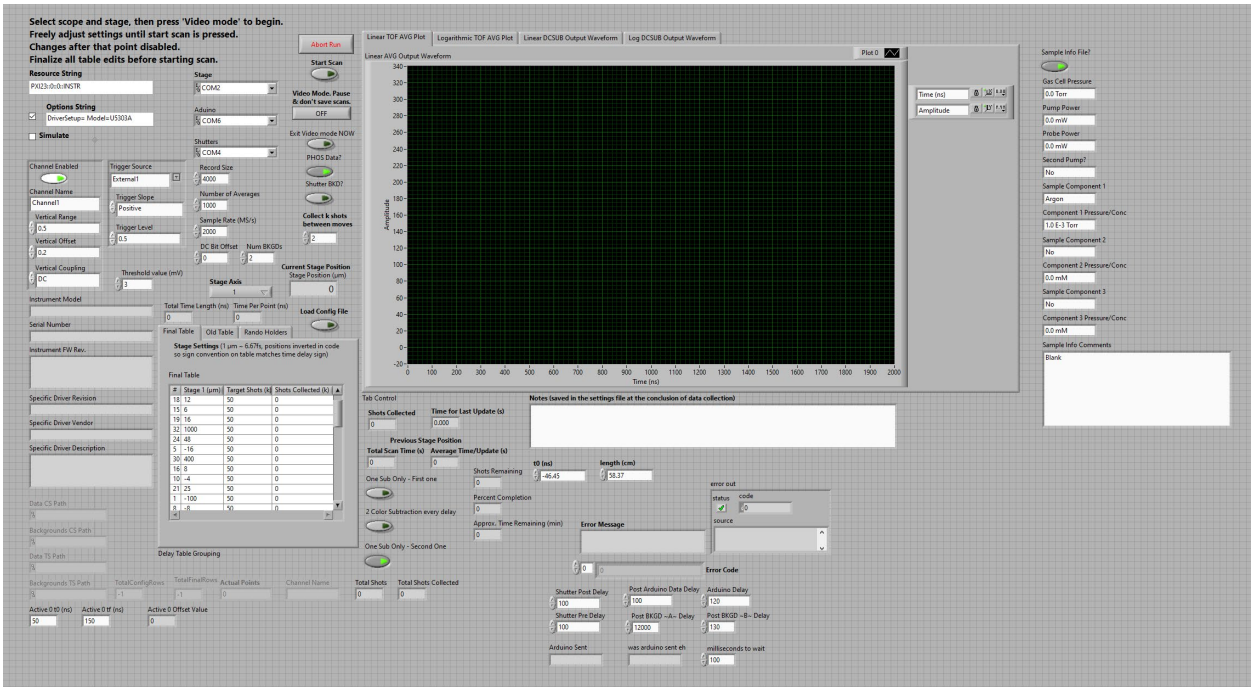

Figure A.4 – The front panel of the time-resolved photoelectron spectra collection program.

The time-resolved data collection code has been modified to include functionality for DC thresholding the spectra collected on a shot-to-shot basis, control of both Arduino shutters and Uniblitz shutters with controllable delays before and after actuating each shutter, randomizing the order of delays at which data is collected, optionally taking one or more backgrounds after collecting spectra at each delay, inverting the data depending on whether signal is coupled off the back MCP or phosphor screen, and saving relevant information for each scan in a sample info file along with an expanded settings file.

The DC thresholding and data inversion functionality in the time-resolved code are identical to the functionality described in the static code in Section A.2 and will not be described here. This functionality is implemented in both the "video mode" and data collection loops. The implemented code is shown in Figure A.5 for reference should to current code be lost.

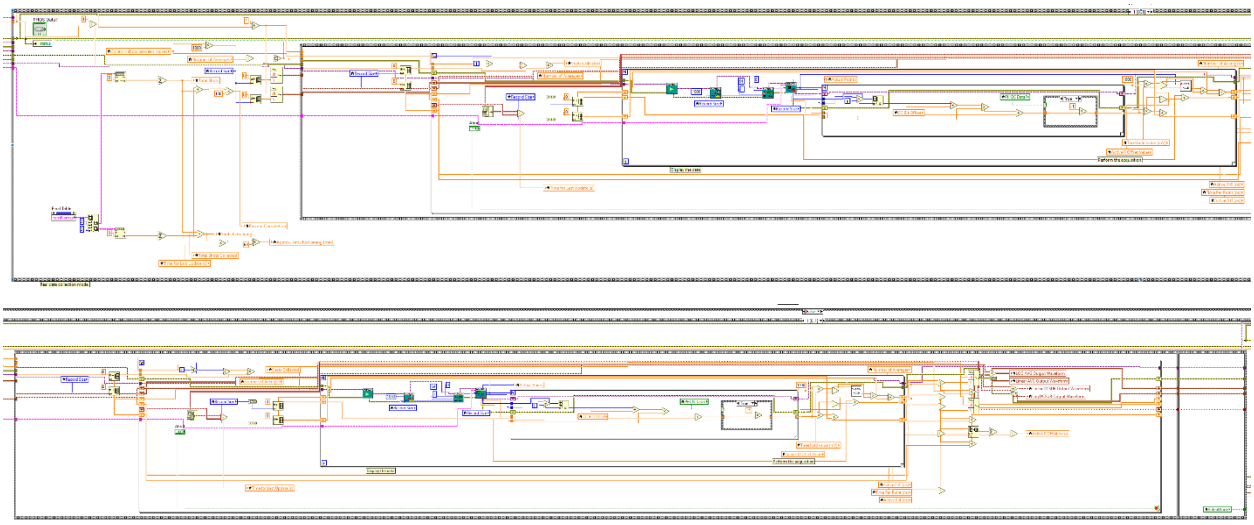

Figure A.5 – Implementation of the DC thresholding algorithm into the data collection loop.

A substantial source of systematic error in the experiment was the drifting of the liquid microjet coupled with the unrandomized delay ordering leading to a clear bias in data collected. To combat this, the order of delays was randomized in the LabVIEW code. In the process of randomizing the delays, it is convenient to restructure the delay table to optionally include one or more backgrounds after each delay rather than at the end of the table. The code implementing this is shown in Figure A.6, a brief explanation is given here. First, the number of data delays and backgrounds are determined. The configuration table is then broken into subarrays of data delays and backgrounds. A random number generator is used to randomize the data delay subarray. Depending on if none, one, or two backgrounds are taken after each data

delay point, the relevant background lines are spliced into the randomized data delay subarray and the resulting table is checked to make sure the length is correct.

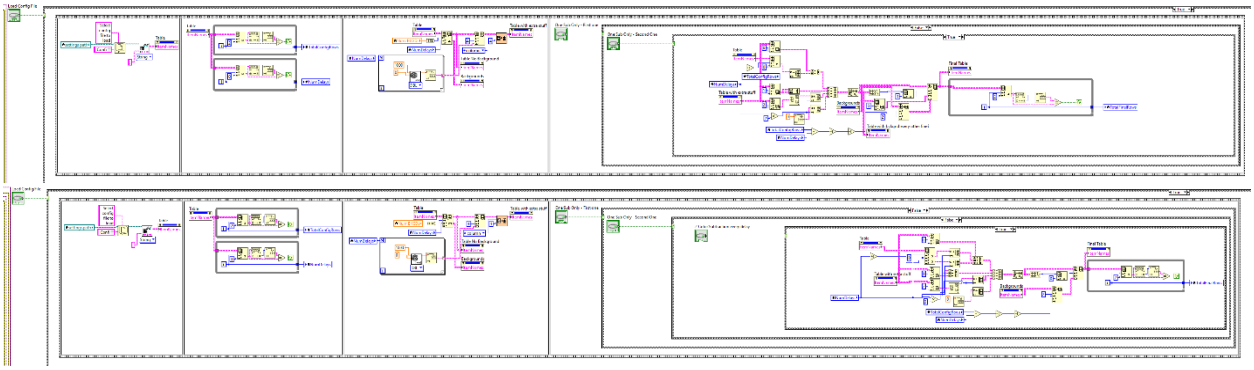

Figure A.6 – Delay randomization and background subtraction code.

The added shutter functionality is implemented as shown in Figure A.7. The code is derived from what was developed by H. L. Williams [2], with modification to ensure adequate time after shutters are reopened is allowed so the XUV, in particular, has time to stabilize. Parallel to this is code to operate the fast (sub 10 ms) shutters from Uniblitz that are vacuum compatible so the XUV itself can be blocked rather than the HHG driving beam. Due to the way communication with the new shutter controller is set up, each shutter channel must be sent a command to either open or close each loop through the configuration table. All shutter actuation commands are followed by user-adjustable delays to allow flexibility in making the code run as quickly as possible while making sure each action is complete before the program moves to the next set of actions.

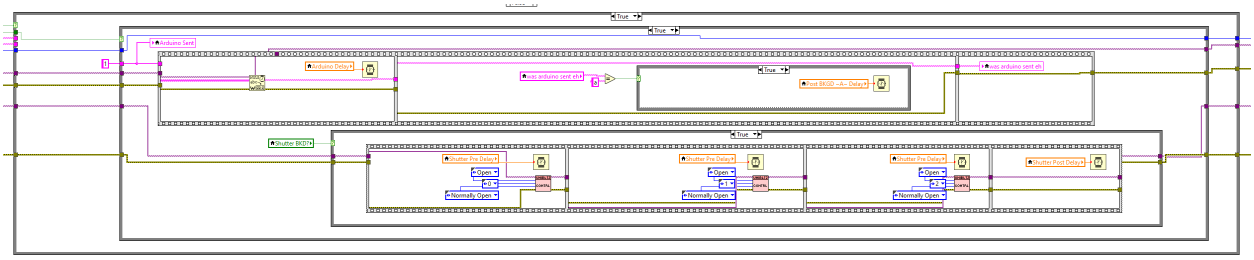

Figure A.7 – Added shutter functionality implemented after data is collected and before the delay stage is moved.

Finally, added user input for describing samples and pump/probe conditions that can be saved with the data itself as a redundancy to information recorded in the lab notebook is implemented. This is done in addition to expanding the number of parameters saved in the settings file to accurately represent the conditions the data was taken under.

A.4 References

[1] Erickson, B. A. Extending Time-Resolved Photoelectron Spectroscopy to the Extreme Ultraviolet. Ph.D., University of California, Berkeley, Proquest, 2021.

[2] Williams, H. L. Ultrafast Dynamics of Adenine Derivatives Studied by Time-Resolved Photoelectron Spectroscopy in Water Microjets. Ph.D., University of California, Berkeley, United States -- California, 2017.

Appendix B – Machine Drawings

B.1 Overview

Machine drawings for the various additions to the instrument carried out over the duration of this Ph.D. work.

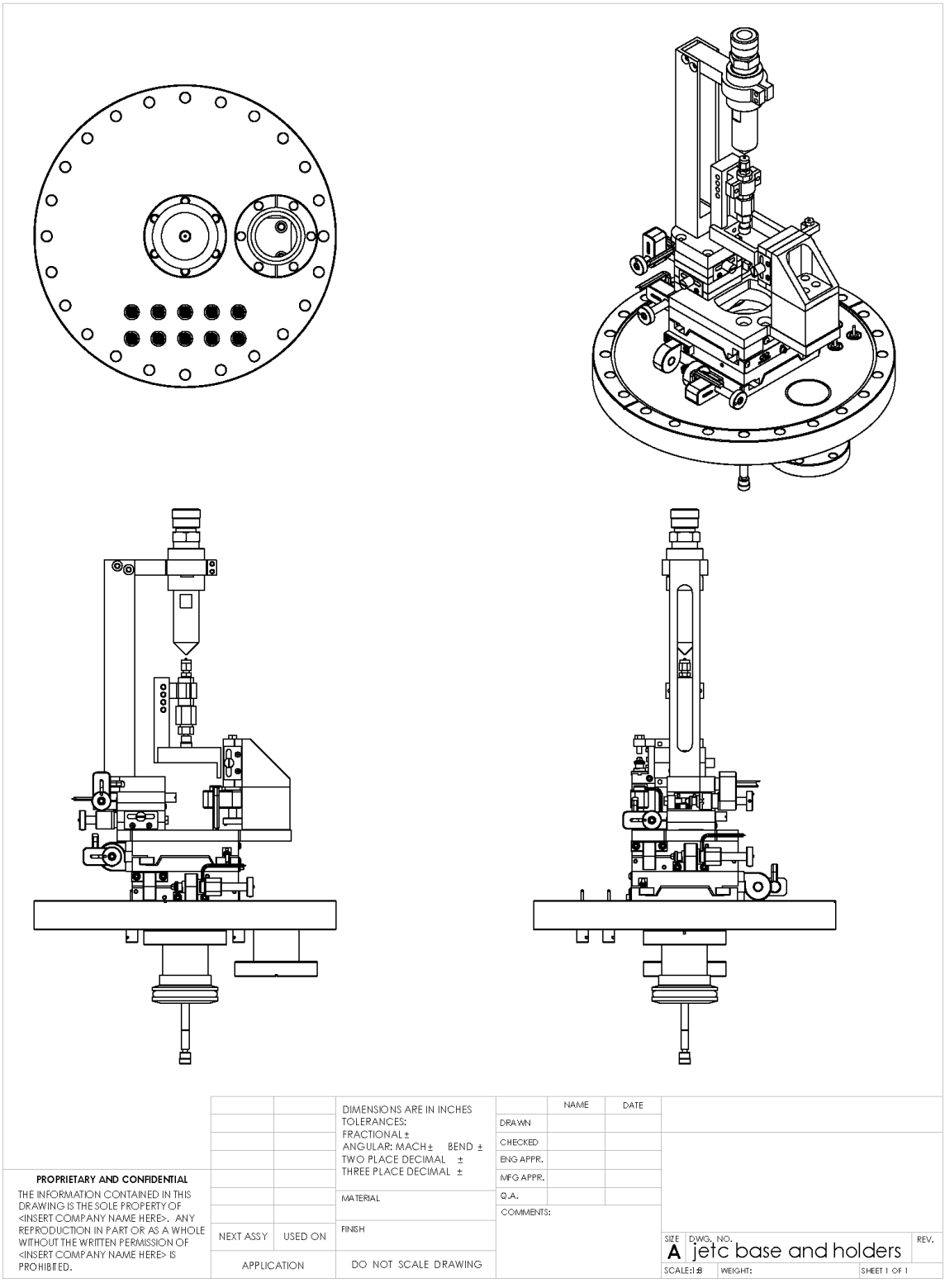

Figure B.1 – Jet manipulation and catcher manipulation assembly overview.

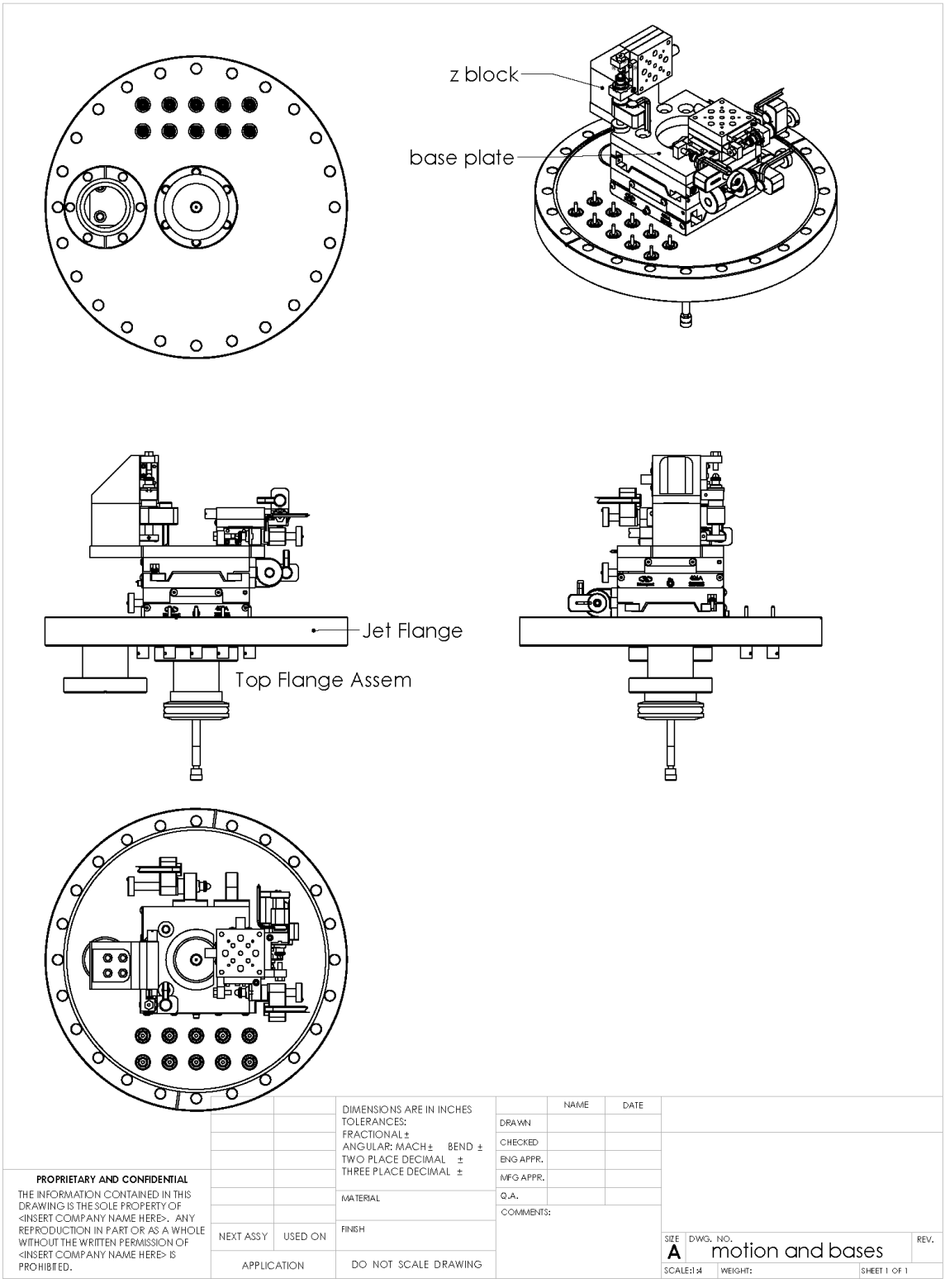

Figure B.2 – Jet and catcher motion assembly overview.

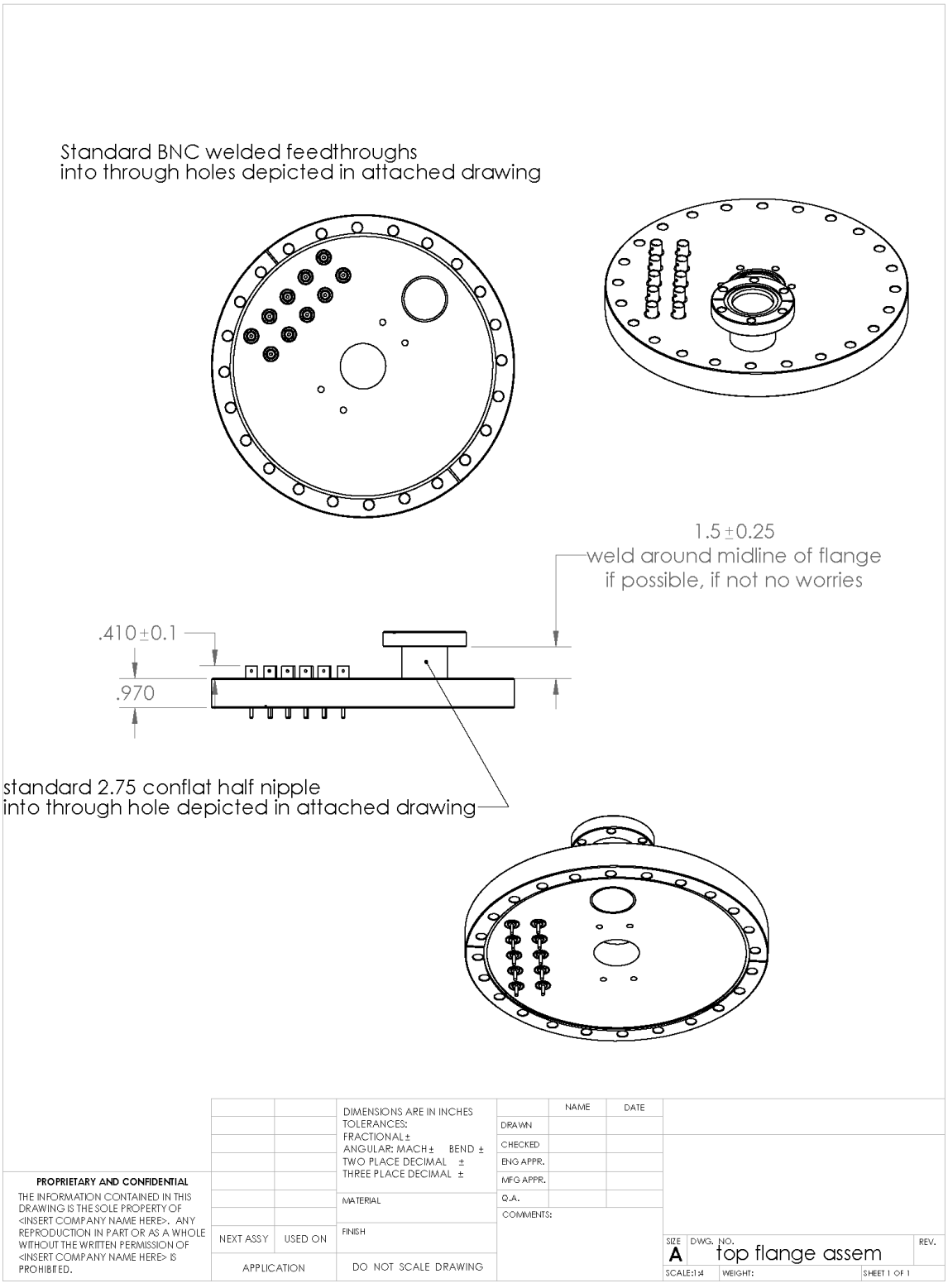

Figure B.3 – Flange with feedthroughs for jet motion and manipulation assembly.

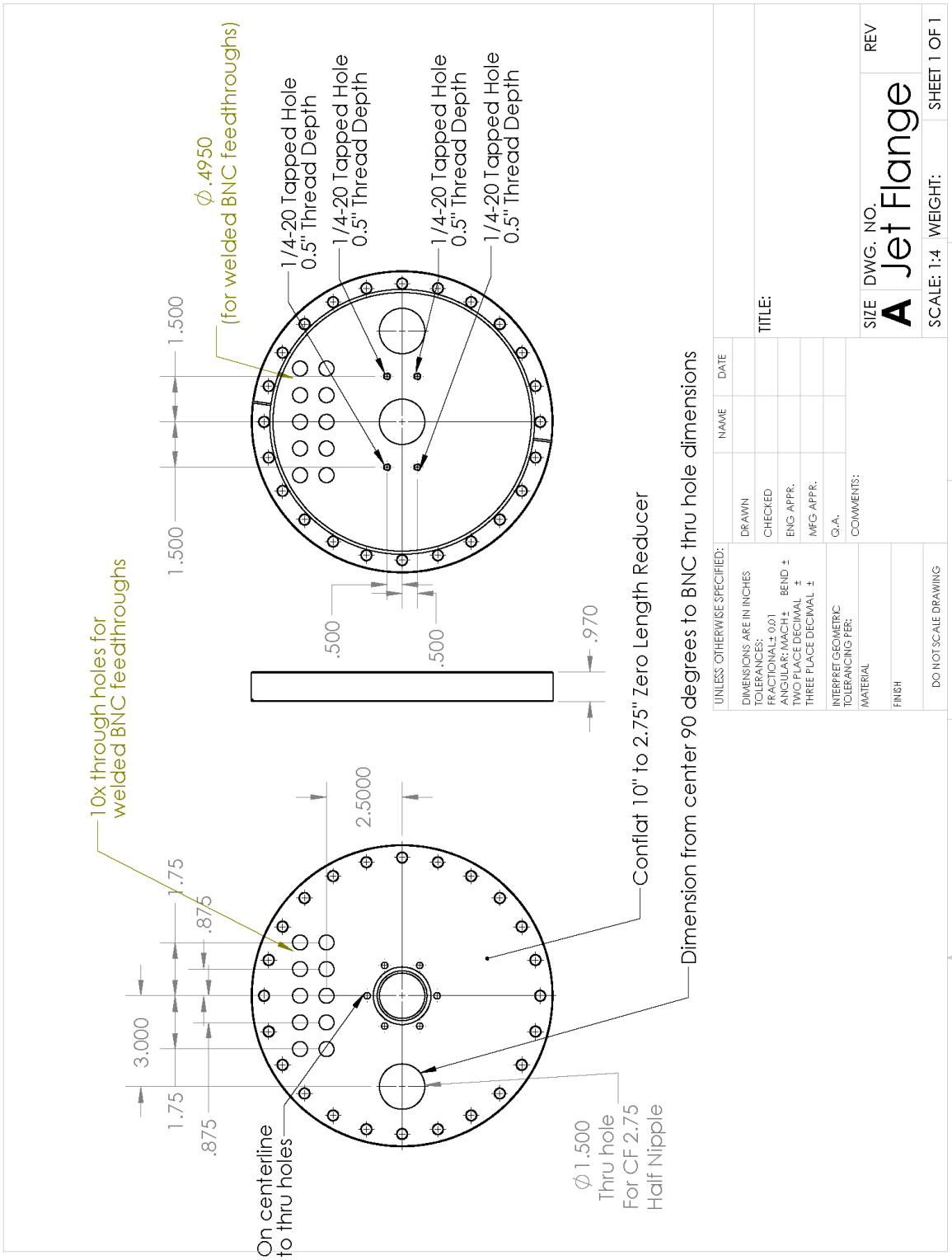

Figure B.4 – Modified 10” conflat flange with holes to weld 10 BNC electrical feedthroughs and a 2.75” conflat half-nipple.

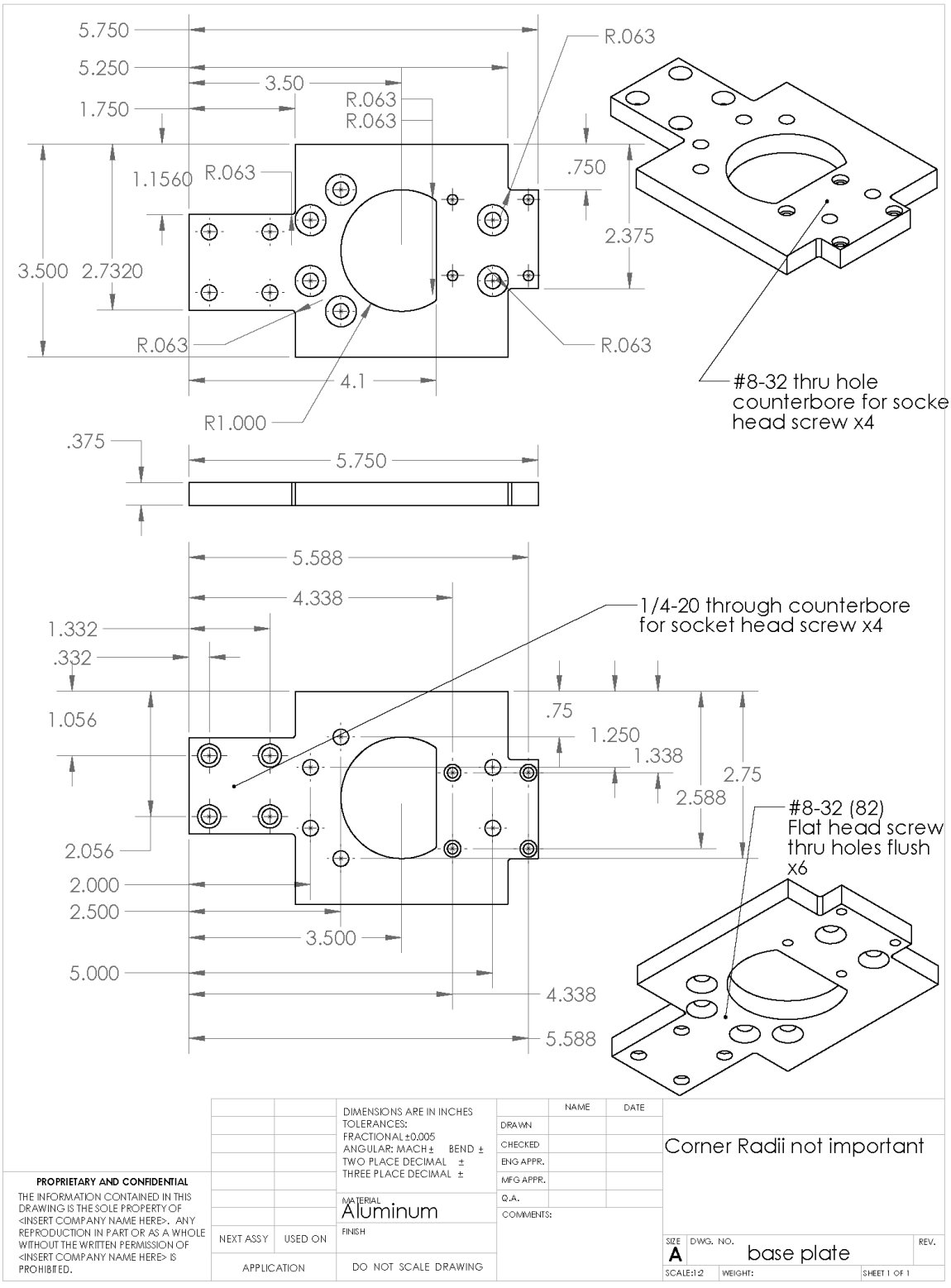

Figure B.5 – Base plate for mounting 0.5” travel stages for independent catcher and jet motion to the 1” travel stages for coupled jet and catcher motion.

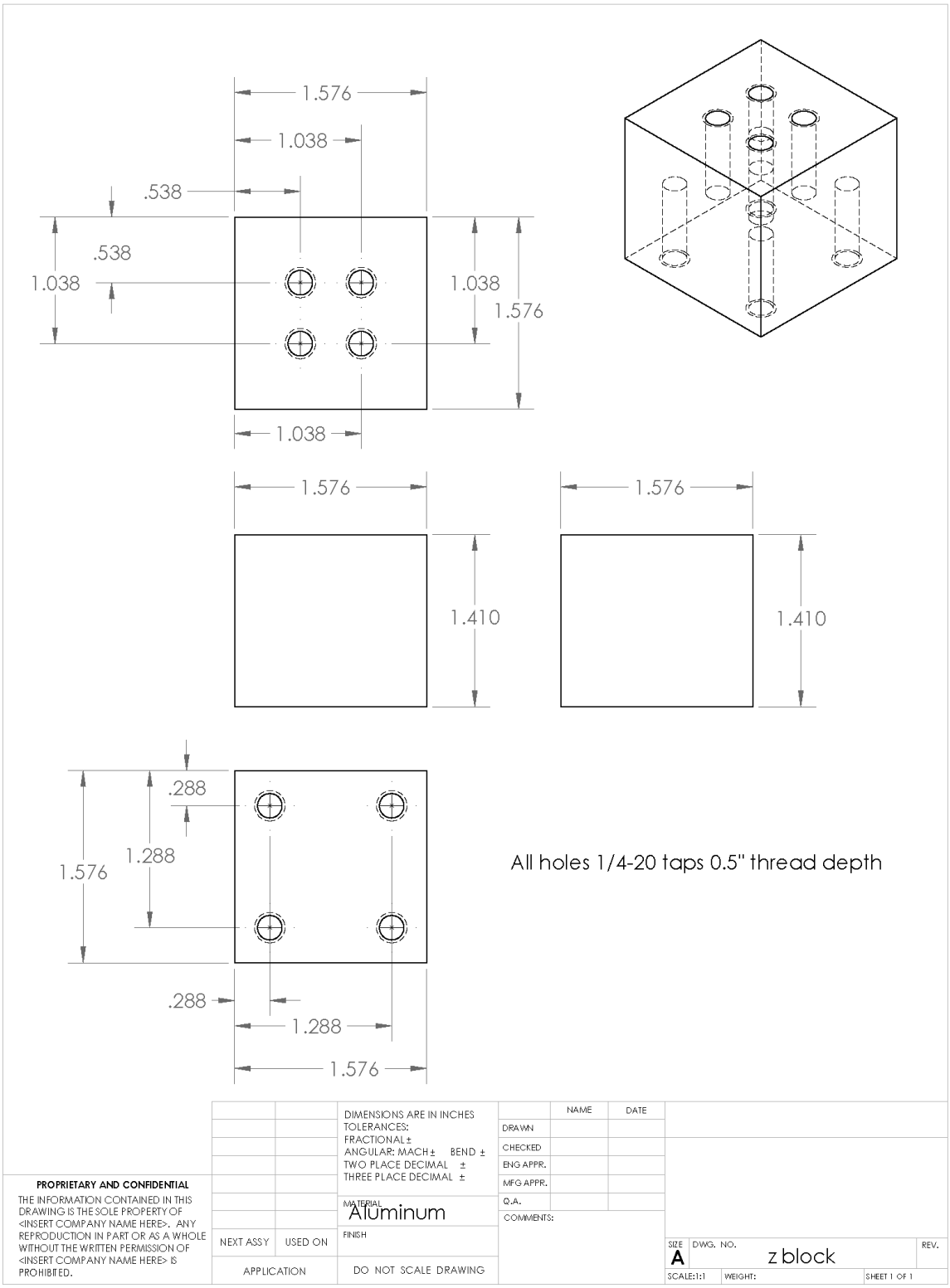

Figure B.6 – Thread adapter for accommodating a z-axis stage for the liquid microjet.

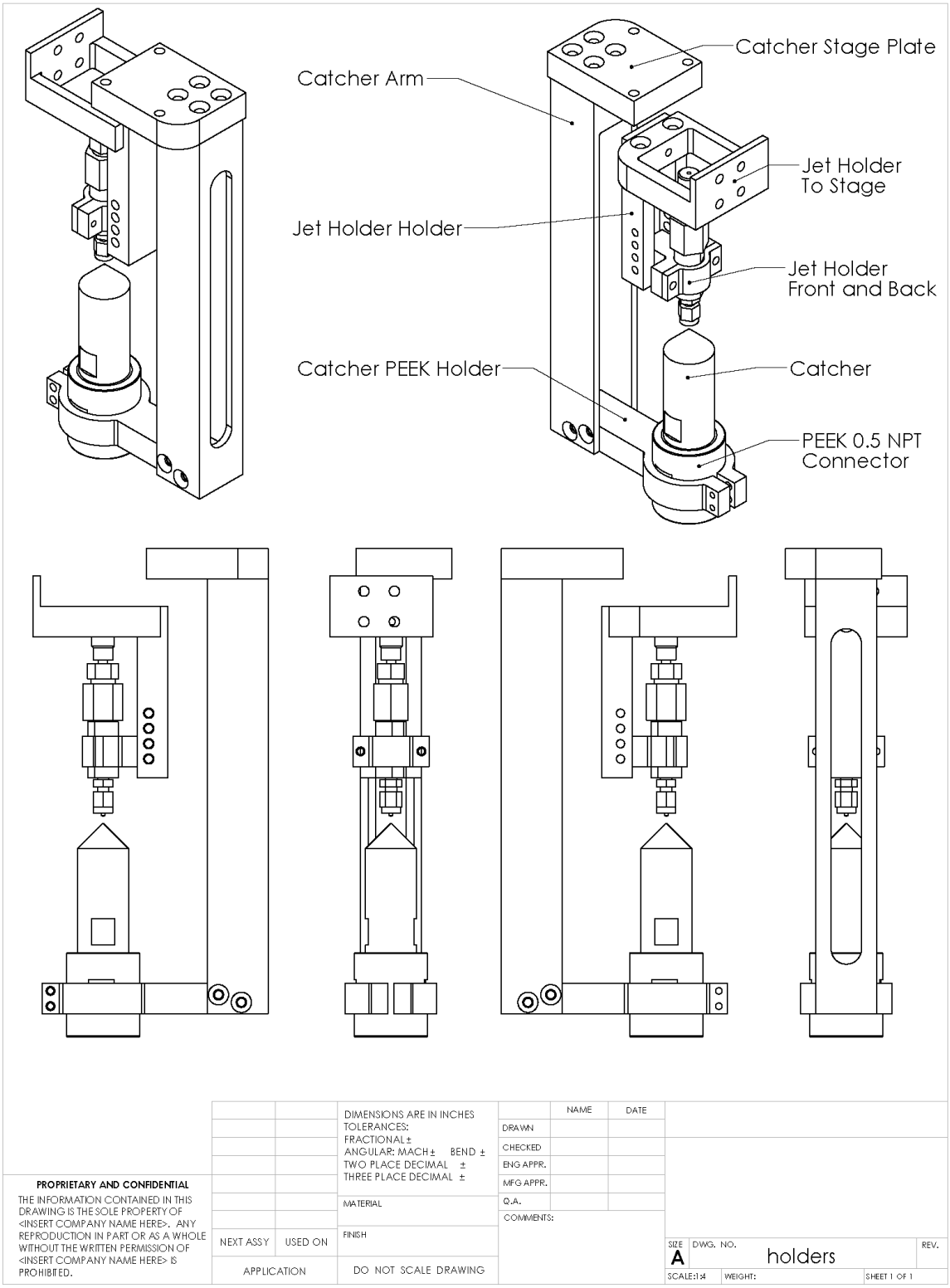

Figure B.7 – Assembly of mounting arms for connecting the liquid microjet and catcher to the motion assembly.

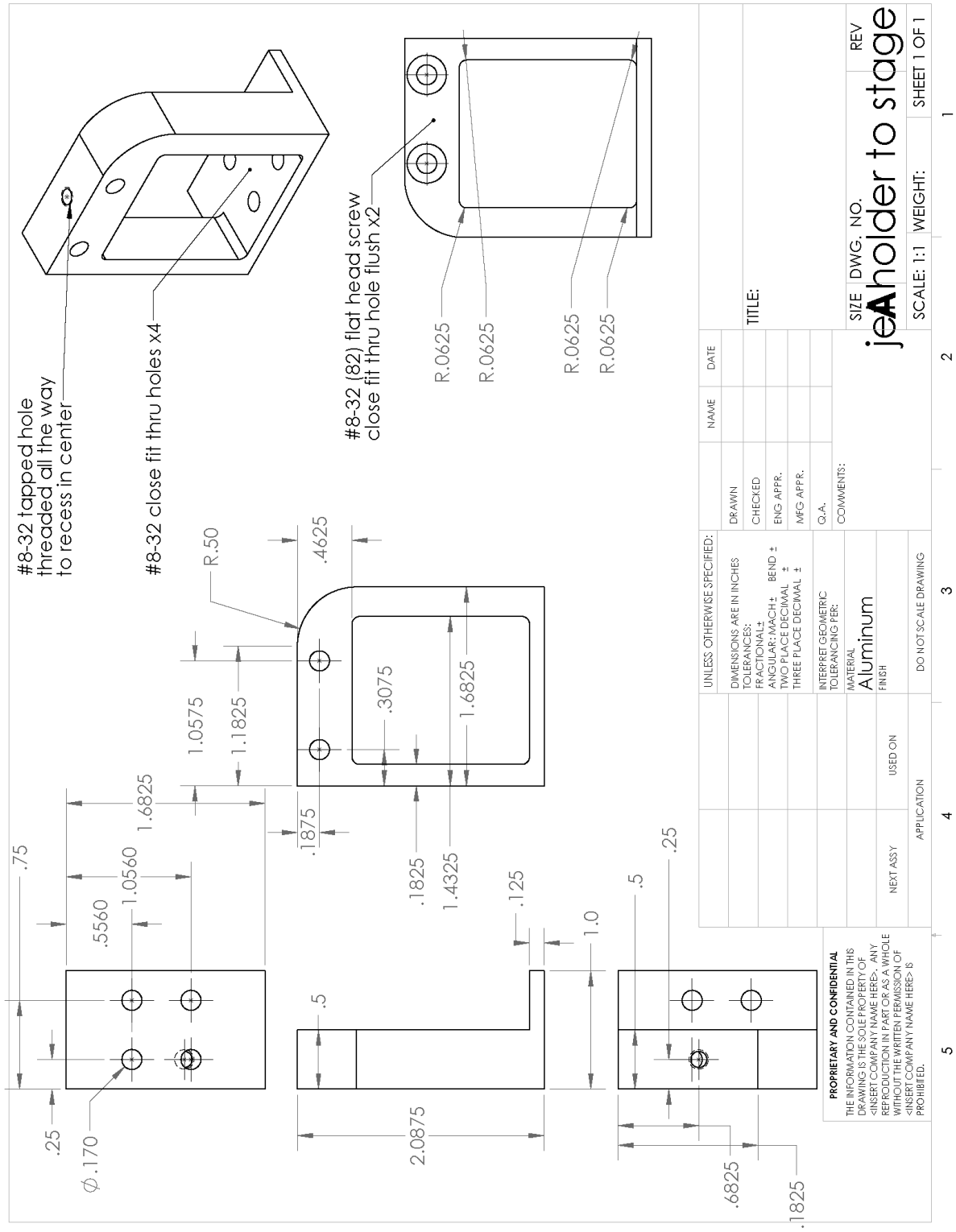

Figure B.8 – Adapter bracket extending horizontally from the microjet z-axis stage to the mounting arm shown in Figure B.11.

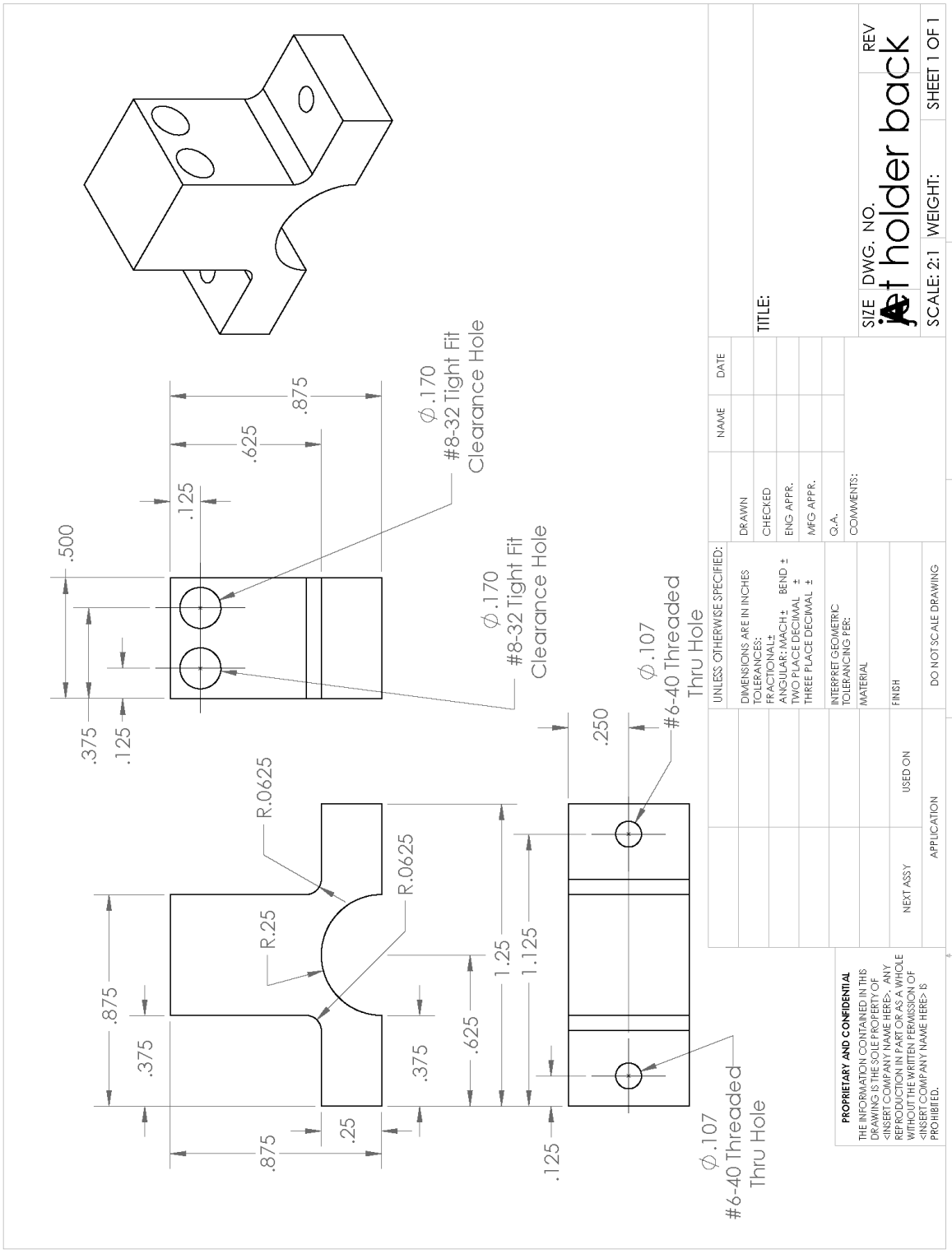

Figure B.9 – The back half of the insulating mounting assembly that holds the microjet.

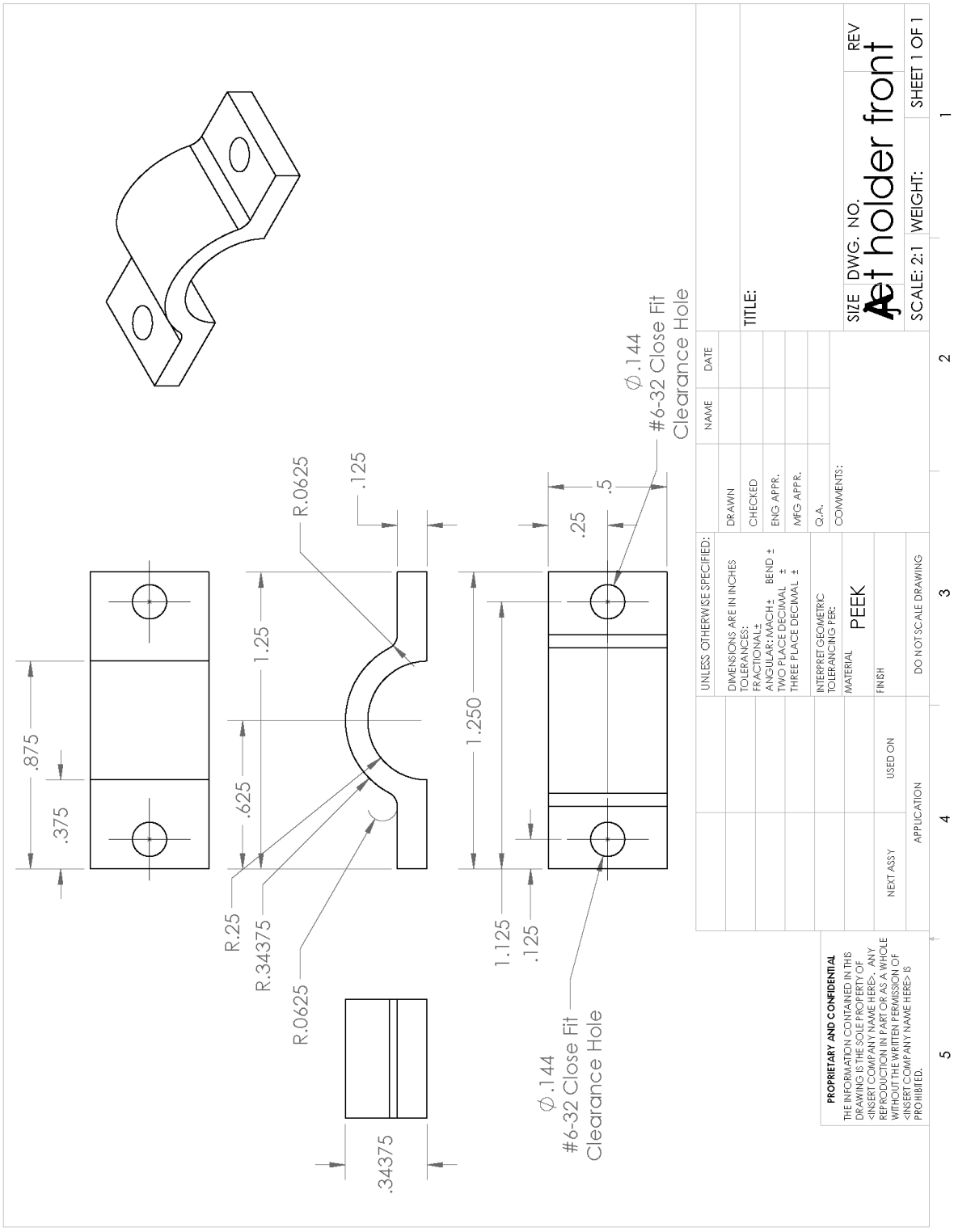

Figure B.10 – The front half of the insulating mounting assembly that holds the microjet.

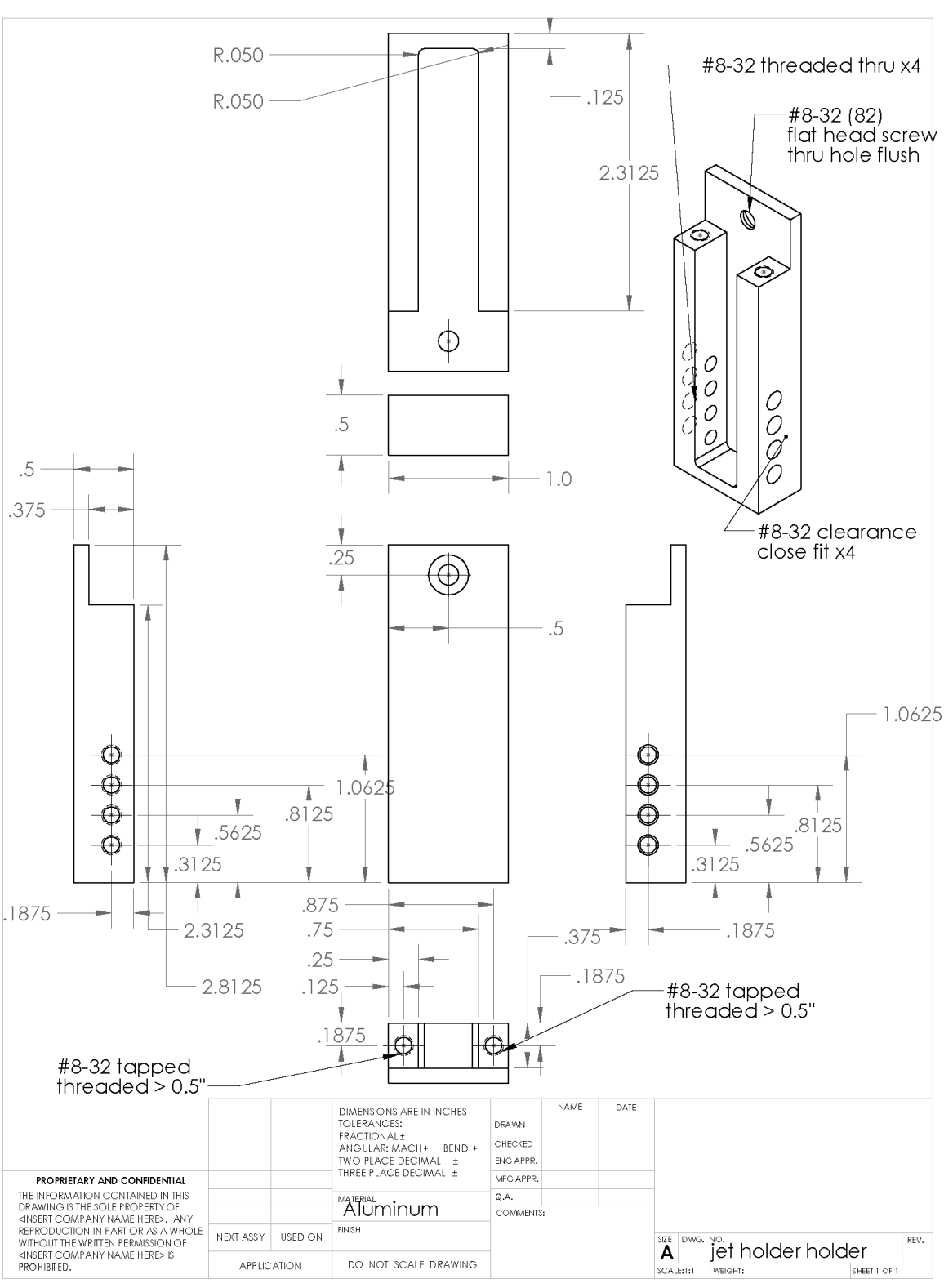

Figure B.11 – Mounting arm extending vertically from the adapter bracket shown in Figure B.8 to the microjet mount shown in Figure B.9.

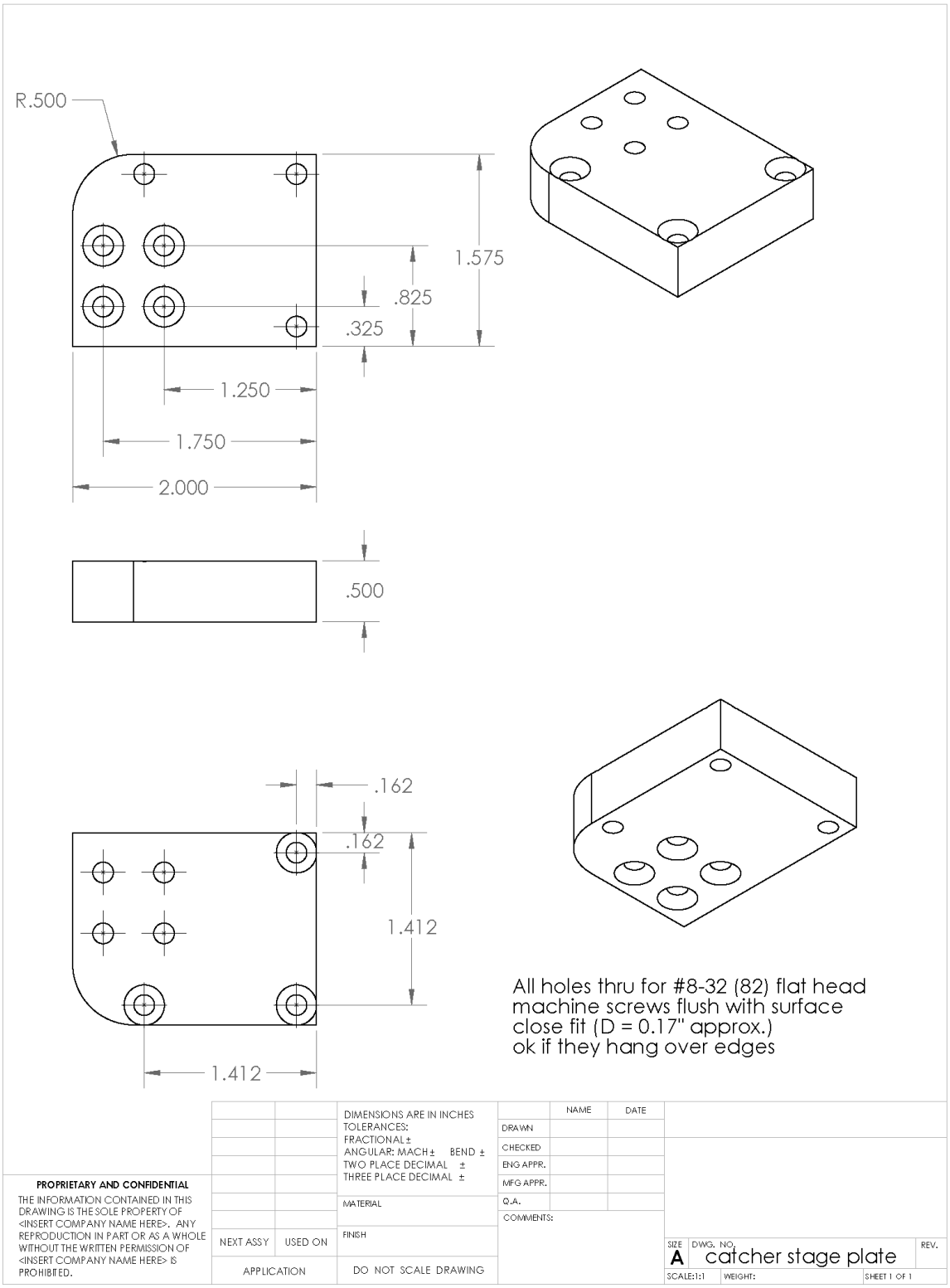

Figure B.12 – Thread adapter plate accommodating the differing hole spacing between the XY-axis stages for the independent catcher motion and the arm extending vertically for mounting the catcher.

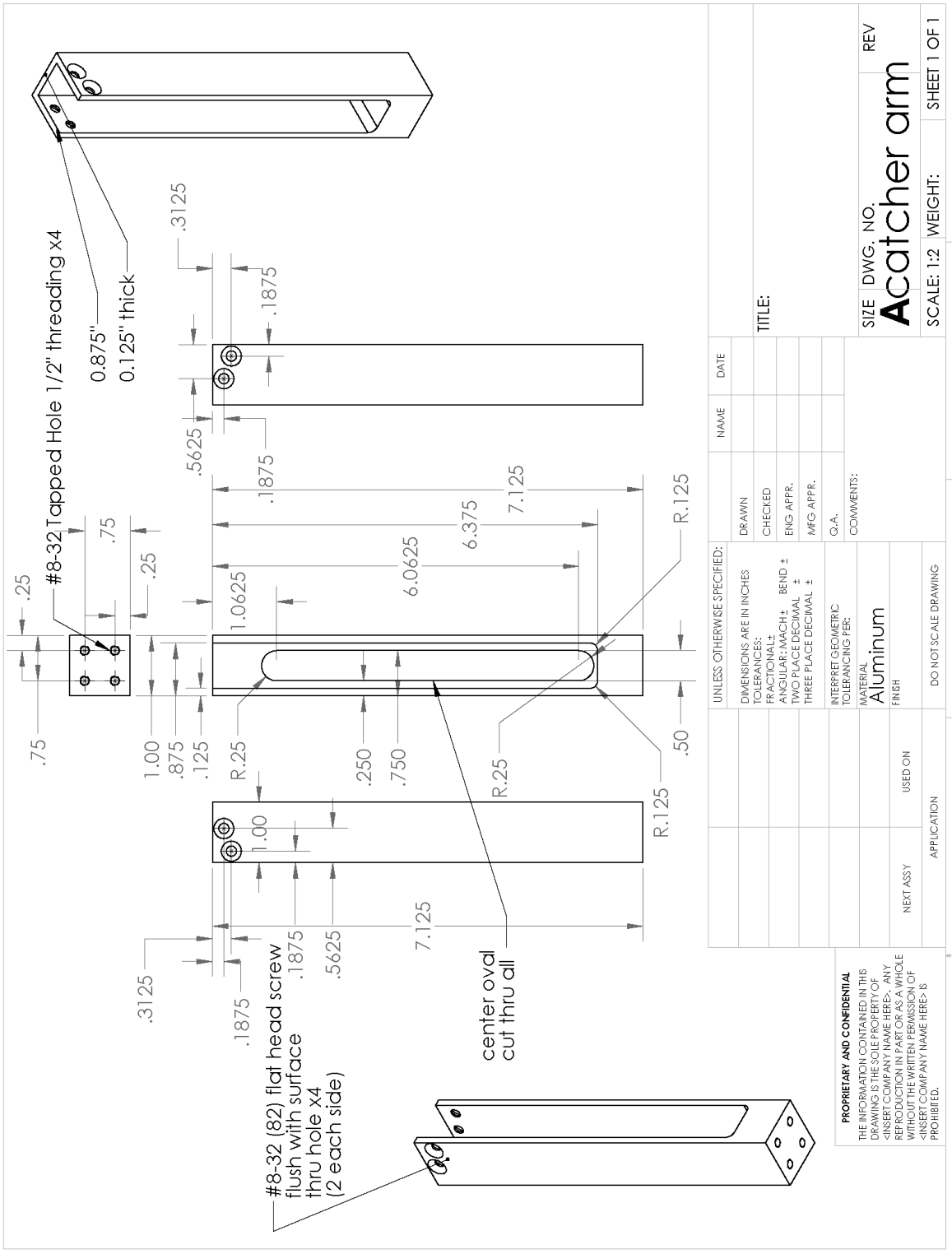

Figure B.13 – Arm extending vertically to connect the catcher to the motion assembly.

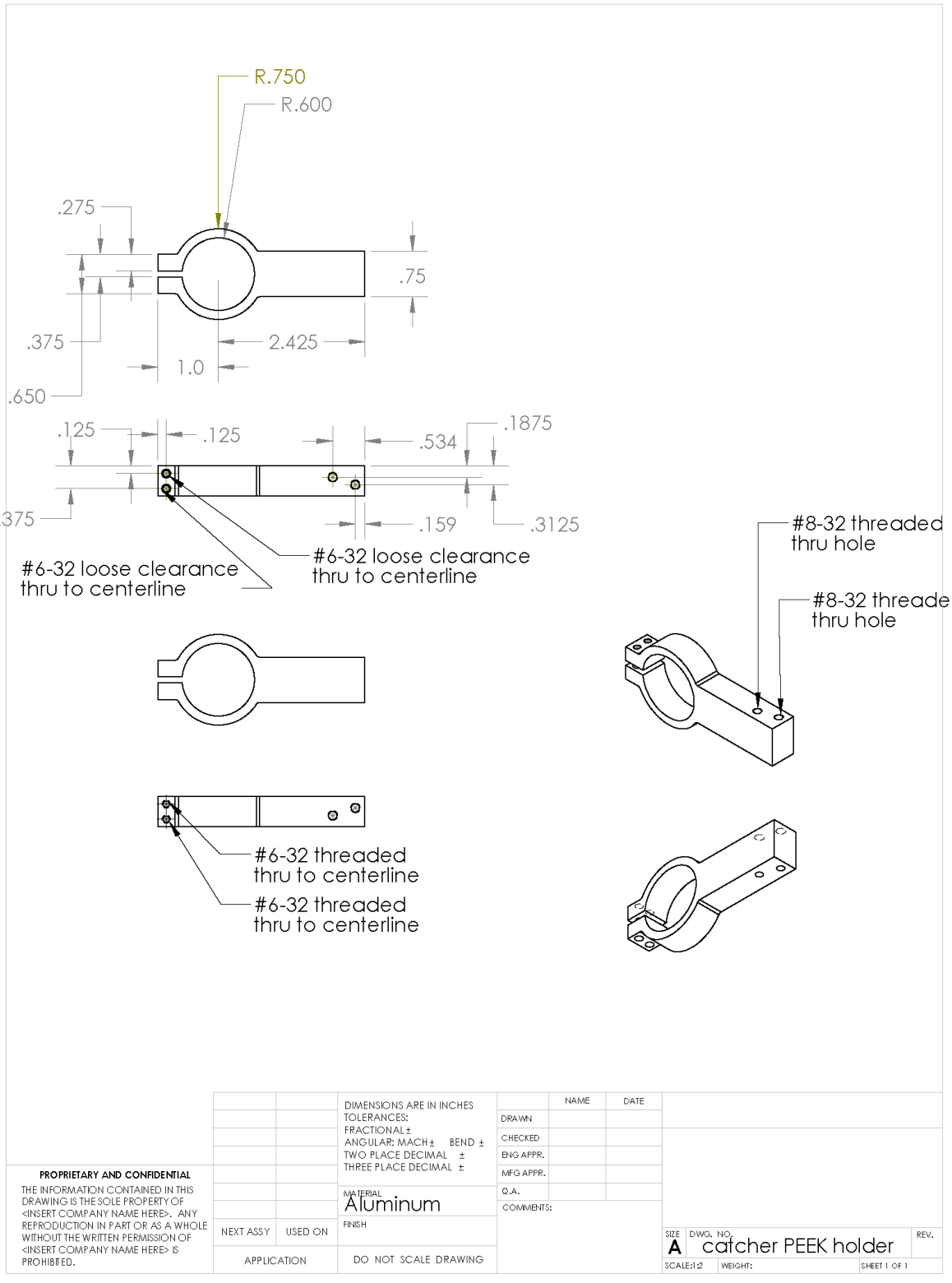

Figure B.14 – The arm extending from the component shown in Figure B.13 to the catcher assembly.

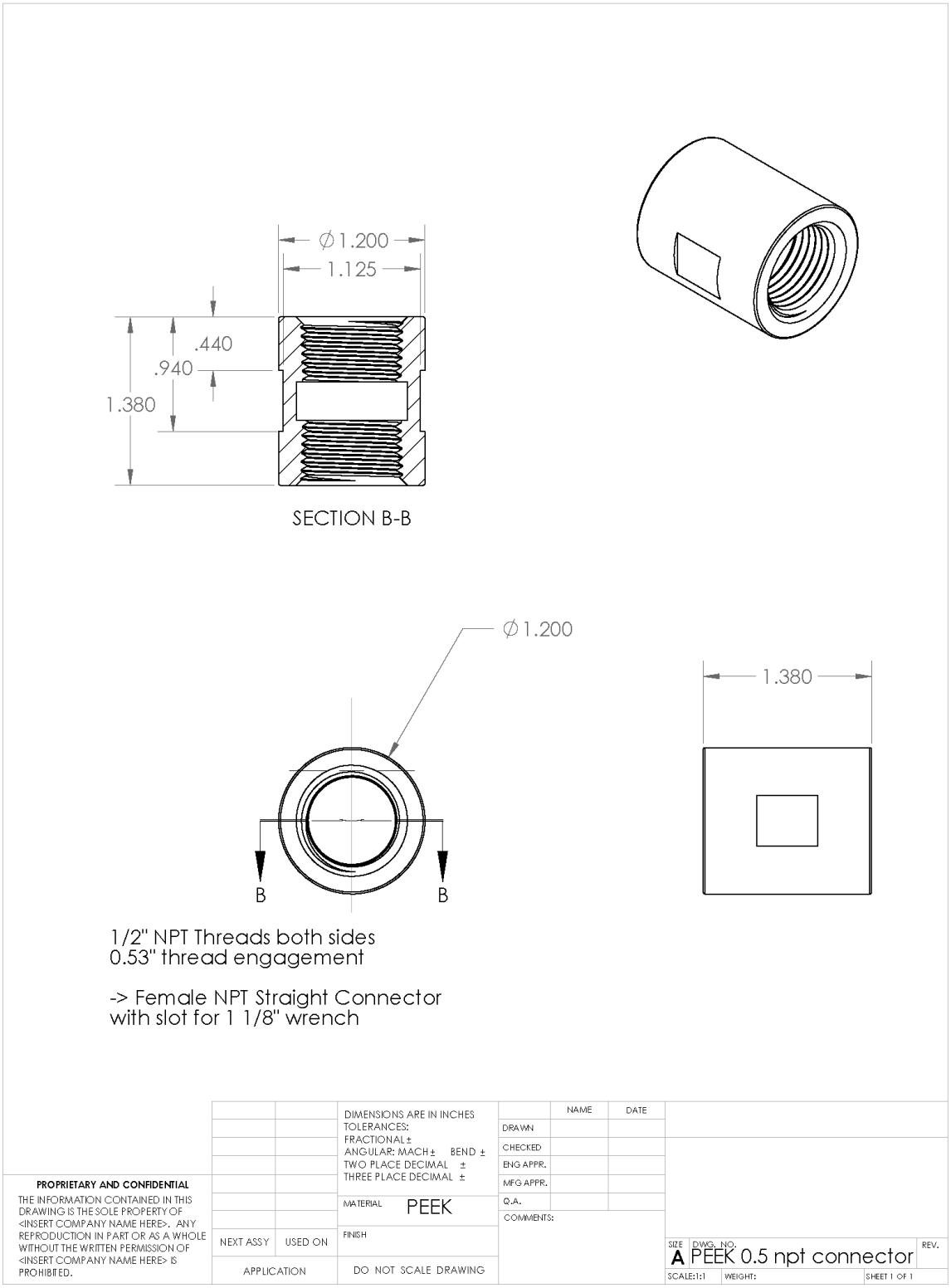

Figure B.15 – PEEK 0.5” NPT union for electrically isolating the catcher from the rest of the apparatus.

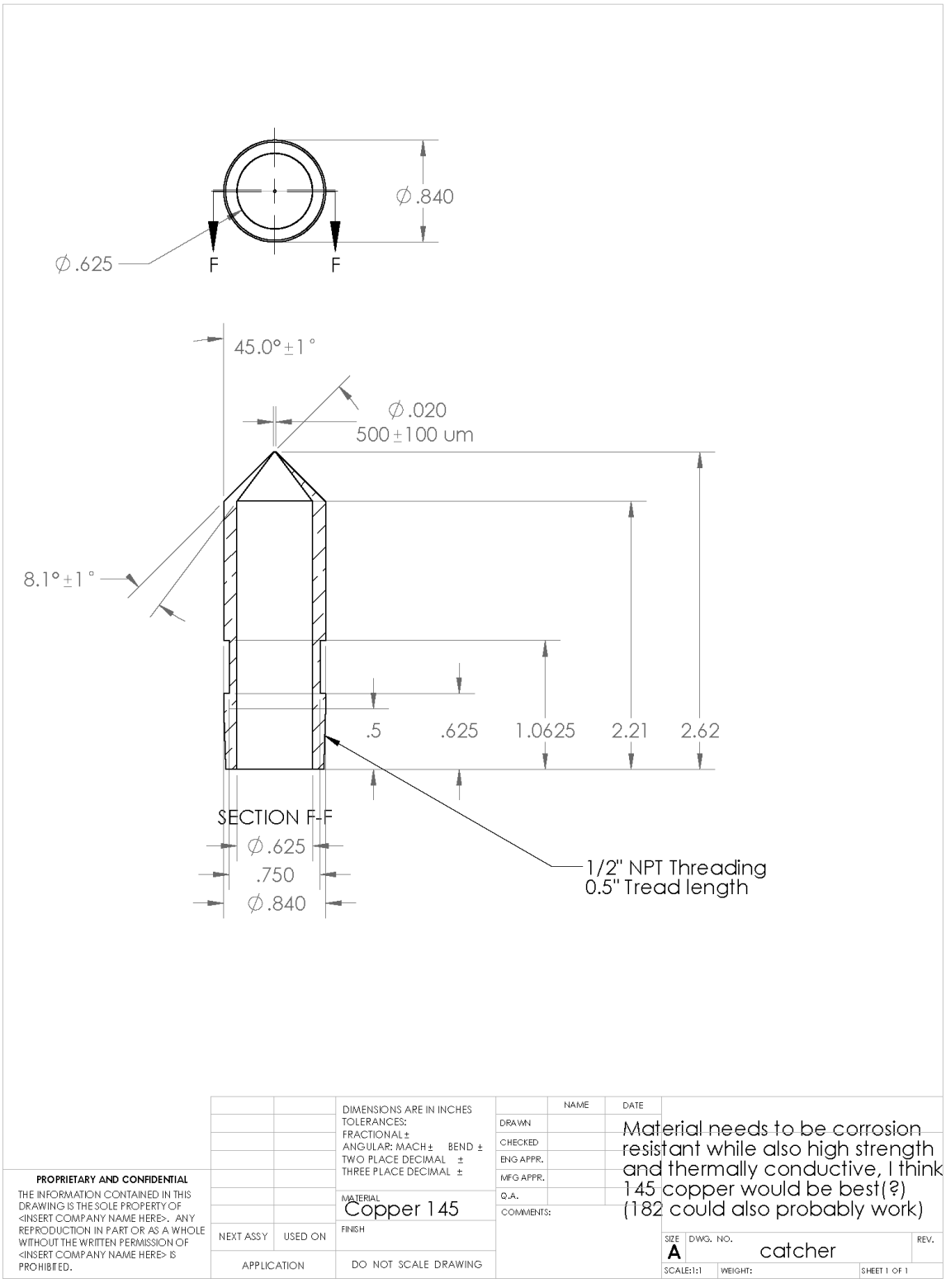

Figure B.16 – First version of the copper catcher made, connecting to the NPT adapter shown in Figure B.15.

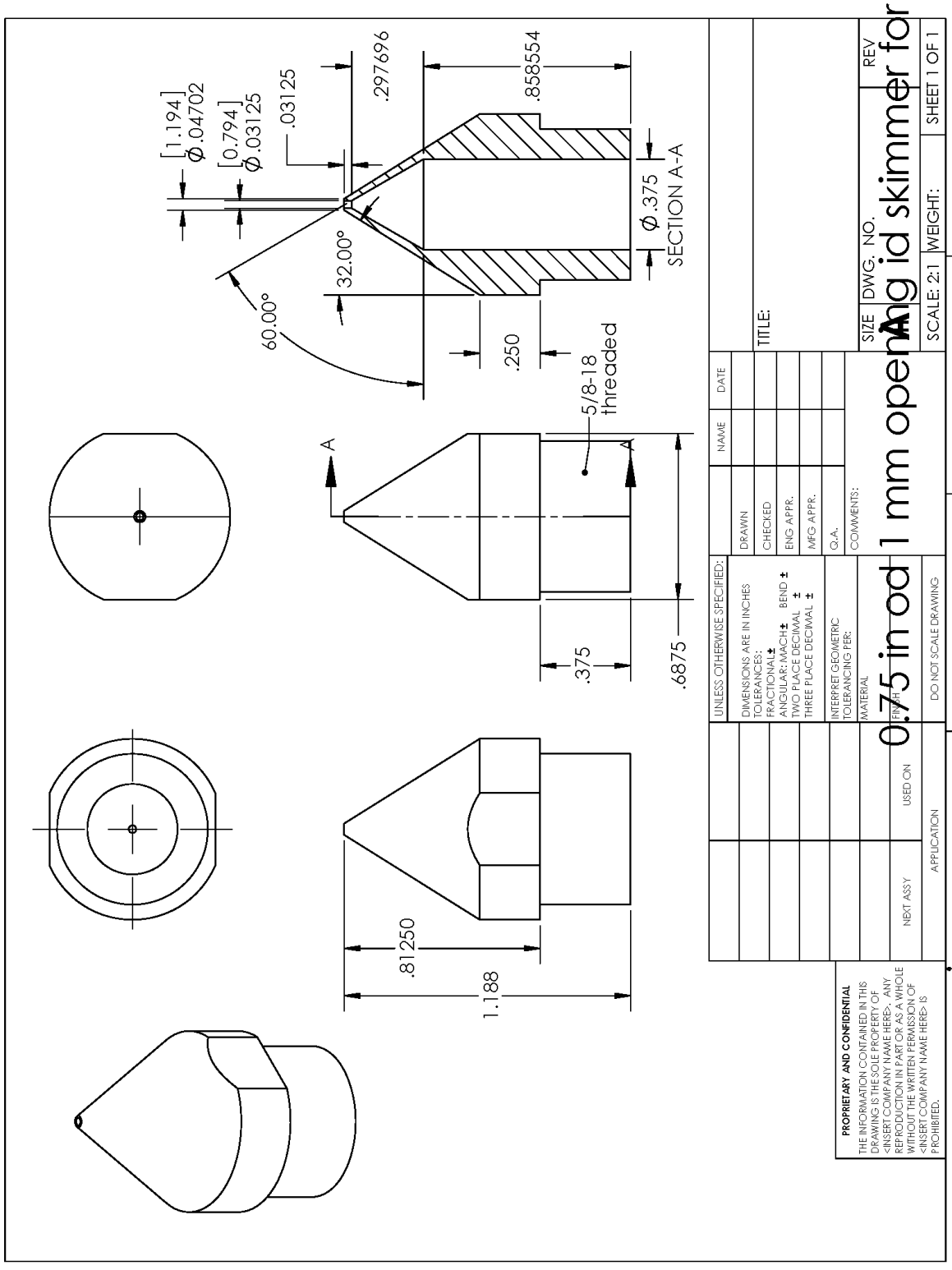

Figure B.17 – Redesigned copper catcher.

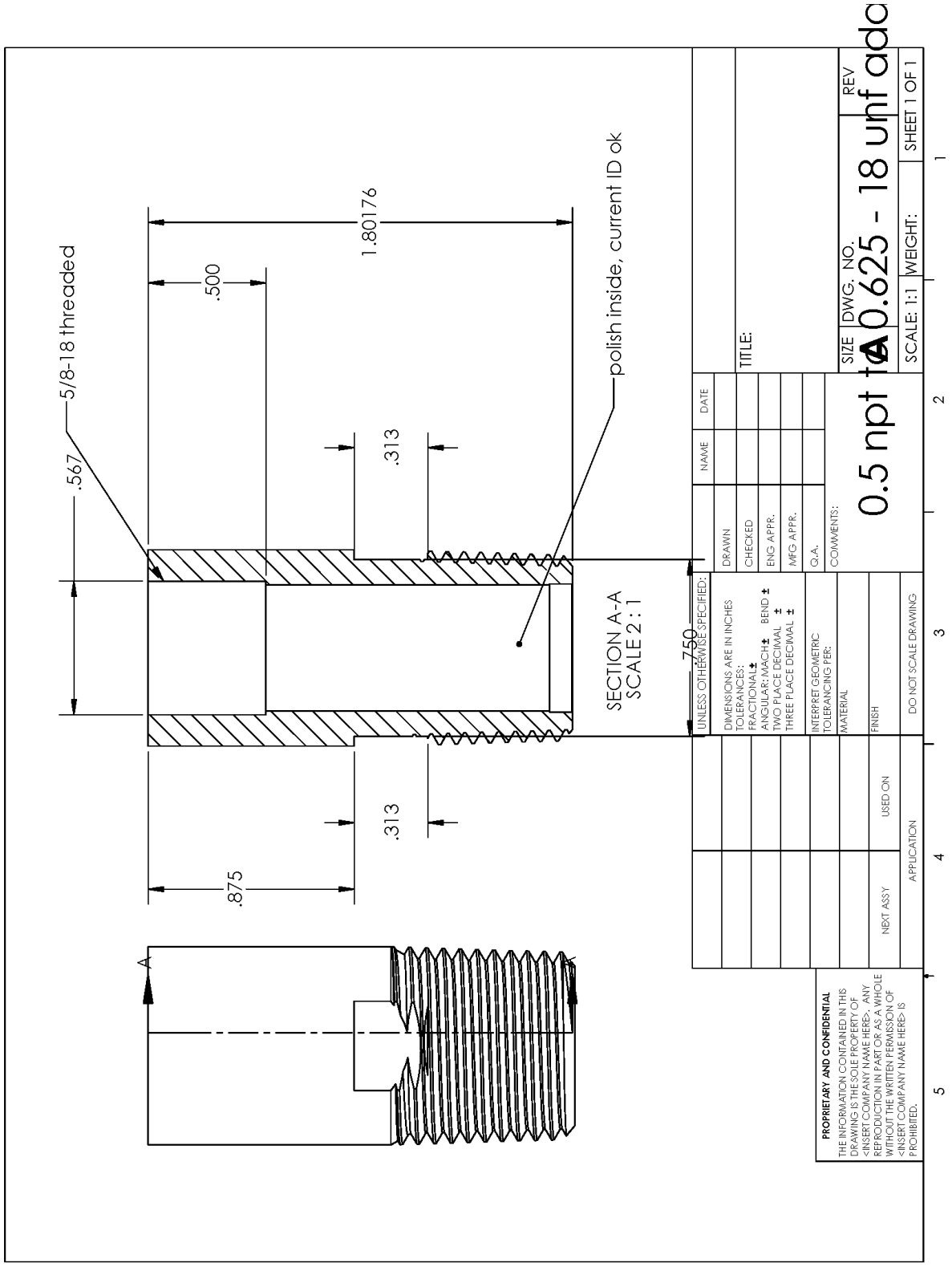

Figure B.18 – NPT to 5/8-18 thread adapter for mounting threaded catcher tips.

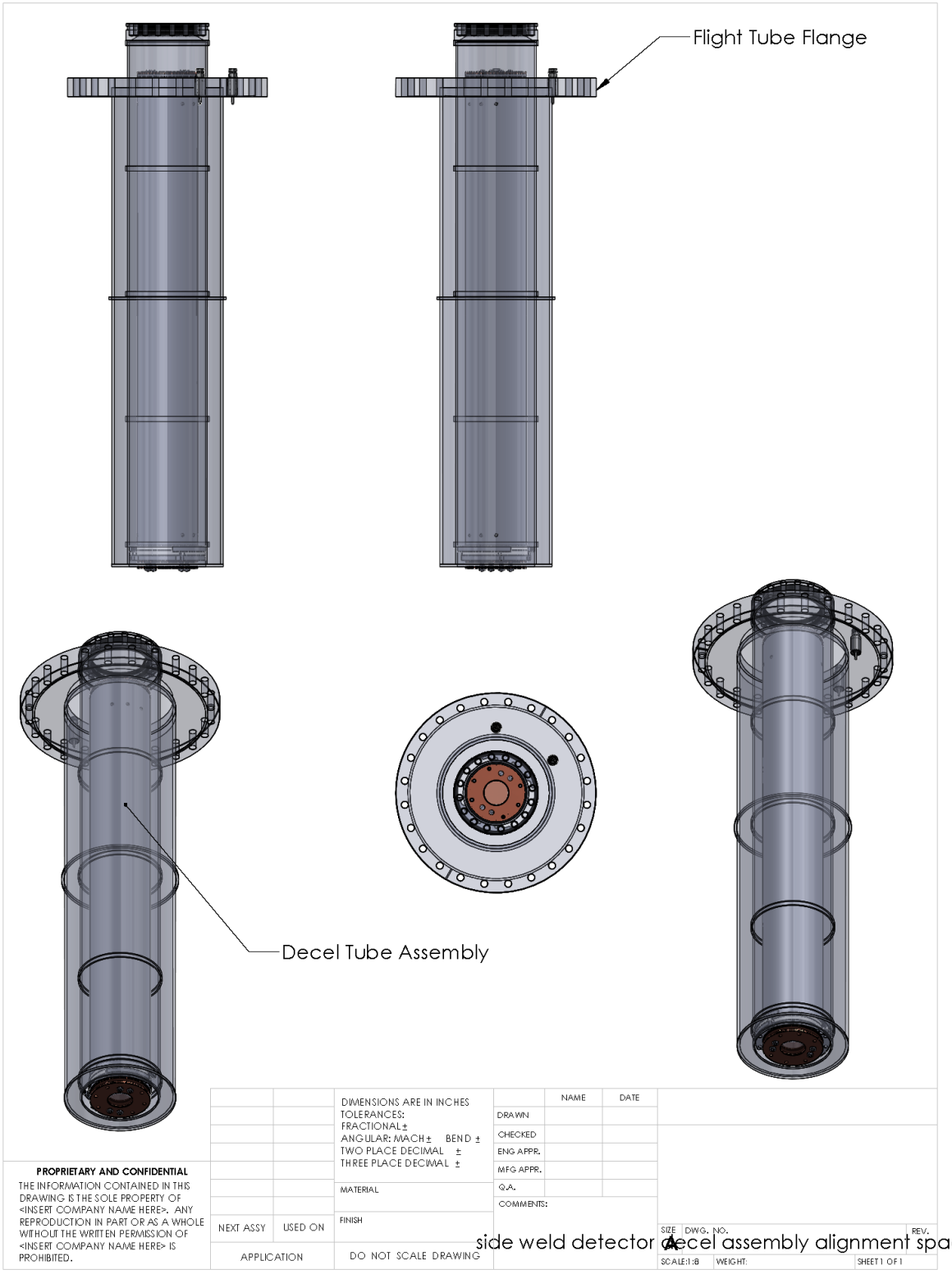

Figure B.19 – Decelerator assembly shown inside of the flight tube.

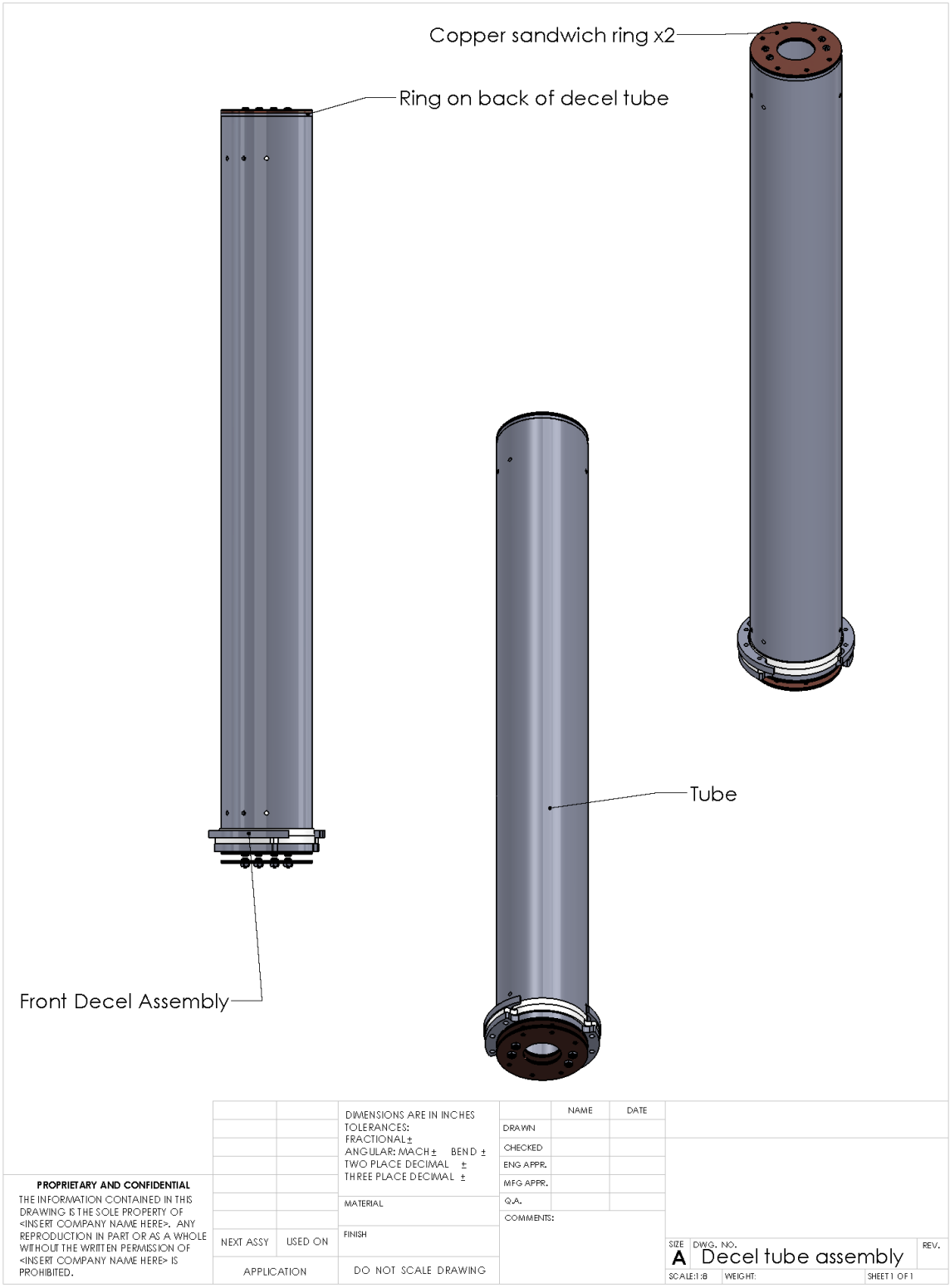

Figure B.20 – Decelerator assembly.

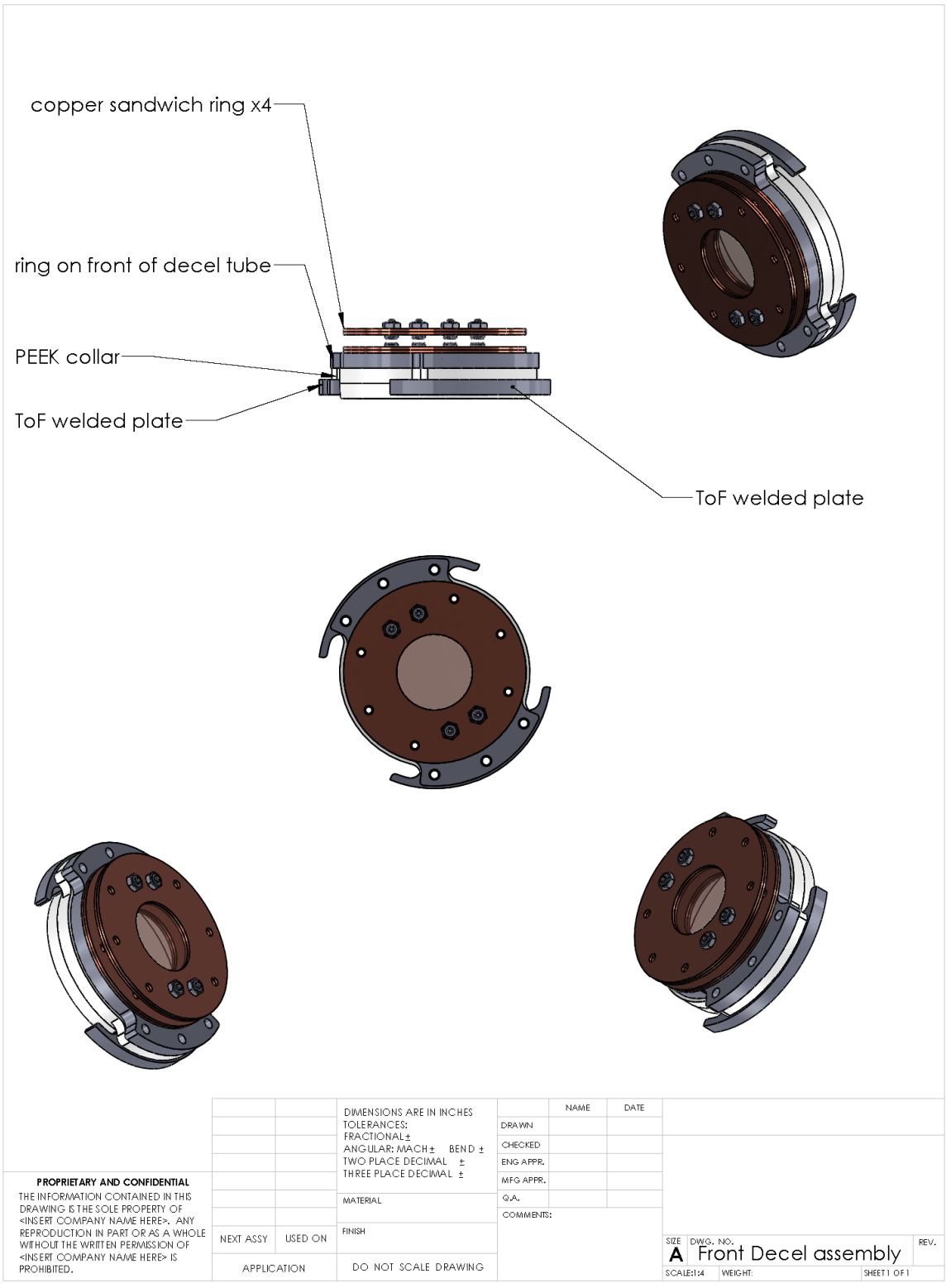

Figure B.21 – Electrode assembly at the front of the decelerator tube with mounting brackets shown.

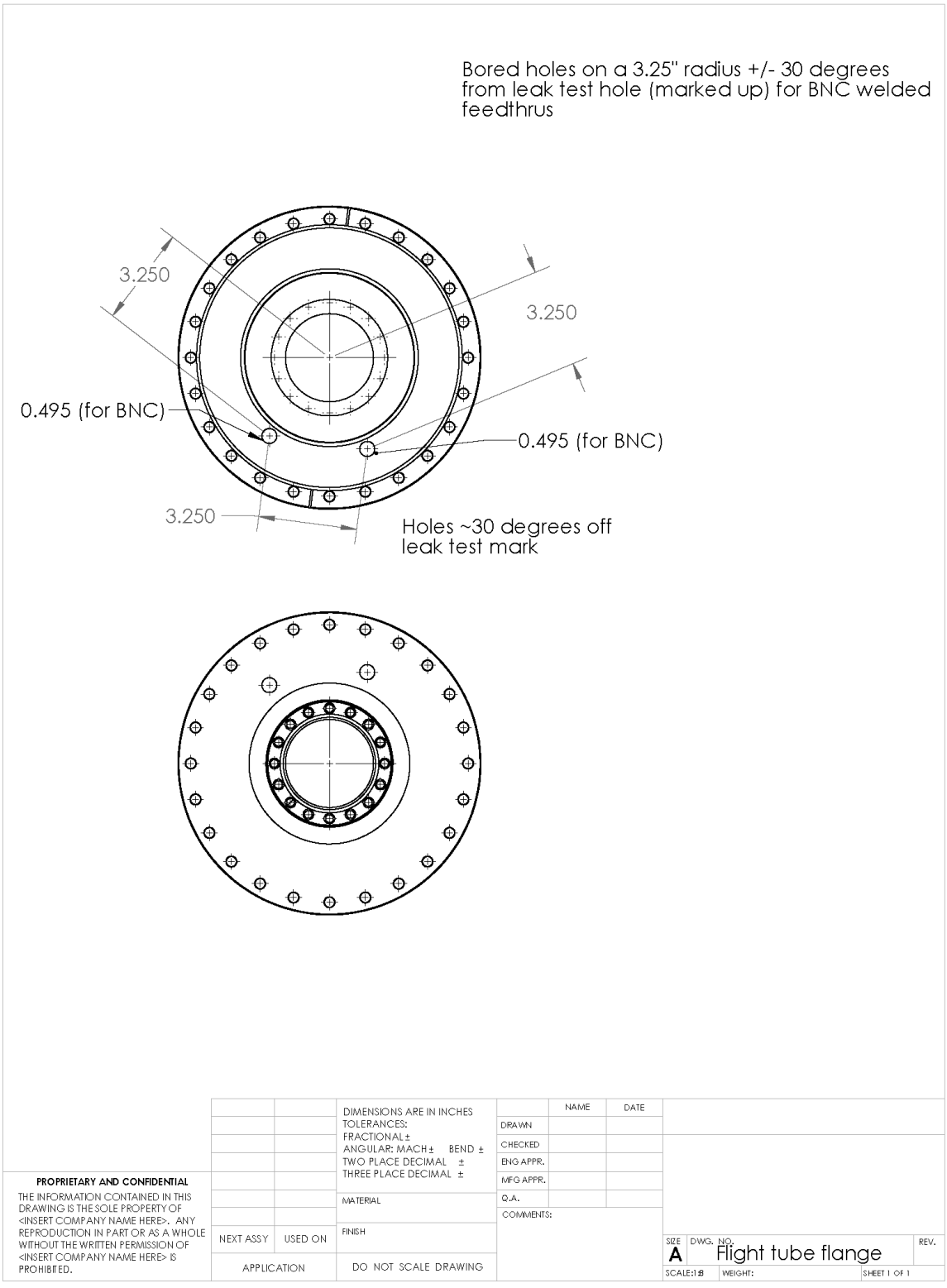

Figure B.22 – Flight tube flange modified with for welding BNC feedthroughs.

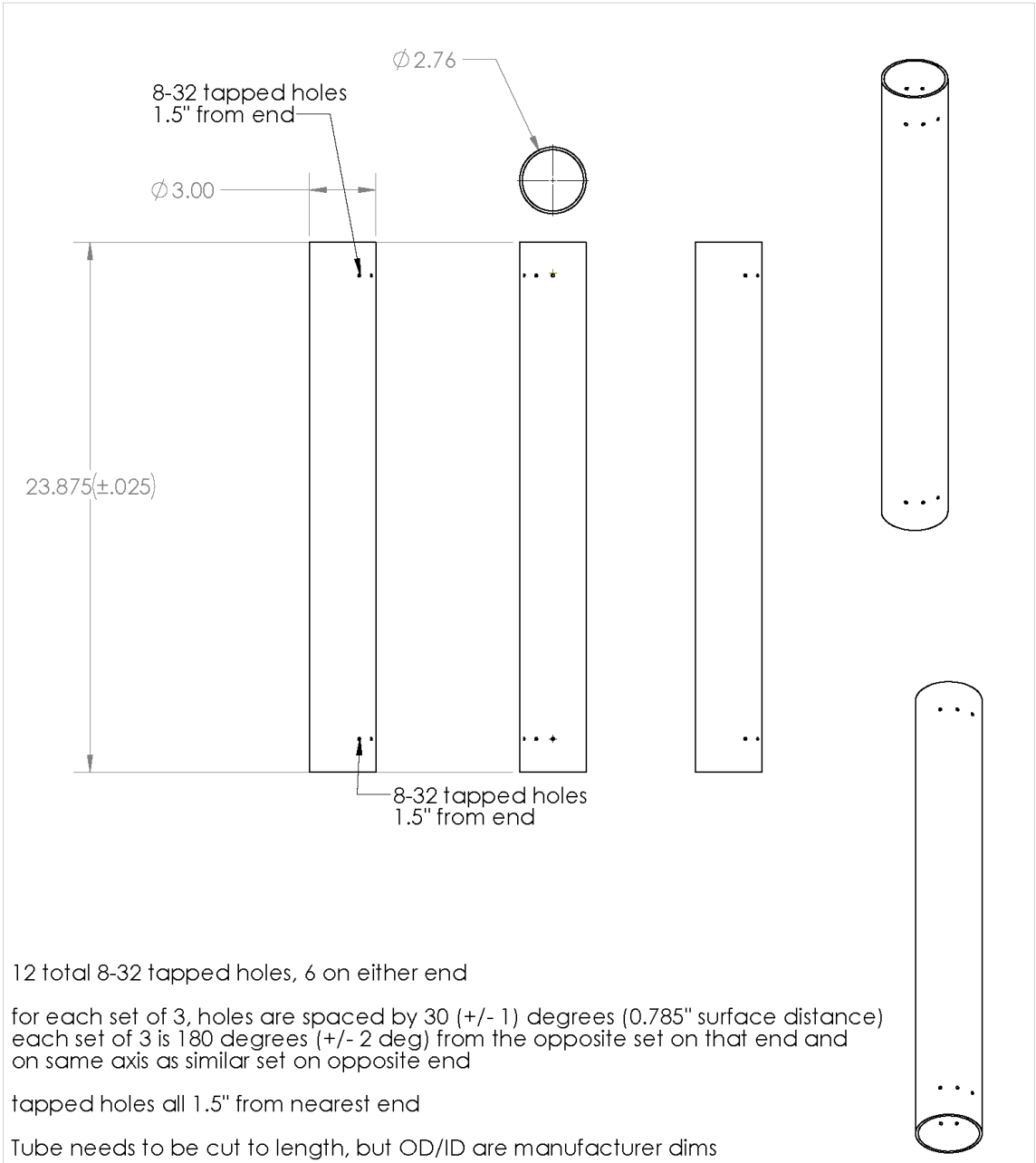

12 total 8-32 tapped holes, 6 on either end

for each set of 3, holes are spaced by 30 (+/- 1) degrees (0.785" surface distance) each set of 3 is 180 degrees (+/- 2 deg) from the opposite set on that end and on same axis as similar set on opposite end

tapped holes all 1.5" from nearest end

Tube needs to be cut to length, but OD/ID are manufacturer dims

		DIMENSIONS ARE IN INCHES TOLERANCES: FRACTIONAL ± ANGULAR: MACH ± BEND ± TWO PLACE DECIMAL ± THREE PLACE DECIMAL ±		NAME	DATE
			DRAWN		
			CHECKED		
			ENG APPR.		
			MFG APPR.		
			Q.A.		
		MATERIAL	COMMENTS:		
NEXT ASSY	USED ON	FINISH			
APPLICATION		DO NOT SCALE DRAWING			

SIZE	DWG. NO.	REV.
A	tube	
SCALE:1:8	WEIGHT:	SHEET 1 OF 1

Figure B.23 – Decelerator tube with threaded holes for adjustment screws.

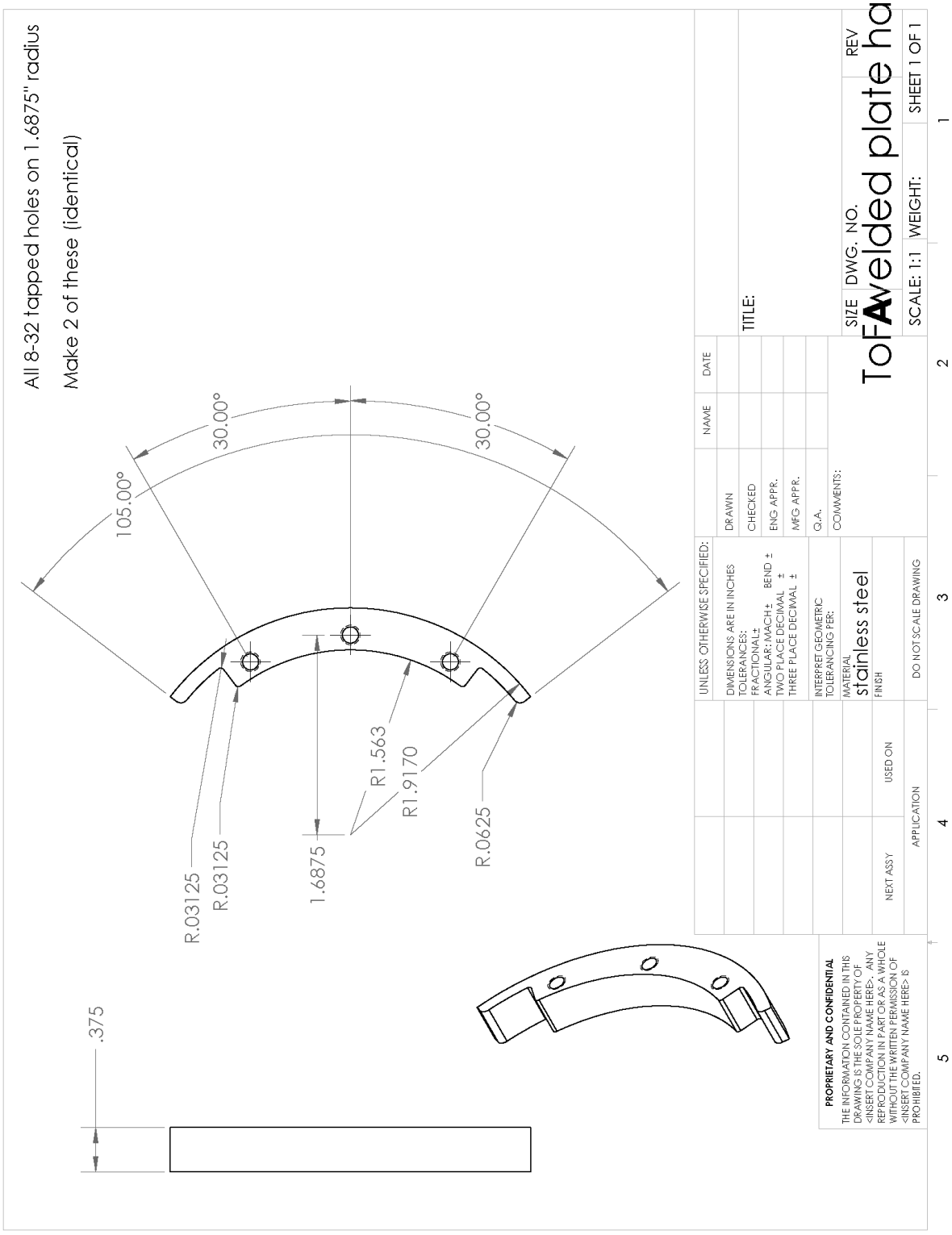

Figure B.24 – Collars for welding inside the flight tube serving as mounting points for the front of the decelerator assembly.

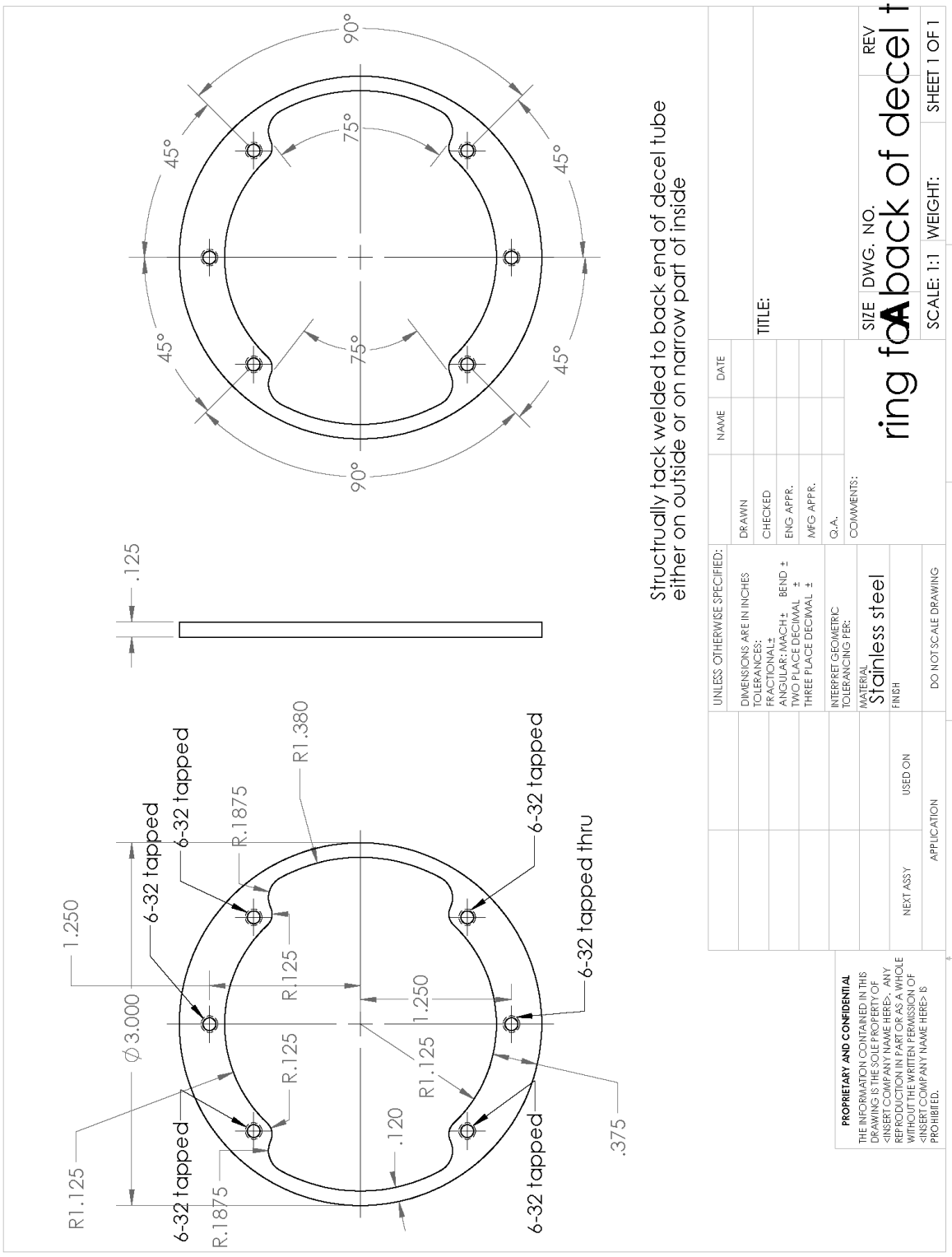

Figure B.25 – Ring welded to the back side of the decelerator tube for mounting the back electrode.

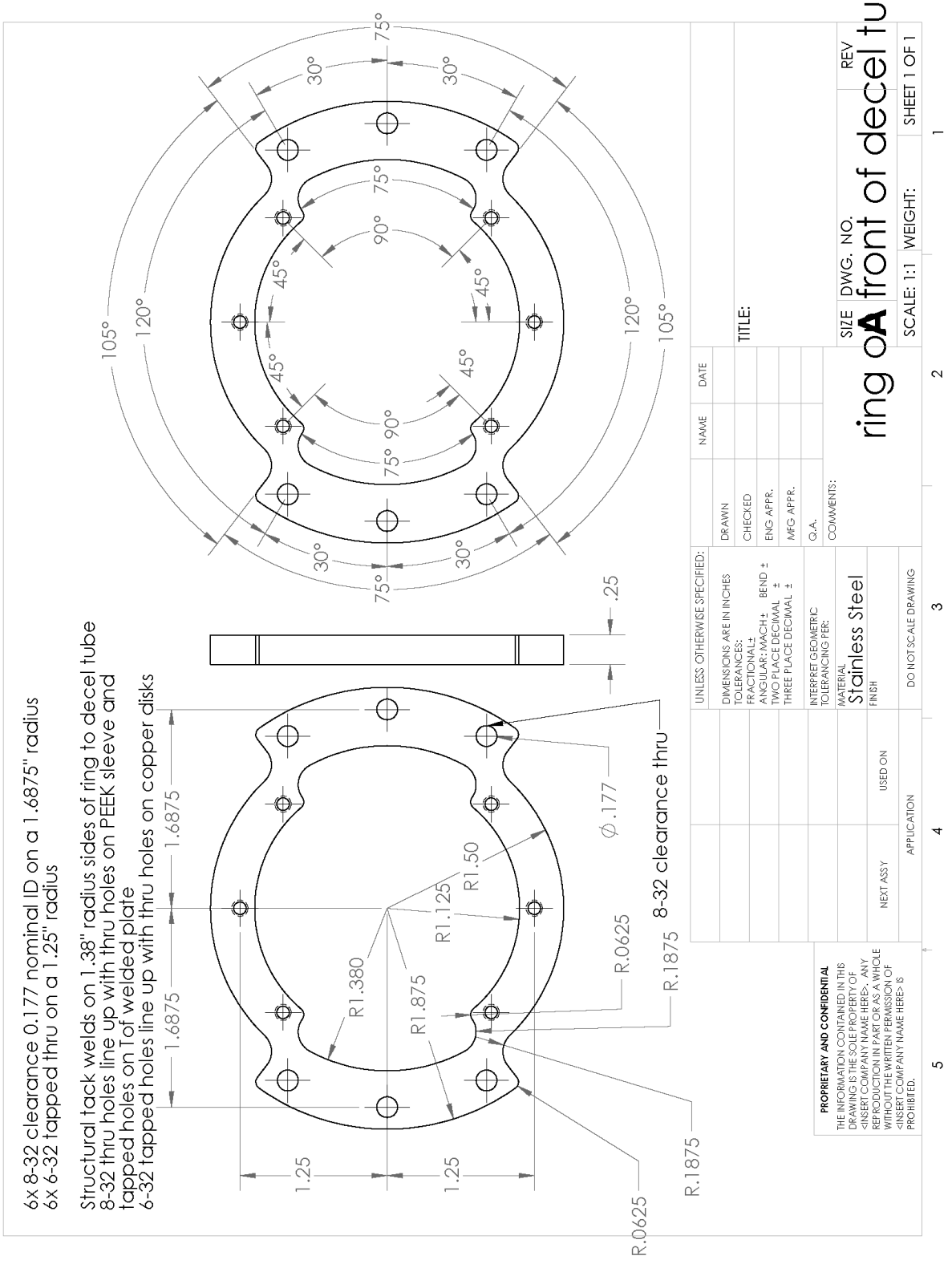

Figure B.26 – Ring welded to the front of the decelerator tube for mounting the front electrodes and securing the decelerator assembly to the mounting brackets inside the flight tube.

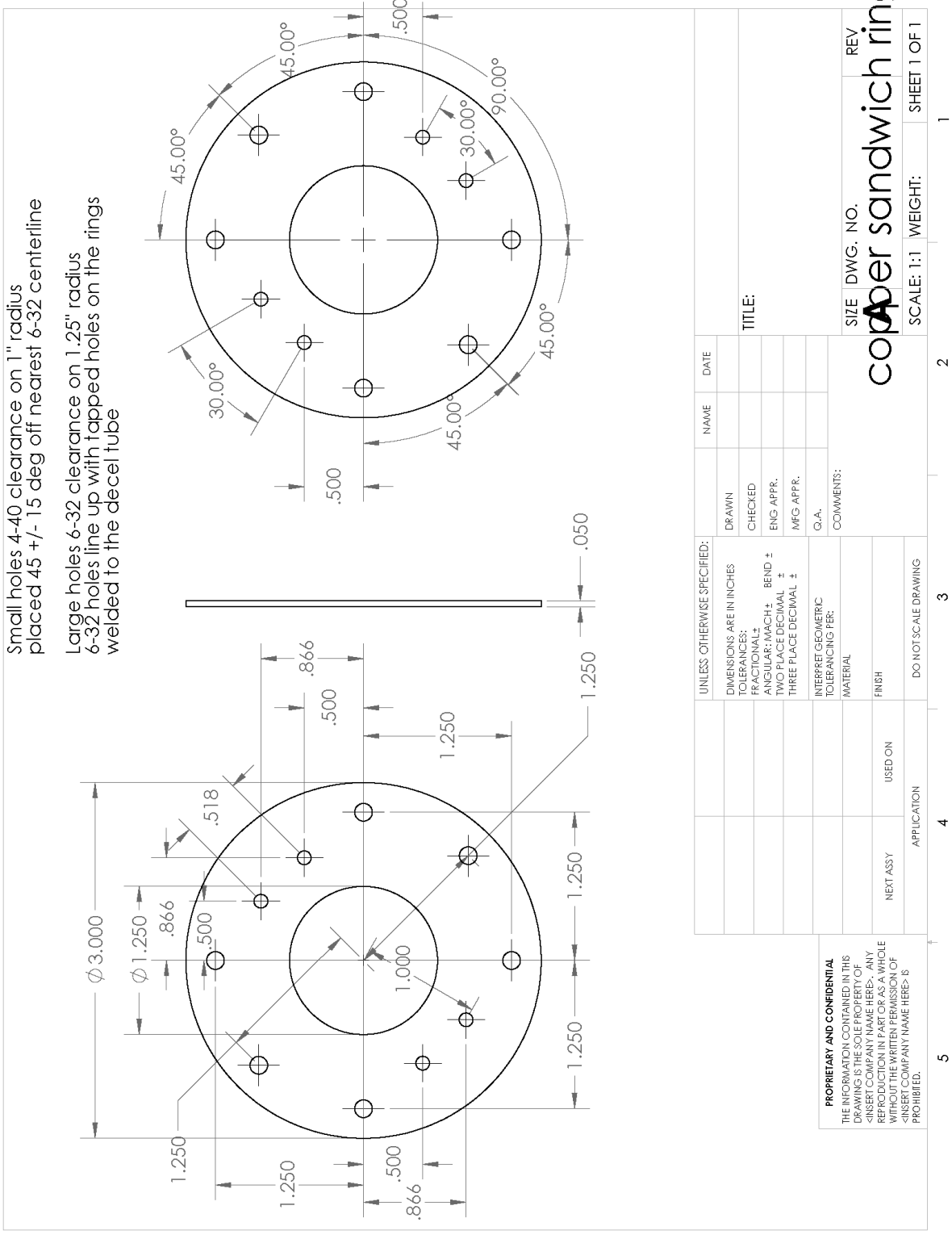

Figure B.27 – Copper electrode plate for mounting nickel mesh along the ToF axis.

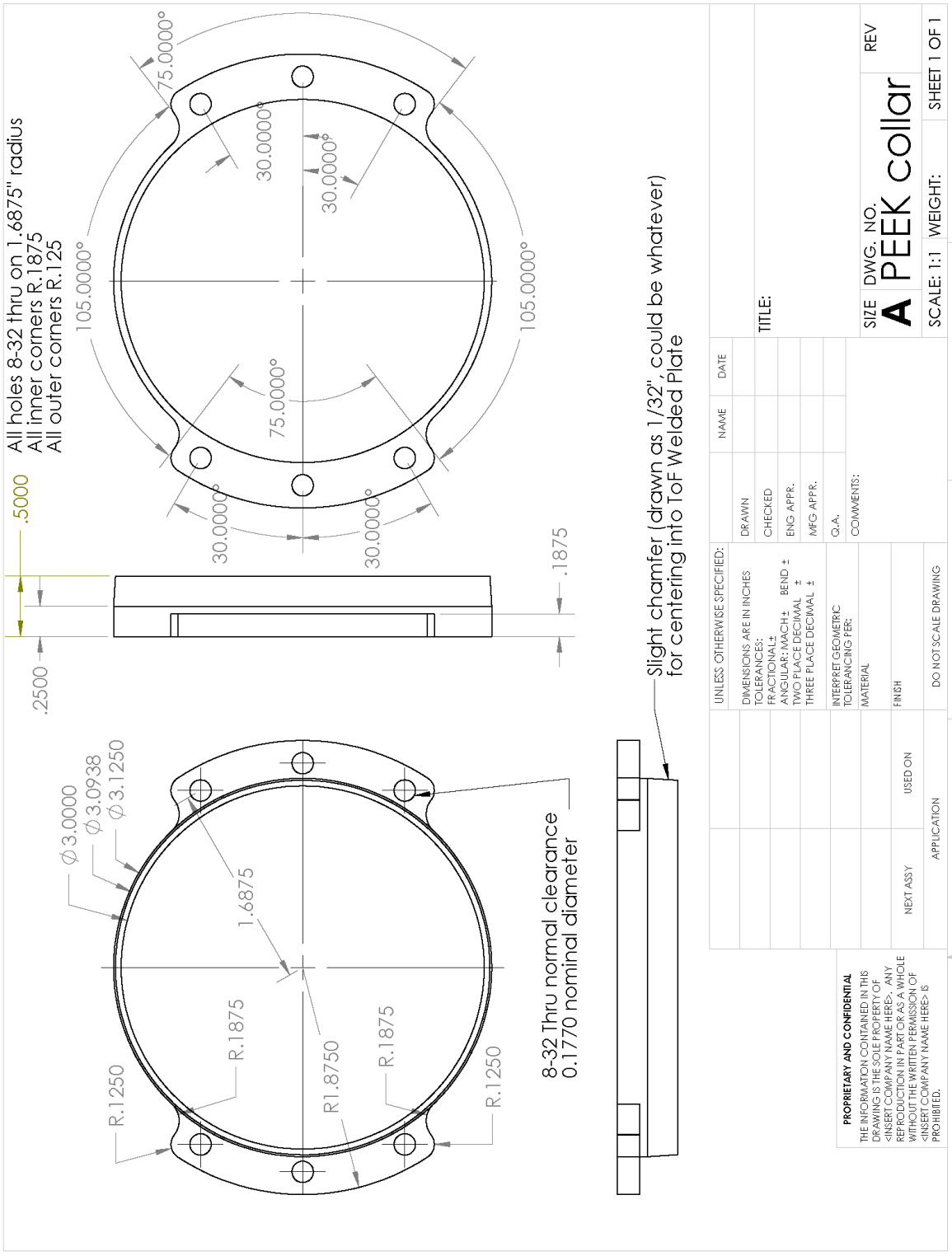

Figure B.28 – PEEK collar for electrically isolating the decelerator tube from the rest of the flight tube.

Appendix C – Laser Alignment Tips and Tricks

C.1 Overview

This appendix is meant to serve as a summary of laser alignment notes for the Astrella turnkey femtosecond laser system and TOPAS-Prime OPA and NirUVis upconversion systems. While there may be some components to the alignment missing, given there is no comprehensive step-by-step instruction for the alignment of the Astrella in particular, it was thought to be prudent to include this here.

C.2 Aligning Ultrafast Laser Pulses

Pre-Alignment Safety

Before beginning any alignment procedures, make sure that LASER CURTAINS ARE FULLY DRAWN around laser table, that all doors to the lab are LOCKED and that the LASER ALIGNMENT IN PROGRESS SIGN IS POSTED ON ALL DOORS into the lab. Any personnel in the lab during alignment should be WEARING LASER protective eyewear FOR 800 nm at all times, and for other wavelengths as specified below.

1. Post the "Laser Alignment in Progress" notice sign outside the laser lab before beginning any alignment procedure.

2. Notify any personnel, both authorized and unauthorized, in adjoining lab space or with access to the lab that laser alignment will be occurring and appropriate precautions will be taken in the event the lab will need to be accessed or personnel contacted during the alignment process.

3. Review alignment procedures listed here.

4. Identify equipment and materials necessary to perform alignment.

5. Check that the laser curtain is securely closed with no gaps.

6. Check that only authorized personnel are present in the laser lab before beginning alignment.

7. Ensure all personnel in the room are aware of and are wearing the appropriate laser protective eyewear before beginning alignment.

8. To reduce accidental reflections, watches, rings, dangling badges, and other reflective jewelry or materials must be taken off before any alignment activity begins.

9. Alignment should only be performed when there are at least two authorized users present who have been trained to respond to a laser safety emergency.

10. Check for and remove any foreign objects in the beam path other than safety controls such as beam blocks. Remove all unnecessary equipment, tools, and combustible materials from the laser table and immediate area to minimize the possibility of stray reflections and non-beam accidents.

C.2.1 General Alignment Safety Concerns

1. Use of non-reflective alignment tools should be considered. When reflective tools are required, be mindful to keep tools out of the beam path.

2. Never allow the beam to propagate beyond the point to which you have aligned and always be aware of the full beam path.

3. Always block the beam upstream when inserting/removing anything into/from the beam path, such as alignment irises.

4. Use a pair of index cards when checking the alignment of the beam so that you never have to leave the beam unblocked to move a card past a mirror.

5. As alignment proceeds down the table, a beam block should always be placed downstream in a position to catch the beam directly after the pair of mirrors being aligned, preventing the beam from propagating through an unaligned path.

6. Be aware that all transmissive optics generate back reflections and some reflective optics have substantial leak through. When working with these components be sure to track, block, and record all stray beams. This is a particular concern with filters (We currently use both ND and Bandpass filters), which generate strong specular reflections that can propagate back up stream a long way before diverging off the beam path due to very slight misalignments. When such a reflection travels back upstream and encounters a beam splitting optic a new beam path can be formed in an unexpected direction. This is also a particular concern with curved transmissive optics. Uncoated focusing elements can potentially lead to back reflections that focus. Despite these being orders of magnitude lower power than the main beam, there may still be sufficient intensity at the focus to burn skin and/or ignite combustible materials, such as index cards. At sufficiently high powers the focus may create plasma in the air resulting in a loud “buzzing” noise at the repetition rate of the laser, a glowing white spot at the focus where nonlinear optical processes are occurring, and the creation of ozone that smells like electric discharge. This can be disconcerting when unexpected. If this occurs simply block the beam upstream from the source of the reflection and

either reduce the power of the beam or change the reflective element to a less reflective optic. These should be treated like other stray beams with the exception that if they can't be eliminated, they should be directed to a beam block and should not be allowed to directly reflect back into the laser system.

7. When working with focusing elements, it is important to be aware that there may be sufficient intensity at the focus to burn skin and/or ignite combustible materials, such as index cards. At sufficiently high powers the focus may create plasma in the air resulting in a loud "popping" noise at the repetition rate of the laser, a glowing white spot at the focus where nonlinear optical processes are occurring, and the creation of ozone that smells like electric discharge. This can be disconcerting when unexpected. If this occurs simply block the beam upstream from the focusing element and either reduce the power of the beam or change the focusing element to a less tightly focusing optic.

8. Keep the plastic or aluminum covers over all the windows or chamber openings whenever they are not being actively used to align the laser through that chamber or check the alignment of the beams/check for clipping. Focusing the laser down to a point in the gas cell and interaction region will create scattered light that can still be harmful and unpredictably scattered off the reflective interior of the chamber. Any thin metal filters in the XUV beamline will also generate a considerable amount of scattered light as they are dichroic filters, not absorptive filters meaning they reflect the driving laser beam back into the chamber. As the filter surfaces are non-uniform, this leads to the full intensity of the beam being scattered back through the vacuum chambers under normal operating conditions and so it is paramount the window covers be used at all times the laser is going through the vacuum chambers. There is still considerable scattered light present after the thin metal filters so no part of the XUV beamline should be considered free of the driving laser light when in use.

C.2.2 Internal Alignment

1. Ensure that all users are wearing appropriate laser protective eyewear, warning signs are posted, and laboratory doors are closed.

2. Place the power meter directly after the first turning mirror or between the laser output and the first turning mirror (careful not to place the power meter normal to the beam to minimize scatter back into the stretcher/compressor)

3. Turn on the laser power supply and turn the key interlocks to the run position.

4. On the Vitara computer, switch control to remote and turn on the Vitara pump laser (the Verdi-G).

a. Optional – to check the performance of the Vitara, you can check the CW power and warmup power increase.

i. To do this, ensure the Vitara has been off for at least 3-4 hours with the chiller running.

ii. Turn on the Verdi-G pump and wait for the Vitara to modelock. If the Vitara is stuck rastering you can turn the starter off and wait for it to start lasing CW and it will typically modelock spontaneously.

iii. Once the laser has modelocked, turn the starter off in the advanced settings menu and drop the pump power down by 2W briefly before returning to the normal set power. This should break modelocking and the laser will come back up with a CW output.

iv. Once in CW mode, record the initial power on the internal power meter. After warming up for 3 minutes record the power again, then continue recording the power in 5 minute intervals for 30 minutes. The CW power will typically only increase 10-15 mW over the course of this 30 minute period if well aligned and adequately temperature controlled. If it goes up more than 30-40 mW, there is likely a problem in the cooling loop for the oscillator or the Verdi-G lasing medium is nearing failure.

v. Finally, turn the starter back on to modelock the oscillator and record the modelocked power. This should be approximately 100 mW more than the CW power once warm.

5. Once the Vitara is modelocked, allow it to warm up for ~10-20 minutes to allow it to stabilize before slowly ramping the Revolution current to the normal operating current. Measure the 800 nm output power and make note of this in the laser log.

6. Turn off the laser and power supply.

7. Take off the lid and screw on safety overrides.

8. With both the Vitara and Revolution off and interlocks deactivated, open the top of the laser and screw the tabs into the laser cover sensors.

    a. If the Vitara is in remote mode and the interlock is engaged, the computer may repeatedly throw a 12C error and the Vitara will turn itself on without user input if the cover sensors are pushed down.

9. The internal layout is pictured on the next page. The beam path between the various internal components is shown with relevant optics labeled.

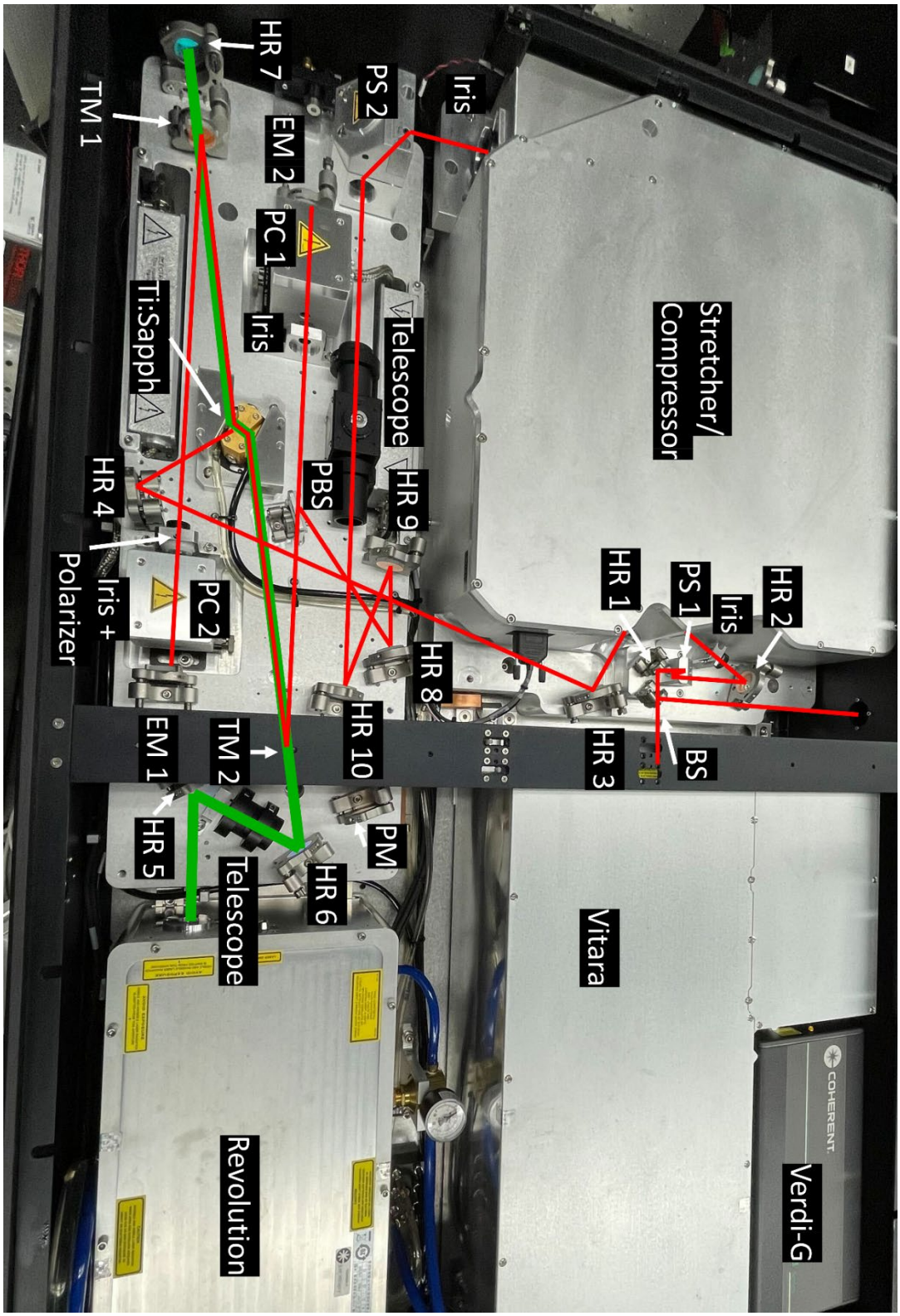

Figure C.1 – Labeled diagram showing the internal mirrors and beam path within the Astrella ultrafast amplifier.

Once the interlocks are engaged, turn the Vitara on and allow it to restabilize. Once stable, check the steering into the stretcher using the iris directly before the stretcher (between the stretcher and Vitara) and the crosshairs on the amplifier cavity side of the stretcher (pictured below, with diffraction from the grating and the center spot to align to the crosshairs).

a. It is important not to block the seed from going into the stretcher as unblocking it rapidly can potentially burn the optics in the stretcher.

Figure C.2 – Image of the seed steering alignment tool on the side of the stretcher/compressor enclosure used to set the far-field alignment of the seed into the stretcher/compressor. The circular beam should be aligned to the center of the cross-mark and the diffraction from grating should align with and be parallel to the center mark.

10. If the steering into the stretcher is good, check the seed steering into the amplifier and compressor to make sure that it is roughly adequate.

a. Note the seed steering does not need to be perfect. Clipping on the Ti:Sapphire mount is both normal and unimportant as a reasonable portion of the seed (~75%) is all that is needed to seed the cavity and is only there to supply the spectrum the amplified pulse will take on, the mode of the beam is determined by the cavity. Thus the seed only needs to be hitting the right spot on the Ti:Sapphire crystal to properly seed the cavity. A typical seed alignment on the crystal mount is shown below.

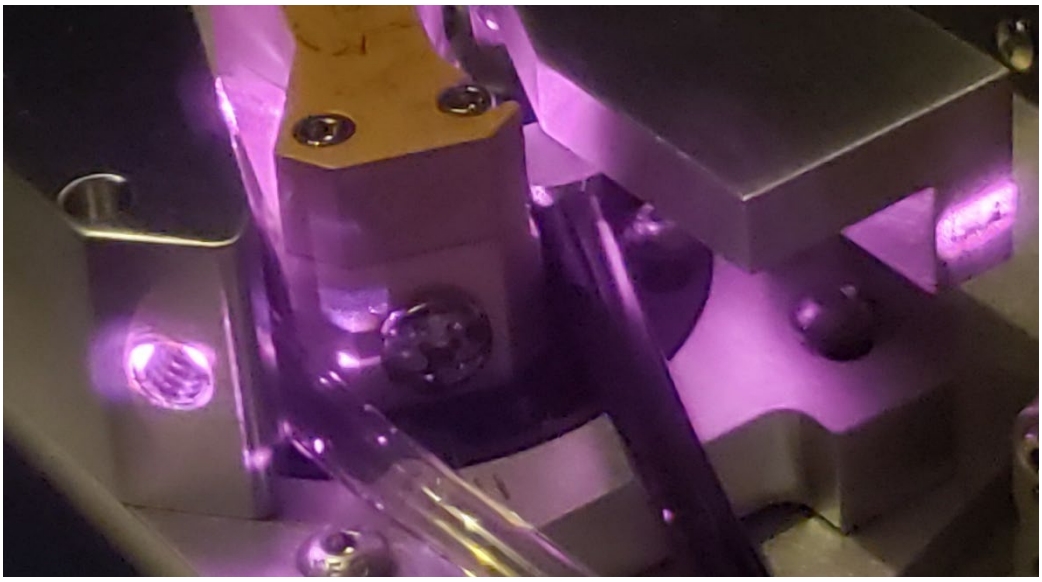

Figure C.3 – Image of the Ti:Sapphire crystal mount in the center of the amplifier. In the lower left corner of the image is the seed entrance aperture, wherein the seed passes before being incident on the crystal face.

b. This is also a good time to check for potential burns in the stretcher. You can measure the power into the stretcher by inserting a power meter between the iris and input of the stretcher. This should be the same as the power measured off the 50/50 beamsplitter (BS) outside the laser through the small inspection port on the side of the Astrella. The stretcher should be approximately 70% efficient and approximately 100-130 mW of seed should make it to the Ti:Sapphire crystal, although the amplifier can be adequately seeded with as little as 10 mW.

c. When checking the oscillator power externally, it is also advisable to check the spectrum of the oscillator output. This should be double bumped and free of modulation as shown below.

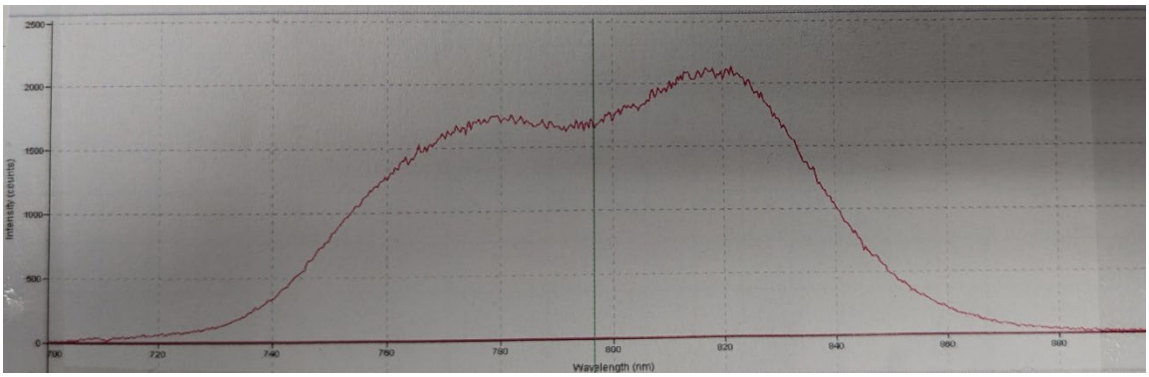

Figure C.4 – Typical spectrum of the seed output with bimodal distribution.

11. If the steering of the seed is good, turn on the Revolution and check the steering of the amplified beam into the compressor.

    a. The Revolution will start to lase at about 11 A and pump steering should be checked at this power. The mode will typically look terrible at these low powers but the alignment on the crystal is easier to check without burning notecards. The seed and pump beams should be well overlapped and centered on the crystal face.

    b. This point is also a good chance to check for burns on the Ti:Sapphire crystal. The green light will scatter off any burns and will be readily apparent at these low powers. If a burn is suspected, you should more closely inspect the crystal by turning off the Revolution and Vitara and removing the interlock defeats, then taking a green laser pointer (class 1 or 2) and shining it through the crystal so you can look for scattering without goggles on.

12. If the Revolution steering is good, measure the initial seeded amplified power inside the cavity by turning the Revolution off, blocking the seed after the stretcher, placing the power meter before the iris into the compressor then unblocking the seed and turning the Revolution back on. This should be recorded in the laser log.

13. With the power meter in place, turn the Revolution off, block the seed ***after*** the stretcher, and turn the Revolution back on. With the Revolution on, increase D2 until the power measured for the ASE light is the same as the power of the seeded amplified light (this should be approximately 35 ns, called burn in reduction time) and record this.

a. It is good to take a picture of the delays before adjusting any to make sure they can all be returned to their previous setting even if you forget what they were. For reference:

i. Delay 1 corresponds to Pockels Cell 1 trigger delay; the duration of triggering can be adjusted in the options menu of the SDG box. (Value as of May 23, 2023 – 5010.00 ns)

ii. Delay 2 corresponds to Pockels Cell 2 trigger delay. (Value as of May 23, 2023 – 5133.75 ns)

iii. Delay 3 corresponds to the oscilloscope trigger for reading the cavity buildup *via* the photodiode behind EM 2 in the amplifier cavity. (Value as of May 23, 2023 – 5226.75 ns)

iv. Delay 4 corresponds to the Revolution trigger. (Value as of May 23, 2023 – 2907.25 ns)

v. Delay 5 corresponds to the trigger running to the oscilloscope above the photoelectron detector. (Value as of May 23, 2023 – 5225.75 ns)

vi. Delay 6 corresponds to the trigger running to the acquiris DAC oscilloscope card. (Value as of May 23, 2023 – 5205.00 ns)

14. Tweak the mirrors directly behind the Pockels cells (EM 1 and EM 2) starting with horizontal alignment for power. When well aligned, the ASE should be around 9W. If this isn't attainable, aligning the afterburner (the backwards mount in the bottom left corner, HR 7) can potentially get the extra power.

a. If aligning the afterburner also doesn't improve the ASE power, there may be an issue with either the Pockels cells or the Revolution power. The Revolution power can be checked by inserting the frosted pickoff mirror (PM) in the Revolution beamline before HR 5 and aligned to an enclosed power meter through the inspection port on the side of the Astrella. This should be aligned at 11 A Revolution current and only measured for a short amount of time as the unexpanded Revolution output will damage the power meter. If this power is adequate, the Pockels cells are probably lossy and the laser will need a service visit.

15. Once power has been maximized, turn the Revolution off and turn D2 back to the previous setting. Then unblock the seed and turn the Revolution back on. The mirrors after the Pockels cells can then be adjusted slightly again to maximize power. The afterburner can then be adjusted slightly again to maximize power.

16. Once maximum power has been reached (should be around 9W), turn off the Revolution and block the seed. Then reduce D2 by 30 ns, unblock the seed, and turn the Revolution on. Check the alignment on the iris before the compressor and make sure the pulse is not clipping by looking at the beam profile after the output.

    a. Slight clipping in the farthest edges of the beam is normal and typically fairly unavoidable. This is the result of the grating in the stretcher compressor being perfectly sized to the beam and so the slightest misalignment will lead to a square "shadow" on the farthest horizontal and vertical edges of the beam. This is typically unavoidable and does not affect the performance of the experiment.

17. If the beam is not clipping and is centered on the iris, D2 can be increased to the operating value. Measure the power after the output to record and check the photodiode reading on the scope to ensure that the last two passes on the cavity are approximately equal.

    a. The measured power should be approximately 7 W, though 6.7-6.9 W is acceptable. Comparison to the seeded uncompressed cavity power is another good chance to check for signs of burning in the stretcher/compressor. If the seeded cavity power is ~9-9.5 W and the compressed power is ~6-6.5W, there is probably a burn in the compressor and a service visit will be needed. The compressor efficiency is typically on the order of 75-80%.

    b. The last two passes do not necessarily need to be approximately equal. This is the typical configuration for running as having the last two passes in the cavity maximizes power while increasing stability in the final output pulse. Reducing the number of passes through the cavity by two (eliminating the final peak in the photodiode output) *can* result in slightly broader spectra so a slightly shorter pulse possible. Adding an additional two trips through will reduce the final output power and increase the minimum attainable pulse duration but can increase shot-to-shot power stability.

    c. At this point, you should also check the spectrum of the amplified output. It should be relatively smooth with no obvious signs of spectral modulation. Examples of sprectra with (needing Ti:Sapphire crystal replacement,

comparable to what was seen with Pockels cells misaligned) and without spectral modulation (what it should be) are shown below.

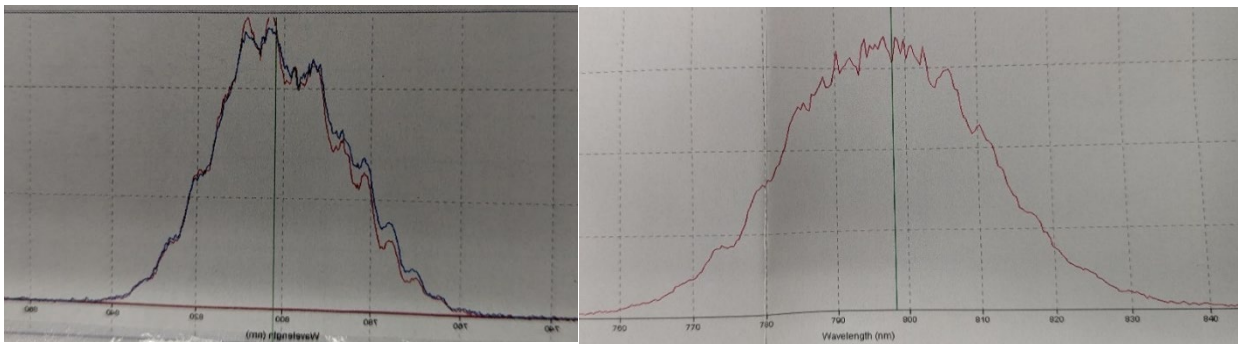

Figure C.5 – Spectra taken of the amplified output. (left) Modulated spectrum indicative of issues present with optics in the amplifier cavity or after. (right) Typical amplified spectrum showing no apparent modulation.

18. When the power is maximized, turn off the laser by gradually powering down the Revo and then turning off the Vitara pump.

19. Replace the laser covering and let the cooling water run for 30 minutes before turning back on.

20. The cavity alignment typically needs to be touched up the day after being realigned as the optics settle. To touch up the cavity, skip to optimizing the seeded cavity power in the internal alignment procedure.

C.2.3 TOPAS-Prime and NirUVis Alignment

- Ensure that all users are wearing appropriate laser protective eyewear, warning signs are posted, and laboratory doors are closed. Check that the laser path will be blocked.

  - Note that no presently available combination of protective eyewear filters can adequately protect against the full spectral range of the TOPAS, so alignment should be done with the NirUVis sealed at all times when Sum Frequency Fundamental + Idler (SFI) or 2nd Harmonic Signal (SHS) light generation processes are present.

- Refer primarily to the alignment notes in H. Williams' thesis (Appendix A) and the alignment notes and diagrams in the TOPAS-Prime/NirUVis/WinTOPAS user manuals. A brief summary of written notes will be provided below and are meant to be used as a quick reference or to supplement the manual, not to replace it.

    - Scanned copies of these documents are attached in Appendix D of this document. The TOPAS and NirUVis beam paths are shown on the following pages.

1. To start alignment, make sure the input is blocked in the telescope before the TOPAS entrence (A0), open the cover, pull the white post in the top right corner up, and place a small black optical post in front of M7 and M9.

2. Before unblocking the beam and opening the TOPAS shutter, add notecards in front of BS1, VF, M3, M4, NC1, M5, and M16. This will ensure you can controllably introduce light once it has been aligned sufficiently for the next stage of alignment without accidentally allowing light through to the next stage of crystal which can quickly burn them.

3. Remove the beam block in the telescope and make sure the beam incident on the final curved mirror in the telescope is centered on the mirror. Then, use the second curved mirror in the telescope and the turning mirror right before the TOPAS to align the 800 to the initial iris (A0) with the curved mirror and the 800 after BS1 and BS2 to A1 initially then A2 once alignment has progressed far enough.

4. Close A1 and set VF so the boundary between the minimum and maximum density is opposite the point the beam passes through. Then, open A1 while monitoring the for white light generation. The iris should be opened until the onset of multiple filaments is seen (as shown in section 4.3 of topas manual), then rotate the neutral density filter (VF) to gradually decrease the 800 power until a single filament is observed. Then, close A2 all the way and tweak the alignment of the turning mirror just in front of A0 to align the white light continuum to the center of A2.

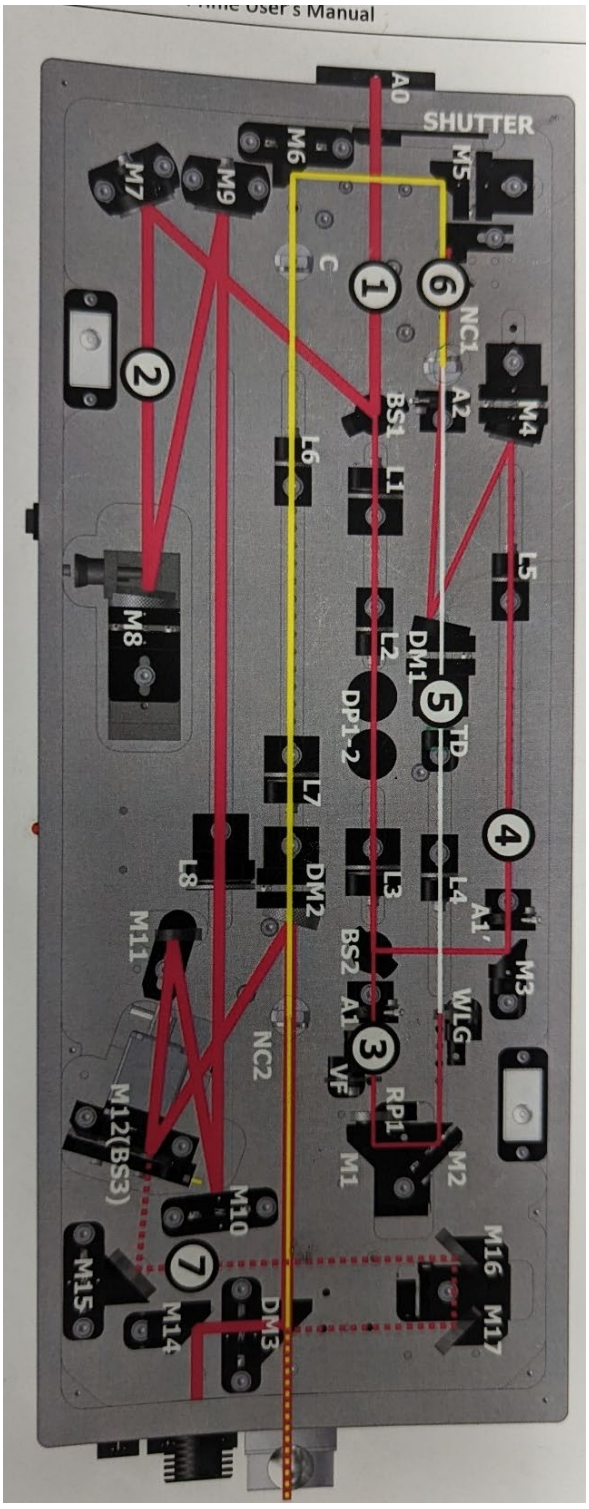

Figure C.6 – Overall TOPAS beam path. Important portions include (1) beam coupling into the TOPAS, (2) pump beam telescope, (3) white light generation, (4) first stage pump focusing and steering, (5) first stage optical parametric amplification, (6) signal separation, steering, and amplification, (7) fresh pump steering.

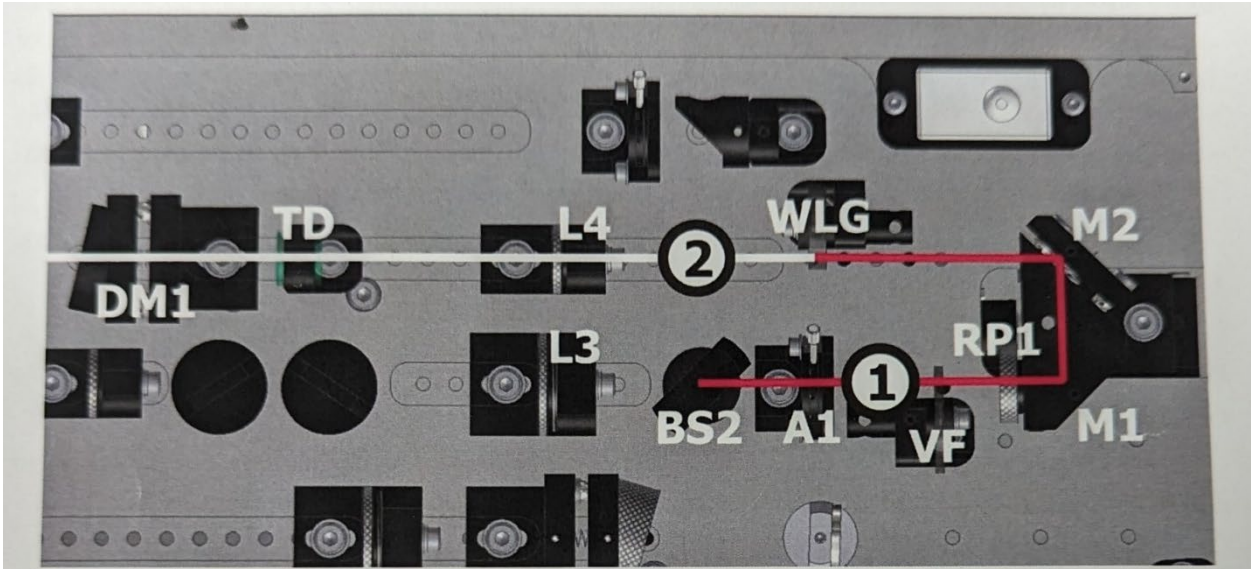

Figure C.7 – White light generation leg of the TOPAS.

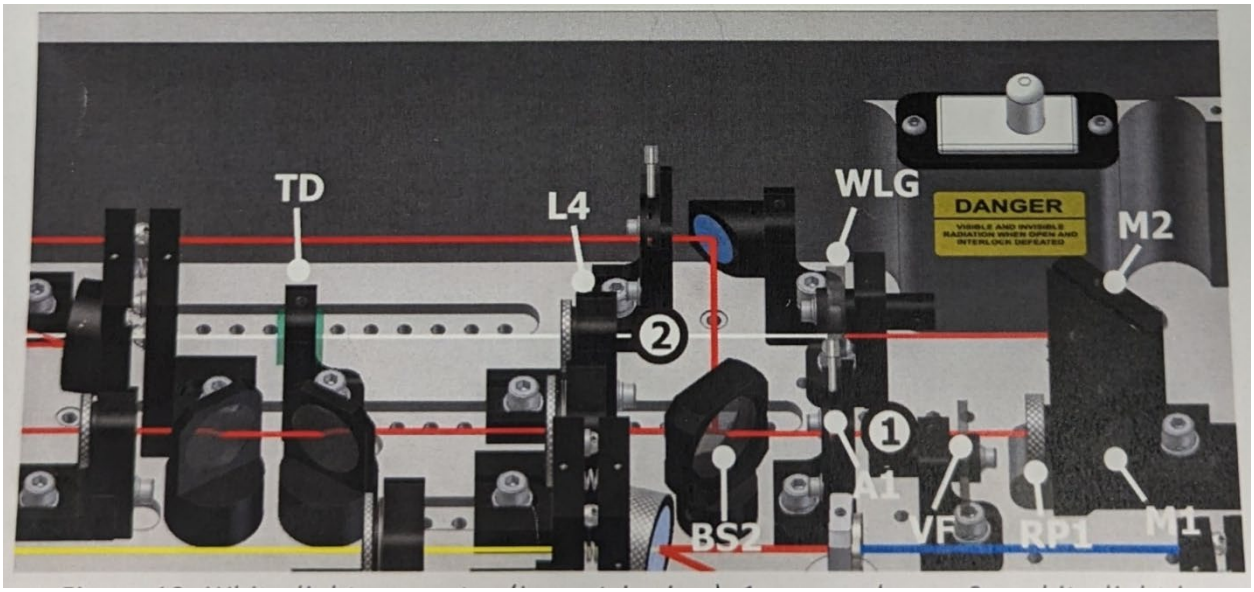

Figure C.8 – Additional view of the white light generation leg of the TOPAS with the steering and attenuation optics for the first stage optical parametric amplification pump beam shown.

5. Next, block the white light continuum anywhere between A1 and DM1 and close the iris A1' all the way down. Then, gradually unblock the pump line labeled 4 making sure it is hitting just left of center on A2 and is hitting well away from the edge of the block between NC1 and M5 to prevent M5 from getting burnt.

6. With a notecard in front of M5 just in case (accidents happen) and with the white light continuum line still blocked, slowly open A1' until you see white light generated in NC1 then quickly close the iris down and block the beam before NC1. Once you've done this, introduce both the white light and pump beams into NC1. Ensure both beams are vertically aligned and then adjust the horizontal to make sure both beams are overlapped just in front of NC1. Then adjust horizontal alignment of M4 and DM1 simultaneously to maximize SFS and SFI intensity (the position of these spots shown at the end of section 4.4 of the TOPAS manual, should be blue and green dots)

a. If you can't find SFS/SFI generation, it is helpful to adjust the delay stage M1 and M2 are on. Once you find the displacement needed to generate the SFI/SFS, you can adjust the path from M4 to NC1 (make it shorter or longer using the DM1 steering to compensate) accordingly to account for the temporal overlap needed.

b. If the mode looks terrible or the amount of 800 needed to generate white light is unusually small or large, you may need to change the position of L4 and L5 to adjust the focusing conditions.

c. To optimize the signal seed mode, adjust L5.

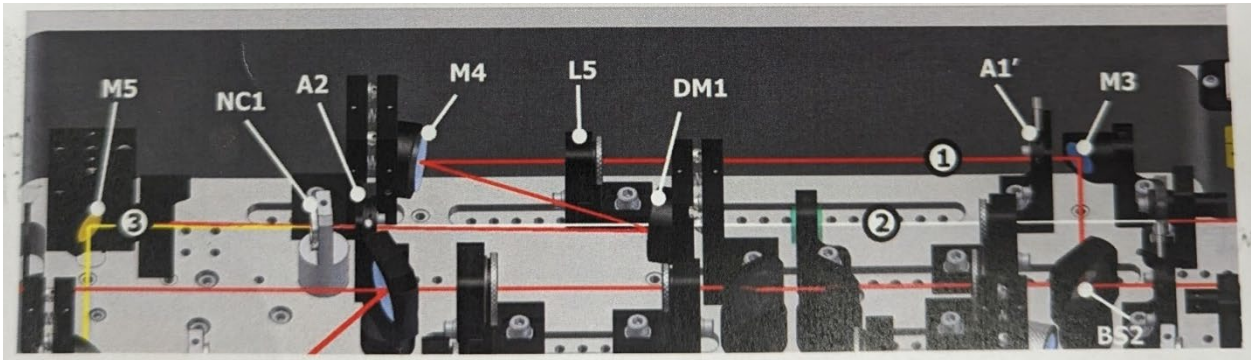

Figure C.9 – Three dimensional view of the optics used for alignment through the first stage of optical parametric amplification and signal isolation.

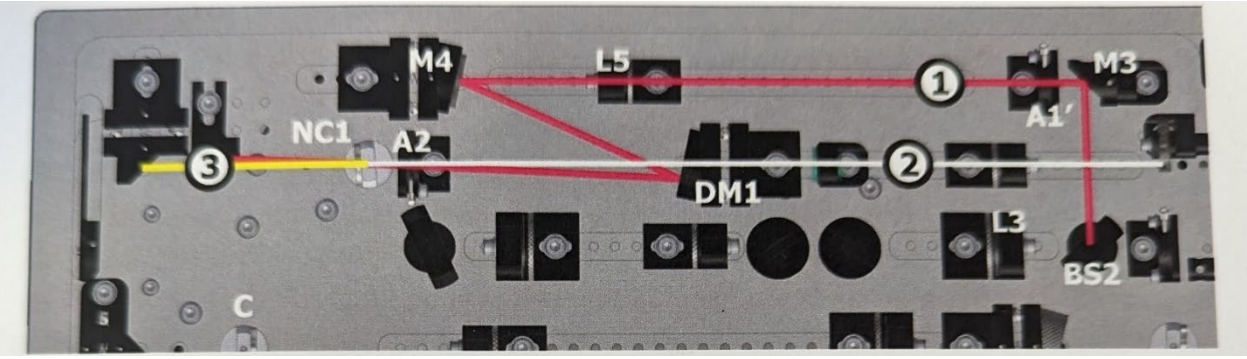

Figure C.10 – Alternate view of the optics used for alignment through the first stage of optical parametric amplification and signal isolation.

7. Once OPG has been optimized, the signal can be aligned to irises that can be inserted before L6 and after NC2. You can use DM1 to optimize power after NC2 and M5/M6 for alignment. Power after NC2 should be 2 mW @ 1300nm.

8. If the signal looks divergent or convergent, use L6 to adjust the size at NC2 and L7 to collimate. Check the collimation after NC2 and 3-10 meters away as this is critical to good conversion efficiency in NC2.

9. Once the signal seed has been aligned and collimated, start alignment of the OPA pump line. Start by checking the pump collimation (lower the pump power and check diameter at NC2 and after M14).

10. Ensure the beam is centered on M9, L8, and M10. If it isn't, use M8 and M9 to compensate.

11. Check the alignment at NC2. Use M10 and DM2 to align the pump beam straight through black plastic apertures that can be placed between DM2 and NC2 and between NC2 and DM3.

12. Once the pump beam is collimated and aligned straight through NC2, use the manual delay adjustment under M8 (accessible through a port on the outside of the casing by the power switch) to optimize the power measured after DM3. This should be done with the fresh pump beam blocked before M16.

13. With the OPA second stage optimized, use DM3 and M15 to maximize the power of the UV light out of the end of the TOPAS.

14. Once UV power is maximized, check the collimation and spectrum and note these in the log. The spectrum shouldn't be more that 1 nm off the set value. The collimation, while compensated for by a telescope after NirUVis, is an important indicator of whether the conversion efficiency can be improved by adjusting lens positions in the TOPAS and, more importantly, can indicate if the beam focuses in the NirUVis which can severely damage the optics.

15. For a quick tune up, go into the motor direct access menu and reset all the motors. This should reoptimize the delays and crystal angles and give a few mW bump in power.

16. If all else fails, try adjusting the Astrella compression slightly, especially if the TOPAS isn't lasing well.

17. Day to day tune up should only consist of adjusting the turning mirror before A0 and M5 externally. If this doesn't increase power and stability sufficiently, you can try adjusting M15 and the delay from M8 externally as well.

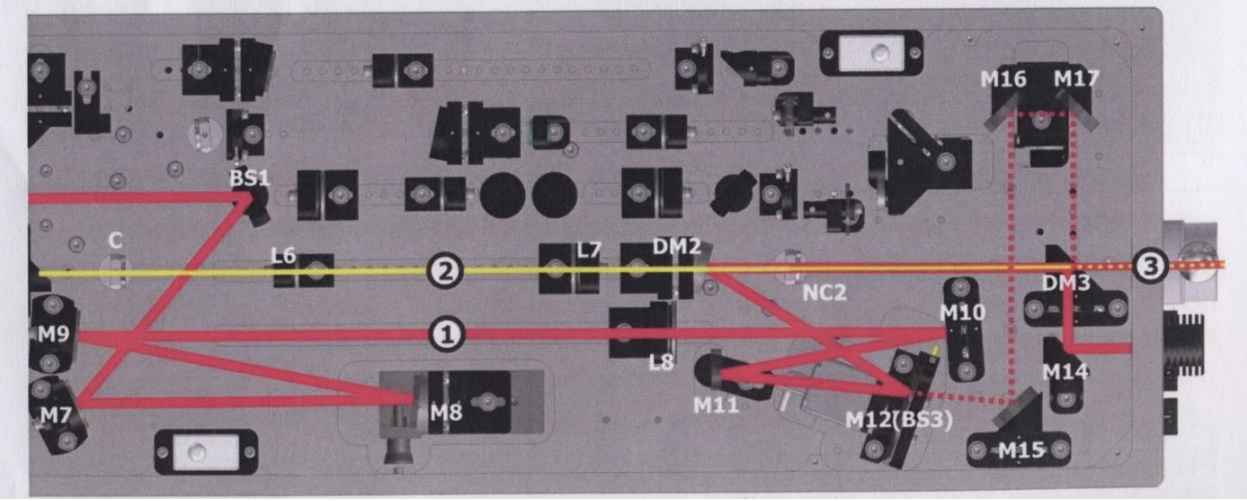

Figure C.11 – Second stage optical parametric amplification alignment optics with fresh pump steering included.

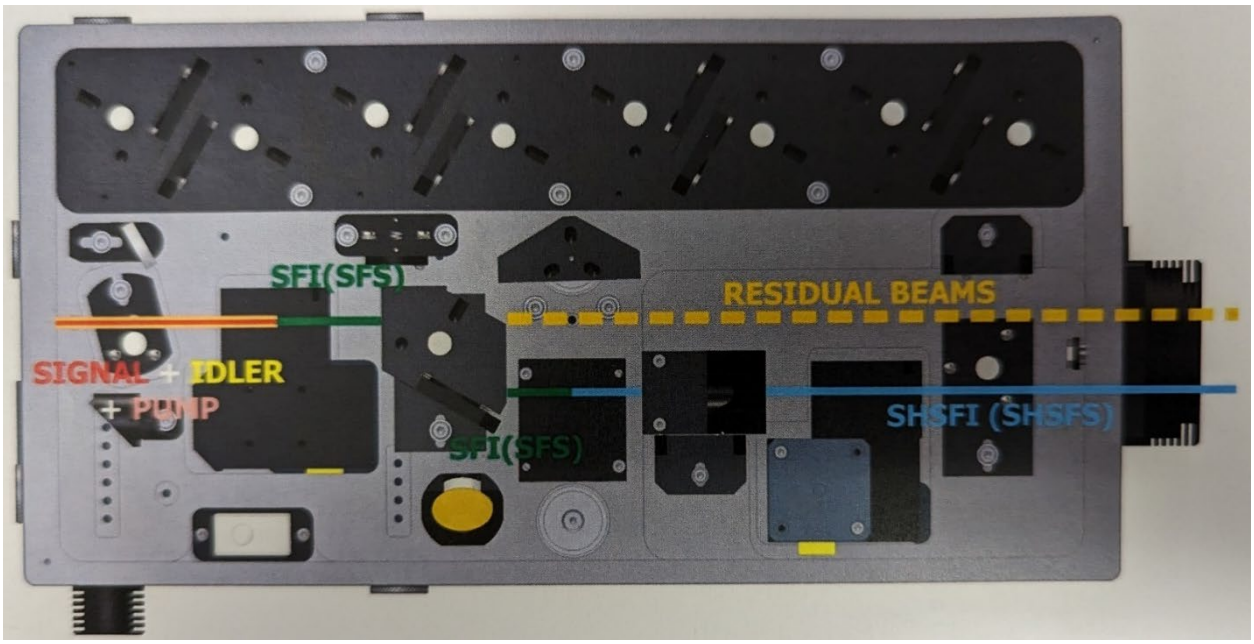

Figure C.12 – NirUVis beam path in the typical configuration used to generate 235 nm to 265 nm tunable UV light.

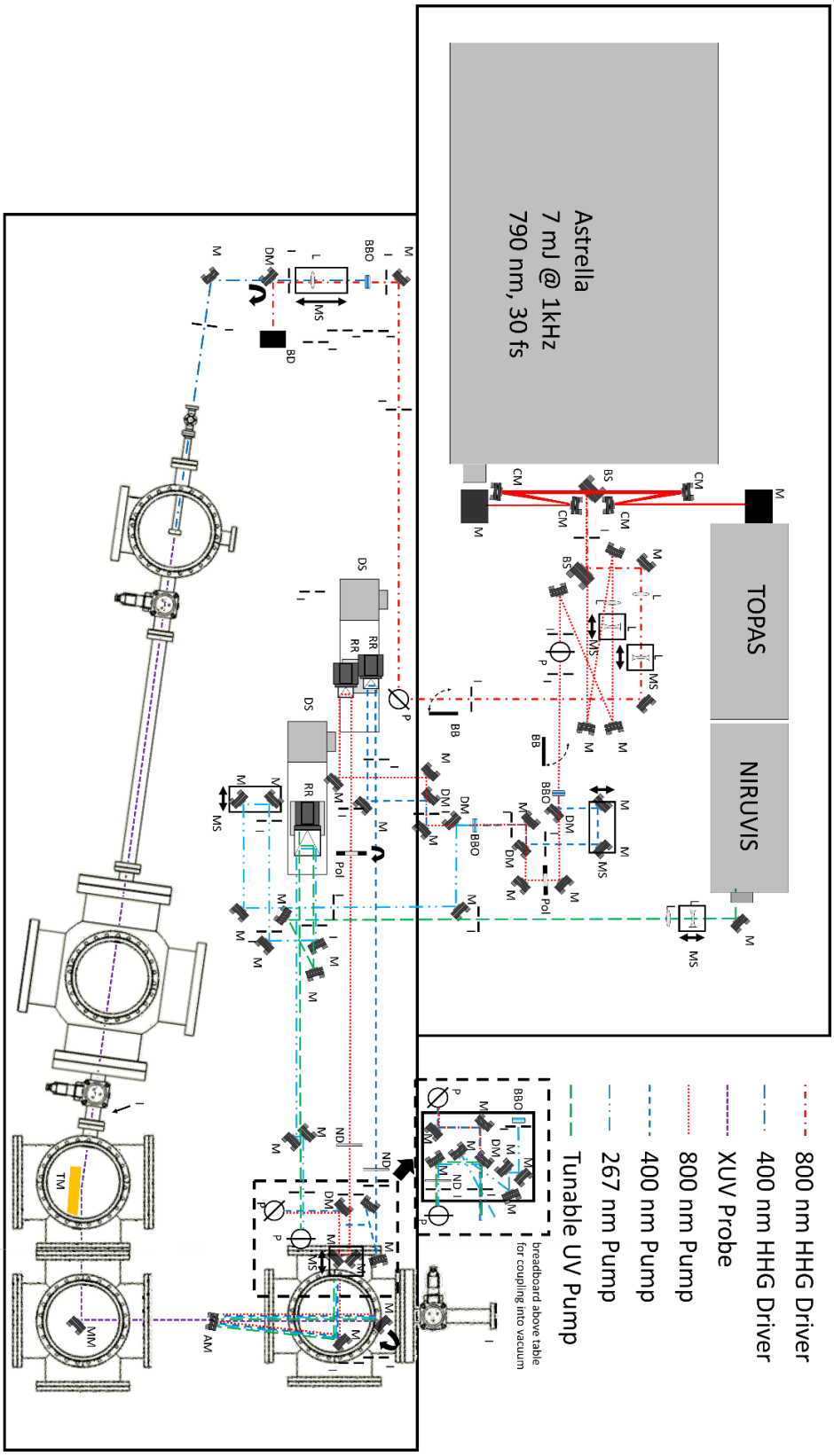

Figure C.13 – External beam path current as of writing this document.

C.2.4 External Optic Alignment

1. The following are general requirements for external optic alignment, alignment notes specific to the various types of optics typically found on the table layout will follow.

2. Ensure that all users are wearing appropriate laser protective eyewear, warning signs are posted, and laboratory doors are closed. Check that the laser path will be blocked.

3. BEFORE UNBLOCKING ASTRELLA OUTPUT, make sure that there are no reflective objects on the table (other than necessary mirrors) which might get in the path of the laser. Select and wear laser-safety eye-wear appropriate to the wavelengths that will be on the table.

4. Set Astrella power to minimum required to perform necessary alignment by reducing the Revolution current.

5. Make sure that all mirrors in periscopes are blocked until necessary for continuation of alignment, as these mirrors direct beam upwards.

6. Align beam on irises along beam-paths appropriate to the experiment. Block beam directly after each iris with index card and align on the iris by viewing the beam profile on the card.

    a. Alignment is substantially easier and much more convenient if irises are placed directly into bolt holes in an optic mount so only the vertical alignment of the iris is possible. This ensures ***temporal overlap is easier to find*** and HRs/dichroics are at the appropriate angle for best performance.

7. Make sure the beam is centered on each mirror in the beam-path, blocking the beam directly after each mirror as you check it. Make sure that beam does not 'clip' (ie. that part of the beam does not go past the mirror, or strike the corner of another mirror and get sent off at unexpected angles.) Use a fluorescent notecard held directly in front of mirror to determine that beam is centered, and directly after the mirror to check beam profile for 'clipping.'

8. If a mirror mount has to be moved, block beam before the mirror, unscrew mount and re-tighten. Make sure to block beam with card directly after the mirror which has been moved, and use card to 'follow' the beam path. Adjust mirror mount controls to make sure that beam strikes center of the next mirror along the beam-path.

9. If the TOPAS is used, wear LASER PROTECTIVE EYEWEAR COVERING the Signal, Idler, SHS, SHI, SFS or SFI as appropriate IN ADDITION TO 800nm which will be on the table whenever the laser output is open.

10. USE EXTREME CAUTION in aligning beam onto stage for input into chamber, and into the vacuum chamber itself, as this is near eye-level.

11. When aligning beam through the vacuum chambers, restrict access to that corner of the lab. The beam is difficult to block as you generally can't visually confirm beam is on the notecard due to the space constraints in the chamber. Aligning through the vacuum chambers is particularly dangerous due to all the reflective surfaces inside so special care should be taken. When aligning through the interaction region, only the person performing alignment should be in that corner of lab during the alignment process as the laser beam is passing from the vacuum chamber to the wall (~5ft.) at near eye-level. If possible, the beam should be blocked at the exit window on the vacuum chambers whenever possible to keep this area safe.

12. When alignment through the vacuum chamber is completed, replace card blocking output from the vacuum chamber, and replace laser curtains.

13. Check that all mounts are tightly in place and will not inadvertently shift, causing changes in alignment.

14. After each step and again after completion of alignment, check for stray beams—using IR viewer or IR card if necessary, and note that check has been performed on checklist posted in working area (See section IV.A.8). Check that all mounts are tightly in place and will not inadvertently shift, causing changes in alignment. Check that all beam enclosures/stops are in place. Add non-reflective aluminum foil or aluminum beam blocks with notecards taped over the front to the enclosure or on the backs/sides of any optic mounts where stray beams are found to help clearly identify and safely block any stray beams found while checking for stray beams.

15. If changes have been made to beam path, note on alignment checklist in work area, inform other researchers of changes and be sure that they signal their understanding by initialing the checklist.

16. Measure/remeasure the optical delay between any optics that have been adjusted and record these in a spreadsheet. This will make finding temporal overlap easier and more reproducible.

17. Replace and check that ALL laser beam enclosure and/or beam stops are in place.

C.2.5 XUV Beamline Alignment Notes

1. The XUV beamline alignment requires a greater degree of care than the remainder of the table alignment as it entails aligning ~5 W of IR at nearly eye-level, so extreme care should be taken and Oscillator goggles should never be used.

2. The most crucial component of the XUV beamline alignment is the initial telescoping of the beam. This can be done with either a transmissive or reflective telescoping geometry. In either case, the final beam diameter should give ~90%-95% power through a 10 mm aperture to maximize the doubling power through the BBO. Additionally, the collimation of the beam needs to be as near perfect as possible. This would entail sending the beam ~8 m up and down the table and checking the diameter after. This ensures the focus into the gas cell is as free from spherical aberration as possible, ideally maximizing harmonic flux out of the gas cell.

3. Aligning the periscope should be done carefully, and always take care to measure the power before and after the HRs in the periscope as the 800 HR dielectric materials can take a good bit of wear and tear from the reflected 400 nm light from the BBO and lens. If the reflectivity is less than ~98%, the optic needs to be replaced.

4. The IR beam should be aligned prior to any other optics. The beam should be aligned at an 8^{o} angle relative to the bolt holes on the table. To figure out the point in space it should be aligned to, the toroidal mirror 2f distance plus the gas cell length is a good estimator of the hypotenuse of a right triangle with an 8^{o} angle corner. This distance (plus ~2 cm) combined with the angle, plus the distance from the edge of the table to the center of the toroidal mirror, can be used to determine the distance from the edge of the table to the point the 800 nm beam needs to be

aligned to. This distance, plus the height of the chambers, determines the point just in front of the gas cell the beam must be aligned to.

5. The beam can be aligned to just before the toroidal mirror using the final two HRs at the end of the table to align to the point in space determined in the last step as the near-field point and the center of the 2 ¾ CF half-nipple just before the toroidal mirror as the far-field point. Be extremely careful aligning through the vacuum chambers as the interior surfaces are very reflective so any scatter off the metal surfaces will end up coming out any opening not covered by an opaque material. Window covers should only be taken off when

6. From here, the BBO can be placed in the beamline and optimized if driving harmonics with 400 nm. The dichroic can then be placed at any point that is convenient between the BBO and the gas cell. Once the dichroic is in, the steering adjustments in the previous steps need to be repeated. Again be extremely careful

7. Once aligned, the lens to focus into the gas cell can be put in place. This should be aligned on a delay stage at a position that would put the focus at the exit of the gas cell with the lens in the middle of the travel range of the stage. The generation efficiency in the gas cell relies considerably on the quality of the focusing into the gas cell. To achieve this, the power into the gas cell should be reduced to ~50 mW and a camera with an OD 4 ND filter mounted to the camera using the C-mount threading on the front of the camera and a C-mount to 1" lens tube adapter. It is important to ensure the ND filter is free from burns as the camera sensor is easily damaged by the intense laser light, even at the low powers used. Once the camera is ready, it can be placed flush to the end of the SIGC and the power increased until a well resolved spot is observed. From here, the position of the lens can be adjusted using the stage and a 5-axis optic mount to minimize the size of the spot on the camera and make it as gaussian as possible. From here, the lens only needs to be moved back on the stage by a distance equal to the distance from the SIGC exit to the camera sensor.

8. With the focus set, the power can be increased to check the alignment through the gas cell and at the conflat flange just before the toroidal mirror. The beam should be reasonably well centered through the gas cell, but as long as it doesn't come close to clipping anywhere the actual positioning isn't crucial. The beam should be well centered on the entrance to the toroidal chamber, this is crucial to proper alignment of the toroidal mirror.

9. If the beam was previously well aligned off the toroidal mirror, reduce the power to ~10 mW and check the current alignment. If it is close enough, you can skip the next 3 steps.

10. Once the beam is well aligned to up to the toroidal chamber, the beam should be irised down to a point and the transmitted power set at approximately 1 mW. This ensures no contaminates are burned onto the surface of the toroidal mirror. The toroidal should now be rotated to near normal incidence with the incident beam such that the reflected beam is caught on a notecard affixed to the coflat between the toroidal chamber and the foil chamber. The mirror should then be adjusted so the beam is centered both vertically and horizontally. Then, the mirror can be rotated and vertical steering adjusted so the beam reflects as near perfectly back along its original path. The angle this is achieved at should be noted.

11. The distance from the mirror to the point harmonics are generated should now be adjusted so the distance is as precisely the 2f distance as possible. The current toroidal mirror has a measured focal length of f = 992 mm, so the mirror-to-HHG and mirror-to-detector distances should be exactly 2x992 mm (or 1.984 m).

12. The mirror should now be rotated as near to exactly 86^{o} from the angle of normal incidence as possible. The beam diameter can now be increased to full size and the power increased to ~10 mW. The toroidal mirror can now be adjusted so the beam clips evenly on both the left and right sides of the incident beam, or on the front and back edges of the mirror.

13. With the beam centered on the toroidal mirror, the diameter can be reduced so the beam no longer clips on the mirror, with a diameter of approximately 5 mm. This can best be done with the iris just before the SIGC, which should minimize hot spots due to the irising of the beam. The beam should now be directed through the chambers to a camera positioned at the focus. The focal diameter should now be optimized to be as small as possible using the rotation stage, the vertical adjusters on the sides of the mirror mount, and the horizontal adjuster on the back of the mount to adjust the pitch, roll, and yaw of the mirror. The mirror is best aligned when the vertical and horizontal focal positions are overlapped, giving an extremely small (~75 micron diameter) focal diameter.

14. If the optimization isn't readily accomplished by imaging the beam after the ML mirror and annular mirror, the multilayer (ML) mirror can be removed and the beam can be imaged directly off the toroidal mirror. Once this is done, the ML mirror can be replaced and the beam aligned through the annular mirror to the

interaction region and imaged again there, checking that the beam isn't clipping and the focus hasn't changed dramatically.

15. Once the toroidal focus is optimized, the beam should be aligned off the ML mirror and through the annular mirror. This is most easily done by removing the annular mirror and moving the ML mirror mount and steering such that the beam travels straight through the chambers to approximately 1 mm in front of the skimmer. It is very important not to change the toroidal mirror steering to accommodate any steering from the ML mirror to the interaction region.

16. Once the steering to the interaction region is completed, the alignment of the annular mirror can be done. The alignment of this optic is detailed in the next section. In the current iteration of the experiment, it is in a fixed position so care should be taken to make sure the focal position of the curved annular mirror is the same as that of the toroidal mirror. This is much easier if the annular mirror is on a delay stage, so a pinhole can be placed at the point at which the toroidal directs the imaged XUV driver focus from the SIGC at approximately the 2f distance from the toroidal mirror. Once placed, the focal position of a concave annular mirror can be optimized to the pinhole and then the stage adjusted forwards or backwards and the mirror steering reoptimized to the pinhole until the maximum amount of light makes it through the pinhole.

Appendix D – Publications from Graduate Work

1. **Z. N. Heim**, D. M. Neumark, Nonadiabatic Dynamics Studied by Liquid-Jet Time-Resolved Photoelectron Spectroscopy. *Acc. Chem. Res.*, **55,** 3652 (2022).

2. B. A. Erickson, **Z. N. Heim**, E. Pieri, E. Liu, T. J. Martinez, D. M. Neumark, Relaxation Dynamics of Hydrated Thymine, Thymidine, and Thymidine Monophosphate Probed by Liquid Jet Time-Resolved Photoelectron Spectroscopy *J. Phys. Chem. A* **123**, 10676 (2019).